Technical Physics, Vol. 46, No. 6, 2001, pp. 645–653. Translated from Zhurnal Tekhnicheskoĭ Fiziki, Vol. 71, No. 6, 2001, pp. 1–9.

Nonsolid Rotation of Structures in Isothermal Magnetized Atmospheres

Yu. V. Vandakurov

Ioffe Physicotechnical Institute, Russian Academy of Sciences, Politekhnicheskaya ul. 26, St. Petersburg, 194021 Russia

Received October 16, 2000

Abstract—Possible equilibrium rotating magnetized plasma configurations in which angular asymmetry due to a nonuniform distribution of the molecular weight is absent are studied. The viscosity of the medium is assumed to be negligible. The variables in exact nonlinear equations are separated by representing the vector fields as series in orthogonal vector spherical harmonics. These series are normally divergent. However, the truncation of the series is also possible. Equilibrium models corresponding to the truncated series are generalizations of a simple rigidly rotating model. They are studied below. It is shown that nonaxisymmetric equilibrium structures with the magnetic field of a tilted dipole are possible. In the case of an isothermal atmosphere, conditions for the superrotation of the medium and meridional circulation of the matter may arise. The feasibility of such conditions in the Earth's upper atmosphere is discussed. © *2001 MAIK "Nauka/Interperiodica".*

INTRODUCTION

We consider simple rotating and magnetized models by expressing all vector fields as series in terms of a complete system of orthogonal vector spherical harmonics. In this case, the separation of variables (angular variables and radius vector) in exact equations is possible, irrespective of whether an equation is linear or nonlinear, and conditions of the regular spatial behavior of the fields are taken into account (Section 1). Analysis of nonlinear equations obtained from the initial equations by separating the variables and having the form of infinite series in the aforementioned harmonics suggests that there exist some purely mathematical problems that have escaped the researchers in considering the sets of complex multidimensional initial equations. The case in point is that, for infinite series with nonlinear terms, the number of terms usually increases more rapidly than the number of variables in going to the next approximation. Because of this, a nonzero solution may become impossible (Section 2). Such a difficulty due to the nonlinearity of the magnetic force was discussed in [1, 2] as applied to the equilibrium problem for an insulated axisymmetric magnetic tube in the radiant zone of a nonrotating star. In this case, the equilibrium problem has a solution only for the dipole field. Probably, spotty chemical inhomogeneities in magnetic stars may be associated with nondipole fields [3, 4].

Thus, a general solution to the equilibrium problem for rotating magnetized nonviscous configurations that corresponds to a nonlinear force described by a finite series in vector spherical harmonics is of great interest. Below, we study the case where these series for the hydrodynamic velocity and magnetic field are truncated at the initial step (Sections 2 and 3). The equilibrium configurations considered are the generalizations of a simple nonmagnetic rigidly rotating model or a fixed model with a dipole magnetic field. Our aim is to answer the following questions: (1) Whether the rigid rotation of the medium is the only possible motion in the above models and (2) whether the equilibrium condition can be satisfied if the dipole magnetic field is tilted about the rotational axis.

To do this, we derived general exact formulas for nonlinear forces under the condition of series truncation (Section 3). The formulas show that a simple exact solution can be found for both the axisymmetric angular rotation velocity and the hydrodynamic velocity having a longitude-dependent component. In the latter case, the meridional component of the hydrodynamic velocity also exists. Such a complex motion of the medium with meridional matter circulation could facilitate temperature equalizing between the near-equatorial and polar regions even in the absence of convective instability. The relations derived allow the numerical study of such models by using exact equations. Nonrotating models with a tilted (with respect to the rotation axis) dipole magnetic field can also be considered.

Section 4 deals with models where the pressure depends only on the density. In particular, this takes place in isothermal zones that are uniform in composition. Such zones are common in the upper atmospheres of stars and planets. Our relations allow one to analyze the onset of the conditions for the superrotaion of the medium and meridional circulation of matter in these partially or totally ionized upper isothermal atmo-

1063-7842/01/4606-0645$21.00

spheres when the generating magnetic field extends into upperlying layers together with charged particles.

The zones with superrotation apparently do exist in the atmospheres of several planets, including the Earth. The presence of the zone in the Earth's atmosphere where the angular rotation velocity increases by approximately 30% follows from changes in the tilts of the satellite orbits [5]. The case in point is altitudes of about 200 km, i.e., the lower bound of the upper isothermal region. Our calculations yield a small superrotation region 30 km wide (Section 4). Below, an attempt will be made to apply our results for the explanation of the strong superrotation observed in Venus' upper atmosphere, which rotates two orders of magnitude faster than the planet itself. Note also that the ejections of matter and field also occur in the solar corona. A brief analysis of these problems is given in Section 5.

1. BASIC EQUATIONS

The equilibrium equation and its curl are given by

$$\frac{1}{2}\nabla(\mathbf{v}\cdot\mathbf{v}) + \mathbf{Q} + \frac{1}{\rho}\nabla p + \nabla\Phi = 0, \quad (1)$$

$$\mathbf{R} + (\nabla p \times \nabla\rho)/\rho^2 = 0, \quad (2)$$

where

$$\mathbf{Q} = (\mathrm{curl}\mathbf{v})\times\mathbf{v} - (\mathrm{curl}\mathbf{B})\times\mathbf{B}/(4\pi\rho), \quad (3)$$

$$\mathbf{R} = \mathrm{curl}\mathbf{Q}. \quad (4)$$

Here, $\mathbf{v}$, $\mathbf{B}$, Φ, p, and ρ are the hydrodynamic velocity, magnetic field, gravitational potential, pressure, and density of the medium, respectively. The two vectors in parentheses mean the scalar product, and ∇ is the nabla operator.

Along with Eq. (1), the complete set involves

$$\mathrm{div}(\rho\mathbf{v}) \approx 0, \quad \mathrm{div}\mathbf{B} = 0 \quad (5)$$

and the equations for field and energy (the last two are omitted). In what follows, we consider the approximation of slow rotation and weak magnetic force. Therefore, the density appearing in the formula for the magnetic force can be treated as spherically symmetric. In this approximation, both the second term in (2) and the term with the pressure gradient in (1) can be linearized. As a result, the basic nonlinear problems reduce to the study of the eddy component of the nonlinear force. However, we will also consider the term with the scalar product $\mathbf{v}\cdot\mathbf{v}$.

The separation of variables is made by expanding any vector $\mathbf{f}$ (or scalar p) in orthogonal vector spherical harmonics $\mathbf{Y}_{JM}^{(\lambda)}$ (or in spherical functions Y_{JM}):

$$\mathbf{f} = \sum_{\lambda JM} f_{JM}^{(\lambda)}\mathbf{Y}_{JM}^{(\lambda)} = \sum_{JM}\left\{\mathbf{i}_r f_{JM}^{(-1)}Y_{JM} + \mathbf{i}_\vartheta \frac{1}{[J(J+1)]^{1/2}}\left[f_{JM}^{(+1)}\frac{\partial Y_{JM}}{\partial\vartheta} - \frac{M}{\sin\vartheta}f_{JM}^{(0)}Y_{JM}\right]\right.$$

$$\left. + \mathbf{i}_\varphi \frac{i}{[J(J+1)]^{1/2}}\left[\frac{M}{\sin\vartheta}f_{JM}^{(+1)}Y_{JM} - f_{JM}^{(0)}\frac{\partial Y_{JM}}{\partial\vartheta}\right]\right\}, \quad (6)$$

$$p = \sum_{JM} p_{JM}Y_{JM}, \quad (7)$$

where $f_{JM}^{(\lambda)} = f_{JM}^{(\lambda)}(r)$; $Y_{JM} = Y_{JM}(\vartheta, \varphi)$; $\mathbf{i}_r$, $\mathbf{i}_\vartheta$, and $\mathbf{i}_\varphi$ are the unit vectors of the spherical coordinate system ($\mathbf{r}$, ϑ, φ); J is a nonnegative integer; $M = -J, -J+1, \ldots, J$; $\lambda = -1$, 0, or +1; and the coefficients $f_{JM}^{(\pm1)}$ and $f_{JM}^{(0)}$ define the poloidal and toroidal components, respectively.

In particular, the coefficients $\upsilon_{J0}^{(0)}$ describe the rotation of the medium for $\mathbf{f} = \mathbf{v}$. For instance, if the only significant term is that with $J = 1$, we have

$$\upsilon_{10}^{(0)} = -ir\Omega(8\pi/3)^{1/2}, \quad (8)$$

where Ω is the angular rotation velocity.

In the case of an axisymmetric dipole magnetic field, $\mathbf{f} = \mathbf{B}$ and the only nonzero coefficient is $B_{10}^{(\pm1)}$. This field is of a latitude structure like the dipole field, but its radial dependence is determined by the equilibrium equation.

Relations (6) and (7) make it possible to reduce the initial nonlinear equilibrium partial differential equations to a set of nonlinear ordinary differential equations for the r-dependent coefficients in the above expansions. Explicit expressions for the expansion coefficients in the case of nonlinear terms were considered earlier [2]. In [2], formulas both for the coefficients $Q_{JM}^{(\lambda)}$ determining the expansion of nonlinear force (3) in vector spherical harmonics and for the quantities Ψ_{JM} appearing in the equation

$$\mathbf{v}\cdot\mathbf{v} = \sum_{JM}\Psi_{JM}Y_{JM} \quad (9)$$

were derived. These formulas will be employed to solve the equations.

2. SOLVABILITY PROBLEM

Nonlinearity-related problems may be illustrated by simple examples. Consider first the rotation of an isothermal nonmagnetic medium with $\nabla p \times \nabla\rho = 0$ and, according to (2)–(4),

$$\mathrm{curl}[(\mathrm{curl}\mathbf{v})\times\mathbf{v}] = 0, \quad (10)$$

where brackets mean the vector product.

The multidimensionality of (10) greatly complicates the problem. If our goal were merely to find the coefficients a_k of the Fourier series $A_n = a_1\sin\varphi + a_2\sin 3\varphi + \ldots + a_n\sin[(2n-1)\varphi]$ ($n = 1, 2, 3, \ldots, \infty$) from the equation

$$(A_n)^2 = 0 \qquad (11)$$

then, for nonzero a_k, two, instead of one, additional trigonometric functions would appear in (11) in going from the nth to the $(n+1)$th approximation. For instance,

$$A_1 = a_1\sin\varphi, \quad (A_1)^2 = (1/2)(a_1)^2(1-\cos 2\varphi),$$

$$A_2 = A_1 + a_2\sin 3\varphi,$$

$$(A_2)^2 = (A_1)^2 + [a_1a_2(\cos 2\varphi - \cos 4\varphi) + (1/2)(a_2)^2(1-\cos 6\varphi)].$$

As a result, the number of equations determined by the number of new trigonometric functions in (11) would increase more rapidly than the number of variables a_k.

Though this example is not directly related to the problem being discussed, it elucidates the heart of the matter as is obvious from what follows. Consider Eq. (10) in the axisymmetric case, for which $M = 0$ and $M_k = 0$. From the formulas in [2], the terms in the left-hand side of (10) that are not identically zeros are determined by the condition that the Clebsch–Gordan coefficients $C^{J0}_{J_10J_20}$ are nonzero. This condition is fulfilled if the well-known triangle rule $|J_1 - J_2| \le J \le J_1 + J_2$ holds provided that $J + J_1 + J_2$ is an even number and $J > 0$ [for $J = 0$, the left-hand side of (10) is evidently equal to zero]. In addition, this equation shows that the subscripts J_1 and J_2 related to the coefficients $\upsilon^{(\lambda)}_{J_10}$ and $\upsilon^{(\lambda)}_{J_20}$ have the same evenness and that J is an even number.

If series (6) for $\upsilon^{(0)}_{J0}$ has only one mode (i.e., the number of modes $N = 1$) and if only one coefficient of the velocity with the first subscript is nonzero ($J_1 = J_2 = 1$), Eq. (10) is reduced to one equation corresponding to $J = 2$. With this equation, the radial dependence of the coefficient $\upsilon^{(0)}_{10}$ can be found. If $N = 2$ and either of the coefficients J_1 and J_2 equals either 1 or 3, the triangle rule yields three equations (for J equal to 2, 4, and 6) for two variables: $\upsilon^{(0)}_{10}$ and $\upsilon^{(0)}_{30}$. In this case, the number of equations and the number of variables differ. It is easy to see that this difference increases with increasing N. Thus, the set of equations under consideration becomes unsolvable for $N > 1$. This conclusion is also valid for more general configurations. For example, if J_1 and J_2 were even numbers (that is, the rotation velocity were distributed antisymmetrically about the equatorial plane), we would have two equations (for $J = 2$ and $J = 4$) for the only variable $\upsilon^{(0)}_{20}$ even at $N = 1$ and the least value of the subscript $J_1 = J_2 = 2$.

If a magnetic configuration rotates in the radiant zone, the second term in the left-hand side of Eq. (4), which depends on the temperature distribution, may become significant. However, the variables involved in this additional term are determined by other equations. Therefore, the above conclusion about the unsolvability of the complete set of the equilibrium equations remains valid (if the condition for the truncation of the series for the nonlinear force is not fulfilled). For instance, if we eliminate unsolvability in Eq. (2) by fitting the temperature distribution, the heat equilibrium condition will be violated. We assume that the formation of spots of different chemical composition in magnetic stars [3, 4] is related to the unsolvability of the equilibrium equations because of the complex configuration of the magnetic field.

Note that complex rotating structures may arise in stellar and atmospheric convective zones. The most prominent examples of such structures are differential solar rotation and the accelerated rotation of Venus' convective atmosphere. In the latter case, convection is due to large horizontal temperature gradients [6–9]. Therefore, it is natural to assume that the accelerated rotation of the atmosphere of a slowly rotating planet, as well as meridional circulation induced by this acceleration, facilitates convective heat transfer. Calculations [9] confirm the possibility of self-generating such convection conditions. However, the validity of the truncation of series describing convective medium motion is in doubt [10, 11]. From the aforesaid, one may infer that some truncation of the series should always take place; otherwise, no solution will exist. Convective turbulent viscosity apparently may favor series truncation. In the case of the Sun, enhanced convective heat transfer is most likely to be related to thermal-to-magnetic energy conversion. This problem, along with the associated series truncation, was studied in [12].

However, there exist configurations described by finite series in the spherical harmonics. In our example, this condition is satisfied for $N = 1$ and $J_1 = J_2 = 1$. In particular, this condition is fulfilled if the rotation is solid. More general models of this type are considered in the next section.

3. POSSIBLE EQUILIBRIUM STRUCTURES

Consider equilibrium rotating magnetized structures for which series (6) for the velocity **v** and the field **B** involve terms with the first subscript $J = 1$ only. Restrictions imposed on other subscripts are assumed to be determined by equilibrium equations (1) and (2). Thus, we believe that the series for hydrodynamical velocity and magnetic field in J are truncated at the very

beginning; i.e., only the coefficients $\upsilon_{1M}^{(\lambda)}$ and $B_{1M}^{(\lambda)}$ are nonzero. Here, $\lambda = 0, \pm 1$. In this case, as follows from general formulas (13) and (22)–(24) in [2], only the coefficients of the nonlinear force $Q_{JM}^{(\lambda)}$ with the subscripts $J = 0$, 1, and 2 may be nonzero provided that $\lambda = 0, \pm 1$ and $|M| \le J$. First, let us consider the problem of compensation of the forces described by these coefficients.

It is easy to see that the coefficients $Q_{1M}^{(0)}$ and $Q_{2M}^{(0)}$ should be equal to zero; otherwise, equilibrium would be impossible. For the equations involving the coefficients $Q_{1M}^{(\pm 1)}$, the gradient of the scalar product of the velocities might make a substantial contribution. However, the solution may be such that the contributions from each of the terms are zero. Then, we come to

$$Q_{1M}^{(\lambda)} = (q^{(\lambda)}/r)\Theta_{11}^{1}[\Xi_{1M}^{(\lambda)}(\upsilon) - \Xi_{1M}^{(\lambda)}(B)/(4\pi\rho)] = 0, \tag{12}$$

$$Q_{2M}^{(0)} = [3/(5^{1/2}r)]K_{11}^{2} \times [\xi_{2M}^{(0)}(\upsilon) - \xi_{2M}^{(0)}(B)/(4\pi\rho)] = 0, \tag{13}$$

$$\Psi_{1M} = -(8/3)^{1/2} y_M C_{111x_M}^{1|M|}\Theta_{11}^{1} \times [\upsilon_{1y_M}^{(0)}\upsilon_{1x_M}^{(+1)} - \upsilon_{1x_M}^{(0)}\upsilon_{1y_M}^{(+1)}] = 0, \tag{14}$$

where

$$\Xi_{1M}^{(-1)}(f) = y_M C_{111x_M}^{1|M|}\Big[f_{1x_M}^{(+1)}\frac{\partial}{\partial r}r f_{1y_M}^{(0)} - f_{1y_M}^{(+1)}\frac{\partial}{\partial r}r f_{1x_M}^{(0)} - f_{1x_M}^{(0)}\frac{\partial}{\partial r}r f_{1y_M}^{(+1)} + f_{1y_M}^{(0)}\frac{\partial}{\partial r}r f_{1x_M}^{(+1)} + 2^{1/2}(f_{1x_M}^{(0)}f_{1y_M}^{(-1)} - f_{1y_M}^{(0)}f_{1x_M}^{(-1)})\Big], \tag{15}$$

$$\Xi_{1M}^{(+1)}(f) = y_M C_{111x_M}^{1|M|}\Big[2^{1/2}\Big(f_{1x_M}^{(-1)}\frac{\partial}{\partial r}r f_{1y_M}^{(0)} - f_{1y_M}^{(-1)}\frac{\partial}{\partial r}r f_{1x_M}^{(0)}\Big) + 2(f_{1y_M}^{(0)}f_{1x_M}^{(+1)} - f_{1x_M}^{(0)}f_{1y_M}^{(+1)})\Big], \tag{16}$$

$$\Xi_{1M}^{(0)}(f) = y_M C_{111x_M}^{1|M|}2^{1/2} \times\Big[f_{1x_M}^{(-1)}\frac{\partial}{\partial r}r f_{1y_M}^{(+1)} - f_{1y_M}^{(-1)}\frac{\partial}{\partial r}r f_{1x_M}^{(+1)}\Big], \tag{17}$$

$$\xi_{20}^{(0)}(f) = C_{111-1}^{20}\Big[2^{3/2}\Big(f_{10}^{(-1)}\frac{\partial}{\partial r}r f_{10}^{(0)} - 2f_{10}^{(0)}f_{10}^{(+1)}\Big) + 2^{1/2}\Big(f_{1-1}^{(-1)}\frac{\partial}{\partial r}r f_{11}^{(0)} + f_{11}^{(-1)}\frac{\partial}{\partial r}r f_{1-1}^{(0)}\Big) - 2(f_{11}^{(0)}f_{1-1}^{(+1)} + f_{1-1}^{(0)}f_{11}^{(+1)})\Big], \tag{18}$$

$$\xi_{2\pm 1}^{(0)}(f) = C_{1110}^{21}\Big[2^{1/2}\Big(f_{10}^{(-1)}\frac{\partial}{\partial r}r f_{1\pm 1}^{(0)} + f_{\pm 1}^{-1}\frac{\partial}{\partial r}r f_{10}^{(0)}\Big) - 2(f_{1\pm 1}^{(0)}f_{10}^{(+1)} + f_{10}^{(0)}f_{1\pm 1}^{(+1)})\Big]. \tag{19}$$

Here, $x_M = |M| - 1$, $y_M = 1 + M - |M|$, $q^{(-1)} = (2/3)^{1/2}$, $q^{(+1)} = q^{(0)} = (1/3)^{1/2}$, $C_{J_1M_1J_2M_2}^{JM}$ are the Clebsch–Gordan coefficients, and $K_{11}^{2} = 1/(4\pi^{1/2})$ and $\Theta_{11}^{1} = -3/(4\pi^{1/2})$ are determined by general formulas (10) and (11) in [2]. Note that $C_{111-1}^{10} = C_{1110}^{11} = C_{1110}^{21} = 2^{-1/2}$, $C_{1010}^{20} = 2C_{111-1}^{20} = (2/3)^{1/2}$, and $C_{1111}^{22} = 1$.

It is readily verified that Eqs. (12)–(14) are satisfied if the following conditions are fulfilled:

$$\upsilon_{10}^{(-1)} = 0, \quad \upsilon_{1\pm 1}^{(-1)} = 0, \quad \upsilon_{10}^{(+1)} = 0, \quad \upsilon_{1\pm 1}^{(+1)} = 0, \quad B_{10}^{(0)} = 0, \quad B_{1\pm 1}^{(0)} = 0, \tag{20}$$

$$B_{1-1}^{(-1)}\frac{\partial^2}{\partial r^2}r^2 B_{11}^{(-1)} - B_{11}^{(-1)}\frac{\partial^2}{\partial r^2}r^2 B_{1-1}^{(-1)} = 0, \tag{21}$$

$$B_{10}^{(-1)}\frac{\partial^2}{\partial r^2}r^2 B_{1\pm 1}^{(-1)} - B_{1\pm 1}^{(-1)}\frac{\partial^2}{\partial r^2}r^2 B_{10}^{(-1)} = 0. \tag{22}$$

In the last two equations, $B_{1M}^{(+1)}$ is eliminated by the relation

$$B_{JM}^{(+1)} = \frac{1}{r[J(J+1)]^{1/2}}\frac{\partial}{\partial r}r^2 B_{JM}^{(-1)}, \tag{23}$$

which follows from (5).

Equations (21) and (22) are satisfied if the radial dependences of all the modes are the same. In other words, we are dealing with a dipole field tilted with respect to the rotation axis. We assume hereafter that Eqs. (20)–(22) are satisfied; i.e., only the modes $\upsilon_{1M}^{(0)}$ and $B_{1M}^{(\pm)}$ are other than zero. The corresponding vector fields **v** and **B** complement each other in the sense that the former field is toroidal and the latter is poloidal. However, the superposition of these vector fields is some vector field of a dipole type. Note that both Eqs. (5) are satisfied under the conditions considered.

When conditions (20)–(22) are met, all the coefficients $Q_{JM}^{(\lambda)}$ and Ψ_{JM} for which $J > 2$ are identically

zero. The other coefficients are given by

$$Q_{00}^{(-1)} = \frac{1}{r(4\pi)^{1/2}}\left\{\upsilon_{10}^{(0)}\frac{\partial}{\partial r}r\upsilon_{10}^{(0)} - \frac{1}{r}\frac{\partial}{\partial r}r^2\upsilon_{11}^{(0)}\upsilon_{1-1}^{(0)} + E^{(+1)} - 2H^{(+1)}\right\}, \quad (24)$$

$$Q_{00}^{(+1)} = 0, \quad Q_{00}^{(0)} = 0, \quad Q_{1M}^{(\lambda)} = 0, \quad \Psi_{1M} = 0, \quad (25)$$

$$Q_{2M}^{(\pm 1)} = -\frac{1}{4r(5\pi)^{1/2}}\kappa_M^{(\pm 1)}S_{2M}^{(\pm 1)}, \quad (26)$$

$$\Psi_{00} = -[1/(4\pi)]^{1/2}[(\upsilon_{10}^{(0)})^2 - 2\upsilon_{11}^{(0)}\upsilon_{1-1}^{(0)}], \quad (27)$$

$$\Psi_{20} = [1/(20\pi)]^{1/2}[(\upsilon_{10}^{(0)})^2 + \upsilon_{11}^{(0)}\upsilon_{1-1}^{(0)}], \quad (28)$$

$$\Psi_{2\pm 1} = [3/(20\pi)]^{1/2}\upsilon_{10}^{(0)}\upsilon_{1\pm 1}^{(0)}, \quad (29)$$

$$\Psi_{2\pm 2} = [3/(40\pi)]^{1/2}(\upsilon_{1\pm 1}^{(0)})^2, \quad (30)$$

where

$$S_{20}^{(-1)} = \upsilon_{10}^{(0)}\frac{\partial}{\partial r}r\upsilon_{10}^{(0)} + \frac{1}{2r}\frac{\partial}{\partial r}r^2\upsilon_{11}^{(0)}\upsilon_{1-1}^{(0)} + E^{(+1)} + H^{(+1)}, \quad (31)$$

$$S_{20}^{(+1)} = 2[(\upsilon_{10}^{(0)})^2 + \upsilon_{11}^{(0)}\upsilon_{1-1}^{(0)}] + 2^{1/2}[E^{(-1)} + H^{(-1)}], \quad (32)$$

$$S_{2\pm 1}^{(-1)} = \frac{1}{r}\frac{\partial}{\partial r}r^2\upsilon_{10}^{(0)}\upsilon_{1\pm 1}^{(0)} + \frac{1}{4\pi\rho}[B_{10}^{(+1)}D_{1\pm 1} + B_{1\pm 1}^{(+1)}D_{10}], \quad (33)$$

$$S_{2\pm 1}^{(+1)} = 4\upsilon_{10}^{(0)}\upsilon_{1\pm 1}^{(0)} + \frac{2^{1/2}}{4\pi\rho}(B_{10}^{(-1)}D_{1\pm 1} + B_{1\pm 1}^{(-1)}D_{10}), \quad (34)$$

$$S_{2\pm 2}^{(-1)} = \frac{1}{2r}\frac{\partial}{\partial r}[r\upsilon_{1\pm 1}^{(0)}]^2 + \frac{1}{4\pi\rho}B_{1\pm 1}^{(+1)}D_{1\pm 1}, \quad (35)$$

$$S_{2\pm 2}^{(+1)} = 2(\upsilon_{1\pm 1}^{(0)})^2 + \frac{2^{1/2}}{4\pi\rho}B_{1\pm 1}^{(-1)}D_{1\pm 1}, \quad (36)$$

$$D_{1M} = \frac{\partial}{\partial r}rB_{1M}^{(+1)} - 2^{1/2}B_{1M}^{(-1)} = \frac{1}{2^{1/2}}\left[\frac{\partial^2}{\partial r^2}r^2B_{1M}^{(-1)} - 2B_{1M}^{(-1)}\right], \quad (37)$$

$$E^{(\pm 1)} = \frac{1}{4\pi\rho}B_{10}^{(\pm 1)}D_{10}, \quad H^{(\pm 1)} = \frac{1}{8\pi\rho}[B_{1-1}^{(\pm 1)}D_{11} + B_{11}^{(\pm 1)}D_{1-1}]. \quad (38)$$

Here,

$$\kappa_M^{(+1)} = (3/2)^{1/2}\kappa_M^{(-1)}, \quad \kappa_0^{(-1)} = 2, \quad \kappa_{\pm 1}^{(-1)} = 3^{1/2}, \quad \kappa_{\pm 2}^{(-1)} = 6^{1/2}.$$

The vector fields **v** and **B** have the form

$$\mathbf{v} = \frac{1}{4}\left(\frac{3}{\pi}\right)^{1/2}\{\mathbf{i}_\vartheta(\upsilon_{11}^{(0)}e^{i\varphi} + \upsilon_{1-1}^{(0)}e^{-i\varphi}) + i\mathbf{i}_\varphi[2^{1/2}\upsilon_{10}^{(0)}\sin\vartheta + (\upsilon_{11}^{(0)}e^{i\varphi} - \upsilon_{1-1}^{(0)}e^{-i\varphi})\cos\vartheta]\}, \quad (39)$$

$$\mathbf{B} = \frac{1}{4}\left(\frac{3}{\pi}\right)^{1/2}\{\mathbf{i}_r[2B_{10}^{(-1)}\cos\vartheta - 2^{1/2}(B_{11}^{(-1)}e^{i\varphi} - B_{1-1}^{(-1)}e^{-i\varphi})\sin\vartheta] - \mathbf{i}_\vartheta[2^{1/2}B_{10}^{(+1)}\sin\vartheta + (B_{11}^{(+1)}e^{i\varphi} - B_{1-1}^{(+1)}e^{-i\varphi})\cos\vartheta] - i\mathbf{i}_\varphi(B_{11}^{(+1)}e^{i\varphi} + B_{1-1}^{(+1)}e^{-i\varphi})\}. \quad (40)$$

From the requirement that the right-hand sides of these equations are real, it follows that

$$\upsilon_{1-1}^{(0)} = \upsilon_{11}^{(0)*}, \quad B_{1-1}^{(\pm 1)} = -B_{11}^{(\pm 1)*}, \quad (41)$$

where * denotes complex conjugation.

Here, $i\upsilon_{10}^{(0)}$ and $B_{10}^{(-1)}$ are real, and the coefficients $B_{1M}^{(+1)}$ can be expressed in terms of $B_{1M}^{(-1)}$ by Eq. (23). Recall that the coefficients should be chosen in accordance with Eqs. (21) and (22); i.e., the radial dependence of these coefficients should be the same for all M. In the case of a tilted dipole field, the magnetic field in the rotated (primed) coordinate system is represented by the sum of the quantities $B_{1M'}^{(\lambda)}\mathbf{Y}_{1M'}^{(\lambda)}(\vartheta', \varphi')$ over M' for given $B_{1M'}^{(\lambda)}$ and $\lambda = \pm 1$. Having denoted the Eulerian angles of rotation by α_e, β_e, and γ_e and having used the formulas from [13], we obtain that the sum of the quantities $a_{MM'}B_{1M'}^{(\lambda)}$ over M' appears in Eqs. (21), (22), and (40) instead of $B_{1M'}^{(\lambda)}$, where

$$a_{MM'} = \frac{1}{2}e^{-i(M\alpha_e + M'\gamma_e)}[(1 + MM'\cos\beta_e)\delta_{|M|1}\delta_{|M'|1} + 2^{1/2}(\sin\beta_e)(M'\delta_{|M|0}\delta_{|M'|1} - M\delta_{|M|1}\delta_{|M'|0}) + 2(\cos\beta_e)\delta_{M0}\delta_{M'0}] \quad (42)$$

and δ_{ab} is equal to 1, for $a = b$, or 0 for $a \neq b$.

Using the formulas derived, one may construct models of rotating or magnetized equilibrium configurations with series (7) for p and ρ involving terms with $J = 0$ and $J = 2$ only. Additional relations in the equilibrium equations do not appear if second-order corrections containing, e.g., the product $p_{2M}\rho_{2M}$ are negligible. Several models have already been considered in [1, 2] for the case where either **v** or **B** is equal to zero. It is clear that not only rigidly rotating models are possible but also those in which the velocity **v** has a component that harmonically depends on the longitude. In this case, the meridional velocity, which is antisymmetric with respect to the equatorial plane, does not depend on ϑ and, eventually, on the latitude. In contrast to the first term in square brackets for the zonal velocity, the second is also antisymmetric with respect to the equatorial plane.

In the case of magnetic field (40), the components that depend and do not depend on the azimuth angle also have different symmetries with respect to the equatorial plane. In this case, the axisymmetric field is antisymmetric with respect to this plane. This field is a dipole field making an arbitrary angle with the axis of rotation. However, the field equation should be taken into account when magnetized media are considered. Obviously, the expression derived for nonlinear force may be used to study various nonstationary processes. In particular, isothermal structures induced by the ejection of the field generated into upper layers are of interest. Such structures are studied in the next section.

4. SUPERROTATION OF AN ISOTHERMAL MODEL

Equation (2) is greatly simplified for a model where the pressure depends only on the density. This takes place, e.g., for uniform distributions of the temperature and molecular weight or in a near-adiabatic convective zone. However, in the latter case, the turbulent viscosity of the medium is of great concern; the associated problems have been discussed in [12]. We assume that the viscosity is negligible and the pressure is only density-dependent. Then, from Eq. (2), it follows that

$$\mathbf{R} = \operatorname{curl}\mathbf{Q} = 0. \tag{43}$$

Substituting (24)–(26) into (43), we arrive at

$$\mathbf{R} = \frac{i}{4r^2(5\pi)^{1/2}}\{2(6)^{1/2}U_{20}\mathbf{Y}_{20}^{(0)} + 3(2)^{1/2}[U_{21}\mathbf{Y}_{21}^{(0)} + U_{2-1}\mathbf{Y}_{2-1}^{(0)}] + 6[U_{22}\mathbf{Y}_{22}^{(0)} + U_{2-2}\mathbf{Y}_{2-2}^{(0)}]\}, \tag{44}$$

where

$$U_{2M} = S_{2M}^{(-1)} - \frac{r}{2}\frac{\partial}{\partial r}S_{2M}^{(+1)} \tag{45}$$

and the quantities in the right-hand side are defined by (28)–(31).

In our case, Eq. (43) is valid; therefore,

$$U_{2M} = 0, \quad M = 0, \pm 1, \pm 2. \tag{46}$$

These equations should be solved simultaneously with the field equation. The heat balance equation omitted means merely the maintenance of the isothermal zone structure in our case.

In nonmagnetic configurations, Eqs. (46) are satisfied if the hydrodynamic velocities are proportional to r. Both solid rotation and a more complex nonaxiasymmetric flow of the medium with meridional matter circulation are possible. In a nonrotating medium, Eqs. (46) are satisfied when $B_{1M}^{(-1)}$ are either constant or proportional to r^{-3}. The latter case corresponds to the field of a magnetic dipole. In addition, models with the zero sum of the magnetic and Coriolis forces are possible. These models are studied by the following simple example.

Let, in an isothermal layer, the radial dependences of the equilibrium density and of any mode having the dimension of velocity approximately be represented as

$$\rho \approx \text{const}\, r^{-s}, \quad \upsilon_{1M}^{(0)} \approx \text{const}\, r^{\alpha}, \quad B_{1M}^{(-1)}/(4\pi\rho^{1/2}) \approx \text{const}\, r^{\alpha}, \tag{47}$$

where $s \approx \text{const}$ and $\alpha = \text{const}$.

Then, Eqs. (23) and (37) yield

$$B_{1M}^{(+1)} = 2^{-1/2}(\alpha - s/2 + 2)B_{1M}^{(-1)}, \quad D_{1M} = \psi B_{1M}^{(-1)}, \tag{48}$$

where

$$\psi = 2^{-1/2}(\alpha - s/2)(\alpha - s/2 + 3). \tag{49}$$

Eventually, using Eqs. (26), (31)–(36), and (45), we obtain

$$U_{20} = -(\alpha - 1)[(\upsilon_{10}^{(0)})^2 + \upsilon_{11}^{(0)}\upsilon_{1-1}^{(0)}] - 2^{-1/2}\psi(\alpha + s/2 - 2)[(A_{10})^2 + A_{11}A_{1-1}], \tag{50}$$

$$U_{2\pm1} = -2(\alpha - 1)\upsilon_{10}^{(0)}\upsilon_{1\pm1}^{(0)} - 2^{1/2}\psi(\alpha + s/2 - 2)A_{10}A_{1\pm1}, \tag{51}$$

$$U_{2\pm2} = -(\alpha - 1)(\upsilon_{1\pm1}^{(0)})^2 - 2^{1/2}\psi(\alpha + s/2 - 2)(A_{1\pm1})^2. \tag{52}$$

Here,

$$A_{1M} = B_{1M}^{(-1)}/(4\pi\rho)^{1/2}. \tag{53}$$

Equating (51) and (52) to zero, we find

$$(\alpha - 1)(\upsilon_{1M}^{(0)})^2 = -2^{-1/2}\psi(\alpha + s/2 - 2)(A_{1M})^2, \tag{54}$$

where $M = 0, \pm 1$.

In addition, Eq. (46), corresponding to $M = 0$, results in

$$(\alpha - 1)\upsilon_{11}^{(0)}\upsilon_{1-1}^{(0)} = -2^{-1/2}\psi(\alpha + s/2 - 2)A_{11}A_{1-1}. \quad (55)$$

In view of relations (41), we find that the problem of solving the set of Eqs. (46) [or (54) and (55)] is equivalent to solving the following set of two equations:

$$(\alpha - 1)\upsilon_{1M}^{(0)}\upsilon_{1M}^{(0)*} = \left(\alpha - \frac{s}{2}\right)\left(\alpha - \frac{s}{2} + 3\right) \times\left(\alpha + \frac{s}{2} - 2\right)\frac{1}{8\pi\rho}B_{1M}^{(-1)}B_{1M}^{(-1)*}, \quad (56)$$

where $M = 0$ or 1. It is seen that the equations for axisymmetric and nonaxisymmetric components are separated. In the case $M = 0$, $\upsilon_{10}^{(0)}\upsilon_{10}^{(0)*} = (8\pi/3)(r\Omega)^2$, according to (8).

Obviously Eq. (56) should be solved simultaneously with the field equation. It is also clear that, in a nonrigidly rotating medium, the stationary solution of the system does not exist. For instance, in the case of longitude-independent fields (39) and (40), the vector curl$[\mathbf{v}\times\mathbf{B}]$ appearing in the field equation is equal to $\mathbf{i}_\varphi[3(2^{1/2})/(8\pi)]iB_{10}^{(-1)}r(\partial/\partial r)(\upsilon_{10}^{(0)}/r)\sin\vartheta\cos\vartheta$; i.e., it is nonzero if the ratio $\upsilon_{10}^{(0)}/r$ is not a constant. Thus, in the case of nonsolid rotation, an azimuth magnetic field proportional to $\sin 2\vartheta$ is generated.

In view of this circumstance, structures with the angular rotation velocity sharply increasing with altitude are of interest, since, in this case, the probability of ejection of the resulting magnetic field with "frozen-in" charged particles into upper layers increases. Here, we consider the structures generated in the upper isothermal layers of stars and planets. These layers are normally partially or totally ionized. The ejection of field and matter from the atmosphere increases the disorder of the system; hence, the total entropy increases. This means that the self-organization of the field- and matter-ejection processes is in accordance with the laws of irreversible thermodynamics. It is not improbable that field ejection is accompanied by some irregular wave processes.

In view of the foregoing, we will consider models with

$$s \gg 1, \quad \alpha \gg 1. \quad (57)$$

This means that the characteristic radial scale of the equilibrium density is much less than the radius of a star or a planet and that the amplitudes of all the modes with the dimension of velocity sharply increase with increasing altitude. If the difference $\alpha - s/2$ is not large enough, the magnetic field strength is near-uniform under these conditions. When inequalities (57) are fulfilled, Eqs. (56) yield $(\alpha - s/2)(\alpha - s/2 + 3) > 0$, i.e., $\psi > 0$.

In view of Eq. (48) and conditions (57), relation (56) may be represented in the form

$$\frac{B_{1M}^{(+1)}B_{1M}^{(+1)*}}{4\pi\rho} \approx \frac{\alpha(\alpha - s/2 + 2)^2}{(\alpha + s/2)(\alpha - s/2)(\alpha - s/2 + 3)}\upsilon_{1M}^{(0)}\upsilon_{1M}^{(0)*}. \quad (58)$$

Here, M is equal to either 0 or 1, and $\upsilon_{1M}^{(0)}\upsilon_{1M}^{(0)*} = (8\pi/3)(r\Omega)^2$. Also, the denominator in the right-hand side of (58) is positive, since $\psi > 0$, and $\alpha - s/2 + 2$ if the numerator is not small. It is clear that the Alfvén velocity and rotation velocity should be of the same order of magnitude.

A characteristic feature of the isothermal models being discussed is the superrotation of upper layers. In the case of the Earth's atmosphere, variations of the tilts of satellite orbits [5] indicate atmosphere superrotation at altitudes from 150 to 400 km. On average, the angular rotation velocity is 1.3 times greater than its normal value. If the lower bound of the superotation zone is taken to be at an altitude of approximately 200 km, the density is $10^{-12.5}$ g/cm^3 [14]. Then, the corresponding value of the magnetic field is 10^{-1} G, according to (58). This zone seems to be near-isothermal. The field strength obtained is close to those observed at such altitudes.

Relations (58) may be satisfied for a not too large superrotation zone. For example, in the case of a 30-km zone, $s \sim 100$ and $\alpha \sim s/2$ (provided that $\alpha - s/2$ and $\alpha - s/2 + 3$ are far from zero), we find that the angular velocity of the upper layers of the zone may be approximately 1.4 times as great as that of the lower layers. In this case, the density of the medium varies no greater than twofold. Thus, the equations derived can adequately describe the moderate superrotation of a medium with a small tilt of the dipole magnetic field, which is observed in the Earth's atmosphere.

Fast superrotation in Venus' atmosphere at altitudes greater than 50 km has been reported [6–8]. In this case, the planet itself and its upper atmosphere rotate, respectively, 243 and 4 times as slow as the Earth. At least the lower atmosphere is convective in this case. The solution describing fast rotation with circulation in the main convective zone (at altitudes of less than 64 km) has been found in [9]. However, the mechanism of global zonal (four-day) circulation in the upper atmosphere remains to be understood [8]. Note that the circulation symmetry in our model differs from that chosen in [9].

In Venus' atmosphere, the isothermal zone seems to be located at an altitude of about 100 km or higher [7]. If the matter density in this zone is on the order of 10^{-9} g/cm^3, then $\mathbf{B} \sim 1$ G, according to (58). The field decreases with increasing altitude and in configurations where condition (57) holds but the ratio α/s is small. If, in addition, the superrotation zone is wide enough, the

angular velocity may increase even more sharply. Note also that, here, heat transfer between the equatorial and near-polar zones is probably of vital importance. Therefore, the generation of nonaxisymmetric motions with $M = \pm 1$, which cause intense meridional matter circulation, seems to be more likely. Under these conditions, the magnetization outside the superrotation layer may be weak. Moreover, it may appear that a nonmagnetic configuration described by Eqs. (39) takes place in Venus' atmosphere. In these equations, the coefficients $\upsilon_{1M}^{(0)}$ may be rapidly increasing functions of r if the structure is non isothermal or there exist additional forces due to, e.g., matter outflow. Thus, the hypothesis that the solution being discussed might describe fast superrotation, such as that taking place in the Venus' upper atmosphere, deserves attention.

It is well known that intense matter outflow is observed in the solar atmosphere. If the uppermost layers of the solar atmosphere exhibit superrotation, matter outflow may substantially increase. This problem calls for further consideration.

5. DISCUSSION

Our theoretical study shows that nonlinear interactions of various modes that occur in rotating magnetized stellar or atmospherical zones are of vital importance. If the viscosity is negligible, the equilibrium conditions cannot be fulfilled for arbitrary distributions of the hydrodynamic velocity and magnetic field and the complex problem of studying possible equilibrium models arises. The formulas derived for the nonlinear forces (Section 3) allow consideration of permissible solutions of the exact nonlinear equilibrium equations if the density appearing in the expression for magnetic force is assumed to be spherically symmetric. These solutions represent the set of all possible modes with the same value of the first subscript, $J = 1$. In particular, the equations derived in Section 2 make it possible to construct axisymmetric rigidly rotating models with a dipole magnetic field, nonrotating models with a tilted dipole magnetic field, and nonmagnetic models where the velocity of the medium does not have only a rotational component. For example, longitude-dependent motions determined by (39) are possible. Equations (39) and (40) most likely describe the whole set of models for which the equilibrium equations can be satisfied under the conditions considered. In particular, this conclusion is confirmed by the study of the equilibrium conditions for an insulated axisymmetric magnetic tube in the radiant zone of a nonrotating star [1, 2]. Note also that the existence of magnetic stars with the field axis tilted about the rotation axis is supported by observations [3, 4]. Strong field variations may be explained by the presence of the large longitude-dependent field component [see Eq. (40)].

Among the models considered above, the equilibrium magnetized structures arising in isothermal ionized zones where equilibrium density rapidly decreases with increasing altitude (Section 4) are of considerable interest. It is assumed that, in these structures, the rotation velocity sharply increases with altitude and the continuously generated magnetic field is ejected into the upper layers. However, the condition of force balance is met on average. The zonal velocity may have an azimuth-dependent component; then there exists meridional matter circulation, and the mean magnetic field is the field of a tilted dipole. It is natural to assume that such superrotation conditions facilitate matter outflow from the rotating magnetized atmosphere and cause the disorder in the system to increase. As a result, the total entropy grows. This growth is in accordance with the laws of irreversible hydrodynamics.

We have preliminarily studied the superrotation problem by the example of the Earth and Venus's upper atmospheres. The equilibrium magnetic field obtained depends substantially on the equilibrium density of the medium. Configurations with relatively weak magnetic fields are also possible. It seems probable that the theoretical structures under discussion have to do with those observed in Earth and Venus' atmospheres. Meridional matter circulation arising in them may favor temperatures equalizing between near-equatorial and polar regions.

It is well known that intense matter outflow is observed in the solar atmosphere. Studies [15] show that the matter flow from the polar holes is too high to be generated by acceleration due to conventional heat conduction only. If the upper layers of the solar atmosphere exhibit superrotation, the increase in the matter outflow can be substantial. This problem needs further consideration.

ACKNOWLEDGMENTS

This work was supported by the "Integratsiya" Foundation (contract no. KO854) and the Russian Foundation for Basic Research (project no. 00-02-16939).

REFERENCES

1. Yu. V. Vandakurov, Pis'ma Astron. Zh. **25**, 143 (1999) [Astron. Lett. **25**, 111 (1999)].
2. Yu. V. Vandakurov, Astron. Zh. **76**, 29 (1999) [Astron. Rep. **43**, 24 (1999)].
3. E. F. Borra, J. D. Landstreet, and L. Mestel, Annu. Rev. Astron. Astrophys. **20**, 191 (1982).
4. V. L. Khokhlova, Itogi Nauki Tekh., Ser.: Astron. **24**, 233 (1983).
5. D. G. King-Hele and D. M. C. Walker, Planet. Space Sci. **25**, 313 (1977).

6. G. Schubert, C. C. Counselman, III, J. Hansen, *et al.*, Space Sci. Rev. **20**, 357 (1977).
7. M. Ya. Marov, *Planets of the Solar System* (Nauka, Moscow, 1981).
8. K. Ya. Kondrat'ev, N. N. Krupenio, and A. S. Selivanov, *The Venus Planet* (Gidrometeoizdat, Leningrad, 1987).
9. R. E. Young and J. B. Pollack, J. Atmos. Sci. **34**, 1315 (1977).
10. W. B. Rossow, S. B. Fels, and P. H. Stone, J. Atmos. Sci. **37**, 250 (1980).
11. R. E. Young and J. B. Pollack, J. Atmos. Sci. **37**, 253 (1980).
12. Yu. V. Vandakurov, Pis'ma Astron. Zh. **25**, 868 (1999) [Astron. Lett. **25**, 758 (1999)].
13. D. A. Varshalovich, A. N. Moskalev, and V. K. Khersonskiĭ, *The Quantum Theory of Angular Momentum* (Nauka, Leningrad, 1975; World Scientific, Singapore, 1988).
14. C. W. Allen, *Astrophysical Quantities* (Athlone Press, London, 1973; Mir, Moscow, 1977).
15. A. Barnes, P. R. Gazis, and J. L. Phillips, in *Proceedings of the 8th Solar Wind Conference*, Ed. by D. Winterhalter, J. T. Gosling, S. R. Habbal, *et al.*, AIP Conf. Proc. (Woodbury, New York, 1996), no. 382, pp. 50–53.

Translated by M. Fofanov

Technical Physics, Vol. 46, No. 6, 2001, pp. 654–661. Translated from Zhurnal Tekhnicheskoĭ Fiziki, Vol. 71, No. 6, 2001, pp. 10–16.

GASES AND LIQUIDS

Radiation Excited by Shock Waves in a CO_2–N_2–Ar Mixture: Experiment and Theory

G. N. Zalogin*, P. V. Kozlov*, L. A. Kuznetsova*, S. A. Losev*, V. N. Makarov*, Yu. V. Romanenko*, and S. T. Surzhikov**

** Institute of Mechanics, Moscow State University, Moscow, 117192 Russia*

e-mail:kozlov@imec.msu.ru

*** Institute for Problems of Mechanics, Russian Academy of Sciences, Moscow, 117526 Russia*

Received April 10, 2000; in final form August 15, 2000

Abstract—On the basis of experimental data both published and obtained by the authors on radiation excited in CO_2–N_2–Ar mixtures by shock waves, a physicochemical model of such mixtures is developed that can be recommended for calculating the heat exchange and radiation of vehicles descending in the Martian atmosphere. It is shown that the usually adopted assumption of the locally equilibrium population of the electron-exited states is invalid. This makes it necessary to consider each electron-excited state separately. The rate constants of the excitation processes of electron states $CN(A^2\Pi)$, $CN(B^2\Sigma^+)$, and $C_2(d^3\Pi_g)$ produced as a result of collisions with heavy particles are determined. © *2001 MAIK "Nauka/Interperiodica".*

INTRODUCTION

In astrophysical problems relating to the descent of landing modules (LMs) in the Martian atmosphere, the range of altitudes where nonequilibrium physicochemical processes play a determinative role is considerably wider than in the earth's atmosphere. Therefore, the influence of nonequilibrium processes on heat exchange and radiation becomes essential for a wider range of LMs, including ballistic descent modules. For solving these problems a thermochemical model of the processes in CO_2–N_2–Ar mixtures is needed which would take into account various nonequilibrium physicochemical processes and, in particular, the mechanisms of the emergence of electron-excited states of the molecules that determine the intensity of radiation.

Nonequilibrium physicochemical processes in such mixtures were considered in a great number of experimental and computational-theoretical investigations associated with projected flights to Mars and Venus. The models developed earlier in a number of studies [1–7] use various sets of chemical reactions with widely differing rate constants. Investigations of this kind were carried out in the 1960s [7–10]. In these studies the radiation was assumed to be locally equilibrium. However, already in the early investigations it was shown that in the relaxation zone behind a shock wave or in the shock layer, the Boltzmann distribution of atoms and molecules over electron-excited states can be invalid. This effect was called a "limit by collisions" [11]. It can occur in air [12] and other gases like CO_2 [13] or CO_2–N_2 mixtures [14], leading to a considerable difference between the radiation intensity and the corresponding locally equilibrium values, especially at low densities.

At high entry velocities, the radiation from CO_2–N_2 mixtures can make a considerable contribution to the total heat flux toward the surface of an LM. However, even at low entry velocities, when radiation does not play a part in the heat exchange, it remains an important factor affecting the operation of optical devices aboard an LM. Besides, as shown in [15], the radiation coming from the shock layer ahead of an LM makes it possible to determine more precisely some parameters of the atmosphere of a planet. In solving the last two problems, not only should the principal contributions to radiation be taken into account but also the radiation sources of low intensity, which significantly expands the scope of processes to be taken into consideration. In calculating the radiation intensity, not only its integrated value is of interest but also its spectral distribution. Compared with the radiation from air under comparable conditions, the mixtures under consideration have two qualitatively different characteristics. Firstly, at moderate flight velocities, the radiation intensity of such mixtures is considerably higher than that of air, and, secondly, the major radiation sources are the molecules produced in chemical reactions (CN, CO, C_2), similar to molecules of nitric oxide in high-temperature air. In the relaxation zone behind the shock wave in air, O_2 and N_2 molecules pass into excited states as a result of collisions with electrons and other particles in the mixture. In calculating the radiation from CO_2–N_2 mixtures, one must additionally consider the possible direct formation of molecules in the electron-excited states in the course of the chemical transformation, which sig-

1063-7842/01/4606-0654$21.00

nificantly complicates interpretation of the experimental data.

In this study, analysis of the nonequilibrium radiation behind a shock wave propagating in a CO_2–N_2–Ar mixture is made using an approach proposed in [16]. In this approach, values of the rate constants of the principal chemical reactions are assumed fixed and the calculated and measured radiation intensities are made to fit by varying only the excitation cross sections of the electron states; in this way, more accurate values of the latter are obtained. The rate constants of the principal chemical ionization reactions were borrowed from published data, and some excitation cross sections of the electron states of CN and C_2 molecules, which are the major radiation sources, were derived from data obtained in additional experiments in a shock tube.

AN EXPERIMENTAL INVESTIGATION OF THE RADIATION FROM THE AREA BEHIND A SHOCK WAVE

Figure 1 displays a block diagram of the experimental setup [17]. The Martian atmosphere composition was the same as in the INTERMARSNET project [18]. For a more intensive heating, the gas mixture behind the shock wave front was diluted with argon in a ratio of 1 : 10 or 1 : 20. Such a dilution of the mixture, by making the "plug" of the heated gas longer, also reduced the possible influence of the driver gas and contact surface on the radiation characteristics of the mixture under study. On the basis of this reasoning, two mixture compositions were chosen: (I) $CO_2 : N_2 : Ar = 0.096 : 0.003 : 0.901$, and (II) $CO_2 : N_2 : Ar = 0.048 : 0.0015 : 0.9595$. Using these gas mixtures, three series of experiments were carried out: the first one with mixture (I) at an initial pressure of $P_1 = 1$ torr and an average shock wave velocity of $V_s = 3.45$ km/s; the second series used mixture (I) at $P_1 = 5$ torr and $V_s = 2.94$ km/s; and in the third, mixture (II) at $P_1 = 0.5$ torr and $V_s = 3.75$ km/s.

The absolute radiation intensity was measured by comparison with radiation from a calibrated source [17]. The receiving chamber registered the intensity distribution $U_c(\lambda) = \Delta t_c k_c(d_L, d_S) F_{SI\text{-}8}(\lambda)$, where Δt_c is the time the SIT-500 receiving chamber was exposed to the SI-8 standard lamp; $k_c(d_L, d_S)$ is a coefficient depending on the geometry of the optical system (size of the diaphragm d_L in front of the lens and the spectrograph slit width d_S); and $F_{SI\text{-}8}(\lambda)$ is the spectral density of radiance of the SI-8 lamp in units of W/(cm^2 μm sr).

The experimental data were processed under the assumption that there was no absorption of the radiation by gas. To verify this assumption, an aluminum mirror was placed behind the window opposite the viewing window; this increased twofold the radiation signal registered from the C_2 and CN molecules. The total error of determining the spectral radiance of the gas behind the shock wave amounted to 90%, in which the following were taken into account: the calibration error of the OSA-WP4 spectrum analyzer (comprising inaccuracies of the monochromator slits, the time in which the shutter was open, and the optical-system alignment) and an error of filling by the gas under study and leakage of the shock tube.

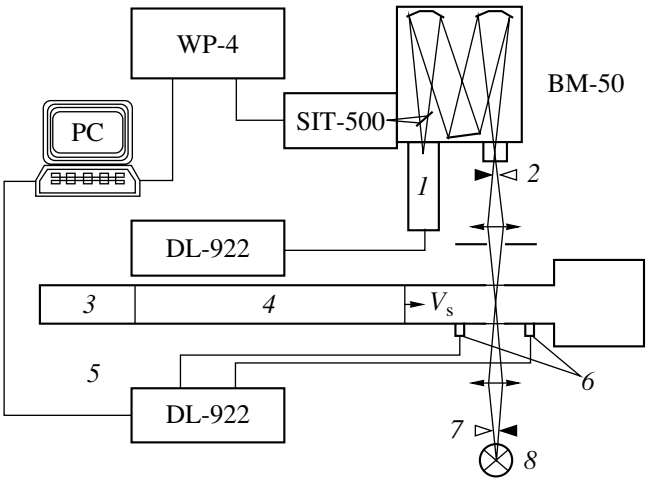

Fig. 1. Schematic diagram of the experimental setup. (*1*) Photomultiplier connected to a DL-922digital oscilloscope; (*2*) chopper; (*3*), (*4*) high- and low-pressure chambers, respectively; (*5*) diaphragm; (*6*) piezoelectric transducers; (*7*) shutter; (*8*) tungsten tape lamp.

The experimentally determined distribution of the spectral intensities of the shock wave radiation in three series of experiments is shown in Fig. 2. To identify the spectra, we used reference data from [19, 20]. The spectra were obtained with a spectral resolution of 0.6 nm and feature red and violet bands of CN molecules, the Swan bands of C_2 molecules, and the spectral lines of monatomic oxygen and carbon. The spectral lines of sodium, potassium, and calcium observed in the second series of experiments are associated with the radiation from a boundary layer next to the viewing window of the shock tube detector section. This is confirmed by the fact that these lines could be detected quite far beyond the shock wave and that their intensities increased approximately by an order of magnitude if the MgF_2 window were replaced by K8 glass.

Figure 3 (curve *1*) shows a time variation of the radiation intensity of the violet band of CN (band 0–0) in a spectral interval of 1.33 nm centered at a wavelength of 387 nm detected by a photomultiplier. Radiation in one of the red bands of CN over an interval of 1.33 nm centered at 650 nm is presented by curve *2*. Characteristically different rise times should be noted for radiation in the violet and red bands of CN from immediately behind the shock wave front. Curve *3* represents the behavior with time of one of the Swan bands of C_2 molecules in an interval of 7.8 nm around the 470-nm wavelength. In the oscillogram there is a pronounced

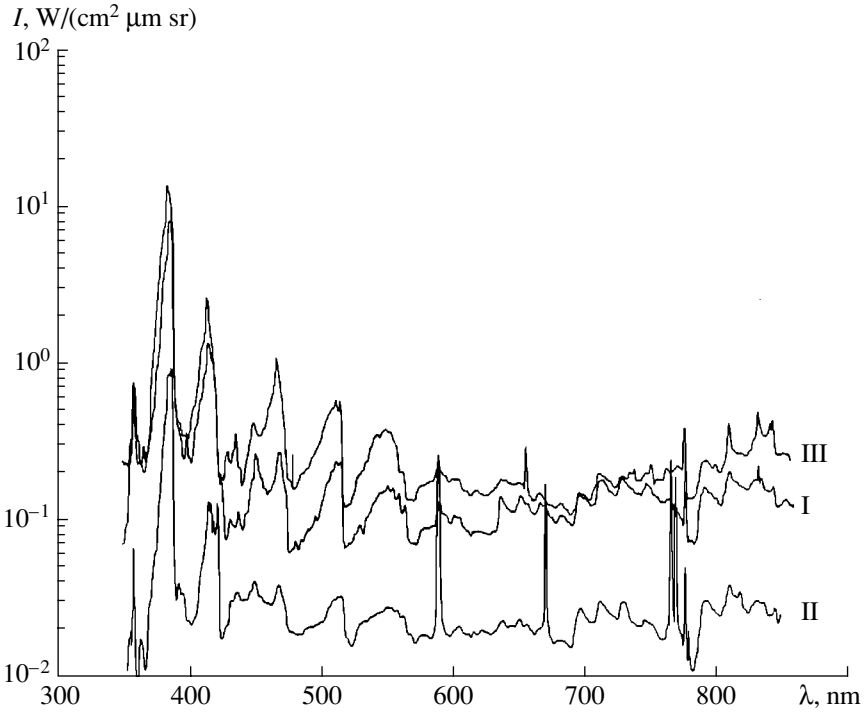

Fig. 2. The radiation intensity from behind the shock wave recalculated for "foreward" direction. (I): $CO_2 : N_2 : Ar = 0.096 : 0.003 : 0.901$ at $P_1 = 1$ torr and $V_s = 3.45$ km/s; (II): $CO_2 : N_2 : Ar = 0.096 : 0.003 : 0.901$, at $P_1 = 5$ torr and $V_s = 2.94$ km/s; (III): $CO_2 : N_2 : Ar = 0.048 : 0.0015 : 0.9595$ at $P_1 = 0.5$ torr and $V_s = 3.75$ km/s.

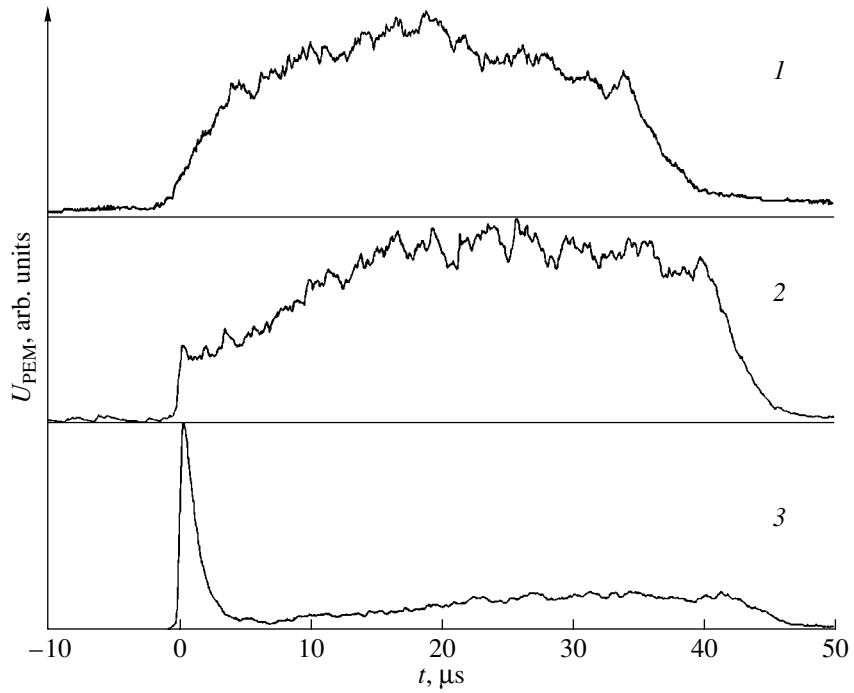

Fig. 3. Variation with time of the radiation from behind the shock wave for a $CO_2 : N_2 : Ar = 0.096 : 0.003 : 0.901$ mixture at $P_1 =$ 1 torr and $V_s = 3.45$ km/s. (*1*) Violet band system of CN (*B*): $\lambda = 387$ nm, $\Delta\lambda = 1.33$ nm; (*2*) red band system of CN (*A*): $\lambda = 650$ nm, $\Delta\lambda = 1.33$ nm; (*3*) the Swan band of C_2: $\lambda = 470$ nm, $\Delta\lambda = 7.8$ nm.

Table 1

Process no.	Process	A	n	E, K	A
1	$CN(X^2\Sigma^+) + M_1 \longleftrightarrow CN(B^2\Sigma^+) + M_1$	2.24×10^{10}	0.5	37000	1.8×10^{11}
2	$CN(X^2\Sigma^+) + e \longleftrightarrow CN(B^2\Sigma^+) + e$	7.8×10^{13}	0.5	37000	6.24×10^{14}
3	$CN(X^2\Sigma^+) + M_1 \longleftrightarrow CN(A^3\Pi) + M_1$	1.5×10^{10}	0.5	13300	1.5×10^{11}
4	$CN(X^2\Sigma^+) + e \longleftrightarrow CN(A^2\Pi) + e$	6×10^{13}	0.5	13300	6×10^{14}
5	$CO(X^1\Sigma^+) + M \longleftrightarrow CO(A^1\Pi) + M$	4.5×10^{2}	2.86	93000	
6	$CO(X^1\Sigma^+) + M \longleftrightarrow CO(A^1\Sigma^+) + M$	2.2×10^{2}	2.86	125000	
7	$CO(X^1\Sigma^+) + M \longleftrightarrow CO(b^3\Sigma^+) + M$	10^{14}	0.5	120900	
8	$CO(X^1\Sigma^+) + e \longleftrightarrow CO(A^2\Sigma^+) + e$	2×10^{14}	0.5	66000	
9	$C_2(X^1\Sigma_g^+) + e \longleftrightarrow C_2(d^3\Pi_g) + e$	7.82×10^{15}	0.15	28807	
10	$C_2(X^2\Sigma_g^+) + M_1 \longleftrightarrow C_2(d^3\Pi_g) + M_1$	1.95×10^{12}	0.15	28807	5.2×10^{13}

peak of radiation from a region directly behind the shock wave. Such a peak was present in all Swan bands observed in the experiment. An additional experimental study of the spectral structure of the radiation peak was carried out. In those experiments, the radiation peak was recorded by an OSA gated multichannel spectrum analyzer which was recording for 2 and 3 μs after the shock wave front reached the detector section. The spectral composition of the peak turned out to be identical with that of the shock wave radiation for the entire time period that it could be observed in this spectral range, which was identified as Swan bands of C_2.

A THERMOCHEMICAL MODEL OF THE HIGH-TEMPERATURE NONEQUILIBRIUM RADIATING CO_2–N_2–Ar MIXTURES

In the numerical simulations of the principal phenomena taking place behind the shock wave (used for comparing experimental and calculated data), the following components and their electronic and vibrational states were taken into account:

CO_2, N_2, CO, O_2, O, NO, N, Ar, C, C_2 CN,

e, N^+, O^+, N_2^+, NO^+, O_2^+, C^+, CO^+, Ar^+,

$CN(X^2\Sigma^+)$, $CN(A^2\Pi)$, $CN(B^2\Sigma^+)$, $C_2(X^1\Sigma_g^+)$, $C_2(d^3\Pi_g)$,

$CO(X^1\Sigma^+)$, $CO(A^1\Pi)$, $CO(B^1\Sigma^+)$, $CO(b^3\Sigma^+)$, $CO(d^3\Pi)$,

$CO^+(X^2\Sigma^+)$, $CO^+(B^2\Sigma^+)$,

$CO_2(v_1)$, $CO_2(v_2)$, $CO_2(v_3)$, $N_2(v)$, $O_2(v)$,

$CO(v)$, $NO(v)$.

Excited electron states of N_2, NO, … molecules were not taken into account because the initial N_2 concentration was much lower than the CO_2 concentration. The thermochemical model of a mixture corresponding to Martian atmosphere took into account the following processes taking place at high temperatures: chemical reactions involving neutral and charged species, excitation and deactivation of electron states of molecules, radiation involving excited species, vibrational (*VT* and *VV*') energy exchange with the participation of various modes of polyatomic molecules, and *CV*-processes (the influence of chemical reactions on vibrational relaxation) [21, 22].

The rate constants of the chemical reactions were taken from works [1, 5, 22, 23]. The rate constants of the reverse reactions were calculated using the equilibrium constant and the reduced thermodynamic potential [24]. The complete list of the reactions and the vibrational energy exchange times are given in [17].

In a thermally nonequilibrium gas, where there is no equilibrium between translational and vibrational degrees of freedom of the reactant molecules, the rate constant of a chemical reaction depends not only on the translational temperature T but also on the vibrational temperature T_v. In this case, it is convenient to write the rate constant in the form $k(T, T_v) = Z(T, T_v)k^0(T)$, where $k^0(T)$ is the rate constant of the thermally equilibrium

Table 2

Process	τ_{mn}, s
$CN(B^2\Sigma^+) \longrightarrow CN(A^2\Pi) + h\nu$	6.25×10^{-8}
$CN(B^2\Sigma^+) \longrightarrow CN(X^2\Sigma^+) + h\nu$	6.25×10^{-8}
$CN(A^2\Pi) \longrightarrow CN(X^2\Sigma^+) + h\nu$	8.0×10^{-6}
$C_2(d^3\Pi_g) \longrightarrow C_2(a^3\Pi_u) + h\nu$	1.07×10^{-7}
$CO(A^1\Pi) \longrightarrow CO(X^1\Sigma^+) + h\nu$	1.0×10^{-8}
$CO(B^1\Sigma^+) \longrightarrow CO(A^1\Pi) + h\nu$	2.37×10^{-8}
$CO(B^1\Sigma^+) \longrightarrow CO(X^1\Sigma^+) + h\nu$	2.37×10^{-8}
$CO(b^3\Sigma^+) \longrightarrow CO(a^3\Pi) + h\nu$	5.62×10^{-8}
$CO^+(B^2\Sigma^+) \longrightarrow CO^+(X^2\Sigma^+) + h\nu$	5.2×10^{-8}
$CO^+(B^2\Sigma^+) \longrightarrow CO^+(A^2\Pi) + h\nu$	5.2×10^{-8}

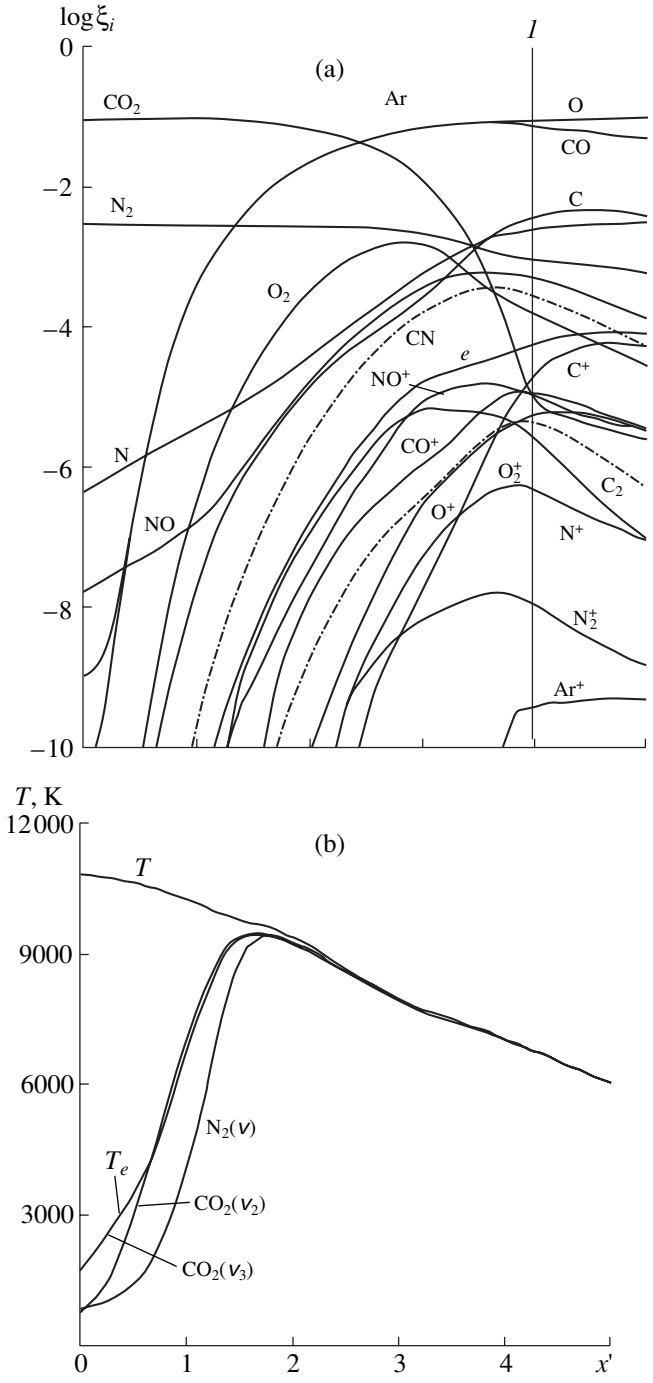

Fig. 4. Variations of (a) the molar fractions ξ_i for neutral and charged species as well as (b) the translational T, electron T_e, and vibrational temperatures in a $CO_2 : N_2 : Ar = 0.096 : 0.003 : 0.901$ mixture at $P_1 = 1$ torr and $V_s = 3.45$ km/s with $x' = \log(x/L_c)$, where x is the distance from the shock wave-front and L_c is the mean free path of a particle behind the shock wave front (at $x = 0$); the radiating region behind the shock wave front is indicated by the vertical line (*1*).

process and $Z(T, T_v)$ is a nonequilibrium factor. An analysis of the two existing models of the temperature-dependent rate constants of chemical reactions and of the nonequilibrium factor was given in [25]. For describing the thermally nonequilibrium disintegration of CO_2 molecules, we used a model by Kuznetsov [26].

The processes of excitation and deexcitation of the electron states of molecules taken into account in our model are presented in Table 1. Given in the same table are the rate constants $k_j = AT^n\exp(-E/T)$ of the forward reactions. The rates of reverse processes were calculated using the equilibrium constant. In the kinetic formulas for the processes 1, 3, and 10 (see Table 1), M_1 denotes any particle other than an electron. For the radiation processes, the lifetimes τ_{mn} of the corresponding electron states were chosen according to [27]; they are given in Table 2. The excitation rate constant of electron states $B^2\Sigma^+$ and $A^2\Pi$ of cyanogen molecules (reactions 1 and 3 in Table 1) were obtained from comparing the calculated data on the radiation intensity of the bands of violet and red peaks with experimental data given in [7]. Since in the excitation reaction the particles involved were assumed indistinguishable, the determined quantity in fact represented some effective excitation rate constant resulting from all the processes that was likely to cause excitation of the corresponding states. Data on the excitation rate constants of $CN(B^2\Sigma^+)$ and $CN(A^2\Pi)$ for collisions with electrons (processes 2 and 4 in Table 1) were obtained using Drawin's formulas [26]. The rate constants obtained in this way are in fair agreement with experimental data of various authors on the intensity of nonequilibrium radiation from CO_2–N_2 mixtures over a fairly wide range of the shock wave velocities and gas pressures.

The inverse processes to those of radiation are important in optically dense gases. In the relaxation zone behind the shock wave, the gas, as a rule, is optically transparent (at least to radiation from the principal radiation sources); therefore, the absorption of radiation will be not considered here.

In the collision processes leading to excitation of the electron states, the most effective particles are electrons. To determine the electron temperature T_e of the gas behind the shock wave front we used an electron energy balance equation $n_e\Sigma_k Q_k^e = 0$, where n_e is the electron concentration; Q_k^e is the electron energy exchange rate for various processes (elastic collisions with atoms, molecules; elastic collisions with ions; the excitation of rotations and vibrations of molecules; the excitation of electron states of atoms and molecules; the ionization of atoms and molecules, and recombination of charges).

Below we describe the results concerning determination and refinement of the rate constants of excitation for the molecules making a major contribution to the radiation intensity of the gas simulating the Martian atmosphere at temperatures of several thousand degrees. The study will focus on the electron-excited states of C_2 and CN molecules and include both the

above-described experiments [28] carried out in a shock tube and aimed at obtaining a quantitative description of the radiation from the Martian atmosphere and calculations of the radiation spectrum taking into account principal kinetic processes behind the shock wave. More accurate values of the rate constants of the above processes were obtained by fitting the experimental and calculated spectral distributions. Concentrations of the components behind the shock wave were calculated with the use of an automated system described in [21, 29].

As seen from Fig. 2, under the conditions of our experiments, molecular spectral bands systems make the major contribution to the radiation of a shock-heated gas. For each of the band systems, the integrated radiation intensity over the registration range (350–850 nm) was calculated. Radiation from diatomic molecules can be calculated with the use of various models [30]. The choice of model depends on the volume of calculations to be made and the required accuracy. The most accurate model is a "line-by-line" model, which takes into account the multiple spectrum structure and contours of the rotational lines [31]. However, this model demands a large expenditure of computer time; therefore, it is used only in solving diagnostic problems requiring high accuracy and also for calculations in narrow spectral ranges. As the intensity measurement error in our experiments could be up to 90%, we could not justify using this precision model. We used a model of averaging of the rotational spectrum structure, known as a "just overlapping line model" or a *Q*-branch model [32]. In this model, the spectrum is assumed to consist of a single branch. Each line of this branch is characterized by an average spectral radiation coefficient, which is the ratio of the line's integrated coefficient and the distance to the adjacent rotational line. The integrated radiation coefficient of this line is equal to the sum of the integrated radiation coefficients of all rotational lines of an electron-vibrational band with a given value of J'' (determined according to the recommendation in [33, 34]).

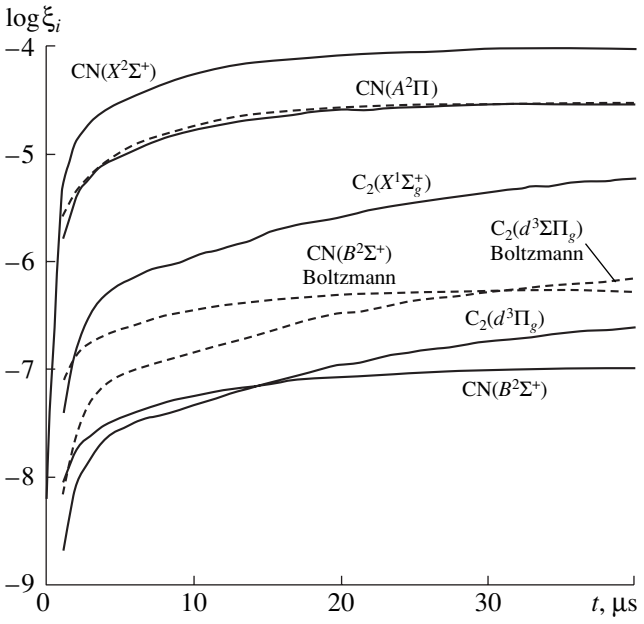

Fig. 5. Molar fractions ξ_i as functions of the "laboratory" time t of the species CN($X^2\Sigma^+$), CN($A^2\Pi$), CN($B^2\Sigma^+$), CN($X^1\Sigma_g^+$), and $C_2(d^3\Pi_g)$ for a $CO_2 : N_2 : Ar = 0.096 : 0.003 : 0.901$ mixture at $P_1 = 1$ torr and $V_s = 3.45$ km/s. The solid lines represent the calculation results with the electron-excited states considered as isolated components. The dashed curves correspond to a model assuming the Boltzmann distribution of the radiating components in the electron states.

RESULTS

Using the developed model, calculations were made of component concentrations in the ground and excited states behind the shock wave front propagating through a simulated Martian atmosphere and through a mixture of 10% Martian atmosphere and 90% argon, for velocities up to 8 km/s and pressures of a few torr. The calculation results were compared with similar numerical data by other authors, in particular, Park *et al*. [5]. Our data on the concentrations of neutral and charged particles, as well as the vibration temperatures, were close to those of [5]. Note that the authors of [5] did not take into account the nonequilibrium distribution of the electron-excited species.

As for the kinetics involving electron-excited particles, the following should be noted. Though the electron-excited species make the greatest contribution to the radiation spectrum of the Martian atmosphere, their concentrations are low and, therefore, distribution of the concentrations of component in the ground states cannot be affected by varying the formation rate constants k_j of these species. Besides, the characteristic wavelengths in the radiation spectra of CN($A^2\Pi$), CN($B^2\Sigma^+$), and $C_2(d^3\Pi_g)$ species (just these molecules make a major contribution to the radiation spectrum in our case) do not coincide. This practically excludes the mutual correlation of the rate constants k_j that determine the concentrations of the excited states of these molecules [17]. In this case, the above solution of the inverse problem by fitting the calculated and experimental spectra patterns makes it possible to determine several rate constants for excitation and deactivation of the electron states of the species simultaneously in a single experiment.

Figure 4a shows the variation of the concentrations of the neutral and charged species behind the shock wave ($V_s = 3.45$ km/s, $P_1 = 1$ torr, $CO_2 : N_2 : Ar = 0.096 : 0.003 : 0.901$), demonstrating that variation of the component concentrations in the region under study is nonequilibrium (the extent of the region of emitted gas behind the shock wave is indicated by the vertical

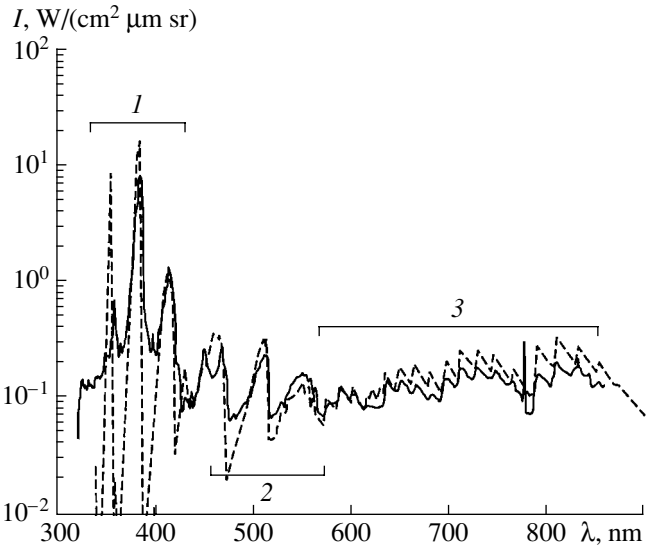

Fig. 6. The experimental (solid lines) and total calculated (dashed lines) radiation spectrafor transitions: λ for the transitions (*1*) $CN(B^2\Sigma^+) \longrightarrow CN(X^2\Sigma^+)$, (*2*) $C_2(d^3\Pi_g) \longrightarrow C_2(a^3\Pi_u)$, and (*3*) $CN(A^2\Pi) \longrightarrow CN(X^2\Sigma^+)$ for a $CO_2 : N_2 : Ar = 0.096 : 0.003 : 0.901$ mixture at $P_1 = 1$ torr and $V_s = 3.45$ km/s.

line). Note that in Fig. 4a distributions of the concentrations of the species that determine the radiation spectrum are not shown; these data are given in Fig. 5. Curves in Fig. 4b show distributions of the translational *T*, electronic T_e, and vibrational temperatures. It is seen that in the region studied, all the temperatures are close to each other.

Calculated spectra in the red and violet bands of CN can be fitted to the experiment if the rate constants are increased eightfold for processes 1 and 2 (Table 1) and 10-fold for processes 3 and 4. The calculated and experimental data in the Swan band for C_2 can be made to agree if the rate constant of the process $C_2(X^1\Sigma_g^+) + M_1 \longrightarrow C_2(d^3\Pi_g) + M_1$ (reaction 10 in Table 1) is taken as $k_{10} = k_9/150$, where k_9 is the rate constant of the channel considered for collisions with electrons (reaction 9 in Table 1). Recommended values of *A* for the rate constant of forward processes 1–4 and 10 are given in the last column of Table 1.

Figure 5 shows the calculated variation of the concentrations of $CN(A^2\Pi)$, $CN(B^2\Sigma^+)$, $C_2(d^3\Pi_g)$, $CN(X^2\Sigma_g^+)$, and $C_2(X^1\Sigma_g^+)$ behind the shock wave from experiments in the shock tube, taking into account the above-mentioned corrections to the rate constants of the processes 1–4, 9, and 10 of Table 1. The solid lines represent calculation results obtained under the assumption that each of the electron-excited states is considered as an isolated component. The dashed curves in Fig. 5 relate to a model assuming the Boltzmann distribution of the radiating components over the electron states. From the results presented in Fig. 5, it follows that the populations of the states $CN(B^2\Sigma^+)$ and $C_2(d^3\Pi_g)$ are considerably different from the Boltzmann distribution, and the population of the state $CN(A^2\Pi)$ is close to it. This indicates that in the simulations each of the electron-excited states should be considered as an isolated component.

The experimental and calculated radiation distributions for the optimum choice of the rate constants of processes 1–4, 9, and 10 of Table 1 obtained in the first series of the experiments are shown in Fig. 6. Calculated and experimental data have been found to agree both in the violet and red band systems of CN and in the Swan band for C_2 molecules.

It should be noted that the kinetic model employed cannot describe the anomalies of radiation in the Swan bands of C_2 molecules directly behind the shock wave occurring in the "laboratory" time interval of $t_l \sim 1$ μs at a shock wave velocity of $V_s = 3.45$ km/s (Fig. 3). Therefore, the initial kinetic model of [17] was supplemented by processes occurring behind the shock wave prior to dissociation of CO_2. These processes are $CO_2 + CO_2 \longrightarrow C_2(X^1\Sigma_g^+) + O_2 + O_2$ and $CO_2 + CO_2 \longrightarrow C_2(d^3\Pi_g) + O_2 + O_2$. An attempt to determine the rate constants of these processes was undertaken in [17].

The calculations showed also that under the experimental conditions the contribution to the radiation of CO molecules is small. Note that CO molecules are formed as a result of CO_2 dissociation ($CO_2 + M \longrightarrow CO + O + M$) and formation of the electron-excited states of CO in chemical reactions seems unlikely.

CONCLUSIONS

(1) The proposed physicochemical model of CO_2–N_2–Ar mixtures satisfactorily describes both the integrated and spectral intensities of the radiation from a gas heated by a shock wave.

(2) In calculating the intensity and spectral distribution of radiation from gas in the relaxation zone behind a shock wave or from the shock layer about objects traveling through an atmosphere, it is necessary to take into account possible deviation of the actual distribution of electron states of the gas molecules from the Boltzmann distribution.

REFERENCES

1. R. N. Gupta and K. P. Lee, AIAA Pap. **94-2025** (1994).
2. R. D. Kay and M. P. Netterfield, AIAA Pap. **93-2841** (1993).
3. M. A. Gallis and J. K. Harvey, AIAA Pap. **95-2095** (1995).
4. L. B. Ibragimova and S. A. Losev, Kinet. Katal. **24**, 263 (1983).

5. C. Park, J. T. Howe, R. L. Jaffe, and G. V. Candler, J. Thermophys. Heat Transfer **8**, 9 (1994).
6. G. V. Candler, AIAA Pap. **90-1695** (1990).
7. R. L. McKenzie and J. O. Arnold, AIAA Pap. **67-322** (1967).
8. G. P. Menees and R. L. McKenzie, AIAA J. **6** (3), 554 (1969).
9. G. M. Thomas and W. A. Menard, AIAA J. **4** (2), 227 (1966).
10. J. O. Arnold, V. H. Reis, and H. T. Woodward, AIAA J. **3** (11), 2019 (1965).
11. T. Tir, S. Georgiev, and R. Allen, in *Hypersonic Flow Reserch*, Ed. by F. R. Riddell (Academic, New York, 1962; Mir, Moscow, 1964).
12. G. N. Zalogin, V. V. Lunev, and Yu. A. Plastinin, Izv. Akad. Nauk SSSR, Mekh. Zhidk. Gaza, No. 1, 105 (1980).
13. A. B. Gorshkov, G. N. Zalogin, and V. V. Lunev, in *Rocket Space Technology* (TsNIIMASh, Moscow, 1994), Ser. 2, issue 1, p. 74.
14. G. N. Zalogin, Izv. Akad. Nauk SSSR, Mekh. Zhidk. Gaza, No. 6, 81 (1974).
15. N. A. Anfimov, Yu. A. Dem'yanov, Yu. A. Zavernyaev, *et al.*, Izv. Akad. Nauk SSSR, Mekh. Zhidk. Gaza, No. 1, 36 (1981).
16. R. C. Flagan and J. P. Appleton, J. Chem. Phys. **56**, 1163 (1972).
17. G. N. Zalogin, P. V. Kozlov, L. A. Kuznetsova, *et al.*, Preprint No. 40-98, Institut Mekhaniki Mosk. Gos. Univ. (Institute of Mechanics, Moscow State University, Moscow, 1998).
18. *INTERMARSNET: Report on Phase-A Study* (European Space Agency, 1996), D/SCI(96) 2, April.
19. R. W. B. Pearse and A. G. Gaydon, *The Identification of Molecular Spectra* (Chapman and Hall, London, 1976).
20. A. N. Zaĭdel', V. K. Prokof'ev, S. M. Raĭskiĭ, *et al.*, *Tables of Spectral Lines* (Nauka, Moscow, 1977; Plemun, New York, 1970).
21. V. N. Makarov, Kvantovaya Élektron. (Moscow) **24** (10), 895 (1997).
22. V. N. Makarov, Prikl. Mekh. Tekh. Fiz. **37** (2), 69 (1996).
23. J. S. Evans, C. J. Schexnayder, and W. L. Grose, J. Spacecr. Rockets **11** (12), 84 (1974).
24. L. V. Gurvich and N. P. Rtishcheva, Teplofiz. Vys. Temp. **3** (1), 33 (1965).
25. É. A. Kovach, S. A. Losev, and A. L. Sergievskaya, Khim. Fiz. **14** (9), 44 (1995).
26. *Physicochemical Processes in Gas Dynamics. Computer Reference Book*, Vol. 1: *Dynamics of Physicochemical Processes in Gas and Plasma*, Ed. by G. G. Chernyĭ and S. A. Losev (Mosk. Gos. Univ., Moscow, 1995).
27. L. A. Kuznetsova, E. A. Pazyuk, and A. V. Stolyarov, Russ. J. Phys. Chem. **67**, 2046 (1993).
28. P. V. Kozlov, S. A. Losev, and Yu. V. Ramanenko, Preprint No. 33-97, Institut Mekhaniki Mosk. Gos. Univ. (Institute of Mechanics, Moscow State University, Moscow, 1997).
29. V. N. Makarov, Khim. Fiz. **18** (4), 48 (1999).
30. L. A. Kuznetsova and S. T. Surzhikov, AIAA Pap. **97-2564** (1997).
31. D. R. Churchill, S. A. Hangstrom, and R. K. M. Landshoff, J. Quant. Spectrosc. Radiat. Transf. **4**, 291 (1964).
32. R. W. Patch, W. L. Shackleford, and S. S. Penner, J. Quant. Spectrosc. Radiat. Transf. **2**, 263 (1962).
33. E. E. Whiting, A. Schadee, J. B. Tatum, *et al.*, J. Mol. Spectrosc. **80**, 249 (1980).
34. L. A. Kuznetsova and S. T. Surzhikov, in *Proceedings of the 7th AIAA/ASME Joint Thermophysics and Heat Transfer Conference, 1998*, Vol. 1, p. 41.

Translated by N. Mende

Technical Physics, Vol. 46, No. 6, 2001, pp. 662–667. Translated from Zhurnal Tekhnicheskoĭ Fiziki, Vol. 71, No. 6, 2001, pp. 17–22.

GASES AND LIQUIDS

Interaction of Shock Waves with Bubble-Liquid Drops

V. S. Surov

Chelyabinsk State University, Chelyabinsk, 454021 Russia

e-mail: svs@csu.ru

Received May 12, 2000; in final form, September 8, 2000

Abstract—The regular reflection of an air shock wave from a spherical drop of a bubble liquid is studied. In the framework of an extended equilibrium model, the effect of the shock waves on single drops of various shapes and on drop ensembles (drop screens) is numerically investigated. It is shown that, when subjected to shock waves, bubble-liquid drops and drops of a bubble-free liquid collapse in a radically different way. © *2001 MAIK "Nauka/Interperiodica".*

INTRODUCTION

In contrast to a solid particle, a liquid drop in a gas flow behind the shock wave front experiences internal motion, causing the drop to deform and break down. The breakdown process is very intricate and depends on the surface tension, viscosity, and inertia of the medium. The effect of air shock wave on drops of various liquids has been studied experimentally in [1–4]. A method for computing the interaction of a water drop with a plane shock wave has been proposed [5]. It uses the assumption that the deformed drop takes the shape of an ellipsoid of revolution that is flattened along the flow direction. The same assumption was used in other papers [6, 7]. Subsequently, direct numerical simulation was used for studying the interaction of shock waves with drops, and various models of liquid were employed. For example, the liquid was assumed to be compressible nonviscous [8] or incompressible viscous [9, 10]. In all the cases, however, the liquid was assumed to be free of gas bubbles.

It is known that a liquid becomes aerated (saturated by gas) under the action of an intense air shock wave [11]. The properties of such a liquid essentially change. It is important to study the effect of gas content on the interaction between a shock wave and a drop (drop ensemble) of a bubble liquid. Here, we extend the equilibrium model used earlier [12, 13].

THE REGULAR REFLECTION OF AN AIR SHOCK WAVE FROM A SPHERICAL BUBBLE-LIQUID DROP

Let a plane air shock wave in the form of a semi-infinite step strike a spherical drop of a bubble liquid. The parameters of the air behind the wave front (they are marked with the subscript *s*) are related to those before the shock (marked with the subscript 0) by the Rankine–Hugoniot equations

$$p_s = p_0\left(1 + \frac{2\gamma(M^2-1)}{\gamma+1}\right), \quad u_s = \frac{2c_0(M^2-1)}{(\gamma+1)M}, \qquad p_s = p_0\left(\frac{(\gamma+1)M^2}{2+(\gamma-1)M^2}\right), \tag{1}$$

where γ is the adiabatic exponent of air, c_0 is the speed of sound, $M = D/c_0$ is the Mach number, and D is velocity of the shock wave front.

Let us analyze liquid and gas flows near the point where the shock wave touches the drop surface. Compatibility equations in a moving coordinate system related to the point of contact (Fig. 1a) have the form

$$\begin{gathered} u_{1n}\sin\varphi - c_0 M\sin(\beta_1+\varphi) = 0, \\ u_{1t}\sin\varphi - c_0 M\cos(\beta_1+\varphi) = 0, \\ u'_{1t}\cos(\beta_1+\delta) - u'_{1t}M\sin(\beta_1+\delta) = 0, \\ u'_{1t} = u_{1t}, \quad u_{2n} - u_2\sin(\beta_2-\vartheta_2) = 0, \\ u_{2t} - u_2\cos(\beta_2-\vartheta_2) = 0, \\ u'_{2n}\cos(\beta_2-\delta) - u'_{2t}\sin(\beta_2-\delta) = 0, \quad u'_{2t} = u_{2t}, \end{gathered} \tag{2}$$

where u_2 and ϑ_2 are found from the equations

$$\begin{gathered} u_2^2 - (c_0 M\cot\varphi)^2 - (c_0 M - u_s)^2 = 0, \\ \tan\vartheta_2 = (1 - M_s/M)\tan\varphi, \\ M_s = u_s/c_0. \end{gathered}$$

The Rankine–Hugoniot equations for the reflected and refracted shock waves are as follows:

$$\begin{gathered} \rho'_2 u'_{2n} - \rho_s u_{2n} = 0, \\ p'_2 + \rho'_2 (u'_{2n})^2 - p_s - \rho_s (u_{2n})^2 = 0, \\ \rho'_1 u'_{1n} - \rho_{10} u_{1n} = 0, \\ p'_1 + \rho'_1 (u'_{1n})^2 - p_0 - \rho_{10} (u_{1n})^2 = 0. \end{gathered} \tag{3}$$

Here, the subscripts n and t denote the velocity components, respectively, normal and tangent to the attached shock waves. A prime marks the parameters behind the reflected and refracted waves. The pressure values must be sewed together at the shock-wave discontinuity:

$$p_1' = p_2' = p. \tag{4}$$

Formulas (2)–(4) should be complemented with the equations of percussive adiabats for the gas and bubble liquid [12]:

$$\frac{\rho_s}{\rho_2'} = \frac{\chi p_2' + p_s}{\chi p_s + p_2'},$$

$$\frac{\rho_{10}}{\rho_1'} = \alpha_0 \frac{\chi_1 p_1' + p_0}{\chi_1 p_0 + p_1'} + (1-\alpha_0)\frac{\chi_*(p_1' + p_*) + p_0 + p_*}{\chi_*(p_0 + p_*) + p_1' + p_*}, \tag{5}$$

where α_0 is the volume fraction of the gas, $\chi = (\gamma - 1)/(\gamma + 1)$, $\chi_1 = (\gamma_1 - 1)/(\gamma_1 + 1)$ is the adiabatic exponent of the gas in the bubbles, $\chi_* = (\gamma_* - 1)/(\gamma_* + 1)$, and γ_* and p_* are the constants of the two-term equation of state [12] whereby the properties of the liquid component are described. For water (glycerol), $\gamma_* = 5.59$ (7.85) and $p_* = 4.106$ (5.936) MPa.

From (2) and (3), we have

$$\frac{\rho_s}{\rho_2'} = \frac{u_{2n}'}{u_{2n}} = \frac{\tan(\beta_2 - \delta)}{\tan(\beta_2 - \vartheta_2)},$$

$$\frac{\rho_{10}}{\rho_1'} = \frac{u_{1n}'}{u_{1n}} = \frac{\tan(\beta_1 + \delta)}{\tan(\beta_1 + \varphi)}, \tag{6}$$

$$p_2' = p_s + p_s u_2^2 \sin^2(\beta_2 - \vartheta_2)(1 - \tan(\beta_2 - \delta)/\tan(\beta_2 - \vartheta_2)),$$

$$p_1' = p_0 + \frac{\rho_{10} c_0^2 M^2 \sin^2(\beta_1 + \varphi)}{\sin^2\varphi}\left(1 - \frac{\tan(\beta_1 + \delta)}{\tan(\beta_1 + \varphi)}\right).$$

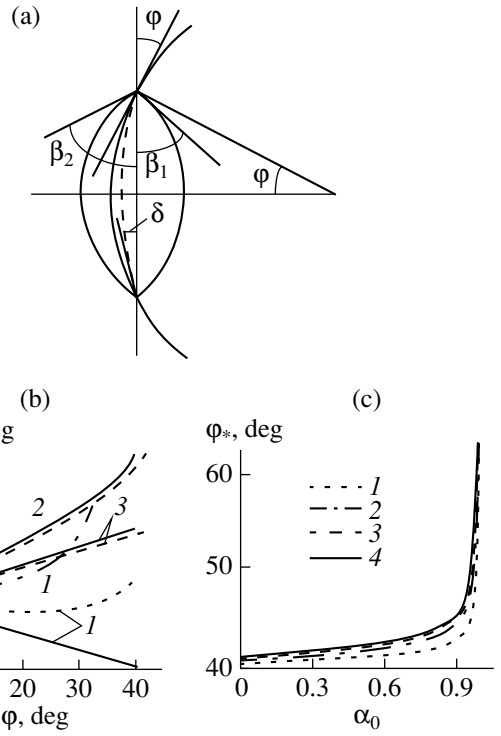

Fig. 1. (a) Regular reflection of the shock wave from a spherical bubble-liquid drop; (b) (*1*–*3*) functions β_1, β_2, and δ for the gas concentrations $\alpha_0 = 0.1$ (solid curves), 0.2 (dashed curves), 0.0001 (dash-and-dot curves), and 0.001 (dotted curves) at $M = 2$; and (c) function $\varphi_*(\alpha_0)$ at $M =$ (*1*) 2, (*2*) 5, (*3*) 10, and (*4*) 20.

Using (6), Eqs. (4) and (5) take the form

$$\tilde{p}_s + \sin^2(\beta_2 - \vartheta_2)(1 - \tan(\beta_2 - \delta)/\tan(\beta_2 - \vartheta_2)) = \tilde{p}_0 + \frac{\rho_{10} c_0^2 M^2 \sin^2(\beta_1 + \varphi)}{\rho_s u_2^2 \sin^2\varphi}\left(1 - \frac{\tan(\beta_1 + \delta)}{\tan(\beta_1 + \varphi)}\right), \tag{7}$$

$$\tan(\beta_2 - \delta)/\tan(\beta_2 - \vartheta_2) = \frac{\chi \sin^2(\beta_2 - \vartheta_2)(1 - \cot(\beta_2 - \vartheta_2)\tan(\beta_2 - \delta)) + \tilde{p}_s'(\chi + 1)}{\sin^2(\beta_2 - \vartheta_2)(1 - \cot(\beta_2 - \vartheta_2)\tan(\beta_2 - \delta)) + \tilde{p}_s'(\chi + 1)}, \tag{8}$$

$$\tan(\beta_1 + \delta)/\tan(\beta_1 + \varphi) = \alpha_0 \frac{\chi_1\left(\frac{\sin(\beta_1 + \varphi)}{\sin\varphi}\right)^2\left(1 - \frac{\tan(\beta_1 + \delta)}{\tan(\beta_1 + \varphi)}\right) + \frac{p_0(\chi_1 + 1)}{\rho_{10} c_0^2 M^2}}{\left(\frac{\sin(\beta_1 + \varphi)}{\sin\varphi}\right)^2\left(1 - \frac{\tan(\beta_1 + \delta)}{\tan(\beta_1 + \varphi)}\right) + \frac{p_0(\chi_1 + 1)}{\rho_{10} c_0^2 M^2}} + (1 - \alpha_0)\frac{\chi_*\left(\frac{\sin(\beta_1 + \varphi)}{\sin\varphi}\right)^2\left(1 - \frac{\tan(\beta_1 + \delta)}{\tan(\beta_1 + \varphi)}\right) + \frac{(p_0 + p_*)(\chi_* + 1)}{\rho_{10} c_0^2 M^2}}{\left(\frac{\sin(\beta_1 + \varphi)}{\sin\varphi}\right)^2\left(1 - \frac{\tan(\beta_1 + \delta)}{\tan(\beta_1 + \varphi)}\right) + \frac{(p_0 + p_*)(\chi_* + 1)}{\rho_{10} c_0^2 M^2}}, \tag{9}$$

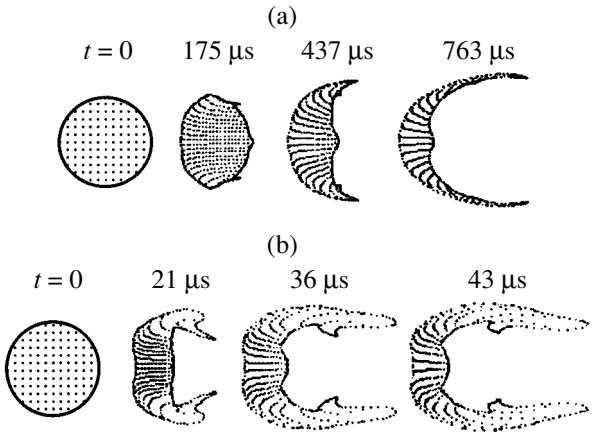

Fig. 2. Shape of an initially spherical drop with $\alpha_0 = 0.9$ at various time instants of interaction with the shock wave with M = (a) 1.3 and (b) 6.

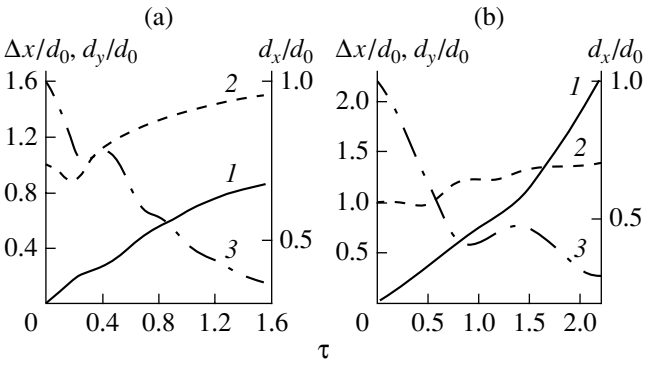

Fig. 3. (*1*) Relative shift, (*2*) lateral extension, and (*3*) longitudinal size of the drop as functions of τ for the shock wave with M = (a) 1.3 and (b) 6.

where $\tilde{p}_s = p_s/(\rho_s u_2^2)$, $\tilde{p}_0 = p_0/(\rho_s u_2^2)$, and $\tilde{p}_s' = p_s/(\rho_s u_2^2)$.

Thus, we have the system of three nonlinear equations [Eqs. (7)–(9)] for unknown β_1, β_2, and δ. This system was solved by the Newton–Raphson iteration method.

Figure 1b shows the angles β_1, β_2, and δ as functions of φ when the shock wave is reflected from the drop at various α_0. It is seen that the angle β_1 of the refracted wave strongly depends on α_0 when the concentration of the gas in the liquid is small. At $M = 2$, β_1 is negative even if the gas concentration in the drop is 0.1%. Note that relationships derived from (7)–(9) for a gas-free drop, i.e., when $\alpha_0 = 0$, coincide with those obtained in [9].

From Eqs. (7)–(9), one can also find the critical angle φ_*; i.e., the limit angle φ at which a solution involving the reflected and refracted shock waves attached to the contact point still exists. The critical angle separates the regular and Mach conditions of reflection. The angle φ_* as a function of α_0 is shown in Fig. 1c at various Mach numbers for the shock wave striking the drop. It is seen that φ_* first grows insignificantly as the gas concentration in the drop increases. With α_0 approaching unity, which is typical of foamed liquids, the critical angle, however, rises sharply. It has to be noted that the basic interaction parameters depend on the type of a gas in the bubbles only slightly. Systems with a large gas content are usually treated as foams, which are media that, along with gas and liquid, contain surfactants, imparting specific strengthening properties. Foams can be "wet" or "dry," depending on their density. Wet water foams have a density of more than 5 kg/m^3, as a stable bubble structure, and retain their properties when interacting even with intense shock waves [14]. In dry foams, bubbles collapse under the action of shock waves, forming an air–drop mixture [15]. Wet foams are stable because the bubbles not only collapse, but also form due to the foaming of the liquid [16]. It should also be noted that the basic flow characteristics, such as the speed of an oscillatory shock wave and the averaged pressure behind its front, which coincide with the equilibrium ones, do not depend on the bubble size [17].

NUMERICAL SIMULATION OF INTERACTION

In the previous section, we described the initial stage of shock wave diffraction by a bubble-liquid drop. For a better representation of the interaction, it is necessary to integrate the general system of partial differential equations [12] that simulates the simultaneous flow of a gas and a bubble liquid. This can be done only numerically.

Let a plane shock wave strike an initially spherical fixed drop of a bubble liquid in ideal gas. The gas parameters behind the wave front are calculated from (1). We assume that the wave front touches the drop surface at $t = 0$. The Mach number in the incident wave and the gas concentration in the drop are varied. The numerical method [18] is used in the calculations. We consider sufficiently large drops. In this case, aerodynamic forces due to the gas flow that act on the drop are several orders greater than the surface tension forces; therefore, the latter are omitted in the calculations.

It follows from the numerical results that the interaction pattern is similar to a flow about a solid particle. The detached shock wave forms in front of the drop; however, its shape and position vary in time because of the deformation and acceleration of the drop.

The evolution of the shape of an initially spherical foamed-liquid drop ($r_0 = 5$ mm and $\alpha_0 = 0.9$) under the action of a shock wave is shown in Fig. 2a. The calculation was performed at various time instants for a Mach number of 1.3. Unlike [8–10], weightless markers moving with the speed the medium has at a given point of the space are used only to visualize the defor-

mation of a fragment of the dispersive medium and are not functionally involved in the calculations. As follows from Fig. 2a, the deformation of the drop is caused by the development of a flow of the dispersive medium at the leading surface of the drop; i.e., the boundary layer forms. The closer a particle of the dispersive medium to the drop surface, the greater the distance it travels.

The relative shifts ($\Delta x/d_0$) of the drop along the axis of symmetry, as well as its relative lateral extension (d_y/d_0) and longitudinal thickness (d_x/d_0), are shown in Fig. 3a vs. dimensionless time $\tau = t/t_0$, where

$$t_0 = d_0 u_s^{-1} (\rho_0/\rho_s)^{1/2}. \quad (10)$$

Starting from the instant $\tau = 0.3$, when the refracted shock wave propagating in the drop arrives at its back surface, the longitudinal size of the drop increases.

As the shock wave intensity grows, so does the boundary layer, and the drop deforms more vigorously. This is illustrated in Figs. 2b and 3b, where the data for a shock wave with $M = 6$ are given.

With a bubble-liquid drop, the shock wave interacts in a different way. Since bubble-liquid particles are more inertial, the boundary layer is much thinner than in the foamed-liquid case. The surface markers are detached from the drop surface, which is accompanied by a slight deformation of the drop core (see Fig. 4a). The shift of the drop is well described by the formula $\Delta x/d_0 = 0.75\tau^2$ (see Fig. 4b). For a bubble-free liquid, the function approximating experimental data is $\Delta x/d_0 = 0.8\tau^2$ [1]; related functions for bubble-liquid drops tend to this expression at $\alpha_0 \longrightarrow 0$.

Thus, it follows from the calculations that, as the gas content in the drop increases, it becomes more mobile and shifts by larger distances, because the density of the bubble liquid decreases. As α_0 grows, so does the thickness of the boundary layer, which forms in the drop near its front surface. Simultaneously, the maximum lateral size of the deformed drop decreases. This size also diminishes with increasing shock wave intensity.

Besides spherical drops, we considered ellipsoidal and toroidal ones, as well as drops with the front surface concave toward the incoming flow. The collapse of these drops due to the shock wave is shown in Figs. 5a–5c. In all the cases, the Mach number for the shock wave is three and the gas concentration in the water is $\alpha_0 = 0.1$. Note that we consider the pulsed action of the gas stream on the drop when the liquid flow in its boundary layer is developed. Under such conditions, possible Rayleigh–Taylor or Helmholtz instabilities do not lead to catastrophic impacts, which might occur in the absence of the developed boundary layer in the drop. Initial disturbances like small-amplitude surface waves at the head of the drop are removed to the periphery and do not influence the deformation of the drop.

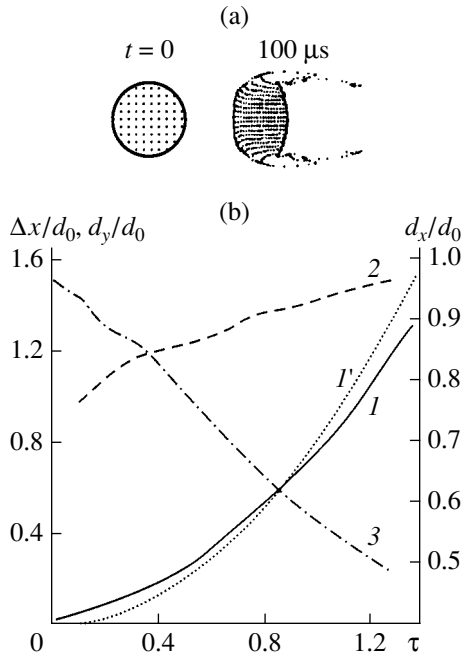

Fig. 4. (a) Shape of the drop with $\alpha_0 = 0.1$ at various time instants for the shock wave with $M = 3$ and (b) dependences of (*1*) relative shift, (*2*) lateral extension, and (*3*) longitudinal size of the drop on τ. Curve *1'* is the experimental dependence of the relative shift at $\alpha_0 = 0$.

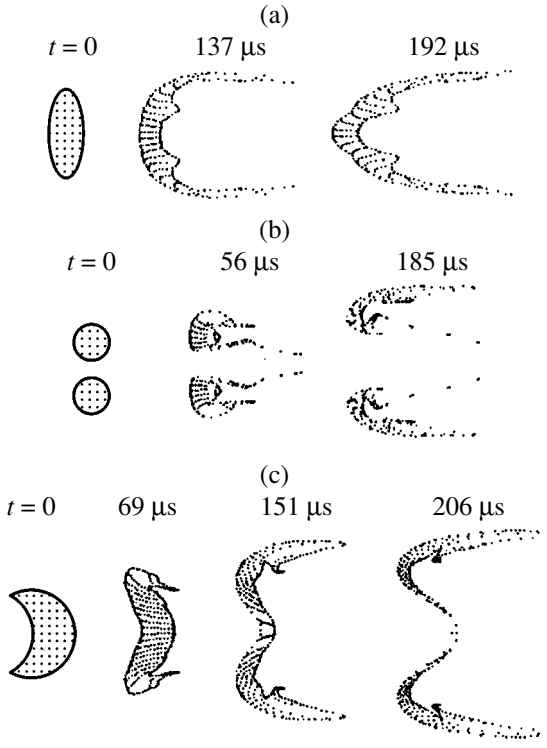

Fig. 5. The shape of initially (a) elliptic, (b) toroidal, and (c) concave spherical drops at characteristic time instants for the shock wave with $M = 3$.

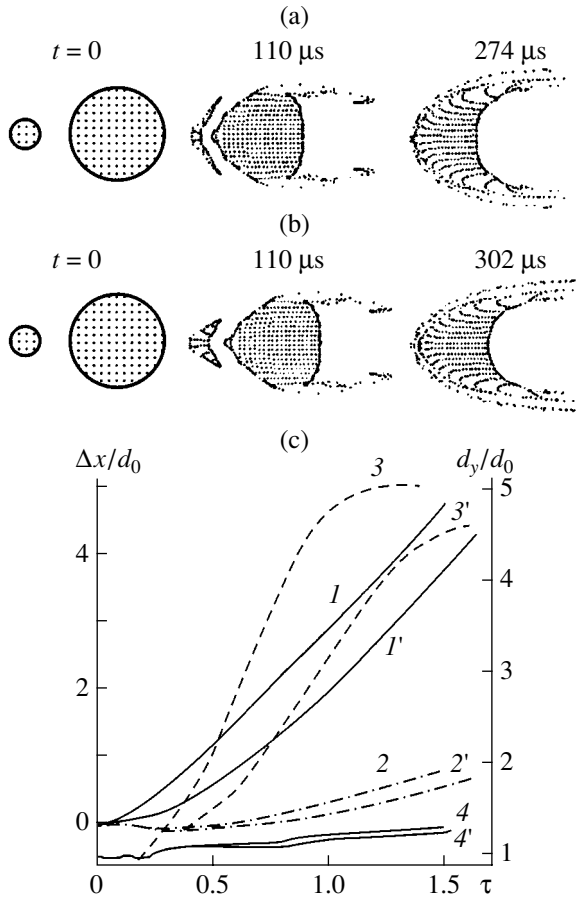

Fig. 6. (a) Interaction of the shock wave with two spherical water drops, (b) the same as in (a) but with glycerol in the first drop, and (c) the relative shift of (*1*) the first and (*2*) the second drops and the relative lateral extension of (*3*) the first and (*4*) the second drops as functions of τ. Curves *1'*–*4'* refer to case (b).

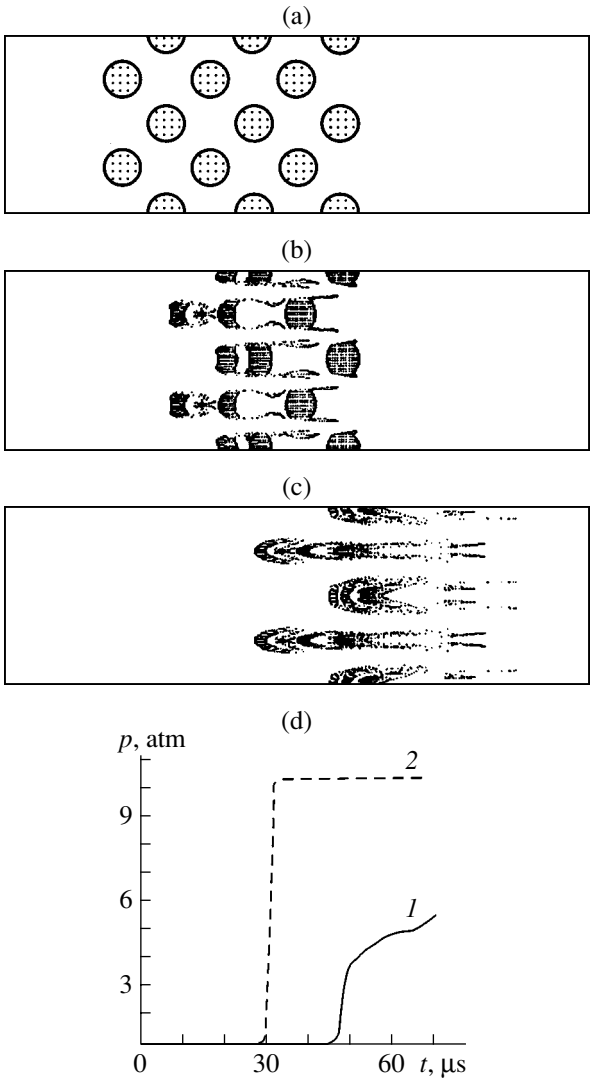

Fig. 7. Shape of foamed-liquid drops when the shock wave interacts with the barrier at $M = 3$ at the time instants $t =$ (a) 0, (b) 24, and (c) 49 μs. (d) The function $p(t)$ in the (*1*) presence and (*2*) absence of the screen.

Let an air shock wave interact with two spherical liquid drops placed one after the other. Assume that the axis of symmetry, running through the centers of the drops, is orthogonal to the shock wave front. Let the wave front touch the surface of the first drop at the instant $t = 0$. The Mach number in the incoming wave is $M = 3$. The drop radii are 1 and 5 mm, and their center distance is 8 mm. The gas concentrations are $\alpha_0 = 0.5$ in the first drop and 0.1 in the second. The interaction dynamics is illustrated in Fig. 6a. As is seen from Fig. 6b, the same pattern takes place when the first drop consists of glycerol ($\alpha_0 = 0.95$ and $\rho_l^0 = 1200$ kg/m^3) instead of foamed water. The geometry of the drops is the same as in the former problem. Comparing the data in Figs. 6a and 6b, one can see that the first drop deforms more slowly since its liquid is more inertial. It has to be noted that the viscosity effect in our case is small and may be neglected, since the intensity of shock waves is assumed to be high [10].

The relative shifts of the drop $\Delta x/d_0$ along the axis of symmetry and its lateral extension d_y/d_0 are shown in Fig. 6c vs. dimensionless time $\tau = t/t_0$. Here, t_0 is calculated using (10) for the parameters of the second drop. It is interesting that, when the second drop deforms, the liquid near the axis of symmetry shifts toward the incoming flow (see Fig. 6a). This is due to the fact a part of the second drop is in the aerodynamic shadow of the first drop, where the pressure is lower. The resulting pressure difference causes a tip at the front surface of the second drop (see Fig. 6a). It also follows from Fig. 6c that the second drop deforms and shifts more slowly if both drops contain glycerol.

Now consider a shock wave interacting with a drop screen. It is obvious that the general flow pattern observed when the shock wave strikes an ensemble of

bubble-liquid drops differs from that when the drops are free of bubbles. Let a plane shock wave be orthogonally incident on the screen consisting of staggered drops of the same size. The numerical results are given for drops of foamed water–air mixture with $\alpha_0 = 0.9$. The Mach number in the shock wave is three; the drop diameter, 1.92 mm; and the number of the drop layers in the screen equals six.

Figures 7a–7c show the screen at characteristic time instants. It is seen that the interaction pattern is essentially different from that when the drops are free of the gas [10]. In the presence of the bubbles, the boundary layer is nearly completely detached from the drops in the screen (see Fig. 7b). As a result, the drops whose centers are aligned approach each other, forming liquid streams with the large heads, from which the dispersive medium is vigorously detached (see Fig. 7c). Such a process develops until the drops fully collapse.

The pressure at the border of the domain of calculation ($x = 0.032$ m) as a function of time with and without the screen is shown in Fig. 7d. It is seen that the refracted wave formed behind the screen reaches the border of the domain with some delay and its amplitude drops more than twice. Subsequently, as the drops break down and shift, the pressure attains its no-screen level.

ACKNOWLEDGMENTS

The work was financially supported by the Russian Foundation for Basic Research (project no. 00-01-00523).

REFERENCES

1. W. G. Reinecke and G. D. Waldman, in *Proceedings of the 3rd International Conference on Rain Erosion and Related Phenomena, England, 1970*, p. 1.
2. V. M. Boĭko, A. N. Papyrin, and S. V. Poplavskiĭ, Prikl. Mekh. Tekh. Fiz., No. 2, 108 (1987).
3. A. Wierzba and K. Takayama, AIAA J. **26**, 1329 (1988).
4. K. Takayama, Trans. Jpn. Soc. Mech. Eng., Ser. B **55**, 1271 (1989).
5. V. V. Mitrofanov, Din. Sploshnoĭ Sredy, No. 39, 76 (1979).
6. L. A. Klyachko, Inzh. Zh. **27**, 554 (1963).
7. M. S. Volynskiĭ and A. S. Lipatov, Inzh.-Fiz. Zh. **18**, 838 (1970).
8. V. S. Surov and S. G. Ageev, *Simulation in Mechanics* (Inst. Teor. Prikl. Mekh., Sib. Otd. Akad. Nauk SSSR, Novosibirsk, 1990), Vol. 4, No. 3, p. 149–154.
9. V. S. Surov and V. M. Fomin, Prikl. Mekh. Tekh. Fiz. **34** (1), 48 (1993).
10. V. S. Surov, Prikl. Mekh. Tekh. Fiz. **36** (3), 38 (1995).
11. R. I. Nigmatulin, A. A. Gubaĭdullin, A. T. Akhmetov, *et al.*, Dokl. Akad. Nauk **346**, 46 (1996) [Phys. Dokl. **41**, 32 (1996)].
12. V. S. Surov, Zh. Tekh. Fiz. **68** (11), 12 (1998) [Tech. Phys. **43**, 1280 (1998)].
13. V. S. Surov, Zh. Tekh. Fiz. **69** (1), 42 (1999) [Tech. Phys. **44**, 37 (1999)].
14. A. A. Borisov, B. E. Gelfand, *et al.*, Acta Astron. **5**, 1027 (1978).
15. A. B. Britan, I. I. Zinovik, and V. A. Levin, Fiz. Goreniya Vzryva **28** (5), 108 (1992).
16. V. S. Surov, Teplofiz. Vys. Temp. **35**, 25 (1997).
17. V. S. Surov, Teplofiz. Aéromekh. **4** (1), 101 (1997).
18. V. S. Surov, Mat. Model. **10** (3), 29 (1998).

Translated by V. Gursky

Technical Physics, Vol. 46, No. 6, 2001, pp. 668–672. Translated from Zhurnal Tekhnicheskoĭ Fiziki, Vol. 71, No. 6, 2001, pp. 23–27.

A Spherical Plasmoid with a Diffuse Boundary in a Linearly Polarized Quasistatic Electromagnetic Field

L. P. Grachev, I. I. Esakov, and S. G. Malyk

Moscow Radiotechnical Institute, Russian Academy of Sciences, Varshavskoe sh. 132, Moscow, 113519 Russia

e-mail: esakov@dataforce.net

Received September 18, 2000; in final form, November 30, 2000

Abstract—The problem of a spherically symmetric plasmoid placed in a linearly polarized uniform quasistatic electromagnetic field is considered. The electric field in the vicinity of a plasmoid with a Gaussian electron density distribution is calculated. The results of calculations are compared with the known solution for a spherical plasmoid with a uniform density. The possibility of the transformation of an initial plasmoid that arises in an electrodeless microwave gas discharge into a microwave streamer is discussed. *© 2001 MAIK "Nauka/Interperiodica".*

INTRODUCTION

Experiments show that a high-pressure electrodeless microwave discharge in air in the field of a linearly polarized wave of a high-Q two-mirror open resonator can have the form of a microwave streamer [1, 2]. Such a discharge arises from a point seed (e.g., a background free electron) in the antinode of the electric component of an electromagnetic (EM) field **E** produced in a standing-wave resonator. The discharge initially develops as a spherically symmetric plasma formation with a Gaussian electron density distribution and then stretches along the field (in both directions from the origination site) as a thin plasma channel [1].

In [3], a physical mechanism that may be responsible for the stretching of the initial plasmoid was proposed. When obtaining quantitative estimates, the plasmoid was assumed to be shaped like a sphere with a sharp boundary and uniform electron density. The electrostatic interaction between this sphere and the microwave field leads to an increase in the field at the sphere poles, where the **E** vector is perpendicular to the sphere surface, and a decrease in the field in the equatorial region. As a result, the ionization rate increases at the poles of the seed plasmoid so that it starts stretching along the field due to the ionization–diffusive mechanism for the discharge boundary propagation.

Such an approach (in the quasistatic approximation) was employed in [4] to analyze the dynamics of a uniform plasma ellipsoid that stretched along the ionizing field **E**. However, in that paper, the growth rate of a two-dimensional microwave streamer obtained from numerical calculations turned out to be less than that predicted by analytic estimates. In [5], in which the ionization–diffusive mechanism for the development of a two-dimensional microwave streamer was analyzed taking into account the field lag effect, the above discrepancy was attributed to the diffusive broadening of the plasma boundaries, which are formed during streamer development. In [6], the dynamics of a microwave streamer was numerically investigated assuming that the ionizing radiation from the discharge played a decisive role in the discharge front propagation.

In this paper, an attempt is made to evaluate the influence of the diffuse Gaussian boundaries of a microwave discharge on the initial stage of the development of a spherically symmetric streamer. We do not consider here the ionization processes, and the electron density and its spatial distribution are assumed to be given and time-independent.

FORMULATION OF THE PROBLEM

By a high gas pressure, we mean such a pressure p at which the condition

$$\nu_c \gg \omega \tag{1}$$

is satisfied. Here, ν_c is the electron–neutral collision frequency and ω is the circular frequency of the EM field.

For example, in air, at a field strength E slightly higher than the breakdown field E_c, we have $\nu_c \cong 4 \times 10^9 p$, s^{-1} [7]. Here and below, the pressure p is in torr. Under the experimental conditions of [1], in which the experiments were carried out at atmospheric pressure, we have $\omega \cong 2 \times 10^{10}$ s^{-1}, so that inequality (1) is certainly satisfied. Under condition (1), the complex plasma permittivity ε can be written in the form [8] $\varepsilon = 1 - iN$, where $N = n/n_0$ is the relative plasma electron density, n is the absolute plasma electron density, and its characteristic value is

$$n_0 = (m_e \varepsilon_0 / q_e^2)\omega\nu_c, \text{ m}^{-3}. \tag{2}$$

1063-7842/01/4606-0668$21.00

Here, $m_e = 9.1 \times 10^{-31}$ kg is the electron mass, $q_e = 1.6 \times 10^{-19}$ C is the electron charge, and $\varepsilon_0 = 10^{-9}/(36\pi)$ F/m is the permittivity of a vacuum. For example, under the conditions of [1], we have $n_0 = 2.5 \times 10^{10} p$ cm^{-3}, and at $p = 760$ torr, we have $n_0 \cong 2 \times 10^{13}$ cm^{-3}. If a plasma sphere with an uniform permittivity ε is placed in an initially uniform linearly polarized microwave field $\mathbf{E}_0$, then, for a sphere radius $a \ll 1/k$ (where $k = \omega/c$ is the EM field wavenumber and c is the speed of light), the field $\mathbf{E}_i$ inside the sphere is also uniform and is equal to [8]

$$E_i = |3/(\varepsilon + 2)|E_0. \quad (3)$$

At the poles of the sphere the field strength is maximum,

$$E_m = |\varepsilon|E_i. \quad (4)$$

Let a free electron that initiates the microwave breakdown in air in a microwave field $E_0 > E_c$ appear at time $t = 0$. We will assume the point at which the electron is born to be the coordinate origin. Obviously, for $N \ll 1$, the produced plasma hardly distorts the initial field. Moreover, we assume that, over the time interval under consideration, the discharge plasma is still free of plasmochemical reaction products responsible for the ionizing radiation from the discharge [9]. In this case, assuming that the plasma expands only due to diffusion, the spatiotemporal dynamics of the electron avalanche can be described by the formula [3]

$$n = \frac{e^{(\nu_i - \nu_a)t}}{\pi^{3/2} a^3} e^{-(r/a)^2}, \quad (5)$$

where r is the radial coordinate, $\nu_a = 2 \times 10^4 p$ s^{-1} is the electron attachment rate [10], and the characteristic size of a spherically symmetric plasma cloud is equal to

$$a = 2\sqrt{Dt}. \quad (6)$$

For $E_0 \le 3E_c$, the ionization rate [10]

$$\nu_i = \nu_a(|E_0|/E_c)^{5.34} \quad (7)$$

is a function of the field absolute value only and does not depend on the field direction. In Eq. (6), the diffusion coefficient D is determined by the values of n and a. For small n, while the electron Debye radius satisfies the inequality $r_d = \sqrt{\varepsilon_0 U_e/(2q_e n)} > a$ (where $U_e \cong 1$ eV is the energy of plasma electrons [11]), the electrons diffuse freely with the diffusion coefficient $D = D_e \cong 1.6 \times 10^6/p$ cm^2/s [11]. For $r_d < a$, diffusion becomes ambipolar with the coefficient $D = D_a \cong 1.4 \times 10^4/p$ cm^2/s [11].

It follows from Eqs. (5) and (6) that, at this stage of the discharge, the point at the discharge boundary corresponding to a given small electron density propagates along r with a velocity

$$V = 2\sqrt{D(\nu_i - \nu_a)}. \quad (8)$$

Keeping in mind Eq. (4), we will assume that a spherically symmetric plasmoid with a nonuniform permittivity

$$\varepsilon = 1 - iNe^{-(r/a)^2} \quad (9)$$

and a characteristic size $a \ll 1/k$ is placed in a uniform linearly polarized EM field $\mathbf{E}_0$. In this case, we can use the quasistatic approximation and assume that the scalar potential Φ near the plasmoid is described by the equation [8]

$$\mathrm{div}(\varepsilon \nabla \Phi) = 0, \quad (10)$$

the electric field is

$$\mathbf{E} = -\nabla \Phi, \quad (11)$$

and the field strength at $r \gg a$ is equal to $E = E_0$.

Equations (9)–(11) were solved in spherical coordinates. The coordinate origin was placed in the center of the plasmoid, and the polar angle was counted from the direction of the external field vector $\mathbf{E}_0$. The radial coordinate was normalized as $x = r/a$.

RESULTS OF CALCULATIONS

The results of calculations are shown in Figs. 1–7. Figure 1 shows, as an example, the electric field strength and the electron density as functions of x at $\Theta = 0$ and $\pi/2$ for $N = 10$. It is seen that, at $r = 0$, the field E_i in the center of the plasmoid is less than the external field E_0 (to which the electric field strength tends at $r \gg a$), while in the polar region, the field increases.

Figure 2 shows the maximum amplification factors of the field in the polar regions for both the plasmoid under consideration and a plasmoid with a uniform electron density as functions of N. It is seen that, even

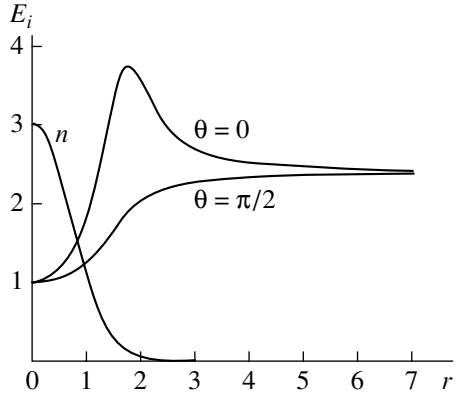

Fig. 1. Radius profiles of the electron density and electric field in a plasmoid for $N = 1$.

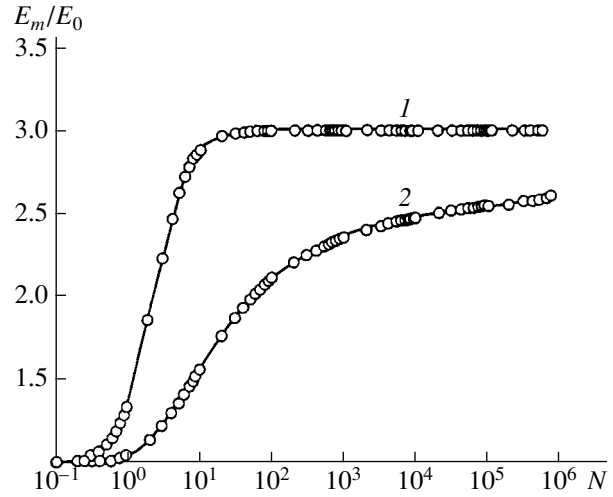

Fig. 2. Maximum field amplification in the polar region of a plasmoid vs. the central electron density for plasmoids with uniform (*1*) and Gaussian (*2*) electron density distributions.

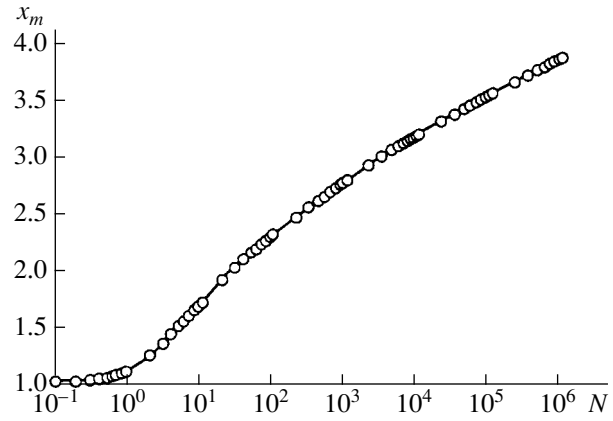

Fig. 3. Position of the field maximum in the polar region of a plasmoid vs. the central electron density.

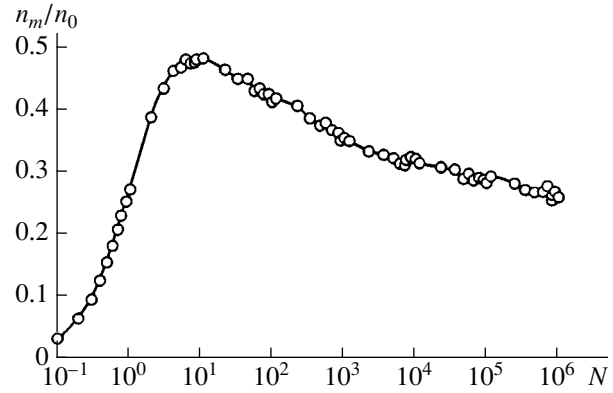

Fig. 4. Electron density at the point where the field is maximum vs. the central electron density.

at the initial stage of a microwave discharge, ignoring the diffuse boundaries of the seed plasmoid can result in substantial quantitative errors. For such a plasmoid, the field in the polar regions increases more slowly with increasing N as compared to a plasmoid with a uniform electron density. Thus, for a uniform plasmoid at $N = 1$, we obtain $E_m/E_0 = 1.34$ (where E_m is the maximum field strength), whereas for a plasmoid with a diffuse boundary, this ratio is as low as 1.05; i.e., according to formula (7), the ionization rate would increase almost by a factor of five at the poles of a uniform plasmoid, while for a real plasmoid, it increases by only 30%.

Figure 3 shows the position of the field maximum x_m in the polar region of a plasmoid with a Gaussian electron density distribution as a function of N. It is seen that, for $N \ll 1$, the radius at which the field is maximum is close to a. As N increases, the position of the field maximum moves away from the plasmoid center. Figure 4 shows the electron density n_m at the distance x_m as a function of N for the same plasmoid. It is seen that, as the density N in the plasmoid center increases, the value of n_m is almost stabilized at a level of $n_m/n_0 \cong 0.25$.

The field attenuation in the plasmoid center is shown in Fig. 5 for plasmoids with both uniform and Gaussian distributions of the electron density. It is seen that, for $N \leq 1$, the field strength in both plasmoids is nearly equal to the external one. For example, for $N = 1$, E_i differs from E_0 by only 5%. At large N, the field decreases somewhat more slowly for a plasmoid with a diffuse boundary. Thus, for a uniform plasmoid, we have $E_i/E_0 \cong 3/N$ for $N > 50$, whereas for a plasmoid with a Gaussian distribution of N, the ratio E_i/E_0 at $N > 500$ can be approximated by the formula $8/N^{0.9}$.

Figure 6 shows the radius x_e at which the field in the equatorial plane of a plasmoid with a diffuse boundary is attenuated to a level of $E_i + (E_0 - E_i)/\sqrt{2}$ as a function of N. It is seen that x_e is nearly equal to one for $N \leq 1$ and increases with increasing N. Figure 7 shows the electron density n_e in the equatorial region of a plasmoid with a diffuse boundary at $x = x_e$ as a function of N (curve *1*). At $N > 10$, the dependence n_e/n_0 on N can be approximated by the formula $10/N^{1.4}$ (curve *2*).

DISCUSSION OF THE RESULTS AS APPLIED TO AN ELECTRODELESS MICROWAVE DISCHARGE

Let us discuss the results. It follows from Eq. (8) that an ionization–diffusive velocity of the discharge boundary propagation depends strongly on the character of electron diffusion, because the coefficient D_e is two orders of magnitude higher than D_a. For small N (such that $r_d > a$ even in the center of the plasmoid), this velocity can be easily estimated because, in this case, $D = D_e$ throughout the entire plasmoid. The situation

becomes more complicated at higher N for which $r_d < a$ and, accordingly, $D = D_a$ in the central region of the plasmoid (including x_m). For example, under the experimental conditions of [1] at an air pressure of p = 760 torr, assuming that $E_0/E_c = 1.3$ and $D = D_e$, the time during which the plasma density in the center of the plasmoid increases to $N = 1$ can be estimated from Eqs. (5) and (6) as $t_1 = 5.4 \times 10^{-7}$ s; the corresponding characteristic size of the plasmoid is $a_1 = 7 \times 10^{-2}$ cm. It follows from Fig. 4 that, in this case, the plasma density at the radius x_m is equal to $n_m = 0.2n_0 = 4 \times 10^{12}$ cm^{-3}; i.e., $r_d = 3 \times 10^{-4}$ cm $\ll a_1$ even for $N = 1$.

At the same time, because of the Gaussian distribution of n, there is always a polar region far from the center in which $r_d > a$ and the electrons diffuse freely. For example, in the case corresponding to Fig. 1, in spite of the increase in the field by a factor of 1.5 and nearly 10-fold increase in ν_i [see Eq. (7)], the local velocity V at the poles calculated according to Eq. (8) for the radius x_m, at which $D = D_a$, is less than that in the region $r \gg a$, where $D = D_e$ and ionization proceeds in the nonamplified field E_0. It is shown in [12] that it is free electron diffusion that determines the formation of the microwave discharge front.

A similar situation takes place in the equatorial region of the plasmoid. Here, we can also find such a radius $r \gg a$ at which $D = D_e$ and ionization proceeds in an undistorted field $\mathbf{E}_0$.

Therefore, the calculations show that electrostatic ionization–drift effects themselves can hardly lead to the stretching of a real breakdown plasmoid with diffuse boundaries along the external field $\mathbf{E}_0$.

The stretching observed in numerical simulations [4, 5] was related to a prescribed initial distribution of **n**. In [4], the calculations started with a small rectangular region with a uniform electron density. Obviously, such an approach is qualitatively the same as that used in [3]. In [5], a certain initial smooth electron density profile in the plasmoid was prescribed; nevertheless, there was a distinct boundary between the regions with $n = 0$ and $n \neq 0$. In [6], the calculations began with a plasmoid with a Gaussian electron density distribution and also resulted in the formation of a microwave streamer. However, in that paper, the propagation of the discharge boundary was caused by photoionization and did not depend on the plasma density.

Nevertheless, the photoionization mechanism is unlikely to be responsible for the streamer growth observed in experiments. First, the properties of microwave streamers in air and hydrogen are qualitatively the same [13] despite the fact that the photoionization mechanisms in these streamers are quite different. Second, even in subcritical fields, high-pressure microwave discharges develop in the form of streamers. Experimental data on this kind of a discharge [14] show that the properties of these discharges in different gases

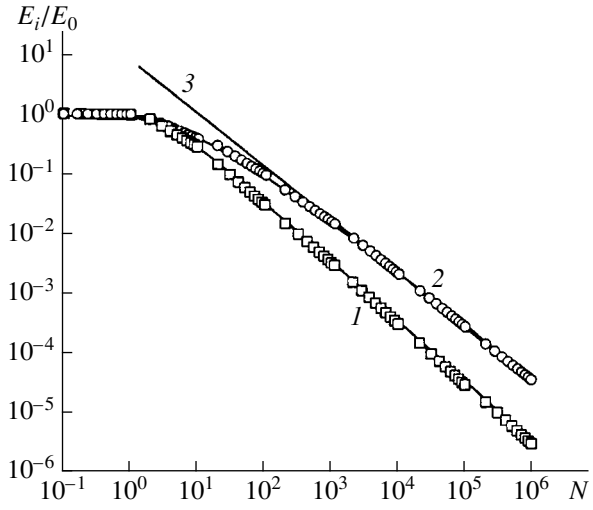

Fig. 5. Field attenuation in the center of a plasmoid vs. the central electron density for plasmoids with (*1*) uniform and (*2*) Gaussian electron density distributions. Curve *3* is the approximation.

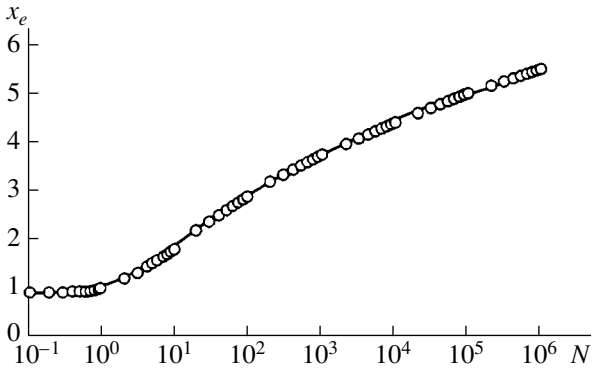

Fig. 6. Characteristic spatial scale at which the field is attenuated in the equatorial plane of a plasmoid vs. the central electron density.

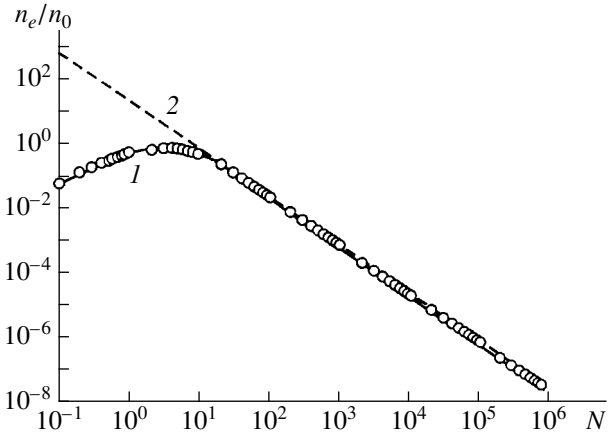

Fig. 7. Electron density at the radius x_e vs. the central electron density.

are qualitatively the same. Thus, it is most likely that the ionization-diffusive mechanism for the plasma boundary propagation, which is independent of the type of a gas, is responsible for the streamer character of a microwave discharge. Finally, the results of our calculations of the field structure in a diffuse plasmoid explain the main features of the spatial structure of a microwave discharge in air in the initial stage of its evolution (see the photographs in [13]).

In [13], it was shown that, in the pressure range from 20 to 60 torr, microwave discharges in air and hydrogen in the field of a focused traveling wave pass through several stages: diffusion, thermal–ionizational, streamer, etc. As p increases, the number and order of these stages do not change, although the time and spatial scales decrease, so that, at high p, they can hardly be identified experimentally. In this paper, we have shown that, in the diffusion stage, the discharge region broadens almost isotropically. The stretching of the discharge region along the field is always preceded by the thermal–ionizational stage. At this stage, bright channels stretched along the field $\mathbf{E}_0$ are formed in the polar regions of the initial diffuse plasmoid. As p increases, these channels elongate due to the ionization–diffusive mechanism and form a streamer.

It is natural to assume that this mechanism is also responsible for a microwave discharge in the field of a standing wave. Then, the results of our calculations explain the positions of the initial thermal–ionizational channels. Naturally, the probability for these channels to appear is higher in the polar ellipsoidal regions with an amplified field, which are formed at the end of the quasistatic spherically symmetric diffusive stage of the discharge evolution.

CONCLUSION

Thus, using quite simple numerical simulations, we have estimated the characteristics of a high-pressure electrodeless microwave discharge in a linearly polarized EM field at a very initial stage of the discharge evolution. It follows from these simulations that the simplest model of an initial plasmoid with a sharp boundary is hardly reasonable. Estimates show that the effects of the electrostatic interaction between the discharge plasma and external field with allowance for the ionization–diffusive mechanism for the discharge boundary propagation are insufficient to initiate a microwave streamer. The streamer can form only if additional physical processes related to spatially nonuniform gas heating in the discharge plasma are incorporated in the model.

A simplified model of the initial stage of a microwave discharge without allowance for ionization can be used to calculate the field near a plasma ellipsoid with a diffuse boundary. Such calculations allow one to find the conditions for the transformation of a discharge into a microwave streamer, i.e., to estimate the characteristics of the next stage of the discharge evolution. The same approach can be used to develop a model of a microwave streamer in which the full length of the plasma channel is on the order of the wavelength of the microwave field. The results obtained can be used as a reference when constructing a full-scale model of a microwave streamer with allowance for ionization.

REFERENCES

1. L. P. Grachev, I. I. Esakov, G. I. Mishin, and K. V. Khodataev, Zh. Tekh. Fiz. **64** (2), 26 (1994) [Tech. Phys. **39,** 130 (1994)].
2. A. L. Vikharev and B. G. Eremin, Zh. Éksp. Teor. Fiz. **68**, 452 (1975) [Sov. Phys. JETP **41**, 219 (1975)].
3. S. A. Dvinin, Vestn. Mosk. Univ., Ser. 3: Fiz., Astron. **26** (6), 30 (1985).
4. V. B. Gil'denburg, I. S. Gushchin, S. A. Dvinin, and A. V. Kim, Zh. Éksp. Teor. Fiz. **97**, 1151 (1990) [Sov. Phys. JETP **70**, 645 (1990)].
5. P. V. Vedenin and N. E. Rozanov, Zh. Éksp. Teor. Fiz. **105**, 868 (1994) [JETP **78**, 465 (1994)].
6. G. V. Naĭdis, Zh. Éksp. Teor. Fiz. **109**, 1288 (1996) [JETP **82**, 694 (1996)].
7. A. D. MacDonald, *Microwave Breakdown in Gases* (Wiley, New York, 1966; Mir, Moscow, 1969).
8. L. D. Landau and E. M. Lifshitz, *Electrodynamics of Continuous Media* (Nauka, Moscow, 1982; Pergamon, New York, 1984).
9. N. A. Bogatov, S. V. Golubev, and V. G. Zorin, Pis'ma Zh. Tekh. Fiz. **9**, 888 (1983) [Sov. Tech. Phys. Lett. **9**, 382 (1983)].
10. Yu. A. Lupan, Zh. Tekh. Fiz. **46**, 2321 (1976) [Sov. Phys. Tech. Phys. **21**, 1367 (1976)].
11. A. V. Gurevich, Geomagn. Aéron. **19**, 633 (1979).
12. B. R. Gorelik and K. V. Khodataev, Fiz. Plazmy **23**, 236 (1997) [Plasma Phys. Rep. **23**, 215 (1997)].
13. L. P. Grachev, I. I. Esakov, G. I. Mishin, and K. V. Khadataev, Zh. Tekh. Fiz. **66** (7), 32 (1996) [Tech. Phys. **41**, 652 (1996)].
14. L. P. Grachev, I. I. Esakov, and K. V. Khodataev, Zh. Tekh. Fiz. **68** (4), 33 (1998) [Tech. Phys. **43**, 378 (1998)].

Translated by M. Astrov

Technical Physics, Vol. 46, No. 6, 2001, pp. 673–676. Translated from Zhurnal Tekhnicheskoĭ Fiziki, Vol. 71, No. 6, 2001, pp. 28–31.

SOLIDS

Effect of Annealing on the Deformation and Fracture of Metallic Glass under Local Loading

V. A. Fedorov and I. V. Ushakov

Tambov State University, Internatsional'naya ul. 33, Tambov, 392622 Russia

e-mail: feodorov@tsu.tmb.ru

Received March 13, 2000; in final form, August 15, 2000

Abstract—An investigation is undertaken into the variations observed in the cracking resistance, the plasticity, and the structure of an 82K3KhSR metallic glass upon annealing. A method of evaluating the mechanical properties and the structural state of metallic glasses is proposed. This method is based on the indentation of the metallic glass deposited onto a substrate prepared from a polyester material and a metal. The critical annealing temperature that corresponds to drastic changes in the mechanical properties of the metallic glass is determined. It is found that dependences of the cracking resistance of metallic glasses on the indenter load exhibit a linear behavior at annealing temperatures above the critical point. An exponential decrease in the cracking resistance upon indentation is observed with an increase in the annealing temperature of metallic glasses. © *2001 MAIK "Nauka/Interperiodica".*

INTRODUCTION

Fabrication and application of metallic glasses is of particular scientific and practical interest. The considerable attention focused on metallic glasses is motivated by the unique properties of these materials and prospects of their practical use [1–3].

Under operating conditions, structural inhomogeneities can arise in metallic glasses, for example, due to local heating [4]. The development of methods for evaluating the mechanical properties of glasses and the ascertainment of their serviceability or unserviceability are a topical problem. Similar investigations are also of strictly scientific significance, because they can provide a means for establishing the interrelation between the change in a number of mechanical properties (microhardness, cracking resistance, etc.) and the structural transformations revealed by X-ray techniques in a glass.

In this work, we determined the character of the fracture and strain of an annealed metallic glass upon indentation and elucidated how the annealing of metallic glasses affects their mechanical properties and structure.

MATERIALS AND EXPERIMENTAL TECHNIQUE

We studied an 82K3KhSR metallic glass of the composition (wt %) 83.7Co + 3.7Fe + 3.2Cr + 9.4Si in the form of a ribbon 30 μm thick. Prior to experiments, samples were annealed in a furnace at a temperature of T_{an} = 373–973 K. The samples were heated and cooled at a rate of ≈10 K/min and were held at a specified temperature for 3 min. X-ray structure analysis was carried out on a DRON-2 diffractometer.

The relatively small thickness of the metallic glass (≈30 μm) rules out the indentation under considerable loads according to the standard techniques. As was shown in our earlier work [5], some mechanical characteristics, for example, the cracking resistance, can clearly manifest themselves on an elastic substrate. Furthermore, the deformation and fracture of composites consisting of a relatively thick polymer substrate and a thin metallic coating are currently a topical trend in applied research [6–8], because these materials are very promising in practical applications.

Investigations of metallic glasses by the indentation technique have been performed using different substrates. However, the influence of these substrates on the results of indentation is not always taken into account [9]. In these cases, the indentation data can be correctly interpreted only after evaluating the contribution of different substrates to the results obtained.

In this work, the samples prior to indentation were cemented to a metallic base. Polyester composite TY 2312-021-11748532-97 with a layer thickness of ≈1 mm and a microhardness of ≈151 kG/mm^2 was used as an adhesive. The character of the deformation and fracture of the metallic glass and its cracking resistance was examined on a PMT-3 microhardness gauge.

EXPERIMENTAL RESULTS

(1) For the metallic glass preliminarily annealed at temperatures ≤743 K, the indentation under a load of less than 100 g leads to the formation of a Vickers pyramid indentation. In the case when the indenter load is

1063-7842/01/4606-0673$21.00

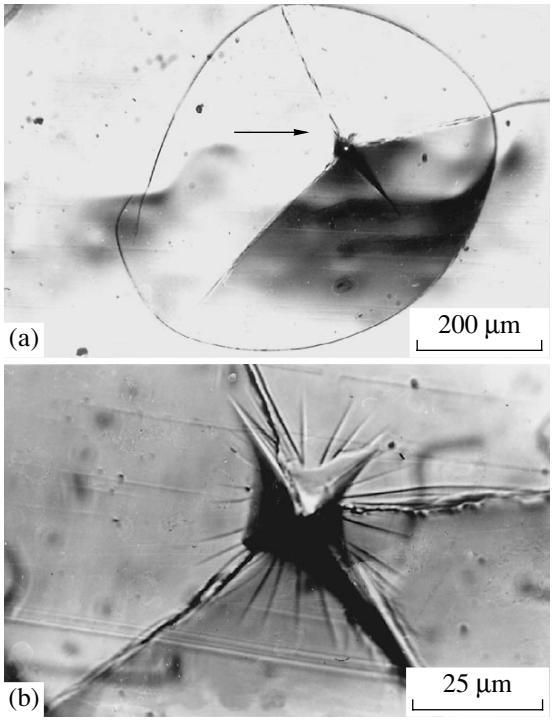

Fig. 1. (a) Surface of the annealed metallic glass after indentation under the load P = 200 g. The arrow indicates the indentation region shown in Fig. 1b at a larger magnification. (b) A Vickers pyramid indentation surrounded by the strained zone.

equal to ≈100 g and larger, a characteristic strained zone appears around the indentation.

(2) For the metallic glass annealed at temperatures ≥743 K, the indentation results in the formation of macrocracks several millimeters long. Both radial and circumferential (associated with the deflection of a substrate material) cracks can be formed (Fig. 1a). The crack formation becomes possible at indenter loads of 60 g and larger.

(3) For samples annealed at T_{an} = 743–783 K, the indentation can bring about the formation of a strained zone and micro- and macrocracks (Figs. 1a, 1b). The strained zone becomes less pronounced with an increase in the annealing temperature and is not observed at T_{an} > 783 K.

(4) At T_{an} > 743 K, the probability of crack formation under indentation is directly proportional to the indenter load (Fig. 2). The experimental results (Fig. 2, symbols) were obtained in the following way. Upon indentation, the formation of an impression is accompanied (or not accompanied) by the initiation of cracks. When the indentation resulted in the formation of a crack, the probability was taken equal to unity. Otherwise, the probability was taken as zero. Each experimental symbol in Fig. 2 corresponds to twenty measurements. The experimental data were approximated by relationships of the form $W = aP + b$ with correlation coefficients of no less than 0.92.

It is found that an increase in the annealing temperature leads to a decrease in the load required for the crack formation; i.e., the metallic glass becomes more brittle. The kinetics of crystallization, relaxation, embrittlement, and a number of other processes occurring in amorphous metals are determined by the diffusive atomic mobility which exponentially depends on the temperature [9]. Therefore, it can be concluded that the dependence of the cracking resistance on the annealing temperature should also be exponential. This is confirmed by small errors in the approximation of the experimental results by the relationship $P = P_0 + A\exp[(T_0 - T)/C]$ (Fig. 3).

According to X-ray diffraction analysis, the metallic glass remains X-ray amorphous up to T_{an} = 973 K. A comparison between the X-ray diffraction patterns of the annealed and unannealed samples revealed an increase in the half-width of the amorphous halo from 8.2° for the unannealed glass to 8.9° for the glass annealed at 973 K and a decrease in the angular position of its center of gravity by ≈0.02°, which suggests a decrease in the mean interatomic distances and an increase in the density. The X-ray diffraction patterns were processed according to the procedure described in [10]. An increase in the density indicates a decrease in the excess free volume. Consequently, it can be argued that the change in the cracking resistance of the metallic glass is caused by the atomic rearrangements unrelated to the crystallization.

DISCUSSION

In the initial state of metallic glasses, high mechanical stresses can undergo relaxation owing to plastic deformation [11]. This can be responsible for the formation of the strained zone upon indentation of the unannealed metallic glass under large loads (Fig. 1b). This morphology corresponds to the heterogeneous deformation at low annealing temperatures and high mechanical stresses [11].

As follows from X-ray structure analysis, an increase in the annealing temperature leads to atomic rearrangements in the metallic glass. The structural evolution brings about an increase in the brittleness of the material. As a consequence, macrocracks can be formed in the course of indentation (Fig. 1a). The dependence of the cracking resistance on the annealing temperature exhibits an exponential behavior, and the atomic rearrangement process has a thermoactivated character (Fig. 3).

Analysis of the exponential dependence of the cracking resistance on the annealing temperature (Fig. 3) allows us to infer that the load necessary for the crack formation drastically decreases at a temperature of ≈748 K. This implies that the energy of thermal fluctuations (at $T \approx 748$ K) becomes sufficient for the struc-

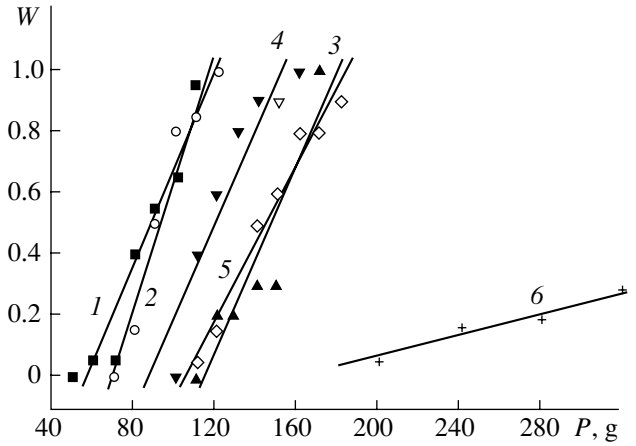

Fig. 2. Dependences of the probability W of the crack formation upon indentation on the indenter load P. Annealing temperatures and the coefficients for the given dependences: (*1*) T_{an} = 888 K, a = 0.016, and b = –0.905; (*2*) T_{an} = 823 K, a = 0.021, and b = –1.459; (*3*) T_{an} = 783 K, a = 0.015, and b = –1.75; (*4*) T_{an} = 773 K, a = 0.015, and b = –1.339; (*5*) T_{an} = 763 K, a = 0.013, and b = –1.352; and (*6*) T_{an} = 748 K, a = 0.002, and b = –0.262.

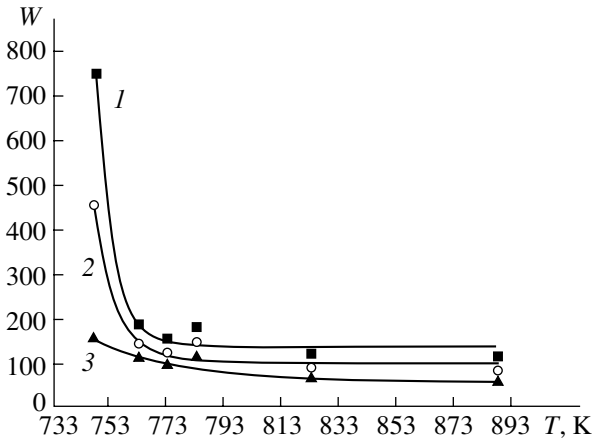

Fig. 3. Dependences of load P upon indentation on the annealing temperature T. Probability of crack formation W = (*1*) 1, (*2*) 0.5, and (*3*) 0 (the dependence corresponds to the maximum indenter load at which the crack formation is not observed). Parameters: (*1*) W = 1, P_0 = 137.7 ± 15.8 g, A_1 = 612.1 ± 32.4 g, T_0 = 475 K, and C = 6.0 ± 1.6 K; (*2*) W = 0.5, P_0 = 106.8 ± 14.8 g, A_1 = 345.2 ± 29.5 g, T_0 = 475 K, and C = 7.2 ± 2.4 K; and (*3*) W = 0, P_0 = 58.8 ± 18.1 g, A_1 = 90.0 ± 22.3 g, T_0 = 475 K, and C = 33.9 ± 19.9 K.

tural relaxation that results in a sharp increase in the brittleness of the material. Reasoning from the drastic decrease in the cracking resistance at $T > 748$ K, this temperature can be referred to as a critical point. The temperature $T_{an} \approx 748$ K is essentially the temperature of a ductile–brittle transition for the metallic glass under investigation. At the same time, the data of X-ray structure analysis and differential scanning calorimetry (DSC) indicate that these changes are not attended by the crystallization of the metallic glass.

The indentation of the samples annealed at temperatures in the range ≈743–783 K can lead to the formation of the strained zone and micro- and macrocracks. At lower temperatures, no crack initiation is observed. On the other hand, the strained zone is not formed at higher temperatures. At these temperatures, despite a substantial embrittlement of the metallic glass, considerable plastic deformations can occur, and, hence, we are dealing here with the transition temperature range.

The experimental data should be processed with due regard for the influence of the substrate on the qualitative indentation characteristics and accidental deviations. This is explained by the small thickness of the metallic glass, which makes indentation under considerable loads (≥100 g) impossible according to standard techniques. Therefore, the boundaries of the transition temperature range and the critical temperature can be approximately determined by this method. Analysis of the experimental data shows that the substrate, when coated with the metallic glass, brings about specific changes in the indentation procedure and provides a high reproducibility of the results and a sensitivity to the structural state of the metallic glass. The high reproducibility of the indentation data and large correlation coefficients (from 0.92 to 0.986) prove that minimum accidental deviations can be achieved with the use of this substrate.

It is known that, upon structural relaxation, the density increases insignificantly (by ~1%), whereas the change in the excess free volume can be as much as 50% [12] (similar results are obtained in the present work). This leads to substantial changes in the mechanical properties, which are well identified upon indentation of the metallic glass deposited onto the substrate. Thus, the proposed method of indentation of the metallic glass (deposited onto the substrate) under large loads makes it possible, with a sufficient accuracy, to evaluate the mechanical properties of the metallic glass and its structural changes.

CONCLUSIONS

(1) According to X-ray structure analysis and differential scanning calorimetry, the change in the cracking resistance of metallic glasses at annealing temperatures above the critical point is caused by thermoactivated atomic rearrangements which are unrelated to the crystallization.

(2) The proposed method of indentation of the metallic glass deposited onto the substrate can be used for determining the cracking resistance and the thermal prehistory of the metallic glasses under investigation.

ACKNOWLEDGMENTS

We are grateful to V.A. Khonik for supplying the samples for investigations and the DSC data.

This work was supported by the Ministry of General and Professional Education of the Russian Federation, the Grant on Basic Research in the Field of Natural Science (project no. 97-0-4.3-185).

REFERENCES

1. I. V. Zolotukhin, *Physical Properties of Amorphous Metallic Materials* (Moscow, 1986).
2. D. K. Belashchenko, *Structure of Liquid and Amorphous Metals* (Moscow, 1985).
3. A. M. Glezer and B. V. Molotilov, *Structure and Mechanical Properties of Amorphous Alloys* (Moscow, 1992).
4. V. A. Likhachev and V. E. Shudegov, *Organization Principles of Amorphous Structures* (St. Petersburg Gos. Univ., St. Petersburg, 1999).
5. V. A. Fedorov, I. V. Ushakov, and E. I. Klimacheva, in *Proceedings of the II International Conference "Micromechanisms of Plasticity, Fracture, and Attendant Phenomena," Tambov, 2000*, Vol. 5, Issues 2–3, p. 370.
6. A. L. Volynskiĭ, S. L. Bazhenov, O. V. Lebedev, *et al.*, Vysokomol. Soedin., Ser. A **39**, 1805 (1997).
7. D. L. Bykov and D. N. Konovalov, in *Proceedings of the II International Conference "Micromechanisms of Plasticity, Fracture, and Attendant Phenomena," Tambov, 2000*, Vol. 5, Issues 2–3, p. 224.
8. Yu. I. Golovin, A. I. Tyurin, V. I. Ivolgin, and V. V. Korenkov, in *Proceedings of XXXV International Workshop "Topical Problems of Strength," Pskov, 1999*, p. 161.
9. A. I. Manokhin, B. S. Mitin, V. A. Vasil'ev, and A. V. Revyakin, *Amorphous Alloys* (Metallurgiya, Moscow, 1984).
10. S. S. Gorelik, L. N. Rastorguev, and Yu. A. Skakov, *X-ray Diffraction and Electron Optical Analysis* (Metallurgiya, Moscow, 1970, 2nd ed.).
11. C. A. Pampillo, J. Mater. Sci. **10** (7), 1194 (1975).
12. S. S. Tsao and F. Spaepen, in *Proceedings of the 4th International Conference on Rapidly Quenched Metals* (Japanese Inst. of Metals, Sendai, 1982), Vol. 1, p. 463.

Translated by O. Borovik-Romanova

Technical Physics, Vol. 46, No. 6, 2001, pp. 677–681. Translated from Zhurnal Tekhnicheskoĭ Fiziki, Vol. 71, No. 6, 2001, pp. 32–36.

SOLIDS

Magnetic Field Dependence of the Gilinsky Mode of the Domain Wall Spectrum in a Uniaxial Ferromagnet

G. E. Khodenkov

Magnitooptoelektronika Joint Laboratory at the Institute of General Physics, Russian Academy of Sciences, Ogarev Mordovian State University, Russia

e-mail: angeline@mtu-net.ru

Received August 7, 2000

Abstract—The dependences of the translation mode and the Gilinsky mode of the domain wall spectrum on the value of an external magnetic field directed along the plane of the Bloch domain wall and perpendicular to the axis of anisotropy are determined. The diagram of stability of the domain wall polarity in a magnetic field is calculated. The behavior of the modes in the vicinity of the point of reorientation of the domain wall polarity is analyzed. *© 2001 MAIK "Nauka/Interperiodica".*

INTRODUCTION

Magnetic materials find application as working media in modern devices for processing microwave and optical information signals [1, 2]. Ferromagnets with domain structure, i.e., containing domain walls (DWs), are of particular interest. It was suggested in 1976 that domain walls could be used as two-dimensional waveguide channels [1]. The DW spectrum contains a number of normal modes localized on the DW surface, which can also be used in designing devices for signal processing and improve their performance capabilities. In addition, the use of these modes favors a decrease in the size of the processing devices.

In the presence of surface modes, magnetostatic interactions cause significant rearrangement in the spectrum even of the simplest DWs (180° DW in a uniaxial ferromagnet). The only initial localized mode (in the one-dimensional approximation), the shift (translation) mode, becomes nonreciprocal. A new nonreciprocal optical mode, the Gilinsky mode, arises [3]. Numerical computation showed that additional normal modes localized on the DW can split off the bottom of the bulk spin-wave band at certain values of the wave vector **k** directed along the DW plane [4]. Additional components of anisotropy were taken into account using numerical methods [5, 6]. The structure of the spectrum was found to be rather complicated: anomalous dispersion, level crossing, etc. were revealed. Only the translation mode has been studied experimentally at length, whereas the Gilinsky mode has been revealed in ferromagnets only recently [6].

It is of particular interest to study the effect of an external magnetic field on the modes of the DW spectrum under consideration. An external magnetic field changes the dispersion characteristics of the DW. This can be used for identification of spectrum branches and for controlling the procedure of information signal processing.

It should be also noted that internal structural transitions, such as polarity reorientation, Bloch-to-Neel DW transitions, etc., occur in DWs at certain critical values of the magnetic field. The effect of the magnetic field on the dispersion characteristics can be especially strong in the vicinity of these critical fields. This problem was studied in some detail for the lower translation mode of DWs in strongly anisotropic ferromagnets (see, e.g., [7–9]). The Gilinsky mode, which is located higher than the latter mode, has been revealed only recently [6], so that, to our knowledge, there have not been similar studies of the Gilinsky mode so far. The goal of this work was to fill this gap. We restrict our consideration to the case of a uniaxial strongly anisotropic ferromagnet exposed to an external magnetic field either aligned with the DW polarity or opposed to it.

GENERAL EQUATIONS AND REORIENTATION OF DW POLARITY

Let us consider a uniaxial ferromagnet with the easy magnetic axis parallel to the z axis of the reference frame. The energy density in the ferromagnet is described by the equation

$$w = A(\nabla\mathbf{M})^2/M^2 - KM_z^2/M^2 - \mathbf{HM} - \frac{1}{2}\nabla\chi\mathbf{M}, \quad (1)$$

where $\mathbf{M}(\mathbf{r}, t)$ is the magnetization (its absolute value remains unchanged); A and K are the exchange stiffness and uniaxial anisotropy constants, respectively ($A > 0$ and $K > 0$); $\mathbf{H}$ is the external magnetic field; and χ is the magnetostatic potential. The equation of motion $\partial\mathbf{M}/\partial t = \gamma[\mathbf{H}^{\text{eff}} \times \mathbf{M}]$, where γ is the gyromagnetic ratio ($\gamma > 0$) and $\mathbf{H}^{\text{eff}} = -\delta w/\delta\mathbf{M}$ is the effective internal field,

and the Maxwell equation $\mathrm{div}(-\nabla\chi + 4\pi\mathbf{M}) = 0$ were used in calculations.

If a DW lies in the $x0z$ plane and the external magnetic field is directed along the x axis, the structure of the ground state is characterized by an angle $\varphi = \varphi(y)$ measured from the z axis:

$$\varphi'(y) = \sin\varphi - H,$$
$$\cos\varphi = -\sqrt{1-H^2}\,\frac{\sinh(y\sqrt{1-H^2})}{H + \cosh(y\sqrt{1-H^2})}, \qquad (2)$$

where the distances along the y axis (normal to the DW plane) are measured in units of the DW width $\Delta = \sqrt{A/K}$ (below, the distances along the x axis are also measured in these units). The external magnetic field H is measured in the units of the effective anisotropy field $H_a = 2K/M$.

Equations (2) are valid only for $|H| \le 1$. If $H < 0$ or $|H| > 1$, the DW has 360° structure. These cases are not considered in this work. Below, the DW polarity is defined as the direction (sign) of the magnetization component $M_x(y)$ at the center of the wall ($y = 0$), where $\varphi(0) = \pm\pi/2$.

Let our consideration be restricted to the case of type $\sim\exp(-i\omega t + ikx)f(y)$ small-amplitude magnetization oscillations propagating along the x axis (i.e., perpendicularly to the easy magnetic axis). It should be noted that similar restrictions were imposed on the fundamental system considered by Gilinsky [3]. In the reference frame, local with respect to the ground state (2), the equations for small-amplitude oscillations of the components of the magnetization vector take the form similar to that obtained in [3]:

$$-i\omega m_\perp = (k^2 + \hat{L}_\parallel)m_\parallel + \frac{ik}{Q}\chi\cos\varphi, \qquad (3.1)$$

$$-i\omega m_\parallel = -(k^2 + \hat{L}_\perp)m_\perp - \frac{\chi'}{Q}, \qquad (3.2)$$

$$\chi'' - k^2\chi = m'_\perp + ik\cos\varphi\, m_\parallel, \qquad (3.3)$$

where the initial one-dimensional operators

$$\hat{L}_\parallel = -\frac{d^2}{dy^2} + \cos 2\varphi + H\sin\varphi, \qquad (4.1)$$

$$\hat{L}_\perp = \hat{L}_\parallel + 2H(\sin\varphi - H) + H^2, \qquad (4.2)$$

as well as the set of equations (3), depend only on the coordinate y (see Eq. (2)). The dependent variables $m_\perp(y)$ and $m_\parallel(y)$ in the set of equations (3) are small dimensionless amplitudes of magnetization directed perpendicularly and parallel to the DW plane $x0z$, respectively; Q is the quality factor ($Q = H_a/4\pi M$); the frequency ω is measured in the units of γH_a; and k is the wave vector along the x axis (the wave vector is measured in the units of $1/\Delta$).

The longitudinal magnetic field H directed along the x axis (aligned or opposed to the DW polarity) is taken into account in Eqs. (3) and (4). This is the only difference between the set of equations (3) and (4) and a similar set of equations used in [3]. In certain respects, this difference is very important. First, the commutator $[\hat{L}_\perp, \hat{L}_\parallel]$ differs from zero, whereas in [3] these operators are equal to each other, making it difficult to select the set of basic functions for analytical solution. Second, in [3] both operators are nonnegative and have zero eigenvalues for the ground levels, whereas, in the case under consideration, only the operator $\hat{L}_\parallel\varphi'(y) = 0$ has such characteristics (see Eq. (2)). Finally, in our case, the operator $\hat{L}_\perp$ (see Eq. (4.2)) can have negative eigenvalues within a certain range of magnetic fields.

Let us prove the last statement in the limit of small magnetic fields. It can be concluded from the structure of the operator $\hat{L}_\perp$ (see Eq. (4.2)) and the equation $\hat{L}_\parallel\varphi'(y) = 0$ that the only nonzero contribution to the eigenvalue is made (in the first approximation) by the term $2H\sin\varphi$. Using the first-order perturbation theory, we obtain that

$$E(H) = \frac{\langle\varphi'(y)|2H\sin\varphi|\varphi'(y)\rangle}{\langle\varphi'(y)|\varphi'(y)\rangle} \approx \frac{\pi H}{2}. \qquad (5)$$

Thus, at $H < 0$, the eigenvalue is negative. In strong magnetic fields, the DW has 360° structure and the external field is directed oppositely to the DW polarity. It can be shown (see [10]) that, in strong magnetic fields, the lower eigenvalue of the operator $\hat{L}_\perp$ is negative ($E(H) = -3|H|$). This conclusion is of fundamental importance. It shows that the initial structure of the DW described by Eq. (2) can be unstable if the external magnetic field is directed oppositely to the DW polarity. Indeed, in the one-dimensional approximation, $\chi' = m_\perp$ (see Eq. (3.3)), so that the energy balance equation can be written as follows:

$$\frac{d}{dt}\int_{-\infty}^{\infty} dy\left[m_\parallel\hat{L}_\parallel m_\parallel + m_\perp\left(\hat{L}_\perp + \frac{1}{Q}\right)m_\perp\right] < 0. \qquad (6)$$

Inequality (6) is strict because the dissipation in the system is taken into account. Within the framework of the linear theory, the negative eigenvalue implies that small perturbations increase unlimitedly with time. The magnetostatic interaction ($\sim 1/Q$) stabilizes the system. However, at a certain critical value of the magnetic field $H = H_c(Q)$, the system becomes unstable and the DW polarity is reoriented.

The dependence $H_c(Q)$ can be obtained from the condition that the equation

$$(\hat{L}_\perp + 1/Q)m_\perp = 0 \qquad (7)$$

should have solutions localized on the DW. Using the second-order perturbation theory, we obtain for uniaxial ferromagnets with $Q \gg 1$

$$\left|\frac{H_c}{4\pi M}\right| = \frac{2}{\pi} - \left(\frac{2}{\pi}\right)^2 \frac{1}{Q} \times \left[\frac{2}{5\pi} + \frac{1}{8\pi}\left(\frac{32}{5\pi} + \frac{4}{\pi} + \pi - \frac{14}{\pi}\zeta(3)\right)\right], \quad (8)$$

where $\zeta(3)$ is the Riemann zeta function ($\zeta(3) = 1.202\ldots$). The coefficient of $1/Q$ is equal to 0.069.

The first term in the right-hand side of Eq. (8) is well known (see [7–9]). The second term is the correction calculated using the second-order perturbation theory. In a similar manner, for ferromagnets with $Q \ll 1$, we obtain

$$\left|\frac{H_c}{4\pi M}\right| = \frac{1}{3} + \frac{4}{15}Q. \quad (9)$$

The first term in the right-hand side of Eq. (9) was determined in [10]. It should be noted, however, that according to [10] this term is overestimated. The variational estimate $|H_c/4\pi M| = 0.543Q$ was obtained in [10] using two-dimensional equations (3) in the static approximation (the magnetostatic contribution becomes zero). The results of calculating the critical field on the basis of the solution of Eq. (7) and the estimations made above are shown in the figure. Note that the discrepancy between the results of exact calculations (points) and the results obtained using the second-order perturbation theory (curve *1*) decreases with increasing Q.

REDUCTION OF BASIC EQUATIONS

Of special interest is the solution of the problem for small values of k. The approach suggested in [11] was used for this purpose. This approach provides results consistent with the exact analytical solution [3]. The approach is based on the quantum-mechanical theory of the shallow state and on the method of model pseudopotentials widely used in the theory of metals (see, e.g., [12]). To make sure that the theory of the shallow state can be applied to the set of equations (3), let us consider the characteristic roots p of the set (3) for $|y| \longrightarrow \infty$ (in this case, all solutions are proportional to $\exp(-|py|)$):

$$p_{1,2}(\omega) = \left[1 + k^2 + \frac{1}{2}\left(\frac{1}{Q} - H^2\right) \pm \sqrt{\frac{1}{4}\left(\frac{1}{Q} + H^2\right)^2 + k^2\frac{H^2}{Q} + \omega^2}\right]^{1/2}, \quad p_3 = |k|. \quad (10)$$

These are the three positive roots of the six roots of the set; the other three roots are equal to these in absolute value but opposite in sign. It follows from Eqs. (10) that the asymptotic behavior of the solution for small values of k is determined by the third root. In this case, the dependences of the coefficients in set (3) on the spatial coordinates become insignificant. Thus, the potentials involved in the operators $\hat{L}_{\perp,\parallel}$ could be assumed to be of a simple shape (for example, the Dirac delta function). The potentials and coefficients in the set of equations (3) are selected so that the characteristic roots (10) and the eigenvalues of the operators (4.1) and (4.2) remain unchanged.

Thus, the following substitutions can be made in the set of equations (3):

$$\hat{L}_\parallel \longrightarrow \hat{L}_\parallel^* = -\frac{d^2}{dy^2} + 1 - H^2 - 2\sqrt{1 - H^2}\,\delta(y), \quad (11.1)$$

$$\hat{L}_\perp \longrightarrow \hat{L}_\perp^* = -\frac{d^2}{dy^2} + 1 - 2\sqrt{1 - E(H)}\,\delta(y), \quad (11.2)$$

$$\cos\varphi \longrightarrow -\mathrm{sgn}(y)\sqrt{1 - H^2}, \quad (11.3)$$

where $\mathrm{sgn}(y)$ is the sign function and $E(H)$ is the lower eigenvalue of the exact operator $\hat{L}_\perp$ (see Eq. (5)).

These substitutions allow the initial set of equations (3) to be significantly simplified by reducing it to a set of equations with constant coefficients. The following boundary conditions determined by the delta

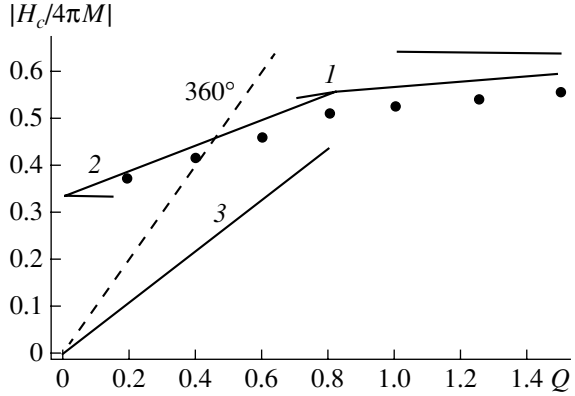

Diagram of the stability of the DW polarity in the longitudinal magnetic field: (*1*) critical field calculated using the second-order perturbation theory for $Q > 1$; (*2*) the same for $Q < 1$; and (*3*) variational estimate of the critical field made using a two-dimensional theory for $Q < 1$ [10]. Points show the critical field values calculated using the one-dimensional theory. Asymptotic values of the field of the DW polarity reorientation in the limits $Q \ll 1$ and $Q \gg 1$ are indicated by horizontal lines 1/3 and $2/\pi$, respectively (one-dimensional approximation). Above the dashed line, the DW has a 360° structure.

potentials (11) are imposed on the set of equations:

$$\chi(0+) = \chi(0-), \quad \chi'(0+) = \chi'(0-);$$
$$m_{\parallel,\perp}(0+) = m_{\parallel,\perp}(0-), \tag{12}$$
$$-m'_{\parallel,\perp}(0+) + m'_{\parallel,\perp}(0-) = 2(\sqrt{1-H^2}, \sqrt{1-E(H)}).$$

The magnetization components, the magnetostatic potential, and its first derivative with respect to y are continuous at the center of DW ($y = 0$). Therefore, as expected, the normal component of the magnetic induction vector is also continuous. The magnetization derivatives are discontinuous at the center of DW.

The lower eigenvalue and the eigenfunction asymptotics for the modified operator $\hat{L}_\parallel^*$ are the same as for the exact operator $\hat{L}_\parallel$ ($E = 0$ and $\varphi'(y) \sim \exp(-|y|\sqrt{1-H^2})$). The same is true for the operators $\hat{L}_\perp^*$ and $\hat{L}_\perp$ if eigenvalue (5) is taken into account.

Strictly speaking, delta potentials are insufficient for complete description of the system of local DW levels in the one-dimensional approximation. As shown in [8], even in the limit $H \ll 1$, the DW has an additional discrete level due to oscillations of the effective width of the DW. However, this level is very close to the bottom of the bulk spin-wave band, and it exists only if the external magnetic field is directed along the DW polarity. In this work we consider the modes lower than this level and magnetic fields directed oppositely to the DW polarity (i.e., magnetic fields inducing polarity reorientation). That is why this level is not taken into account.

RESULTS AND DISCUSSION

The modified set of equations (3) with constant coefficients and boundary conditions (12) has solutions decreasing with $|y| \longrightarrow \infty$. These solutions can be expressed in terms of exponential functions with exponents (10):

$$(m_\perp, m_\parallel, \chi) = \sum_{j=1}^{3} C_j^{\pm} \exp(-p_j|y|)(1, is(p_j), \operatorname{sgn}(y) r(p_j)), \tag{13}$$

where $C_j^{\pm}$ are six unknown constants (constants for the negative and positive y semiaxes are different). The number of constants corresponds to the number of boundary conditions (12).

However, it can be shown, by analogy with [11], that the localized levels can be determined taking into account only symmetric combinations of the exponential functions (i.e., $C_j^+ = C_j^- = C_j$, where $j = 1, 2, 3$). The other combinations are antisymmetric and correspond to a continuous spectrum. In addition, only three of the six boundary conditions (12) should be taken into account. These are the conditions for the discontinuity of derivatives of the magnetization components $m_{\parallel,\perp}$ and the continuity of the magnetostatic potential χ. Thus, we obtain the following algebraic equation:

$$\begin{vmatrix} r(p_1) & r(p_2) & r(p_3) \\ p_1 - \sqrt{1-\pi H/2} & p_2 - \sqrt{1-\pi H/2} & p_3 - \sqrt{1-\pi H/2} \\ (p_1 - \sqrt{1-H^2})s(p_1) & (p_2 - \sqrt{1-H^2})s(p_2) & (p_3 - \sqrt{1-H^2})s(p_3) \end{vmatrix} \begin{pmatrix} C_1 \\ C_2 \\ C_3 \end{pmatrix} = 0, \tag{14}$$

where

$$r(p_j) = -[(k^2 - p_j^2 + 1 - H^2)p_j + \omega k_x \sqrt{1-H^2}]/D(p_j), \tag{15.1}$$

$$s(p_j) = -\left[\omega(p_j^2 - k^2) + \frac{1}{Q} p_j k_x \sqrt{1-H^2}\right]/D(p_j), \tag{15.2}$$

$$D(p_j) = (p_j^2 - k^2)(1 - H^2 - p_j^2 + k^2) - \frac{k^2}{Q}(1-H^2). \tag{15.3}$$

The dispersion relation determining the dependences $\omega(k)$ is obtained by equating the determinant of the matrix 3×3 involved in Eq. (14) to zero.

The solution of the dispersion relation for $k \longrightarrow 0$ depends on the limit value of ω. The case of $\omega \longrightarrow 0$ and $k \longrightarrow 0$ corresponds to the translation (shift) mode of the DW:

$$\omega_{tr} = \frac{k}{\sqrt{Q}} + |k| \sqrt{1 + \frac{1}{Q}} \sqrt{\frac{1}{Q} - \frac{\pi H}{2}}. \tag{16}$$

The result obtained for $H = 0$ coincides with the exact value calculated in [3]. The result obtained for $H \neq 0$ and $Q > 1$ coincides with the value obtained using the Slonczewski theory [7]. The polarity reorientation occurs in the magnetic field $H_c = 2\pi/Q$ ($H_c = 8M$). However, taking into account the greater powers of k [9], we obtain that the transition is nonuniform ($k_0 \sim 1/Q$, where $Q \gg 1$). If $Q \ll 1$, the small-field expansion used above is insufficient for describing the transition,

although Eq. (16) correctly describes the effect of a small field $H \ll 1$ on the spectrum.

Another limit $k \longrightarrow 0$ and $\omega \longrightarrow$ const corresponds to the Gilinsky mode with regard for the effect of the external magnetic field. Let us consider the leading term of expansion of the dispersion relation determinant (determinant of the matrix involved in Eq. (14)):

$$r(p_3) = Q(1 + \omega \operatorname{sgn}(k)/\sqrt{1 - H^2})/|k|.$$

This term diverges for $k \longrightarrow 0$, whereas the other terms of the expansion are finite in this limit. Therefore, the other terms can be taken at $k = 0$ and $\omega = \omega_0 = \sqrt{1 - H^2}$. Thus, the solution for the Gilinsky mode is obtained in two limits:

$$\frac{\omega_G}{\omega_0} = \vartheta(-k) \times \begin{cases} 1 + \dfrac{|k|}{Q}\left(2 + \dfrac{3Q}{2} - \dfrac{\pi Q H}{4}\right) & Q \ll 1 \\ 1 + \dfrac{|k|}{Q}\left(2\sqrt{Q} + 1 + \dfrac{3}{4\sqrt{2Q}} - \dfrac{3}{8\sqrt{2}Q} - \dfrac{\pi H}{8}\right) & Q \gg 1, \end{cases} \quad (17)$$

where $\vartheta(-k)$ is the Heaviside step function different from zero at $k < 0$.

The external magnetic field H causes a decrease in the limit value $\omega_G(k \longrightarrow 0)$. The group velocity of the wave increases or decreases according to the direction (sign) of the external magnetic field. At $Q \gg 1$, the group velocity changes abruptly by $H_c = 2\pi/Q$, $H_c = 8M(\pm\pi H_c/(4Q))$ at the point of the DW polarity reversal.

The diagram of stability of the DW polarity in a magnetic field directed oppositely to the polarity vector was determined (figure). The DW dispersion characteristics for small values of the wave vector ($k \ll 1$) can be rather easily determined using the approach to the spectral problems of the DW dynamics suggested in [11] (use of numerical methods for calculations within this range of k often involves some difficulties). The approach suggested in [11] can also be used for calculating the dispersion characteristics in the region of the polarity reorientation. The magnetic field dependences of the translation mode and the Gilinsky mode of the DW spectrum are described by Eqs. (16) and (17), respectively. These dependences can be used in experiments for identifying the translation and Gilinsky modes.

REFERENCES

1. A. K. Zvezdin and V. A. Kotov, *Modern Magnetooptics and Magnetooptical Materials* (Institute of Physics Publ., Bristol, 1997); A. K. Zvezdin and V. A. Kotov, *Magnetooptics of Thin Films* (Nauka, Moscow, 1988).
2. *Nonlinear Microwave Processing: Towards a New Range of Devices*, Ed. by R. Marcelli and S. Nikitov (Kluwer, Dodrecht, 1996).
3. I. A. Gilinsky, Zh. Éksp. Teor. Fiz. **68** (3), 1032 (1975) [Sov. Phys. JETP **41**, 511 (1975)].
4. A. V. Mikhaĭlov and I. A. Shimokhin, Zh. Éksp. Teor. Fiz. **97** (6), 1966 (1990) [Sov. Phys. JETP **70**, 1109 (1990)].
5. A. M. Alekseev, A. F. Popkov, and A. I. Popov, Izv. Vyssh. Uchebn. Zaved., Élektron., No. 1, 13 (1998).
6. A. M. Alekseev, H. Doetsch, N. E. Kulagin, *et al.*, Zh. Tekh. Fiz. **69** (6), 55 (1999) [Tech. Phys. **44**, 657 (1999)].
7. A. P. Malozemoff and J. C. Slonczewski, *Magnetic Domain Walls in Bubble Materials* (Academic, New York, 1979; Mir, Moscow, 1982).
8. G. E. Khodenkov, Fiz. Met. Metalloved. **61** (5), 850 (1986).
9. Yu. A. Dimashko, P. P. Shatskiĭ, and D. A. Yablonskiĭ, Fiz. Tverd. Tela (Leningrad) **30** (10), 3084 (1988) [Sov. Phys. Solid State **30**, 1774 (1988)].
10. R. M. Hornreich and H. Thomas, Phys. Rev. B **17** (3), 1406 (1978).
11. G. E. Khodenkov, Fiz. Met. Metalloved. **75** (5), 5 (1993).
12. W. A. Harrison, *Solid State Theory* (McGraw-Hill, New York, 1970; Mir, Moscow, 1972).

Translated by K. Chamorovskiĭ

Technical Physics, Vol. 46, No. 6, 2001, pp. 682–685. Translated from Zhurnal Tekhnicheskoĭ Fiziki, Vol. 71, No. 6, 2001, pp. 37–40.

SOLIDS

The Size Effect in the Ultralow-Frequency Electrical Excitation Spectrum of Bridgman Instability

E. G. Fateev

Institute of Applied Mechanics, Ural Division, Russian Academy of Sciences, Izhevsk, 426001 Russia
e-mail: fateev@ipm.uni.udm.ru, e@fateev.udm.ru

Received August 23, 2000

Abstract—With crystal hydrates growing in size, the amplitude of the ultralow-frequency (ULF) electric field responsible for a drastic drop in their mechanical stability under high uniaxial compression is found to markedly decrease. This effect is demonstrated with oxalic acid crystal hydrates $H_2C_2O_4 \cdot 2H_2O$ in experiments on Bridgman explosive instability. As the size of the crystal hydrates grows, the ULF stability spectrum exhibits no less than three narrow dips imposed on a broader dip. This spectrum correlates with the permittivity burst spectra. These phenomena can be explained if, at ULFs, the compressible crystal hydrates are considered as nonlinear disperse systems in chains of variable-moment giant (comparable to a disperse particle in size) dipole oscillators. © *2001 MAIK "Nauka/Interperiodica".*

INTRODUCTION

The dramatic drop of the mechanical stability threshold in highly compressible crystal hydrates in ULF ($10 < \omega_1 < 100$ Hz) electric fields has been discovered in both model [1–3] and natural [4, 5] objects. Similar results have also been obtained in experiments that explored the Bridgman effect: an explosive instability arising when insulators are subjected to uniaxial compression at high pressures ($P < 10$ GPa) in open-ended anvils [6–10]. This effect appears in ULF fields of strength $E < 0.1$–2.0 kV/cm, which are 10^3 to 10^4 times weaker than the breakdown fields for such crystal hydrates [11]. Interest in this effect stems from the abundance of crystal hydrates in the lithosphere, to which only ULF electromagnetic oscillations (with a skin depth of no less than 10 km [12]) can penetrate.

Usually, the frequency spectrum of the stability threshold (critical pressure) $P_c(\omega)$ for the anvils with the diameter of the operating area $d_1 = 5$ mm shows one narrow deep dip at frequencies $20 < \omega_1 < 40$ Hz and one broader dip at $\omega_2 \approx 10^4$ Hz. The depth $\Delta P = P_c(U = 0) - P_c(U)$ of the dips in the stability threshold spectrum grows with the amplitude U of ULF voltage pulses as $\Delta P(U) \propto U^2$. For pulses with $U \approx 65$ V and crystal hydrates of thickness $h \approx 0.25$ mm, the maximum relative depth is $\Delta P/P_c(U = 0) \approx 0.5$ [1–5].

Earlier [2], a frequency shift of the deep dip in the ULF electrical spectrum $P_c(\omega)$ for crystal hydrates was predicted. Later, this prediction was confirmed in a basic experiment [5]. This shift followed from two earlier models of the effect [3–5]; however, the coincidence of the models turned out to be formal, as shown below. In this work, the existence of deep dips in the ULF spectrum $P_c(\omega)$ for crystal hydrates with large characteristic sizes was checked and fundamentally new results that seem contrary to earlier model concepts of microbreakdowns occurring at ULFs were obtained.

EXPERIMENT

We used oxalic acid crystal hydrate $H_2C_2O_4 \cdot 2H_2O$ as a model object. This compound, having a low stability threshold P_c, allows vast experimentation with the Bridgman effect in order to collect reliable statistic data for the excitation of the $P_c(\omega)$ spectrum at ULFs.

The ULF spectrum $P_c(\omega)$ for $H_2C_2O_4 \cdot 2H_2O$ was found by the same technique as for model compounds in [3–5]. The rate of compression on the Bridgman anvils (with VK-8 superhard alloy inserts) was $dP/dt \approx 0.1$ GPa/s at $T \approx 293$ K. We experimented with anvils with operating area diameters $d_2 = 10$ mm and $d_1 = 5$ mm. For $d_2 = 10$ mm, the powder, at the prethreshold stage of compression, was compacted into a disk of thickness $h \approx 0.40$ mm. In the case of $d_1 = 5$ mm, the mean thickness of the disk before explosion was $h_1 \approx 0.25$ mm. Each data point was obtained from ten explosion runs.

EXPERIMENTAL RESULTS

For $d_2 = 10$ mm, the ULF $P_c(\omega)$ spectrum for $H_2C_2O_4 \cdot 2H_2O$ has deep dips. Their shapes, depths, and positions are much different from those observed for $d_1 = 5$ mm (Fig. 1). Also, for d_2, the excitation threshold of the Bridgman effect is ≈1.5 times lower than for d_1 throughout the ULF $P_c(\omega)$ spectrum. Such a size effect in solids at the secondary elastic stage under high uniaxial compression [13] was first found in [14] and is

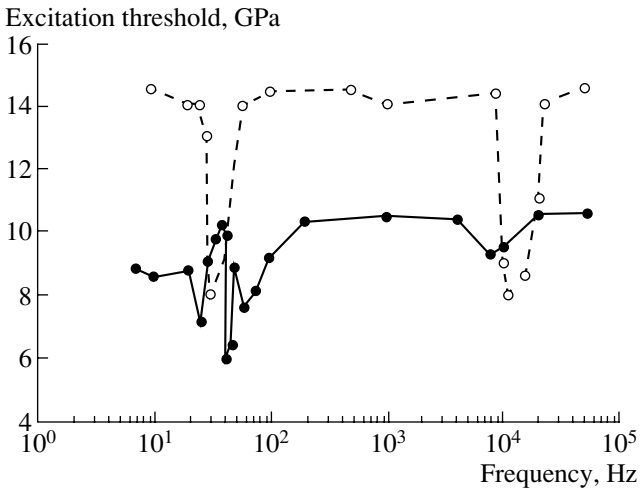

Fig. 1. Electrical spectra $P_c(\omega)$ for the excitation threshold of the Bridgman effect in $H_2C_2O_4 \cdot 2H_2O$ crystal hydrates at ULFs. The pulse amplitude is U = 65 V. (○) d_1 = 5 mm and (●) d_2 = 10 mm.

easy to explain in terms of the thermal fluctuation theory of strength [15] and also by considering the mechanic stress fields at a given ratio h/d. Note that, for this crystal hydrate, the shape of the ULF $P_c(\omega)$ spectrum for d_1 is nearly the same as in earlier experiments [3] in the frequency range $25 < \omega_1 < 35$ Hz. For the experiments discussed in this work and those in [3], the hydrates were taken from the same lot. For d_2, the spectrum shows the deep broad dip at $5 < \omega_1 < 100$ Hz. In this range, the spectrum is strongly irregular with three dips in the intervals 21–27, 41–48, and 58–68 Hz and a high peak at 30–40 Hz near the deepest dip. In the broad ULF dip, the mean values of the threshold are close to $\approx 0.75\, P_c(U = 0)$. In the deepest dip, the threshold is $\approx 0.5 P_c(U = 0)$, while in the peak, it nearly coincides with $P_c(U = 0)$.

To further clarify the nature of the dips in the $P_c(\omega)$ spectrum of $H_2C_2O_4 \cdot 2H_2O$ crystal hydrate in a wide ULF range under uniaxial compression, we studied the frequency variation of the dielectric constant $\varepsilon(\omega)$ of this compound at ULFs (for the measuring technique, see [3]). The nonmonotonic $\varepsilon(\omega)$ curve for d_2 = 10 mm is compared with that for d_1 = 5 mm in Fig. 2. A giant burst of the dielectric constant is observed in both cases. For d_2 = 10 mm, however, the dielectric constant curve has an unusual form with peaks and dips. The ratio of ε in the peaks to that in the dips may reach 10. Moreover, the values of $\varepsilon(\omega)$ at ULFs are, on the average, approximately 20 times higher than $\varepsilon_\infty \approx 6$, as follows from Fig. 2. It should be noted that the giant values of ULF $\varepsilon(\omega)$ under conditions of uniaxial compression show up as bursts within the short time interval $\Delta t \leq 1$ s [3–5]. In both cases, at frequencies near $\omega_1 \approx 10^4$ Hz, dips identified earlier as dielectric losses [1] are observed. However, for d_2, the dip in this range is of lesser depth and width, while at ULFs, a dip simpler in shape and having lesser depth and width is observed for d_1.

Figure 3 plots the excitation threshold of the Bridgman effect P_c against the voltage pulse amplitude U at the characteristic frequencies $\omega_1 \approx 42$ Hz (deep dip) and $\omega_1 \approx 200$ Hz (stability domain) of the $P_c(\omega)$ spectrum for d_2 = 10 mm. For d_1, similar curves were obtained at

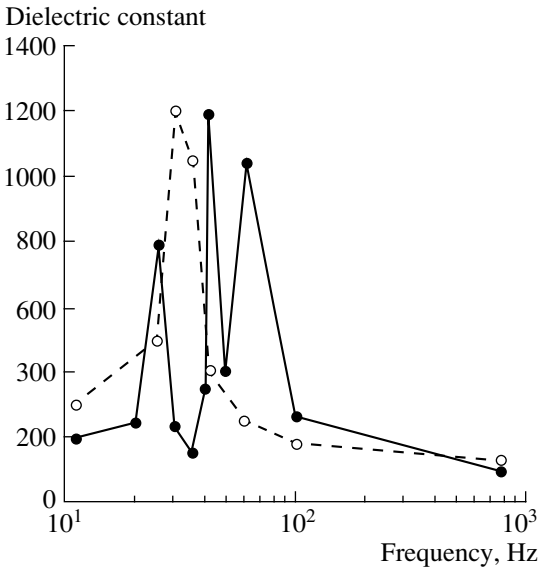

Fig. 2. $\varepsilon(\omega)$ spectra at the instant of the maximum burst when $H_2C_2O_4 \cdot 2H_2O$ crystal hydrates are subjected to high uniaxial compression at U = 65 V. (○) d_1 = 5 mm and (●) d_2 = 10 mm.

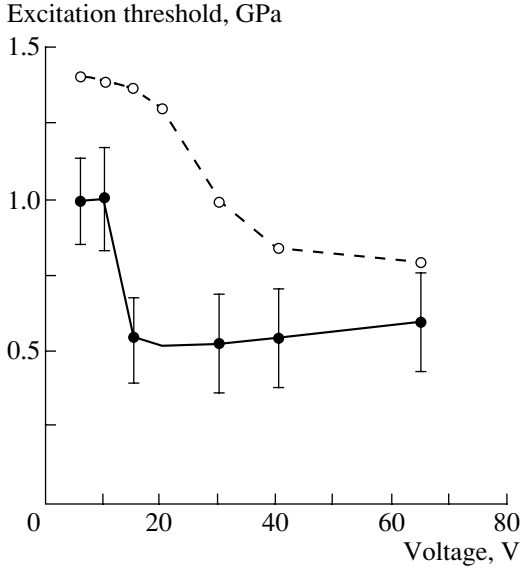

Fig. 3. Excitation threshold of the Bridgman effect for $H_2C_2O_4 \cdot 2H_2O$ crystal hydrates vs. amplitude of voltage pulses. (○) d_1 = 5 mm, $\omega \approx 33$ Hz; (●) d_2 = 10 mm, $\omega \approx 42$ Hz.

$\omega_1 \approx 32$ Hz (deep dip) and $\omega_1 \approx 200$ Hz (Fig. 3). In the case of d_2, the curve $P_c(U)$ is of a distinct threshold character: at $\omega_1 \approx 42$ Hz, the critical pressure P_c sharply drops at the amplitude $U = 11$–15 V and then remains unchanged up to $U = 65$ V. For d_1, this dependence at ULFs exhibits greater monotonic behavior, following the $\Delta P(U) \propto U^2$ law up to the amplitude $U \approx 35$ V, and then attains a plateau with the minimal threshold $U > 40$ V. For $\omega_1 \approx 200$ Hz, the pulse amplitude does not have an effect on P_c up to 65 V for both characteristic sizes d_1 and d_2.

DISCUSSION

The spectra $P_c(\omega)$ and $\varepsilon(\omega)$, while of statistical nature, qualitatively correlate in the range $5 < \omega_1 < 100$ Hz. This is a clear indication of the interplay between processes responsible for the drop of the excitation threshold of Bridgman instability in this frequency range and the giant bursts of the ULF dielectric constant when the crystal hydrates are subjected to high uniaxial compression. It is evident that polarization reversal, which might take place in hydrogen-containing ferroelectrics ($H_2C_2O_4 \cdot 2H_2O$ like compounds [16]) under other conditions [3, 4], cannot explain our experimental data, since resonant excitations in domain structures are usually observed at high and superhigh frequencies ($\omega = 10$–1000 MHz [17]). Moreover, at medium pressures ($P > 0.3$ GPa), the vibrational motion of domains is damped in almost any ferroelectric [17]. Our results are essentially inconsistent with those obtained from earlier models [3], where the dips in the $P_c(\omega)$ spectra are explained by the localization of the maximum density of the energy spent on an electric breakdown in a microcrack or on a breakdown advancing by percolation.

Indeed, previous models [3–5] imply that the frequency shift of the dip is formally possible if some parameters (for example, temperature) are changed; however, they do not imply that several dips must exist at ULFs (Fig. 1). Moreover, when the sample thickness increases with the ULF permittivity burst remaining the same, the earlier models predict a substantial decrease in the relative depth of the dips, which is natural for electrical breakdown according to the law $\Delta P/P_c(U = 0) \propto U^2 h^{-2}$ [3, 4]. However, our data suggest the presence of a size effect that acts in the opposite direction. As the characteristic sizes of the samples increase, the excitation amplitude at which the relative depth of the ULF dips remains the same decreases (Fig. 3). In addition, extra peaks appear and broaden. Once some threshold amplitude U_t of ULF pulses has been attained, P_c sharply drops but the drop ΔP does not obey the law $\Delta P(U) \propto U^2$, as was observed previously [3].

It becomes evident that the above observations are of an essentially nonlinear nature. That the excitations are localized at ULFs suggests that the nonlinearity is associated with processes taking place in disperse systems with double electrical layers. Apparently, among such systems are the crystal hydrates under the conditions where phase transitions like partial dehydration proceed under highly nonuniform compression [18, 19].

The results obtained can be explained if we consider oscillations in chains of electrostatically coupled nonpoint oscillators with strongly varying dipole moments (with an arm comparable to the disperse particle size) [18, 19]. The condition of nonpoint oscillators follows from the compact-grained structure of the disperse systems considered [20]. The variability of the moments is related to the strong dependence of the charge polarization in the double electrical layers around the grains on the frequency and strength of local and applied electromagnetic fields.

We numerically analyzed one-dimensional finite chains of nonpoint variable-moment oscillators with dissipation and excitation. The parameters (mean grain size, intergranular spacing, maximum possible charge polarization, etc.) involved in the calculations were typical of disperse systems arising under high uniaxial compression. Our numerical results [19] leave room for the above-mentioned size effect. Of primary importance is that, when the dimension of the model chain increases and the amplitude of the ULF exciting fields is fixed, the local bursts of the polarization dramatically grow according to the variations of one or another of the parameters. During the initial several periods of the ULF field action, the fundamental resonance and satellite resonances are excited in the range $\omega < 200$ Hz. After the next several periods, the usual Debye dispersion relation is established.

Thus, the size effect discovered does not count in favor of localized electrical breakdowns between the anvils. Rather, it suggests the occurrence of space- and time-localized interdipole compressions [19] or microbreakdowns that initiate the decrease in the excitation threshold of the Bridgman effect in the crystal hydrates at ULFs.

REFERENCES

1. E. G. Fateev, Pis'ma Zh. Tekh. Fiz. **19** (10), 48 (1993) [Tech. Phys. Lett. **19**, 313 (1993)].
2. E. G. Fateev, Pis'ma Zh. Tekh. Fiz. **20** (20), 83 (1994) [Tech. Phys. Lett. **20**, 847 (1994)].
3. E. G. Fateev, Zh. Tekh. Fiz. **66** (6), 93 (1996) [Tech. Phys. **41**, 571 (1996)].
4. E. G. Fateev, Dokl. Akad. Nauk **354**, 252 (1997).
5. E. G. Fateev, Pis'ma Zh. Éksp. Teor. Fiz. **65**, 876 (1997) [JETP Lett. **65**, 919 (1997)].
6. P. W. Bridgman, Phys. Rev. **48**, 825 (1935).
7. P. W. Bridgman, Proc. Am. Acad. Arts Sci. **71**, 387 (1937).

8. P. W. Bridgman, *Studies in Large Plastic Flow and Fracture with Special Emphasis on the Effects of Hydrostatic Pressure* (McGraw-Hill, New York, 1952).
9. T. Ya. Gorazdovskiĭ, Pis'ma Zh. Éksp. Teor. Fiz. **5** (3), 78 (1967) [JETP Lett. **5**, 64 (1967)].
10. M. A. Yaroslavskiĭ, *Rheological Explosion* (Nauka, Moscow, 1982).
11. A. A. Vorob'ev and G. A. Vorob'ev, *Electric Breakdown and Destruction of Solid Dielectrics* (Vysshaya Shkola, Moscow, 1966).
12. M. A. Yaroslavskiĭ and N. K. Kapustyan, Dokl. Akad. Nauk SSSR **315**, 352 (1990).
13. V. I. Levitas, *Heavy Elasto-Plastic Deformations of Materials under High Pressure* (Naukova Dumka, Kiev, 1987).
14. N. S. Enikolopyan, A. A. Mkhitaryan, A. S. Karagezyan, and A. A. Khzardzhyan, Dokl. Akad. Nauk SSSR **292**, 887 (1987).
15. E. G. Fateev and V. P. Khan, Pis'ma Zh. Tekh. Fiz. **17** (20), 51 (1991) [Sov. Tech. Phys. Lett. **17**, 736 (1991)].
16. M. Fukai and T. Matsuo, J. Phys. Chem. Solids **50**, 743 (1989).
17. *The Physics of Ferroelectric Phenomena*, Ed. by G. A. Smolenskiĭ (Nauka, Leningrad, 1985).
18. E. G. Fateev, Pis'ma Zh. Tekh. Fiz. **26** (14), 103 (2000) [Tech. Phys. Lett. **26**, 640 (2000)].
19. E. G. Fateev, Zh. Tekh. Fiz. **71** (1), 92 (2001) [Tech. Phys. **46**, 89 (2001)].
20. T. L. Chelidze, A. I. Derevyanko, and O. D. Kurilenko, *Electrical Spectroscopy of Heterogeneous Systems* (Naukova Dumka, Kiev, 1977).

Translated by V. Isaakyan

Technical Physics, Vol. 46, No. 6, 2001, pp. 686–689. Translated from Zhurnal Tekhnicheskoĭ Fiziki, Vol. 71, No. 6, 2001, pp. 41–44.

SOLIDS

Elastoplastic Behavior of Marble, Granite, and Quartzite under Shock Compression

A. E. Kovalev, M. N. Pavlovskiĭ, V. M. Bel'skiĭ, and V. V. Komissarov

All-Russia Research Institute of Experimental Physics, Sarov, Nizhni Novgorod oblast, 607190 Russia

e-mail: root@gdd.vniief.ru

Received September 13, 2000

Abstract—Profiles of elastoplastic shock waves were experimentally revealed in three rocks, namely, in marble ($\rho_0 = 2.68$ g/cm^3), quartzite ($\rho_0 = 2.65$ g/cm^3), and granite ($\rho_0 = 2.63$ g/cm^3). In all these substances, the splitting of the shock-wave front into a leading elastic precursor and a following plastic compression wave were revealed. A diffusion of the front of the elastic precursor and a decrease in its amplitude were found to occur as the front propagates through the samples of the substances studied. No sharp decrease in the amplitude of elastic waves (yielding "tooth") was fixed. Pressures in the elastic and plastic compression waves, as well as the wave and mass velocities and the magnitudes of the relative compression were determined. © *2001 MAIK "Nauka/Interperiodica".*

INTRODUCTION

The aim of shock-wave measurements of the elastoplastic properties of rocks is to obtain information that is necessary for calculating the effects of power underground explosions, calculating the effects of meteorite impacts, the explosive stimulation of oil strata, and solving some other application problems. Therefore, the attention of many researchers is primarily turned to the most common geological materials.

The importance of such investigations is also caused by the need of obtaining new experimental data, such that could be used for the development and improvement of theoretical models of the behavior of rocks under conditions of shock compression (marble in this respect is one of the most suitable materials).

No complete clarity exists at present in the treatment of the behavior of rocks upon shock loading. In particular, a fundamental feature is the existence or the absence of a sharp front of the elastic precursor. The available experimental data (including those obtained by the authors of this paper) indicate that in some rocks the front of the elastic wave is smeared. The latter indicates that, possibly, the material has an anomalous compressibility or strength.

The aim of this paper is to investigate the elastoplastic properties of granite, quartzite, and marble.

EXPERIMENTAL

The elastoplastic parameters were determined using a manganin pressure gage, since this technique permits pressure measurements to be performed directly in the materials under study [1, 2]. The gage was made in the form of a bifilar coil of a manganin wire 0.1 mm in diameter, which then was laminated between the forcers of a press tool to a thickness of ~0.03 mm. The initial resistance of the gage was $R_0 \sim 1.5\ \Omega$ and its diameter was ~5 mm.

The profile of a shock-wave pulse in the substances studied was detected in experiments whose scheme is shown in Fig. 1. As an explosive, we used cylinders of TG 50/50 or TNT 90 120 mm in diameter and 40 mm thick. In order to obtain a marking in the oscillogram, necessary for subsequent treatment of experimental

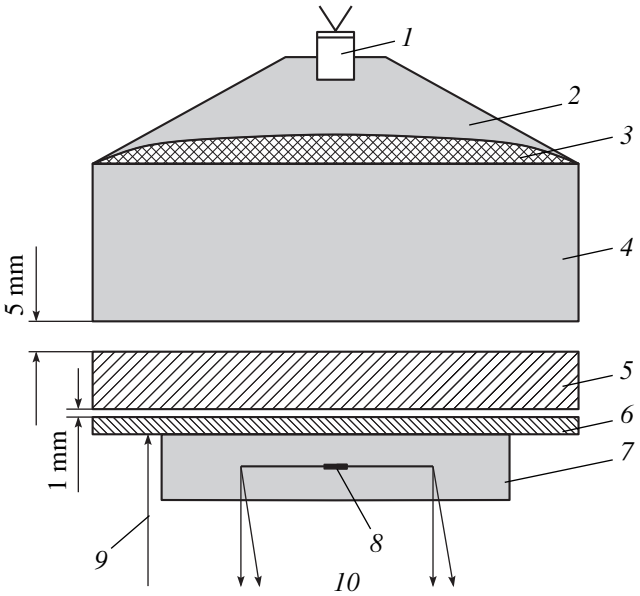

Fig. 1. Schematic of experiments: (*1*) electric detonator; (*2*) plane-wave generator; (*3*) lens of foamed plastic; (*4*) explosive; (*5*) striker; (*6*) screen; (*7*) sample; (*8*) manganin gage; (*9*) electric-contact gage; and (*10*) to oscillographs.

1063-7842/01/4606-0686$21.00

data, an electric contact gage was mounted on the screen. The signals taken from the gage were recorded using an HP54645D (USA) digital oscillograph and an S9-4 (Russia) analog oscillograph. The measurements were performed using the potentiometric method [2].

RESULTS AND DISCUSSION

For illustration, Fig. 2 displays typical oscillograms that were obtained on the S9-4 oscillograph in experiments with marble and quartzite. In order to enhance the time resolution of experimental measurements (to detect the yielding "tooth"), experiments with the use of a quartz pressure transducer were performed as well as with the use of the HP54645D oscillograph. The oscillogram of one of these experiments is given in Fig. 3.

The loading pressure was determined from the experimentally measured magnitude of electrical resistance R of the manganin gage in the compressed state, which was calculated by the formula

$$R = R_0(Z_0 - Z_1 + Z)Z_0^{-1}, \quad (1)$$

where R_0 is the initial resistance of the gage and Z_0, Z_1, and Z are the amplitudes of the deviation of the beam in the oscillograph (Fig. 2a). On going from the resistance ratio R/R_0 to pressure P, dependences of the electrical resistance of manganin on the pressure of the shock loading ($P = f(R/R_0)$ borrowed from [3, 4] were used. The accuracy of measuring pressure was 2–3%.

The experimental results that characterize the elastoplastic parameters of marble are generalized in Table 1. The data for marble listed in Table 1, just as the data for other materials, were calculated by the following formulas:

$$C_1 = \frac{\Delta}{t_1}, \quad D_2' = \frac{\Delta + U_1(t_2 - t_1)}{t_2},$$

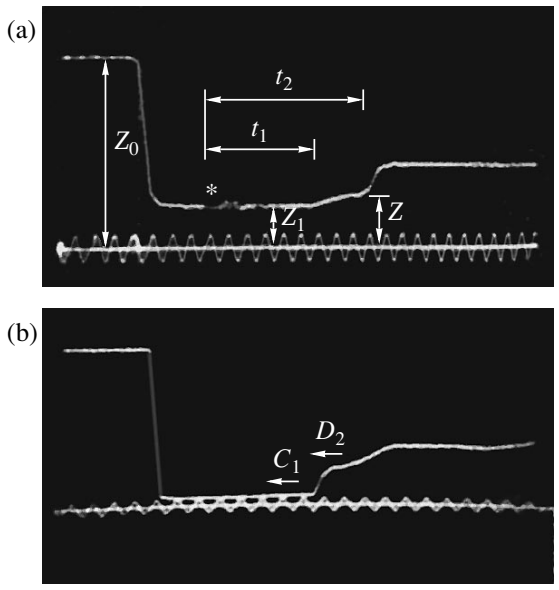

Fig. 2. Typical oscillograms obtained in experiments with marble and quartzite: (a) $\Delta = 3.96$ mm, the loading pressure on the marble sample is 7.36 GPa; asterisk marks the moment at which the shock wave closes the electric contact mounted at the screen–sample boundary; the frequency of the scale sinusoid in the oscillogram is 10 MHz; (b) $\Delta = 15.7$ mm; the loading pressure on the quartzite sample is 10 GPa; the frequency of the scale sinusoid in the oscillogram is 5 MHz.

Table 1. Experimental results of measuring parameters of elastoplastic flow in marble ($\rho_0 = 2.68$ g/cm^3)

No.	Δ, mm	P_1, GPa	C_1, km/s	D_2', km/s	D_2'', km/s	P_2, GPa	t_1, μs	t_2, μs
1	2.00	1.79	8.52	5.07	4.99	7.60	0.24	0.40
2	3.96	1.80	7.04	4.77	4.68	7.36	0.57	0.84
3	4.00	1.70	–	–	–	7.00	–	–
4	5.97	1.64	5.98	4.38	4.28	7.52	1.00	1.38
5	8.10	1.65	–	–	–	6.70	–	–
6	14.03	1.60	5.58	4.36	4.26	10.20	2.50	3.24
7	18.05	1.55	5.61	4.54	4.44	9.76	3.22	4.00
8	24.09	1.48	5.82	4.44	4.34	9.27	4.14	5.46
9	19.40	1.37	–	–	–	6.00	–	–
10	20.00	1.40	–	–	–	6.00	–	–
11	20.00	1.25	–	–	–	5.70	–	–
12	28.70	1.30	–	–	–	4.70	–	–
13	20.00	1.47	–	–	–	–	–	–

Note: The average values of the parameters of elastic ($U_1 = 0.1$ km/s, $\rho_1 = 2.72$ g/cm^3, $\sigma_1 = 1.016$) and plastic ($\rho_2 = 3.14$ g/cm^3, $\sigma_2'' = 1.155$) compression waves did not enter into Table 1.

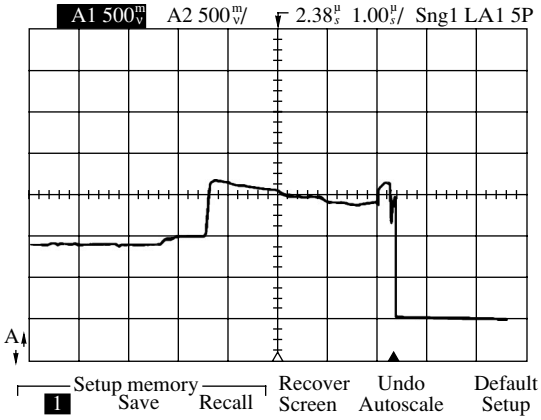

Fig. 3. Oscillogram of the experiment with marble taken using an HP54645-D oscillograph; $\Delta = 8.0$ mm; the loading pressure is 6.98 GPa.

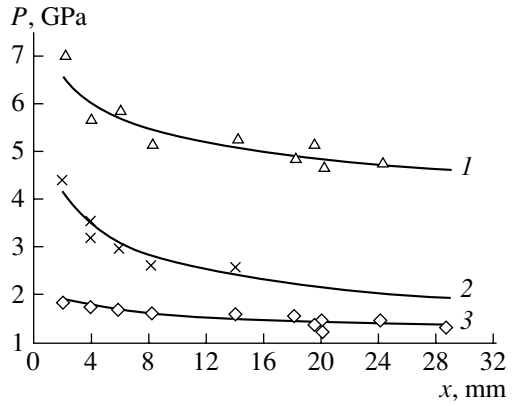

Fig. 4. Damping of the elastic precursor in the rocks studied: (*1*) quartzite; (*2*) granite; and (*3*) marble.

$$U_1 = \frac{P_1}{C_1\rho_0}, \quad D_2'' = D_2' - U_1,$$

$$\sigma_1 = \frac{C_1}{C_1 - U_1}, \quad \sigma_2'' = \frac{D_2''}{D_2'' - (U_2 - U_1)}, \qquad (2)$$

$$\rho_1 = \rho_0\sigma_1, \quad \rho_2 = \rho_1\sigma_2'',$$

where Δ is the sample thickness; t_1 and t_2 are the times of passage of elastic and plastic compression waves from the screen to the manganin gage, respectively; C_1 is the velocity of propagation of the elastic compression wave; P_1 is the pressure in the elastic compression wave; U_1 is the velocity of the substance behind the front of the elastic compression wave; U_2 is the velocity of the substance behind the front of the plastic compression wave; σ_1 is the compression of the substance by the elastic wave; σ_2'' is the compression of the substance by the plastic wave relative to the elastic wave; ρ_0 is the initial density of the substance; ρ_1 is the substance density behind the front of the elastic compression wave; ρ_2 is the density behind the front of the plastic compression wave; and D_2' and D_2'' are the velocities of propagation of the plastic compression wave in the laboratory coordinate system and relative to the moving substance, respectively.

Tables 2 and 3 give the experimental data that characterize the elastoplastic parameters of quartzite and granite, respectively. The experimentally obtained dependences of the amplitudes of elastic precursors on the thickness of the samples of marble, quartzite, and granite are shown in Fig. 4. The above dependences of damping of the amplitudes on the sample thickness $P_1(\chi)$ are described by the formulas $P_1 = 2.0369\chi^{-0.1189}$,

Table 2. Experimental results of measuring parameters of elastoplastic flow in quartzite ($\rho_0 = 2.65$ g/cm^3)

No.	Δ, mm	P_1, GPa	C_1, km/s	D_2', km/s	D_2'', km/s	P_2, GPa
1	4.0	7.1	5.95	–	–	7.6
2	10.0	5.7	–	5.14	4.27	11.0
3	11.0	5.7	–	–	–	11.6
4	11.5	5.9	–	–	–	8.4
5	15.0	5.2	–	–	–	13.8
6	15.7	5.3	5.05	4.65	4.20	10.0
7	20.0	4.9	–	–	–	–
8	25.0	4.8	–	–	–	11.7
9	33.2	5.2	–	–	–	13.0
10	36.3	4.7	–	–	–	11.5

Note: The average values of the parameters of elastic ($U_1 = 0.45$ km/s, $\rho_1 = 2.83$ g/cm^3, $\sigma_1 = 1.063$) and plastic ($U_2 = 1.12$ km/s, $\rho_2 = 3.07$ g/cm^3, $\sigma_2'' = 1.155$) compression waves in quartzite did not enter into Table 2.

Table 3. Experimental results of measuring parameters of elastoplastic flow in granite ($\rho_0 = 2.63$ g/cm^3)

No.	Δ, mm	P_1, GPa	P_2, GPa	t_1, μs
1	9.0	4.4	10.0	1.64
2	15.0	3.6	–	2.73
3	30.0	3.2	–	3.64
4	25.0	3.0	–	4.55
5	31.0	2.6	–	5.64
6	36.0	2.6	–	6.55

$P_1 = 7.206\chi^{-0.13}$, and $P_1 = 5.103\chi^{-0.2848}$ for marble, quartzite, and granite, respectively.

The above thickness dependences of the amplitudes of elastic waves in the rocks studied lead to an obvious conclusion that these amplitudes decrease with the distance passed by an elastic wave in the sample. Naturally, the slopes of the damping curves for various materials are different because of the differences in the physical properties of these materials. It is seen from the oscillograms displayed that the amplitudes of elastic waves in marble and other rocks studied increase in a smooth manner. No yielding "tooth" found in [5, 6] for Fe and LiF is observed in this work. Note that the authors of this paper studied single-crystal samples of LiF (compressed in the ⟨100⟩ direction) and "khilumin" (a ceramic containing 94% Al_2O_3, $\rho_0 = 3.65$ g/cm^3) as control materials and found a smooth character of increasing amplitude of elastic waves without any evidence for yielding a "tooth" in these substances.

CONCLUSIONS

From an analysis of the results obtained, the following conclusions can be made.

(1) The elastic precursor has a diffuse front and its amplitude decreases with increasing distance propagated by the wave in the sample.

(2) No sharp decrease in the amplitude of elastic waves (no yielding "tooth") was revealed for the substances studied in this work.

(3) The results obtained indicate the possible anomalous behavior of some properties of the rocks studied (compressibility, strength) under the conditions of shock-wave compression and suggest the necessity of performing additional investigations, e.g., for studying shear strength of those rocks upon shock loading.

The experimental results obtained can serve as a starting material that can be used for improving existing models of the behavior of solid media under shock-wave compression.

REFERENCES

1. A. N. Dremin and G. I. Kanel', Prikl. Mekh. Tekh. Fiz. **2**, 146 (1976).
2. M. N. Pavlovskiĭ, V. S. Stepanyuk, and V. V. Komissarov, Probl. Prochn., No. 10, 50 (1991).
3. M. N. Pavlovskiĭ and V. V. Komissarov, Zh. Éksp. Teor. Fiz. **83**, 2146 (1982) [Sov. Phys. JETP **56**, 1244 (1982)].
4. M. N. Pavlovskiĭ, V. V. Komissarov, and A. R. Kutsar, Fiz. Goreniya Vzryva **35** (1), 98 (1999).
5. G. E. Duvall, in *The Physics of High Energy Density. Proc. Int. School of Physics "Enrico Fermi"*, Ed. by P. Caldirola and H. Knoepfel (Academic, New York, 1971; Mir, Moscow, 1974).
6. A. G. Ivanov, S. A. Novikov, and V. A. Sinitsyn, Fiz. Tverd. Tela (Leningrad) **5**, 269 (1963) [Sov. Phys. Solid State **5**, 196 (1963)].

Translated by S. Gorin

Technical Physics, Vol. 46, No. 6, 2001, pp. 690–695. Translated from Zhurnal Tekhnicheskoĭ Fiziki, Vol. 71, No. 6, 2001, pp. 45–51.

SOLID-STATE ELECTRONICS

Direct Bonding of Silicon Wafers with the Concurrent Formation of Diffusion Layers

I. V. Grekhov*, L. S. Kostina*, T. S. Argunova*, E. I. Belyakova*, N. M. Shmidt*, K. B. Kostin*, E. D. Kim, and S. Ch. Kim****

** Ioffe Physicotechnical Institute, Russian Academy of Sciences, Politekhnicheskaya ul. 26, St. Petersburg, 194021 Russia*

e-mail: argunava@tania.ioffe.rssi.ru

*** Power Semiconductor Research Laboratory, Korea Electrotechnology Research Institute, P.O. Box 20, Changwon, 641-600 Gyongnam, Republic of Korea*

Received September 12, 2000

Abstract—An original technique for Si–Si direct bonding combined with impurity diffusion in a single process is suggested. A dopant (aluminum) source is located at the interface. The high-temperature treatment of the polished wafers in an oxidizing atmosphere results in the diffusion of Al atoms and the formation of a *p–n* junction in *n*-silicon. The presence of aluminum is shown to improve the continuity of the interface. Results obtained are explained within a model whereby the initial contact between the hydrophilic silicon surfaces in a water solution of aluminum nitrate $Al(NO_3)_3$ serves to increase the bonding area of the wafers at room temperature due to the interaction of Al–OH groups with water molecules adsorbed on the surfaces of the wafers. © *2001 MAIK "Nauka/Interperiodica".*

INTRODUCTION

In the production of power semiconductor devices, deep diffusion of doping impurities is replaced by direct bonding (DB) of wafers with different conduction type and initial impurity concentrations. However, to fabricate directly bonded multilayer structures with *p–n* junctions, impurities are usually introduced into one or both wafers before bonding. As a result, the surface quality and the elastic stress distribution may change to the point where they no longer meet the DB requirements.

In spite of the considerable recent progress in direct bonding of different materials, the obtaining of the continuous large-area interface is still a challenge. This problem, including the discontinuity sources (voids) and conditions for their healing, the effect of the surface roughness on the bonding quality, etc., has been considered in detail (see, e.g., [1–3] and Refs. therein). It was ascertained [4] that the polished surface of a silicon wafer is actually wavy and that the complex relief of the surface can be represented as a superposition of sinusoids with different periods and amplitudes. Nevertheless, during bonding, the surfaces come into close contact even at room temperature (RT). The greater the RT contact area, the higher its surface energy. The contact area grows through elastic deformation of the wafers, which starts at RT and builds up with temperature.

In order to minimize the effect of surface morphology on the structure quality of the interface, we proposed a modified DB process [5–7] where a regular mesoscopic relief is formed on one of the surfaces to be bonded by means of photolithography. It was demonstrated that the artificial relief at the interface assists in reducing in elastic deformation at the contact of nonplanar surfaces and, thus, improves the quality of the interface.

In this paper, we pursue our discussion about conditions ensuring the reliable homogeneous interface. The objects under study are DB structures produced by the original technology, which combines bonding and aluminum diffusion from a source located directly at the interface in a single production cycle. A relation between physicochemical processes at the interface and the actual structure of the surfaces being bonded is considered. A mechanism behind the formation of the continuous interface over the surface of the wafers in the presence of dopant atoms is discussed. The *I–V* characteristic of a p^+–*n* diode obtained by direct bonding with the concurrent diffusion of aluminum is presented.

EXPERIMENTAL

We studied *n–n* and p^+–*n* structures produced by the DB technology. (111)Si wafers 0.3 to 0.5 mm thick and 40–60 mm in diameter were cut from floating-zone *n*-silicon with a resistivity of 20 Ω cm and from Czochralski-grown *p*-silicon with a resistivity of 0.005 Ω cm. The surface profile was determined with an optical profilometer. It was found to be wavy with a typical amplitude ranging from 30 to 60 Å and a period of approxi-

mately 200 μm. In order to reduce the near-interface elastic deformation due to the long-period surface roughness, an artificial relief (a network of orthogonal grooves [5]) was photolithographically formed on the surface of one of the wafers. The grooves were 50 μm wide and 0.3–0.5 μm deep. The distance between the sidewalls of the neighboring grooves was 200 μm. Before bonding, the mirror-polished wafers were subjected to standard rinsing and hydrophilization and then were rinsed in deionized water with a resistivity of 18 MΩ cm.

The wafers were brought in contact in (1) deionized water and (2) a water solution of aluminum nitrate $Al(NO_3)_3$ (0.5–1 wt %), which served as a source of aluminum diffusion during the high-temperature processing of the wafers. They were annealed in air at 95°C for 5 h and at 1250°C for 5 h. The wafers were brought in contact without crystallographic matching. The aluminum profile was recorded by an SRM-3 computerized setup.

We studied the structure of the Si–Si compositions by means of X-ray topography (XRT) [8]. Of all the nondestructive techniques used to test the interface continuity, this method proves to be the most sensitive: its resolution is ≈10 μm. Both the reflection and transmission projection topography methods were employed. Also, the interface quality after bonding was investigated by examining the cross sections of the samples with a scanning electron microscope (SEM).

To study the defect distribution across the depth, the polished taper sections of the samples of both types were etched in an H_2O : HF (anhydrous) : CrO_3 = 1 : 0.4 : 0.2 etchant; then, etch pits were counted.

EXPERIMENTAL RESULTS

Diffusion of Aluminum

An experimental profile of Al in the *n*/*n* structure after bonding is shown in Fig. 1. Between the two *n*-type wafers, an ≈30-μm-thick *p*-type diffusion layer with a surface concentration at the interface of $\approx 5 \times 10^{16}$ cm^{-3} is seen to form. This result indicates that the diffusion of aluminum into a polished silicon wafer during open-tube thermal treatment in an oxidizing atmosphere is a possibility. Note that the diffusant source was located at the interface between the wafers bonded.

Structure Quality Analysis

XRT images of the Si/Si structures include two basic components: (1) the contrast from the regular network of artificial voids the voids result from crystal plane bending at the interface) [5] and (2) the smooth increase and decrease in the reflected intensity due to compression/extension regions existing near the interface and to the local misorientation of the crystal lattice. The type-1 contrast is typical of the contact

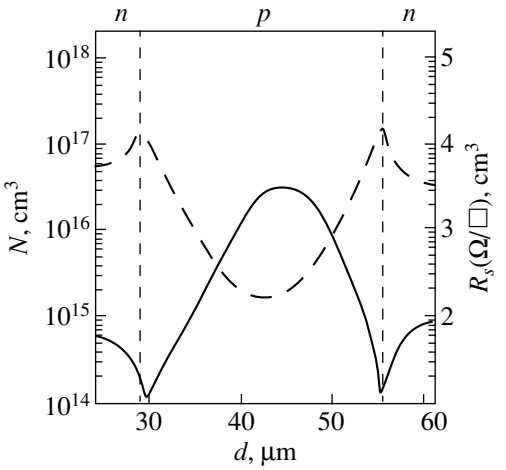

Fig. 1. Profiles of the Al concentration (solid curve) and sheet resistance (dashed curve) across the Si/Si structures. The abscissa is the distance from the interface.

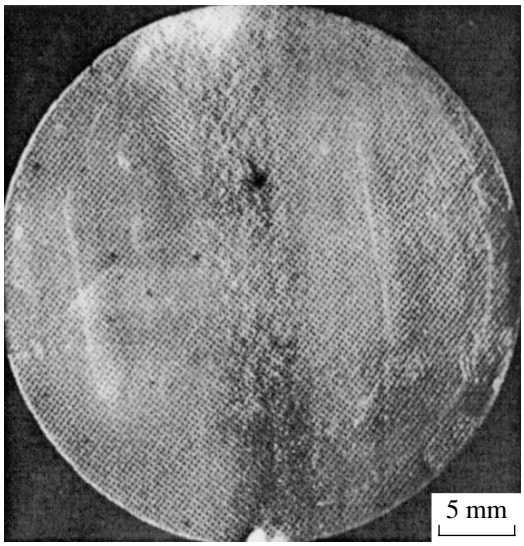

Fig. 2. X-ray diffraction topogram (Lang method) of the entire area of the DB Si/Si structure with the Al diffusion. (202) reflection, MoK_α radiation.

between a smooth surface and an artificial relief. The smoothly varying contrast features any bonded structure. The latter is due to the fact that the bonding of imperfectly planar surfaces always generates elastic strains at the interface [4]. This contrast is not observed where the wafers do not adhere to each other. This XR property is used for the detection of unboned regions or voids.

According to the XRT data, the Si/Si structures that were bonded in the 0.5–1% solution of $Al(NO_3)_3$ exhibit high structure quality. A typical X-ray topogram that demonstrates the continuity of the interface is shows in Fig. 2. The comparative analysis of the XRT data obtained for many samples bonded in the $Al(NO_3)_3$ solution and in the deionized water indicates that the

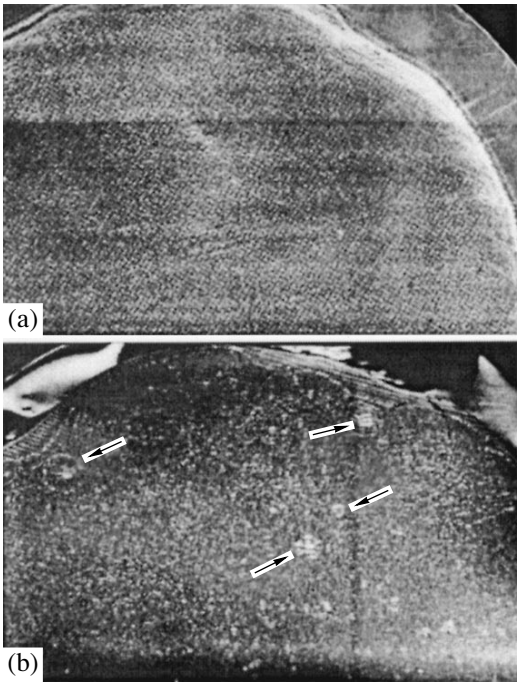

Fig. 3. X-ray diffraction topogram (Lang method) of the structures bonded (a) in the $Al(NO_3)_3$ solution and (b) in H_2O. ($\bar{2}02$) Reflection, MoK_α radiation.

interface continuity is considerably better in the former case. From the topograms in Figs. 3 and 4, we can compare the degree of interface continuity in the compositions studied. An example of good bonding with the Al diffusion is shown in Fig. 3a. Another sample (Fig. 3b, bonding in H_2O) contains voids, some of which are indicated by arrows. The enlarged view of a defect region in the latter sample and the same image after computer processing are seen in Figs. 4a and 4b, respectively. The enhanced contrast due to image filtering allowed us to quantitatively estimate the bonded fraction of the wafer area. To do this, we imposed a fine-mesh network on the image filtered (Fig. 4b) and counted the number of meshes filled by the images of bonded and unbonded regions.

Bonded fraction measured: $S_{bond} = (1 - S_{void}/S_{sample})$, %

	Interval of S_{bond}, %	Number of counts per interval
Bonding in H_2O	80–85	7
	85–90	14
	90–95	19
	95–100	16
Bonding in $Al(NO_3)_3$ solution	88–92	5
	92–96	8
	96–100	24

The histograms in Figs. 5a and 5b demonstrate the bonded fraction calculated for 56 samples bonded in the water and for 37 samples bonded in the nitrate solution, respectively. The data used for constructing the histograms are listed in the table. As follows from the charts, bonding in the solution gives the nearly 100% continuity of the interface, whereas bonding in the water provides a continuity of about 92%.

The X-ray topograms indicate that, for several samples bonded in the water, the varying contrast is lower than for those with the Al diffusion. This fact can be attributed to the higher strength of the latter samples, because increased elastic strains, leading to an increase in the contrast, mean stronger bonds between atoms of the contacting wafers with the imperfectly planar surfaces [4].

According to the SEM data, the interface in the structures that were brought into contact in the water, contains irregularly (voids) and regularly (grooves) distributed microcavities, whereas the samples bonded in the $Al(NO_3)_3$ solution are almost free of them (Fig. 6). The etch pit density on the polished taper section in the vicinity of the continuous interface is roughly equal for both types of the structures and does not exceed 10^4 cm^{-2}.

DISCUSSION

The results presented can be explained within the model for the bonding of hydrophilic surfaces [1]. The hydrophilic surfaces of natural and thermal oxides of silicon are known to incorporate Si–OH silanol groups, which form hydrogen bonds with OH groups of water adsorbed on the surface. Being brought in contact at room temperature, the wafers adhere via the formation of hydrogen-bonded OH chains (Fig. 7a) [9]:

$$SiOH : (OH_2)_2(OH_2)_2 : HOSi.$$

The chains may be as long as 7 Å; that is, bonding takes place over the surface area within which the microroughness is no more than 3.5 Å. A temperature increase from 300 to 700°C gives rise to polymerization: the formation of Si–O–Si siloxane bonds. Water molecules leave the interface, and the gap between the wafers narrows to 1.6 Å. On further heating of the wafers to 1000°C and above, the siloxane bonds are replaced by covalent Si–Si ones. The remaining microvoids are filled due to the diffusion of atoms along the interface and the viscous flow of the oxide.

As follows from our experimental data, the formation of the continuous interface is not a necessary result of bonding of the hydrophilic silicon surfaces. This does not follow from the physicochemical model for the bonding of perfectly planar and smooth surfaces and can be explained only if the real surface structure is taken into account. It was shown [1] that, for wafers whose surfaces have a natural sinusoidal relief with a period R and an amplitude h, the formation of the con-

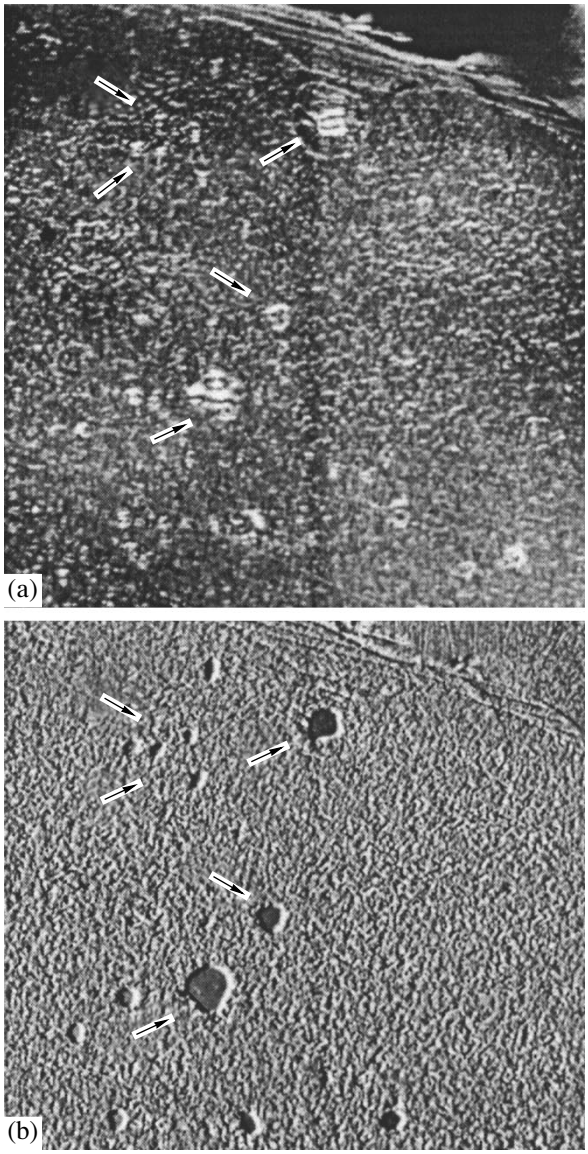

Fig. 4. (a) Enlarged view of the defect region of the sample shown in Fig. 3b and (b) the same image after computer processing.

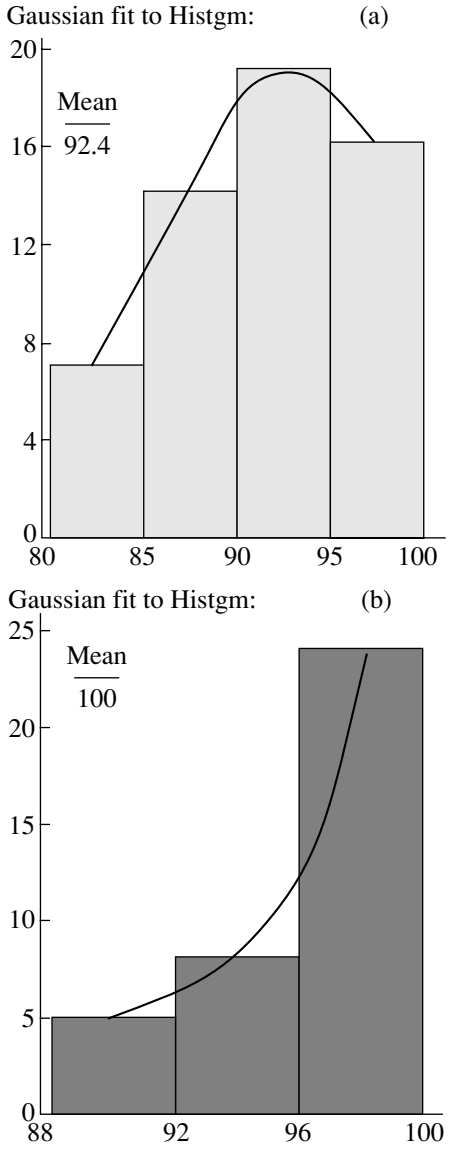

Fig. 5. Histograms of the bonded fraction $S_{bond} = (1 - S_{void}/S_{sample})\%$ for the samples obtained by bonding of Si wafers in (a) H_2O and (b) $Al(NO_3)_3$.

tinuous interface is possible if $h < 3.6\ (R\gamma/E')^{1/2}$ for $R < 2t_w$ (the latter inequality meets our experimental conditions). Here, t_w is the wafer thickness, E' is the effective elastic constant of the material, and γ is the surface energy. At room temperature, γ grows with the amount of surface atoms that ensure the initial contact. An increase in γ with temperature actually stems from the fact that the silanol bonds give way to siloxane bonds, which are considerably shorter and, hence, have a shorter range. Thus the strengthening of the structure bonded and the formation of the continuous interface can take place only at the sites of the initial RT contact; i.e., the area of reliable bonding is almost completely defined by the range of the initial adhesive force.

The high continuity of the interface between the wafers dipped into the water solution of aluminium nitrate $Al(OH_3)_3$ can, in our opinion, be explained by an increase in the initial contact area. In fact, due to the

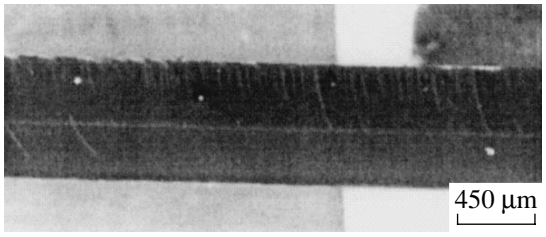

Fig. 6. SEM image of the Si/Si sample obtained by bonding of the wafers in the $Al(NO_3)_3$ solution.

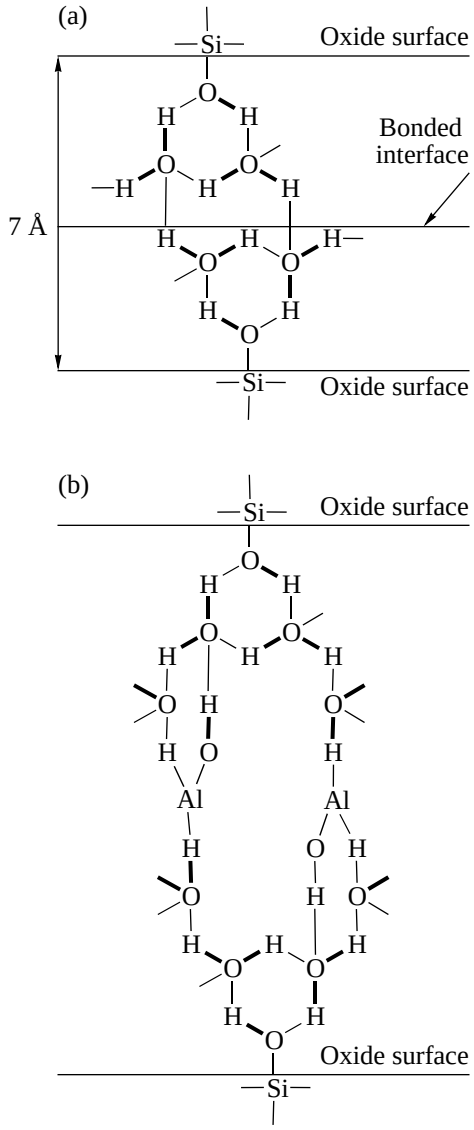

Fig. 7. Model of the initial (RT) stage of direct bonding of the hydrophilic silicon surfaces in (a) H_2O and (b) $Al(NO_3)_3$.

Al–OH groups embedded in the OH chains (Fig. 7b), the chains grow longer, thus enabling initial adhesion to take place over a greater area than for the traditional bonding process (Fig. 7a).

The formation of the continuous interface is thought to proceed as follows. Aluminum nitrate dissociates in the water solution: $Al(NO_3)_3 \longrightarrow Al^{3+} + 3(NO_3)$, and the Al^{3+} ions interact with the water to form aluminum hydroxide $Al(OH)_3$. Then, the RT direct bonding process goes according to Fig. 7b.

As the temperature increases, the hydrogen bonds are replaced by stronger ones:

$$SiOH : (OH_2)_2 : 2Al(OH)_3 : (OH_2)_2OHSi$$

$$\longrightarrow Si-O-\underset{\displaystyle O}{\overset{\displaystyle Al-Al}{\diagdown\ \diagup}}-O-Si + 7H_2O.$$

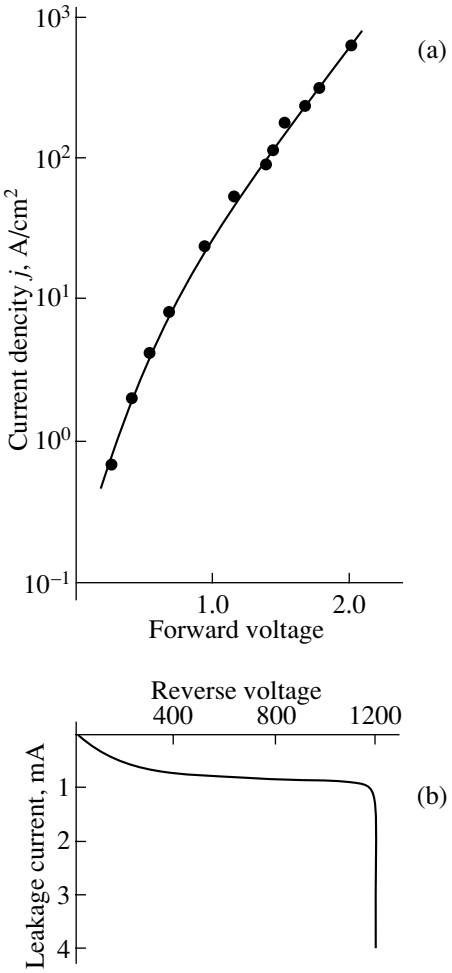

Fig. 8. (a) Forward and (b) reverse branches of the *I–V* characteristic of the p^+–*n* DB diode with an active area of ≈12 cm^2.

Subsequently, the Al atoms interact with the natural oxide [10],

$$(4/3)Al + SiO_2 = (2/3)Al_2O_3 + Si$$

to produce additional free silicon atoms, which heal the microvoids through the diffusion mechanism at the final stage of bonding. Moreover, since the Al–Si bond energy is higher than that of Al–Al bonds, the incorporation of Al atoms into the silicon lattice stimulates Si self-diffusion and facilitates the filling of the microviods.

In the course of the high-temperature treatment, Al diffuses from the interface into the *n*-type silicon and forms a *p–n* junction. Shown in Fig. 8 is the *I–V* characteristic of the p^+–*n* diode obtained by bonding in the 0.5% water solution of $Al(NO_3)_3$. Since the junction is deep, the electric performance of the structure does not depend on the interface quality: the *I–V* curve is typical of a standard diffusion junction, and the voltage drop in the forward direction is ≈2 V at the current density ≈200 A/cm^2. The breakdown voltage of the diode

approximates 1200 V (Fig. 8b), which corresponds to the avalanche breakdown voltage in silicon with the resistivity given (20 Ω cm).

CONCLUSION

We have demonstrated that the high-temperature treatment of silicon wafers brought in contact in an oxidizing atmosphere makes the diffusion of Al atoms from a source at the interface into the polished silicon surface feasible. Furthermore, we argue that aluminum present between the wafers being bonded improves the quality of the interface. It it assumed that the bonding of the wafers in a water solution of aluminium nitrate $Al(NO_3)_3$ may increase the area of initial adhesion, since Al–OH groups between the adsorbed water molecules are built into the chains responsible for bonding the wafers. Finally, it is believed that the formation of diffusion layers combined with the direct bonding of silicon wafers in a single process opens vast opportunities for creating new semiconductor devices

ACKNOWLEDGMENTS

This study was supported by the Russian Foundation for Basic Research, grant no. 98-02-18250.

REFERENCES

1. Q.-Y. Tong and Ü. Gösele, *Semiconductor Wafer Bonding: Science and Technology* (Wiley, New York, 1999).
2. S. J. Bengtsson, Electron. Mater. **21**, 841 (1992).
3. A. Plößl and G. Kräuter, Mater. Sci. Eng., R **25**, 1 (1999).
4. W. P. Maszara, B.-L. Jiang, A. Yamada, *et al.*, J. Appl. Phys. **69**, 257 (1991).
5. T. S. Argunova, R. F. Vitman, I. V. Grekhov, *et al.*, Fiz. Tverd. Tela (St. Petersburg) **41**, 1953 (1999) [Phys. Solid State **41**, 1790 (1999)].
6. T. S. Argunova, I. V. Grekhov, L. S. Kostina, *et al.*, Jpn. J. Appl. Phys. Part 1 **37** (12A), 62 (1998).
7. I. V. Grekhov, L. S. Berman, T. S. Argunova, *et al.*, Pis'ma Zh. Tekh. Fiz. **22** (12), 14 (1996) [Tech. Phys. Lett. **22**, 956 (1996)].
8. D. K. Bowen and B. K. Tanner, *High Resolution X-ray Diffractometry and Topography* (Taylor and Francis, Bristol, 1998).
9. R. Stengl, T. Tan, and U. Gösele, Jpn. J. Appl. Phys. **28**, 1735 (1989).
10. M. Ohring, *The Material Science and Thin Films* (Academic, New York, 1991).

Translated by A. Sidorova-Biryukova

Technical Physics, Vol. 46, No. 6, 2001, pp. 696–699. Translated from Zhurnal Tekhnicheskoĭ Fiziki, Vol. 71, No. 6, 2001, pp. 52–55.

On the Transmission of X-ray Beams through Rough Near-Surface Channels

T. A. Bobrova and L. I. Ognev

Russian Research Centre Kurchatov Institute, pl. Kurchatova 1, Moscow, 123182 Russia

e-mail: ognev@nfi.kiae.ru

Received July 31, 2000

Abstract—The transmission of X-rays through a rough narrow channel in a dielectric material is investigated by numerical simulation with regard for diffraction and loss in coherence. It is found that the transmission factor may sharply decrease in channels with periodic deformations. The effect of roughness on the transmission is explained in terms of the statistical theory of X-ray scattering in a rough boundary layer. The mode damping factors β are related to the channel width d as $1/d^3$ and are proportional to the roughness amplitude. The explanation for the anomalous propagation through thin Cr/C/Cr channels is given. © *2001 MAIK "Nauka/Interperiodica".*

The effect of total external reflection is exploited in laser physics where the beam is captured into a rough narrow dielectric channel [1], submicron diffraction analysis for obtaining thin X-ray beams [2, 3], and other applications [4, 5].

In this paper, we study the role of diffraction, which can be essential for narrow beams, particularly if the surface roughness is considerable. Scattering by rough surfaces calls for a specific approach, since weak-perturbation methods are inapplicable [6].

As a rule, X-ray scattering by rough surfaces is investigated within the Andronov–Leontovich approximation [7]. The case under study is beyond its scope, because the diffraction spreading of the beam results in losses even at the zero grazing angle in reference to the channel surface. Our approach employs the complex refractive index, which takes into consideration the loss in coherence at incoherent scattering [8], and is based on the Tatarskiĭ statistical method [9, 10]. The permittivity of the boundary layer at an arbitrary boundary $x = \xi(z)$ represented as $\varepsilon(x, z) = \varepsilon_1 + (\varepsilon_0 - \varepsilon_1)H(x - \xi(z))$, where ε_1 and ε_0 are the permittivities of the medium and air, respectively; z and x are the longitudinal and transverse coordinates of the rough channel; and $H(x)$ is a step function. It is assumed [1, 4] that, in the case of grazing angles, the number of modes excited is small. We neglect large-angle scattering:

$$\partial^2 A(x, z)/\partial z^2 \ll k\partial A(x, y, z)/\partial z,$$

if the beam width is small,

$$\partial^2 A(x, y, z)/\partial z^2 \ll \partial^2 A(x, y, z)/\partial x^2.$$

With these assumptions, the propagation of an X-ray mode can be described by the parabolic equation for the amplitude of the electric vector $A(x, z)$ [12]:

$$2ik\frac{\partial A}{\partial z} = \Delta_\perp A + k^2\frac{\varepsilon - \varepsilon_0}{\varepsilon_0}A,$$

$$A(x, z = 0) = A_0(x),$$

where z and x are the longitudinal and transverse coordinates of the channel (we consider the case of two-dimensional channels), $k = \sqrt{\varepsilon_0}\frac{\omega}{c}$, and $\Delta_\perp$ is the Laplacian operator.

In this equation, ε_0 is the permittivity of the channel and ε_1 is that of the "walls." This method can readily be extended to the case of a three-dimensional capillary.

Scattering by a rough surface was simulated by integrating Eq. (1) for the energy $E = 10$ keV, channel width $d = 0.5$ μm, $\sigma = 400$ Å, and the roughness correlation length $z_{corr} = 5$ μm. The results averaged over 40 realizations are shown in Fig. 1. Both the total beam intensity r_{tot} and the incoherent part r_{inc} are normalized to the input intensity r_i, $= \int_{-\infty}^{\infty} I_i(x)dx / \int_{-d/2}^{d/2} I_0(x)dx$, where r_i corresponds either r_{tot} or r_{inc}. The angles of incidence are $\vartheta = 0$, 3×10^{-4}, and 6×10^{-4} rad. It is seen that the beam intensity in the narrow channel quickly decreases because of the loss in coherence.

Assuming that $A(x, z)$ is changed within the roughness correlation length z_{corr} very slightly, we can take advantage of the correlator property

$$\langle \delta\varepsilon'(x, z)A(x, z)\rangle = \langle A(x, z)\rangle(-ik/4) \times \int_{-\infty}^{\infty} \langle \delta\varepsilon'(x, z)\delta\varepsilon(x, z')\rangle dz', \quad (1)$$

1063-7842/01/4606-0696$21.00

which holds for a δ-correlated fluctuating medium [10]. The coherent part of the amplitude $A(x, z)$ is calculated from the statistically averaged parabolic equation [8, 10]

$$2ik\partial\langle A(x,z)\rangle/\partial z - \Delta_\perp\langle A(x,z)\rangle - k^2\chi(x)\langle A(x,z)\rangle - ik^2W(x)\langle A(x,z)\rangle = 0, \quad (2)$$
$$\langle A(x, z=0)\rangle = A_0(x),$$

where $\chi(x, z) = (\langle\varepsilon(x)\rangle - \varepsilon_0)/\varepsilon_0$ and angle brackets mean averaging.

The term with $\chi(x)$ in Eq. (2) corresponds to absorption by the channel walls; and that with $W(x)$, to incoherent scattering:

$$W(x) = (-ik/4)\int_{-\infty}^{\infty}\langle\delta\varepsilon'(x,z)\delta\varepsilon'(x,z')\rangle dz'$$
$$= -\frac{k}{4}\frac{(\varepsilon_0-\varepsilon_1)^2}{\pi(\varepsilon_0)^2}\int_{-\infty}^{+\infty}dz'\int_{-\infty}^{x/\sigma}\exp(-\xi^2)d\xi \quad (3)$$
$$\times\int_{x/\sigma}^{\frac{x/\sigma - R(z')\xi}{(1-R^2(z'))^{1/2}}}\exp(-\eta^2)d\eta,$$

where $\delta\varepsilon'(x, z) = (\varepsilon(x, z) - \langle\varepsilon(x)\rangle)/\varepsilon_0$ is the coefficient of autocorrelation and σ is the variance of the distribution of $\xi(z)$.

It can be shown that, in the middle of the boundary layer, which lies between $x = 0$ and $x = d$, the value of $W(x)$ is independent of σ and is almost proportional to the roughness correlation length z_{corr}.

The wave amplitude can be represented as a mode expansion or an expansion in eigenfunctions $\varphi_j(x)$ that are the solutions of the equations

$$\Delta_\perp\varphi_j(x) = k[2k_{jz} - k\mathrm{Re}(\chi(x))]\varphi_j(x).$$

Thus, the attenuation coefficients are found as the overlap integrals $\beta_l = -(k/2)\int\varphi_l^*(x)[\mathrm{Im}(\chi(x)) + W(x)]\varphi_l(x)dx$. Width W is defined, for the most part, by the surface roughness; therefore, the coefficients of lower order mode attenuation due to incoherent scattering are proportional to σ:

$$\beta_{scat} \sim k^2(\varepsilon_0-\varepsilon_1)^2\sigma\int_{-\infty}^{\infty}dz'\int_{-\infty}^{0}\exp(-\xi^2/2)d\xi$$
$$\times\int_{0}^{\frac{-R(z')\xi}{(1-R^2(z'))^{1/2}}}\exp(-\eta^2/2)d\eta.$$

That the intensity loss is proportional to the channel roughness at ultrasmall grazing angles has also been found by the direct numerical integration of the random-boundary parabolic equation (see [11] and Fig. 5 therein).

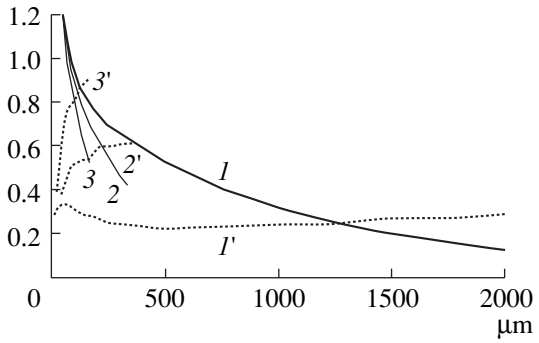

Fig. 1. Variation of the total integral normalized intensity r_{tot} and its relative incoherent part r_{inc}/r_{tot} for different angles of incidence ϑ. (*1*) r_{tot}, ϑ = 0; (*1'*) r_{inc}/r_{tot}, ϑ = 0; (*2*) r_{tot}, $\vartheta = \vartheta_F/10$; (*2'*) r_{inc}/r_{tot}, $\vartheta = \vartheta_F/10$; (*3*) r_{tot}, $\vartheta = \vartheta_F/5$; and (*3'*) r_{inc}/r_{tot}, $\vartheta = \vartheta_F/5$.

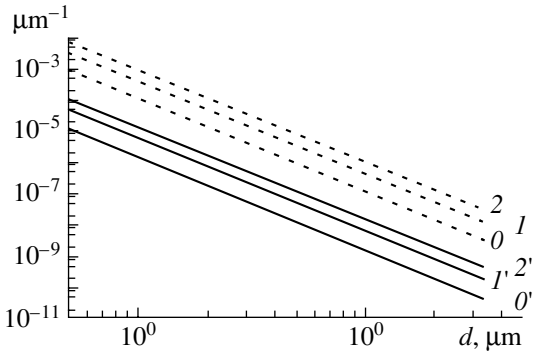

Fig. 2. Attenuation coefficients for the 1-keV X-ray beam passing in the gap between silicon wafers vs. gap width d for modes 0, 1, and 2 at σ = 400 Å and z_{corr} = 5 μm. Dotted lines denote the attenuation coefficient β_{scat} due to scattering, and solid curves refer to the attenuation coefficient β_{abs} due to absorption.

For a 1-keV beam, the attenuation coefficients vs. channel width are shown in Fig. 2 for three lowest modes. It is seen that $\beta \sim 1/d^3$. Thus, as the beam width increases, the diffraction effects decay as $\sim\lambda/d^2$ (where λ is the wavelength) and the portion of the beam that interacts with the surface decreases as $\sim\sigma/d$. With lead used in place of silicon, the attenuation coefficient grows by a factor of 1.5. With a decrease in the energy E, the coefficient β grows faster than $\sim 1/E$, because the effect of diffraction becomes considerable and the optical density of the channel walls increases.

Channeling in a thin layer of a low-density material where the layer is sandwiched in metal layers seems to be promising for obtaining submicron beams of hard X-rays [3]. In experiments with a carbon film (d = 1620 Å) between chromium layers (the Cr/C/Cr chan-

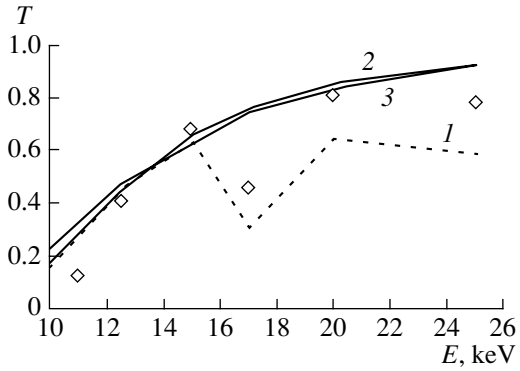

Fig. 3. Transmission factor of mode 0 vs. radiant energy E. Deformation amplitude a = 120 Å; the period Λ = (*1*) 100, (*2*) 500, and (*3*) 1000 μm; and σ = 0. ◇, Data points [2].

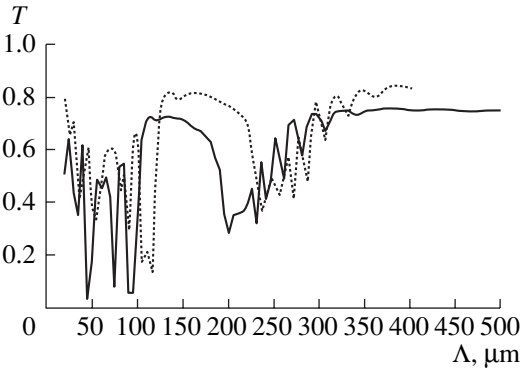

Fig. 4. Transmission factor of mode 0 vs. deformation period. σ = 0, L = 3 mm; solid and dotted lines refer to E = 17 and 20 keV, respectively.

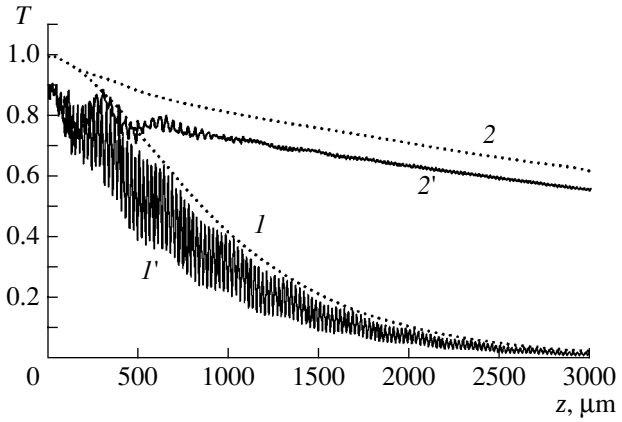

Fig. 5. Variation of the total beam intensity (curves *1*, *2*) and the intensity of fundamental mode 0 (curves *1*', *2*'). E = 17 keV, d = 1620 Å, σ = 0, L = 3 mm, a = 120 Å, and Λ = (*1*, *1*') 45 and (*2*, *2*') 40 μm.

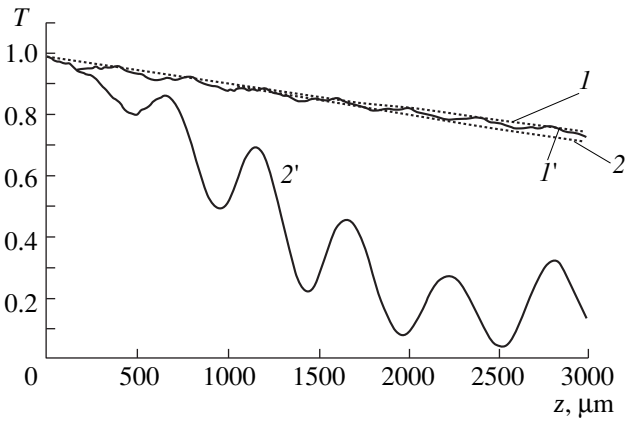

Fig. 6. The same as in Fig. 5 for the undeformed channel (curves *1*, *1*') and under deformations with period Λ = 1000 μm (curves *2*, *2*').

nel length L = 3 mm) [2], the transmission of mode *0* depended on the beam energy nonmonotonically (Fig. 3, ◇). It was assumed [2] that the interface roughness was no more than 10 Å.

The transmission of modes *0* and *1* vs. roughness amplitude was studied by the direct numerical simulation of X-ray beam propagation with the use of Eq. (1). If the roughness is taken into account, the transmission factor of the fundamental mode with E = 17 keV declines by 1.3% for σ = 10 Å and by 5% for σ = 20 Å. This, however, cannot explain a dip in the experimental curve (Fig. 3) even at much worse interface properties if the linear rise in the attenuation coefficient with the roughness amplitude is taken into consideration.

To explain the anomaly in the transmission of the 17-keV fundamental mode through the Cr/C/Cr channel [2], we assumed the presence of periodical disturbances (deformations) of the channel; the relevant results are shown in Fig. 3.

If the roughness is neglected (as noted above, its effect is insignificant), the transmission factor at E = 17 keV and a = 120 Å depends on the deformation period Λ as shown in Fig. 4. There is a number of resonances in the range of short Λ. The results shown in Figs. 3 and 4 are similar to the complicated effects of the radical modification of the wave function of channeled electrons in superlattices [13].

As the beam passes through the Cr/C/Cr channel, its total intensity and the intensity of the fundamental mode vary as shown in Figs. 5 and 6 for different deformation periods Λ. The initial conditions (at the entrance into the channel) correspond to the fundamental mode *0*. For small-scale deformations with the period close to that of oscillations of the fundamental mode amplitude, the transmission factor T depends on whether the deformation period Λ coincides with the period (or a harmonic of the period) of the oscillations in the undeformed channel Fig. 5 (curves *1* and *1*' for Λ = 45 μm) or not Fig. 5, curves *2* and *2*' for Λ = 40 μm. The resonance interaction results in the strong absorption of the beam.

At large-scale deformations ($\Lambda \geq 400$ μm), the total intensity drops in much the same way as in the undeformed channel (cf. curves *1* and *2* in Fig. 6). However, the deformations result in oscillating energy transfer from the fundamental (zero) mode (Fig. 6, curve *2*') to the lowest (*1*, *2*, etc.) modes. This causes the broadening of the angular spectrum of the beam at the exit from the channel.

Thus, the dip in the transmission curve at the energy $E = 17$ keV (Fig. 3) [2] can be explained by periodic disturbances in the Cr/C/Cr layer and by the interference between the resulting higher wave modes. This leads to the attenuation of the beam.

The results obtained provide fresh in sight into experiments with a "slitless X-ray collimator" [14, 15]. From data for the angular separation between interference peaks in a transmitted beam (with regard for diffraction), the gap between the two polished plates is approximately 10 μm [11] rather than 1 μm, as follows from [15] in the geometric optics approximation. At the inclined incidence of the beam, higher transverse modes are excited; these modes give rise to many peaks in the transmitted beam. At the same time, if unpolished areas are left on the plates, the intensity of the emerging beam does not depend on the inclination at the entrance due to the strong absorption of the higher transverse modes with the lowest symmetric mode retained.

Experimentally, this effect can be also measured shows up as a decrease in the angular width of the transmitted beam down to the diffraction value λ/d. The resulting angle is much less than the angle of total external reflection θ_F. The effective narrowing of the angle at which X-ray radiation is captured into the channel can improve the angular discrimination of X-ray detectors.

REFERENCES

1. S. V. Kukhlevsky, G. Lubkovics, K. Negrea, and L. Kozma, Pure Appl. Opt. **6**, 97 (1997).
2. W. Jark, S. Di Fonzo, G. Soullie, *et al.*, J. Alloys Compd. **286**, 9 (1999).
3. C. Riekel, Rep. Prog. Phys. **63**, 232 (2000).
4. V. L. Kantsyrev, R. Bruch, M. Bailey, and A. Shlyaptseva, Appl. Phys. Lett. **66**, 3567 (1995).
5. V. K. Egorov, A. P. Zuev, and B. A. Malyukov, Izv. Vyssh. Uchebn. Zaved., Tsvetn. Metall., No. 5, 54 (1997).
6. S. S. Fanchenko and A. A. Nefedov, Phys. Status Solidi B **212/1**, R3 (1999).
7. A. V. Vinogradov, N. N. Zorev, I. V. Kozhevnikov, and I. G. Yakushkin, Zh. Éksp. Teor. Fiz. **89**, 2124 (1985) [Sov. Phys. JETP **62**, 1225 (1985)].
8. L. I. Ognev, in *Proceedings of the XXVII International Conference on Physics of Interaction between Charged Particles and Crystals, Moscow, 1997*, p. 76.
9. V. Holý and K. T. Gabrielyan, Phys. Status Solidi B **140**, 39 (1987).
10. L. I. Ognev, Zh. Tekh. Fiz. **64** (5), 78 (1994) [Tech. Phys. **39**, 499 (1994)].
11. T. A. Bobrova and L. I. Ognev, Preprint IAÉ-6051/11 (Kurchatov Institute of Atomic Energy, Moscow, 1997).
12. T. A. Bobrova and L. I. Ognev, Pis'ma Zh. Éksp. Teor. Fiz. **69**, 686 (1999) [JETP Lett. **69**, 734 (1999)].
13. T. A. Bobrova and L. I. Ognev, Zh. Tekh. Fiz. **69** (2), 32 (1999) [Tech. Phys. **44**, 161 (1999)].
14. T. A. Mingazin, V. I. Zelenov, and V. N. Leĭkin, Prib. Tekh. Éksp., No. 1, 229 (1981).
15. V. N. Leĭkin, T. A. Mingazin, and V. I. Zelenov, Prib. Tekh. Éksp., No. 6, 33 (1984).

Translated by B. Malyukov

Technical Physics, Vol. 46, No. 6, 2001, pp. 700–703. Translated from Zhurnal Tekhnicheskoĭ Fiziki, Vol. 71, No. 6, 2001, pp. 56–59.

OPTICS, QUANTUM ELECTRONICS

Polarization Optogalvanic Effect in Sodium–Helium Plasma

S. P. Dmitriev, N. A. Dovator, R. A. Zhitnikov, and V. A. Kartoshkin

Ioffe Physicotechnical Institute, Russian Academy of Sciences, Politekhnicheskaya ul. 26, St. Petersburg, 194021 Russia

e-mail: sergei.dmitriev@pop.ioffe.rssi.ru

Received August 8, 2000

Abstract—Experiments on the change in the electric conductivity of a Na–He gas-discharge plasma irradiated by both circularly polarized helium lamp emission and polarization-modulated laser radiation exciting resonant transitions of Na atoms are described. © *2001 MAIK "Nauka/Interperiodica".*

In recent papers [1–3], experiments on the laser optical orientation of sodium atoms in a gas discharge excited in a sodium vapor–helium mixture were reported on. Thus, in [1], the spin polarization of 2^3S_1 metastable helium atoms was produced in a Na–He plasma in which sodium atoms in the $3^2S_{1/2}$ state were optically oriented by laser radiation. Spin polarization was recorded by the change in the absorption of helium lamp emission under the magnetic resonance conditions for the He 2^3S_1 state. In [2, 3], a method was developed and tested for detecting the spin orientation of helium atoms by the change in the absorption of resonant helium emission without using the magnetic resonance technique. In these papers, the effect of circular dichroism of an ensemble of triplet metastable helium atoms in a Na–He plasma in which sodium atoms were pumped by polarization-modulated laser radiation was observed.

In this paper, we continue investigations on the influence of laser radiation exciting resonant transitions of sodium atoms on the physical processes in a Na–He plasma. The aim of this paper is to observe and investigate the optogalvanic effect [4] in a Na–He plasma irradiated by both circularly polarized helium lamp emission and polarization-modulated laser radiation that resonantly excites sodium atoms. It is known [5, 6] that the mutual spin orientation of metastable helium atoms and alkali metal atoms affects the probability of Penning ionization when these atoms collide in a plasma. For this reason, breaking or changing the orientation with the help of magnetic resonance results in the change of the electric conductivity of an alkali metal–helium plasma, as was observed experimentally in [5, 7]. In order to observe the effect of spin orientation on the ionization processes in a plasma, we used a technique based on the modulation of laser polarization [2]. We note that, in our paper, the signal observed was the change in the plasma conductivity; hence, fluctuations in the laser radiation amplitude, which in previous experiments produced substantial interferences during the optical detection of spin polarization of atoms, were of minor importance in our case.

A schematic of the experimental setup is shown in Fig. 1. A gas-discharge cell (a glass cylinder 5 cm in diameter and 6 cm in length) containing helium at a pressure of 0.5–1 torr and metallic sodium was placed in a magnetic field (H_0 ~ 10 Oe) produced by two Helmholtz coils. The necessary pressure of sodium vapor was ensured by heating the discharge cell in a thermostat (~140°C). An RF discharge (~45 MHz at a voltage of 20–100 V) was excited in the discharge cell with the help of external electrodes. The RF circuit used to initiate the discharge consisted of an inductance coil L, a variable capacitor C_1, and a capacitor C_2 produced by the electrodes and the discharge cell placed between them. Near the coil L, there was an antenna A_D with a diode detector D, which recorded the amplitude

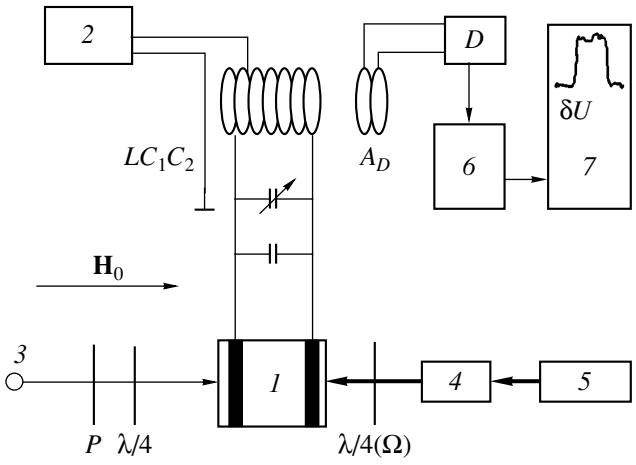

Fig. 1. Schematic of the experimental setup: (*1*) gas-discharge cell, (*2*) RF oscillator, (*3*) helium lamp, (*4*) tunable dye laser, (*5*) argon laser, (*6*) amplifier and synchronous detector, (*7*) recorder, (*P*) polaroid, (λ/4) quarter-wave plate, (λ/4(Ω)) turning mica plate, (A_D) detector antenna, (*D*) RF detector, and (LC_1C_2) RF circuit.

1063-7842/01/4606-0700$21.00 © 2001 MAIK "Nauka/Interperiodica"

of the RF voltage at the antenna A_D. The change in the plasma conductivity resulted in the change in both the voltage in the RF circuit (which also included the discharge cell) and the amplitude of the RF field emitted by the circuit. This change in the amplitude of the emitted field manifested itself in the change in the voltage in the antenna contour A_D and was recorded by the detector D. The increase in the plasma conductivity resulted in the decrease in both the voltage at the electrodes initiating the discharge and the RF voltage U at the antenna. Circularly polarized resonant helium lamp emission entered the discharge cell along the magnetic field $\mathbf{H}_0$. This emission produced the optical orientation of metastable triplet helium atoms. In the opposite direction, the discharge cell was irradiated by a tunable CW rhodamine-6G laser created in our laboratory. An argon LGR-404a laser with a power of ~4 W was used as a pump. The maximum power of the tunable laser was ~50 mW and the spectral width was ~0.01 nm. The laser wavelength was varied in the spectral region corresponding to the resonant doublet of sodium atoms. The laser beam passed through a quarter-wave plate whose orientation determined the sign of circular polarization of laser radiation ($\sigma^{\pm}$). The mechanical rotation of the quarter wave plate with an angular frequency of $\Omega/2\pi \sim 10$ Hz in the plane perpendicular to the beam resulted in the periodical (at a frequency of 2Ω) change in the sign of circular polarization of laser radiation. The optogalvanic signal δU was detected by the modulation (at a frequency of 2Ω) of the RF voltage at the antenna when the laser wavelength was tuned to each of the lines of the resonant doublet of sodium atoms [λ = 589.6 nm (D_1) and λ = 589.0 nm (D_2)]. To increase the signal-to-noise ratio, we employed a narrowband amplification and synchronous detection (at a frequency of 2Ω) with a subsequent recording of the signal δU by a two-coordinate recorder.

The experiment was carried out as follows. Circularly polarized helium lamp emission produced the optical orientation of metastable helium atoms excited in the discharge. Simultaneously, the plasma was irradiated by laser radiation with alternating-sign circular polarization. When the laser wavelength passed through the region of resonant absorption of sodium atoms, the electric conductivity of the plasma changed with the frequency at which the sign of laser polarization varied. The observed δU signals are shown in Fig. 2. The δU signals were recorded at a temperature of about 120–140°C. The maximum signal amplitude $\Delta U \sim 100$ μV (t^0 = 140°C) was obtained at an electrode voltage of ~25 V (near the threshold voltage for the self-sustaining discharge) and an RF voltage at the antenna of $U \sim 4$ V; i.e., the relative change in the RF voltage amplitude was $\delta U/U \sim 2.5 \times 10^{-5}$. The increase in the amplitude of the δU signal near the threshold for the self-sustaining discharge is related to the decrease in the influence of the relaxation of spin orientation of sodium atoms and metastable helium atoms due to collisions with plasma electrons. Moreover, in this case, the optimum conditions for the generation of the optogalvanic signal δU are probably realized [4]. The forced excitation (or quenching) of the discharge near the threshold resulted in a decrease (or an increase) in the detected antenna voltage U by the value $\Delta U \sim 0.5$ V; i.e., the relative change in the RF voltage amplitude was $\Delta U/U \sim 0.1$. Assuming that the quantity $\Delta U/U$ is on the order of the relative contribution from the plasma conductivity in the total impedance of the discharge gap, we can estimate the relative contribution from the effect of the mutual spin orientation of Na and He atoms to

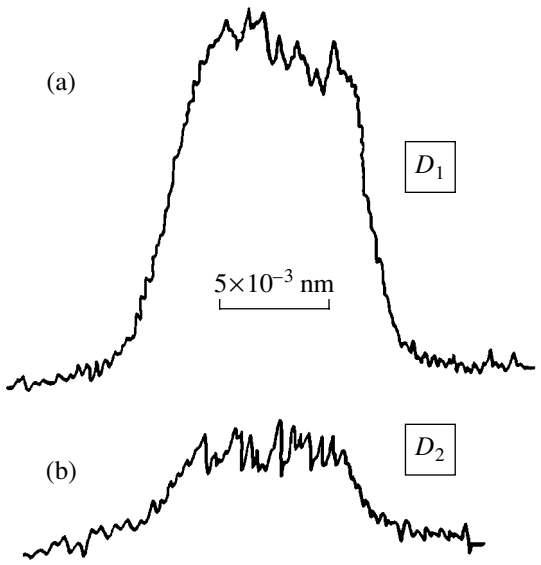

Fig. 2. Variations in the Na–He plasma conductivity observed when scanning the wavelength of the tunable laser (t^0 = 135°C) near λ = (a) 589.6 nm (D_1) and (b) 589.0 nm (D_2).

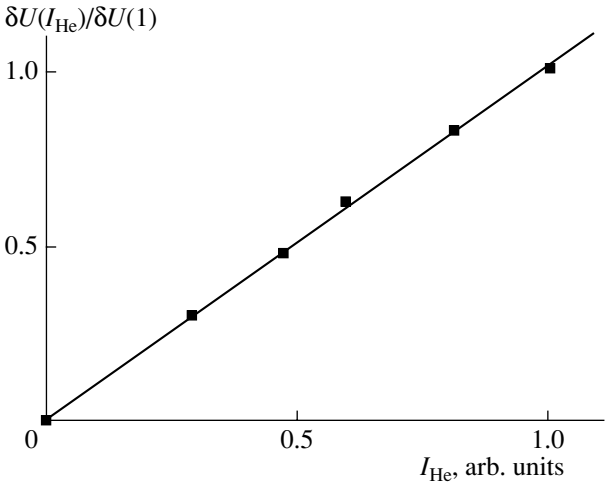

Fig. 3. Amplitude of the optogalvanic signal δU vs. the intensity of helium lamp emission for the laser pumping of sodium atoms (the laser is tuned to the D_1 line of Na atoms); $\delta U(1)$ = 100 μV for the maximum intensity of helium lamp emission.

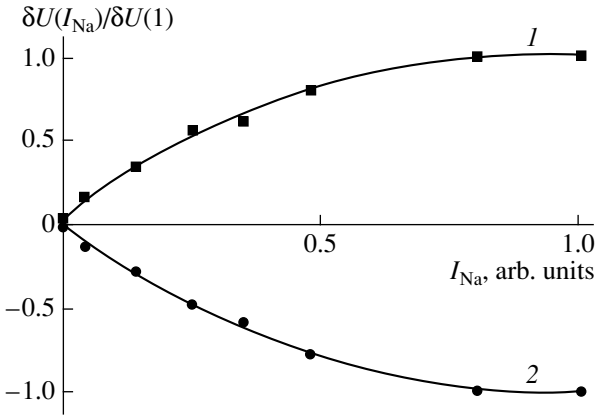

Fig. 4. Amplitude of the optogalvanic signal δU vs. laser intensity (the laser is tuned to the D_1 line of Na atoms) for the pumping of helium atoms by radiation with (*1*) σ^+ and (*2*) σ^- polarization; $\delta U(1) = 100$ μV for a laser intensity of 50 mW.

the plasma conductivity as $\delta U/\Delta U \sim 2.5 \times 10^{-4}$. Accurate calculations of the impedance of the discharge gap and its change due to the optical orientation of atoms in the discharge plasma is a rather complicated problem beyond the scope of our paper.

The change in the sign of circular polarization of helium lamp emission resulted in the change in the polarity of the δU signal. The signal amplitude depended linearly on the intensity of helium lamp emission; i.e., it was determined by the degree of the spin orientation of triplet metastable helium atoms. The dependence of δU on the intensity of helium lamp emission is shown in Fig. 3. The maximum of the signal amplitude corresponds to the maximum intensity of helium lamp emission.

The dependence of the experimentally observed signals on the intensity of laser radiation, which pumped sodium atoms, was quite different. At low intensities, the signal amplitude grows linearly with intensity. As the laser intensity increases, the clearly pronounced saturation is observed at an intensity of ≥10 mW. Curves *1* and *2* in Fig. 4, which are recorded at the opposite signs of circular polarization of helium lamp emission, are symmetric with respect to the $\delta U = 0$ axis. As a rule, in the absence of helium lamp emission and at a noise amplitude corresponding to $\delta U \sim 5$ μV, we did not observe a change in the electric conductivity under the action of laser radiation.[1] For pumping by the D_1 and D_2 lines of sodium atoms, the signals δU had the same polarity. When tuning to the D_1 line, the change in the RF voltage was four to five times larger than for the tuning to the D_2 line. No other difference in the behavior of the $\delta U(D_1)$ and $\delta U(D_2)$ signals was observed.

Therefore, the results presented in Figs. 2–4 show that the polarization optogalvanic effect in a Na–He gas-discharge plasma containing optically oriented 2^3S_1 metastable He atoms and irradiated by circularly polarized laser radiation corresponding to the D_1 and D_2 transitions of Na atoms is related to the value and mutual orientation of the spin momenta of the ensembles of helium and alkali metal atoms. This relation can be explained by the dependence of the probability of the Penning ionization reaction

$$\mathrm{Na}(3^2S_{1/2}) + \mathrm{He}^*(2^3S_1) \longrightarrow \mathrm{Na}^+(2^1S_0) + \mathrm{He}(1^1S_0) + e \quad (1)$$

on the mutual orientation of spin momenta of colliding atoms [5–7].

For the same orientation of spin momenta of colliding atoms, the Penning ionization reaction (1) is forbidden because of the conservation of both the total spin and its projection. The change in the orientation direction of one of the reagents with respect to the orientation of the other (in our case, the change in the sodium atom orientation with the frequency 2Ω or the change in the sign of polarization of helium lamp emission) lifts this restriction. As a result, the number of free electrons in the gas-discharge plasma increases, which manifests itself in the experiment as variations in the conductivity of the discharge plasma at the frequency 2Ω.

The linear dependence of the signal amplitude δU on both the intensity of helium lamp emission I_{He} (Fig. 3) and laser radiation I_{Na} at small laser intensities (Fig. 4) is explained by the linear dependence of the degree of orientation of helium and sodium atoms on the intensity of the corresponding pump radiation. At higher laser intensities, we observed the nonlinear intensity dependence of the signal $\delta U(I_{Na})$. This is explained by the optical saturation of the degree of orientation of sodium atoms [8] due to the competition between the processes of optical orientation and optical relaxation. The difference in the amplitudes of the $\delta U(D_1)$ and $\delta U(D_2)$ signals (see, e.g., Fig. 2) is due to the different intensities of the process of optical orientation of sodium atoms for the $3^2S_{1/2} \longrightarrow 3^2P_{1/2}$ and $3^2S_{1/2} \longrightarrow 3^2P_{3/2}$ transitions [8].

Thus, we have revealed and investigated the polarization optogalvanic effect in a sodium–helium plasma simultaneously irradiated by both resonant (for Na atoms) laser radiation with alternating-sign circular polarization and circularly polarized helium lamp emission. It is shown that this effect is related to the

[1] In some experiments, when tuning to the D_1 line, we observed weak (with a signal-to-noise ratio of 1.5–2) δU signals even in the absence of helium lamp emission. This is probably related to an additional weak (in comparison to the optical orientation produced by helium lamp emission) orientation of helium atoms due to spin-dependent processes occurring during the collisions of helium atoms with oriented sodium atoms or polarized electrons; these weak signals may also be caused by other optogalvanic effects (e.g., the photoexcitation of sodium atoms). These signals require a separate study at a substantially higher signal-to-noise ratio. When analyzing the effects observed, these signals can be ignored.

dependence of the probability of the Penning ionization reaction occurring during the collisions of optically polarized helium and sodium atoms on the mutual orientation of their spin momenta. In the experiment, this dependence manifests itself as a change in the electric conductivity of the gas-discharge plasma at the doubled modulation frequency of the polarization of laser radiation when it is tuned to the lines of the resonant doublet of sodium atoms.

REFERENCES

1. S. P. Dmitriev, N. A. Dovator, R. A. Zhitnikov, *et al.*, Opt. Spektrosk. **84**, 385 (1998) [Opt. Spectrosc. **84**, 334 (1998)].
2. S. P. Dmitriev, N. A. Dovator, R. A. Zhitnikov, *et al.*, Pis'ma Zh. Éksp. Teor. Fiz. **65**, 385 (1997) [JETP Lett. **65**, 399 (1997)].
3. S. P. Dmitriev, N. A. Dovator, R. A. Zhitnikov, *et al.*, Zh. Tekh. Fiz. **70** (1), 16 (2000) [Tech. Phys. **45**, 14 (2000)].
4. V. N. Ochkin, N. G. Preobrazhenskiĭ, and N. Ya. Shaparev, *Optogalvanic Effect in Ionized Gases* (Nauka, Moscow, 1991).
5. S. P. Dmitriev, R. A. Zhitnikov, and A. I. Okunevich, Zh. Éksp. Teor. Fiz. **70**, 69 (1976) [Sov. Phys. JETP **43**, 35 (1976)].
6. A. I. Okunevich, Zh. Éksp. Teor. Fiz. **70**, 899 (1976) [Sov. Phys. JETP **43**, 467 (1976)].
7. S. P. Dmitriev, Opt. Spektrosk. **88**, 737 (2000) [Opt. Spectrosc. **88**, 664 (2000)].
8. W. Happer, Rev. Mod. Phys. **44**, 169 (1972).

Translated by A. Sakharov

Technical Physics, Vol. 46, No. 6, 2001, pp. 704–708. Translated from Zhurnal Tekhnicheskoĭ Fiziki, Vol. 71, No. 6, 2001, pp. 60–65.

Theoretical Study of Thermoelectronic Laser Energy Conversion: II. Characteristics of Optical Discharge

A. P. Budnik and V. A. Zherebtsov

Leipunskiĭ Institute of Physics and Power Engineering, Obninsk, Kaluga oblast, 249033 Russia

e-mail: zherebtsov@ippe.rssi.ru

Received August 23, 2000

Abstract—The dependences of the parameters of a continuous optical discharge in an interelectrode space of a thermoelectronic laser energy converter on the gas pressure, electron emission current, and discharge current are studied. The current–voltage characteristics of the discharge are calculated. © *2001 MAIK "Nauka/Interperiodica".*

1. In the first part of our study [1, 2], we demonstrated the essentially equilibrium character of the plasma in the core of a continuous optical discharge (COD) in the interelectrode space of a thermoelectronic laser energy converter (TELEC) under typical operating conditions [3]. Significant deviations from equilibrium take place only in narrow layers in the vicinity of electrodes and COD edges. With allowance for this fact, we formulated a set of equations describing the equilibrium core of a COD in the TELEC interelectrode space. An analysis of the processes occurring in the nonequilibrium electrode regions yields the corresponding boundary conditions. We developed a method for numerically solving the above set of equations and computer codes for TELEC simulations and created a data base on the thermophysical, optical, and transfer properties of argon plasma in TELEC. We also reported on the preliminary results of calculations of the COD parameters.

In the second part of our study, we employ mathematical simulation to obtain new data on the characteristics of a COD in the TELEC interelectrode space and the effect of the parameters of the converter on the conversion efficiency of laser energy deposited in the discharge.

2. Let us specify the mathematical model of TELEC. We consider an axially symmetric TELEC filled with argon at the pressure P_0. A hot electrode (emitter) with a radius r_1 emits electrons, whereas a relatively cold electrode (collector) with an internal radius $r_2 > r_1$ does not emit charged particles. A stationary COD is maintained in the interelectrode space of the converter by slightly focused laser radiation propagating in the positive direction along the z axis. We assume that the characteristic absorption length of laser light is much larger than the emitter–collector distance L.

This geometry allows us to simplify the mathematical description of the converter using its axial symmetry. On the other hand, it is also possible to take into account the fact that the collector area must be much larger than the emitter area for efficient TELEC operation [4].

Plasma predominantly emits in the short-wavelength spectral region, where the electrode reflectivity is low [5]. Therefore, we can assume that the electrodes are black and completely absorb plasma radiation. Estimates show that the reabsorption of plasma radiation in a TELEC with black electrodes at an interelectrode distance of $L \sim 1$ mm and low gas pressure ($P_0 \le 1$ atm) plays a minor role in the plasma energy balance and, thus, can be neglected. This fact allows one to substantially speed up calculations because, in this case, it is not necessary to calculate the distribution of plasma emission in the interelectrode space.

Let us consider a weakly ionized electrode plasma, which is of special interest for thermoelectronic laser energy conversion.

We performed calculations for an emitter radius of $r_1 = 0.2$ cm and internal collector radius of $r_2 = 0.5$ cm. A slightly focused tubular laser beam with a wavelength $\lambda = 5.3$ μm propagated along the converter axis (the z axis). In the absence of a plasma, the beam was focused into a ring focal spot between the electrodes (the ring radius being $r = (r_1 + r_2)/2$) at a distance of $F = 15$ cm from the entrance to the interelectrode gap (IEG) ($z = 0$). As a rule, the discharge did not reach the IEG boundaries ($z = 0$ and $z = z_{max} = 10$ cm). The temperatures at the boundaries were assumed to be constant and equal to $T_W = (T_E + T_C)/2$, where T_E and T_C are the emitter and collector temperatures, respectively. The calculations were carried out for large densities of the electron emission current eJ_E from the emitter (several hundreds of A/cm^2), because it is this range of eJ_E in which high TELEC efficiency can be achieved [3].

3. Figures show the results of calculations. Figure 1 demonstrates the isotherms of the COD core in the TELEC interelectrode space at an argon pressure of

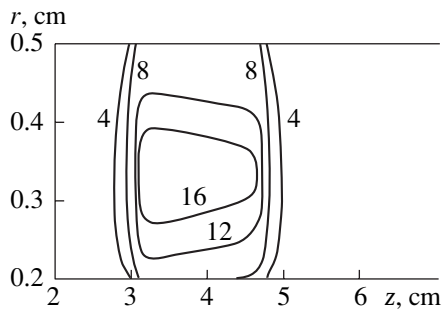

Fig. 1. COD isotherms in the TELEC interelectrode space at P_0 = 1 atm, q_L = 100 kW, T_E = 2000 K, T_C = 1000 K, eJ_E = 500 A/cm^2, F = 15 cm, and J = 0. The numerals at the curves show the plasma temperature in kK.

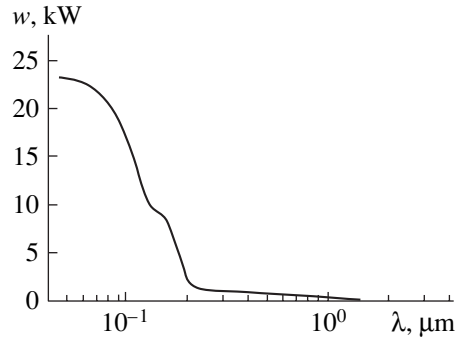

Fig. 2. Radiation energy emitted by a COD at the wavelengths exceeding the given wavelength under the conditions of Fig. 1.

P_0 = 1 atm, a laser power of q_L = 100 kW, and an electron flux density in the discharge core of J = 0. The plasma temperature in the center of the discharge core amounts to 20 kK and decreases to approximately 10 kK in the vicinity of the electrodes. The axial length of the high-temperature discharge region is about 1.5 cm, which is substantially larger than the interelectrode distance. Therefore, the processes of radial transport can be treated in the quasi-one-dimensional approximation. In the case at hand, the discharge absorbs up to ≈25% of laser power entering the IEG. The energy losses in the discharge are mainly determined by plasma emission (≈23 kW), whereas ≈2 kW are lost due to plasma heat conduction. The radiation power density at the electrodes is ≈3.3 kW/cm^2, which is substantially higher than the power spent on heating the electrons from the emitter (≈0.6 kW/cm^2). We note that most of the energy emitted by the plasma is lost and cannot be used for laser energy conversion.

Figure 2 shows the power of COD emission at wavelengths exceeding the given wavelengths. The discharge emits mainly in the UV region: 70% of the emission power falls in the wavelength range below 0.17 μm.

Thus, the COD in the TELEC interelectrode space at an argon pressure of P_0 = 1 atm is five times longer than the IEG. That the discharge length is relatively small leads to substantial energy losses at the discharge ends. This also results in that only a small part of the electrode surface operates in the optimum mode of laser energy conversion. In addition, the losses of the deposited laser energy due to plasma emission give rise to large heat load on the electrodes.

The radiative losses decrease and the discharge length increases with decreasing gas pressure. The decrease in the pressure leads to both the proportional decrease in the intensity of plasma emission per unit length of the COD and the concentration of electrons in the central part of the discharge, which causes a quadratic decrease in the plasma absorbance. Figure 3 shows the z profiles of the plasma temperature in the middle of the IEG (r = 0.35 cm) at two argon pressures. The twofold decrease in the pressure leads to a ≈1.5-fold increase in COD length (cf. curves *1* and *2*), which substantially improves the longitudinal uniformity of the discharge. The energy spent on heating electrons emitted from the emitter increases with decreasing pressure (≈0.04 at P_0 = 1 atm and ≈0.09 at P_0 = 0.5 atm). We also observed the twofold decrease in the light intensity at the electrodes (to ≈1.6 kW/cm^2). At the same time, the temperature of the discharge plasma remains almost unchanged.

Figure 4 shows the radial profiles of the plasma temperature T (curve *1*), electron density n (curve *2*), and electric potential φ (curve *3*) in the midplane of the discharge (z = 2.5 cm) under conditions corresponding to curve *2* in Fig. 3. The plasma temperature profile is bell-shaped. Due to the absorption of laser radiation in the plasma, the curvature of the $T(r)$ profile is negative in the central part of the IEG. The curvature becomes positive when approaching the electrodes due to energy losses caused by plasma emission. The curvature becomes negative again in the vicinity of the emitter because of the cylindrical symmetry of the converter. The plasma temperature in the center of the discharge is approximately two times higher than that in the vicinity of the electrodes. In thin regions near the electrodes (with a width of ~2.6×10^{-2} cm in the midplane of the discharge), the temperature of the heavy components (atoms and ions) falls by one order of magnitude. This leads to large energy fluxes (≈0.25 kW/cm^2) toward the electrodes carried by the heavy plasma components. In the midplane of the discharge, the energy spent on the heating of electrons emitted from the emitter (see formula (31) in [2]) and the generation of ions in nonequilibrium regions near the emitter and collector amounts to 720, 59, and 85 W/cm^2, respectively.

In the center of the IEG, the plasma is almost completely ionized. At the boundaries of the discharge core, the degree of ionization is no higher than one-tenth. The $n(r)$ profile has a minimum in the middle of the IEG due to plasma overheating, which is typical of a stable discharge.

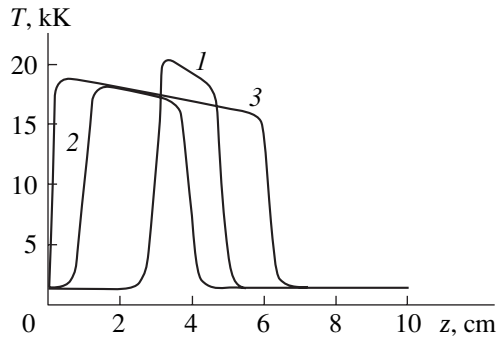

Fig. 3. Axial profiles of the plasma temperature in the middle of the IEG at T_E = 2000 K, T_C = 1000 K, eJ_E = 500 A/cm^2, F = 15 cm, and J = 0 for (*1*) P_0 = 1 atm and q_L = 100 kW, (*2*) P_0 = 0.5 atm and q_L = 169 kW, and (*3*) P_0 = 0.5 atm and q_L = 184 kW.

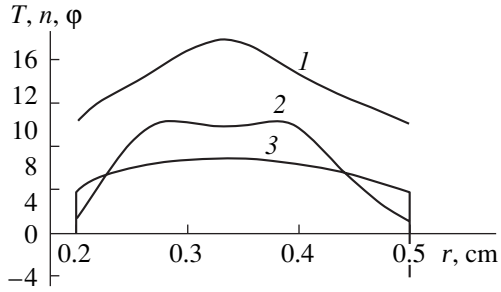

Fig. 4. Radial profiles of (*1*) the plasma temperature (in kK), (*2*) electron density (in units of 10^{16} cm^{-3}), and (*3*) electric potential (in V) in the midplane of the discharge vs. radius at P_0 = 0.5 atm, q_L = 169 kW, T_E = 2000 K, T_C = 1000 K, eJ_E = 500 A/cm^2, F = 15 cm, and J = 0.

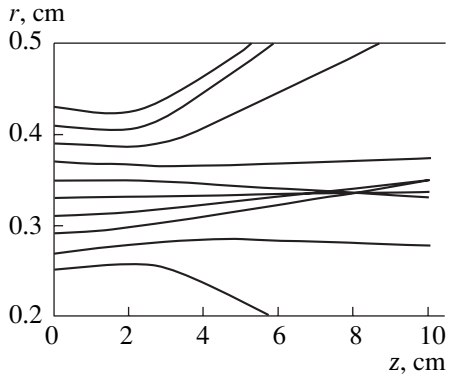

Fig. 5. Paths of laser rays in the TELEC interelectrode space under the conditions of Fig. 4.

The radial profile of the electric potential has a characteristic shape with a large negative drop near the collector, a smaller drop near the emitter (because of a fairly large emission current from the emitter), and a relatively small drop in the discharge core plasma, because the plasma temperatures (and, hence, the electron densities) at the emitter and collector boundaries of the discharge core are close to each other in the case at hand (J = 0). We recall that the electrode potential jump includes both the potential jump in the Langmuir sheath and the changes in the potential in the nonequilibrium and quasi-equilibrium electrode regions.

Thus, the plasma of the COD in the TELEC interelectrode space is strongly nonuniform in the radial direction. In such a plasma, laser radiation undergoes substantial refraction. Figure 5 shows the paths of the laser rays in the TELEC interelectrode space calculated in the geometric-optics approximation. Although this approximation is insufficiently accurate to adequately calculate the propagation of laser radiation in the TELEC interelectrode space, it still gives an idea of the refraction characteristics of the interelectrode plasma. Recall that, in order to determine the COD characteristics, we calculated the propagation of laser radiation in the TELEC interelectrode space in the quasi-optical approximation. As the laser radiation propagates along the interelectrode space, a fraction of laser radiation from the low-intensity peripheral regions is deflected towards the electrodes. The remaining radiation is focused at a distance smaller than that in the absence of a plasma in the IEG (z = 15 cm). The latter fact is illustrated by Fig. 6, which shows the radial profiles of the laser intensity calculated in the quasi-optical approximation.

Steady-state optical discharges under consideration exist only within a narrow range of the laser power. As the power decreases, the discharge length decreases and the discharge is quenched. An increase in the power leads to an increase in the discharge length, which is favorable for the optimum regime of TELEC operation. However, gas heating in front of the leading (left) edge causes the discharge to displace along the IEG towards the laser. In the case at hand, the discharge is stabilized only after it reaches the left IEG boundary (z = 0), at which the temperature is set to $T_W = (T_E + T_C)/2$. Curve *3* in Fig. 3 shows the z profile of the plasma temperature in the middle of the IEG for such a discharge. The formation of a rather sharp leading edge at z = 0 leads to the removal of a substantial amount of heat from the discharge edge, which results in discharge stabilization. In a real TELEC, it is hardly possible to provide a simple method of heat removal from the lens or a transparent window covering the IEG. For a TELEC with an opened left end and laser intensity slightly exceeding that corresponding to the stationary discharge in the IEG (Fig. 3, curves *1, 2*), the discharge diameter can increase after propagating from the IEG to the region $z < 0$. This will give rise to additional energy losses in the edge region of the discharge and will result in discharge stabilization. The stabilization of the discharge can also be attained by using gas being blown along the gap or fairly strong focusing of the laser beam. In the future, we plan to study alternative methods for stabilizing the discharge.

4. When considering the radial transport processes, we can assume that the discharge is quasi-uniform along the *z*-axis. Hence, we can study the electrophysical characteristics of the discharge using a simplified one-dimensional model under the assumption that the laser intensity is independent of *z*. Figure 7 shows the current–voltage (*I–V*) characteristics of the IEG of a converter (*i* is the discharge current density per unit electrode length) for different electron emission currents from the emitter and different argon pressures. These characteristics can be transformed to the *I–V* characteristics of the converter by adding the difference of the collector and emitter work functions to the potential difference *V* between the collector and emitter. Thus, the characteristics presented can be regarded as converter characteristics for equal work functions.

Within the range of the emission currents and argon pressures under study, almost one-half of the *I–V* characteristics lie in the region of negative voltages (conversion region). The increase in the electron emission current eJ_E at a given IEG voltage *V* leads to an increase (somewhat slower than proportional) in the converter current and a corresponding increase in the conversion efficiency, because the absorption of laser radiation is almost unresponsive to the increase in eJ_E. In addition, the increase in eJ_E causes an increase in the off-load voltage (cf. curves *1* and *2* in Fig. 7). The twofold decrease in the pressure (cf. curves *2* and *3* in Fig. 7) insignificantly changes the current but causes a more than twofold decrease in energy losses due to plasma emission and the corresponding increase in the conversion efficiency.

Let us consider the dependence of the parameters of the COD plasma on the converter current. Figure 8 shows the radial profiles of the plasma temperature for three points of the *I–V* characteristic. As the current increases, the plasma temperature increases in the emitter region and decreases in the collector region. The changes in the plasma temperature are caused by the current-dependent changes in the energy flux from the boundary of the equilibrium core of the discharge (see the last term on the right-hand side of formula (31) in [2]) and in the volume heat sources near emitter and heat sinks near collector (see the last two terms on the right-hand side of formula (5) in [2]).

The changes in the plasma temperature in the vicinity of the electrode boundaries of the COD core lead to similar changes in the energy spent on the heating of electrons emitted from the emitter to the plasma temperature, heat transfer to the emitter caused by ions and atoms, and the generation of ions in the nonequilibrium region (see formula (31) in [2]). These energy losses strongly (the second and the third exponentially) depend on the plasma temperature. Their changes, in turn, decrease the variations in the plasma temperature near the electrodes. Consequently, the plasma temperature weakly depends on the current. However, even minor variations in the plasma temperature change the electron density (Fig. 9), which exponentially depends on the temperature in a weakly ionized plasma.

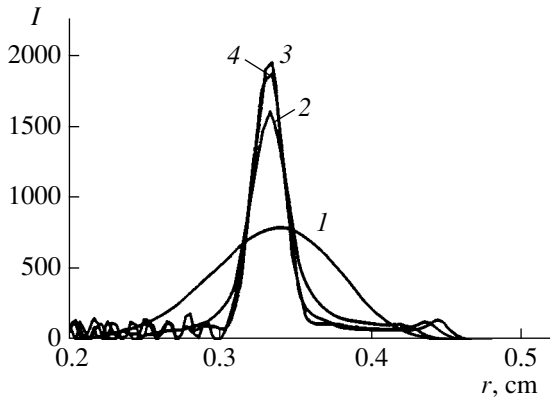

Fig. 6. Radial profiles of the laser intensity (in arbitrary units) under the conditions of Fig. 4 for *z* = (*1*) 0.1, (*2*) 5.0, (*3*) 7.0, and (*4*) 8.0 cm.

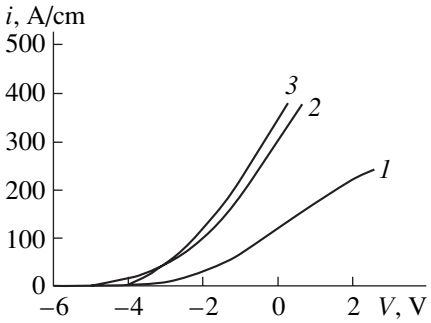

Fig. 7. *I–V* characteristics at T_C = 1000 K for (*1*) P_0 = 1 atm, T_E = 3000 K, eJ_E = 200 A/cm^2, and the absorbed laser power per unit length of the discharge $W_L^{(1)}$ = 17 kW/cm; (*2*) P_0 = 1 atm, T_E = 3000 K, eJ_E = 600 A/cm^2, and $W_L^{(1)}$ = 19 kW/cm; and (*3*) P_0 = 0.5 atm, T_E = 2000 K, eJ_E = 600 A/cm^2, and $W_L^{(1)}$ = 10 kW/cm.

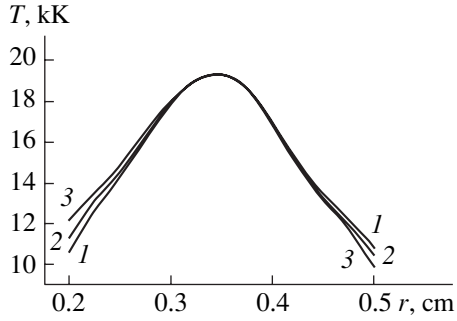

Fig. 8. Radial profiles of the plasma temperature at P_0 = 0.5 atm, T_E = 2000 K, T_C = 1000 K, and eJ_E = 600 A/cm^2 for *i* = (*1*) 0, (*2*) 150, and (*3*) 380 A/cm.

Figure 10 shows the radial profiles of the electric potential for three values of the converter current. As

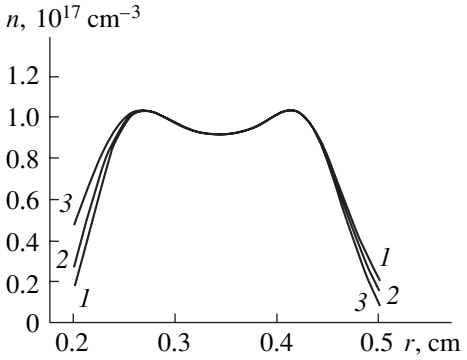

Fig. 9. Radial profiles of the electron density under the conditions of Fig. 8.

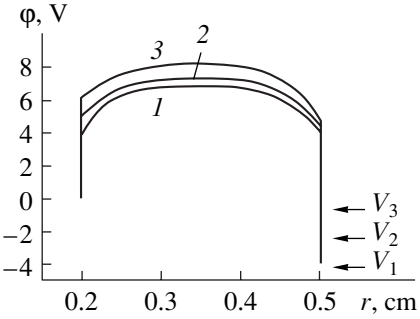

Fig. 10. Radial profiles of the electric potential under the conditions of Fig. 8; V_1, V_2, and V_3 are the IEG voltages for the corresponding curves.

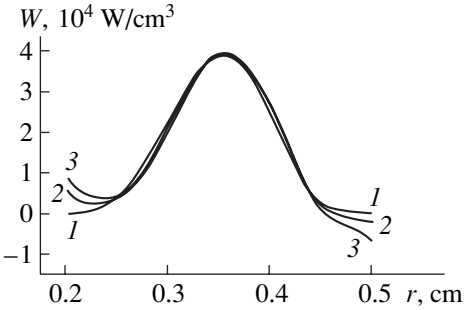

Fig. 11. Radial profiles of the specific power deposited in the plasma under the conditions of Fig. 8.

the current increases, the emitter jump of the potential increases, whereas the absolute value of the collector jump decreases. The potential difference between the collector and emitter boundaries of the discharge core decreases (the absolute value increases) with current due to the change in the plasma temperature and the electron density at these boundaries.

The gradients of the temperature, electron density, and electric potential are low in the middle of the interelectrode gap, where the major part of laser energy is absorbed. Accordingly, the current-dependent volume heat sources and sinks are low in comparison with the absorbed laser energy. Thus, the current only slightly affects the temperature and electron density in that region of the IEG and, consequently, laser energy absorbed in the plasma. Specifically, the change in the current density per unit length i from 0 to 380 A/cm leads to a change in the absorbed laser energy by ~1%. Figure 11 shows the total volume energy deposition in the plasma caused by the current and the absorption of laser radiation. This quantity is the sum of the specific power deposited in the plasma due to the absorption of laser radiation W_L and the last two terms on the right-hand side of formula (5) in [2].

5. Therefore, a COD several centimeters long can exist in the TELEC interelectrode space. The plasma temperatures in the center of the discharge core and electrode regions can attain ≈20 000 and ≈10 000 K, respectively. A decrease in the gas pressure makes it possible to increase the discharge length and its axial uniformity and decrease the radiative losses per unit length of the discharge. In this case, the plasma temperature in the IEG remains almost unchanged.

As the discharge current density per unit length i increases, the plasma temperature in the emitter region of the discharge core increases, whereas in the collector region it decreases. This leads to the corresponding change in the electron density in these regions. Another consequence of the increase in i is the increase in the emitter jump of the potential and the decrease in the absolute value of the collector jump. For the fixed voltage at the IEG, i grows slower than the electron emission current from the emitter. The change in the pressure only slightly affects the value of i.

ACKNOWLEDGMENTS

This work was supported by the Russian Foundation for Basic Research, project no. 97-02-17583.

REFERENCES

1. I. V. Alekseeva, A. P. Budnik, V. A. Zherebtsov, *et al.*, Pis'ma Zh. Tekh. Fiz. **25** (7), 90 (1999) [Tech. Phys. Lett. **25**, 290 (1999)].
2. I. V. Alekseeva, A. P. Budnik, P. P. D'yachenko, *et al.*, Zh. Tekh. Fiz. **70** (11), 91 (2000) [Tech. Phys. **45**, 1462 (2000)].
3. N. P. Kozlov, A. V. Pekshev, Yu. S. Protasov, and V. I. Suslov, in *Radiative Plasmadynamics* (Énergoatomizdat, Moscow, 1991), Vol. 1, p. 462.
4. J. F. Waymouth, J. Inst. Electr. Eng. **8** (8), 380 (1962).
5. L. N. Latyev, V. A. Petrov, V. Ya. Chekhovskoĭ, and V. N. Shestakov, *Handbook of Radiant Properties of Hard Materials*, Ed. by A. E. Sheĭndlin (Énergiya, Moscow, 1974).

Translated by A. Chikishev

Technical Physics, Vol. 46, No. 6, 2001, pp. 709–717. Translated from Zhurnal Tekhnicheskoĭ Fiziki, Vol. 71, No. 6, 2001, pp. 66–74.

RADIOPHYSICS

Two-Mirror Resonator for Studying High-Pressure Electrodeless Microwave Discharge

L. P. Grachev, I. I. Esakov, S. G. Malyk, and K. V. Khodataev

Moscow Radiotechnical Institute, Russian Academy of Sciences, Varshavskoe sh. 132, Moscow, 113519 Russia

e-mail: esakov@dataforce.net

Received March 22, 2000; in final form, July 17, 2000

Abstract—An electromagnetic centimeter-wave quasi-optical two-mirror open resonator is studied. The eigenfrequency spectrum of the resonator is determined and the *Q* factor is measured. The structure of a standing wave in the resonator is visualized by an electrodeless microwave discharge. The experimental results are compared with theoretical values. © *2001 MAIK "Nauka/Interperiodica".*

INTRODUCTION

In the simplest case, electrodynamic systems referred to as open resonators are composed of two plane or spherical concave mirrors placed face-to-face. Initially, interest in these devices was related to their use in electromagnetic oscillators of optical, submillimeter-wave, and millimeter-wave bands [1, 2]. Later, they found applications in plasma diagnostics [3] and in studying high-pressure electrodeless microwave gas discharges [4, 5].

Electrodeless microwave discharges are discharges that occur in wave beams at a significant distance from beam-forming elements. At gas pressures of $p \le 100$ torr, such discharges can be excited by focused microwave beams [6, 7]. At $p \le 150$ torr, resonators whose dimensions are comparable to the wavelength λ are widely used [8]. At higher p (up to tens of atmospheres), quasi-optical open resonators can be used to study electrodeless discharges.

An atmospheric-pressure discharge in the field of a two-mirror resonator was described in [4]. The discharge was excited in air at the center of the resonator at a distance of several tens of centimeters apart from the closest construction elements. It had the form of a thin plasma channel, which efficiently absorbed the energy accumulated in the resonator by the time of the discharge ignition. This energy was accumulated at the center of the discharge channel, in a small nucleus, having the nature of a micropinch [9, 10]. This method for producing the pinch effect opens unique possibilities for its study and applications [11].

At present, a theory exists that relates the geometry of an open resonator with circular spherical mirrors to its eigenmodes and the resonance conditions [12]. Several papers were published on the measurement of the *Q* factor of such resonators in the millimeter-wave band [13, 14]. The ignition of a microwave discharge in an open resonator in the 8-mm and 10-cm wavebands was studied in [4, 5]. However, a number of fundamental problems are still not clearly understood, e.g., the problem concerning efficient coupling between the resonator and the feeding microwave oscillator, the magnitude E_0 of the field in the resonator, and the electromagnetic energy W_{ac} accumulated in it.

1. ELECTROMAGNETIC FIELD STRUCTURE IN A RESONATOR WITH CIRCULAR SPHERICAL MIRRORS

We consider a resonator consisting of two identical circular spherical mirrors placed face-to-face at a distance of $2L < 2R_{mir}$, where R_{mir} is the radius of the mirror curvature. The mirrors reside on the polar x axis with the origin at the resonator center [12]. Let the mirror diameter be $2a_{mir}$. The resonance electromagnetic oscillations may exist in the resonator if its dimensions and the wavelength λ of the feeding field are related as

$$2L/(\lambda/2) = q + (2/\pi)(m + 2n - 1)\arcsin\sqrt{L/R_{mir}}, \quad (1)$$

where q is a large integer; $m = 0, 1, 2, \ldots$; and $n = 1, 2, \ldots$. The integers q, m, and n characterize the variations of the field in the x coordinate, polar angle φ, and radius r, respectively. We are interested in the simplest axially symmetric mode with $m = 0$ and $n = 1$. It has the form of a standing wave along the resonator. At odd q, the distribution of the electric field amplitude along the x axis in the central region of the resonator can be written as

$$E = E_0\cos(2\pi x/\lambda_{res}), \quad (2)$$

where λ_{res} is the wavelength in the resonator, which can be written using relationship (1) as

$$\lambda_{res} = \lambda(1 + [2/(\pi q)]\arcsin\sqrt{L/R_{mir}}). \quad (3)$$

1063-7842/01/4606-0709$21.00

In the focal plane (at $x = 0$), this field component depends on r as

$$E = E_0 e^{-(r/a)^2}, \quad (4)$$

where

$$a = \sqrt{\lambda/\pi}\sqrt[4]{L^2(R_{mir}/L - 1)}. \quad (5)$$

The electric current on the mirrors for this mode is also independent of φ and has a Gaussian distribution similar to distribution (4) with the characteristic dimension

$$a_{cur} = \sqrt{\lambda/\pi}\sqrt[4]{R_{mir}^2/[(R_{mir}/L) - 1]}. \quad (6)$$

It follows from formulas (5) and (6) that, as $L \longrightarrow R_{mir}$, the field is mainly concentrated near the resonator axis, while the characteristic dimension of the current distribution on the mirrors grows. For a high-Q resonator, the ratio of the power of diffraction loss due to the finite mirror radius to the power incident on the mirror (i.e., the diffraction loss factor α_{dif}) can be expressed as

$$\alpha_{dif} = e^{-2(a_{mir}/a_{cur})^2}. \quad (7)$$

The oscillation mode in the resonator is determined not only by expression (1), but also by the excitation conditions. For example, for the mode with $m = 0$ and $n = 1$, the excitation current on the mirrors must be localized in their central regions and be equiphase. To excite the mode with $m = 0$ and $n = 2$, the currents in the central region and in the ring around it must be antiphase.

2. NORMAL INCIDENCE OF AN ELECTROMAGNETIC WAVE ON A METAL MIRROR

Before proceeding to analyzing the resonator energy characteristics, we consider, for reference, the familiar case of the normal incidence of a TEM wave on a plane metal mirror and assume that

$$(\varepsilon_0\omega/\sigma) \ll 1, \quad (8)$$

where $\varepsilon_0 = 10^{-9}/(36\pi)$ F/m, ω is the circular frequency, and σ is the conductivity of the mirror material.

In this case, the magnitude of the reflected-to-incident wave amplitude ratio is

$$\rho = 1 - \sqrt{2(\varepsilon_0\omega/\sigma)}, \quad (9)$$

and the reflected wave is shifted in phase by $[-(\pi - \psi)]$ with respect to the incident one, where

$$\psi = \sqrt{2(\varepsilon_0\omega/\sigma)}. \quad (10)$$

In the centimeter waveband, σ of highly conducting metals is about 10^7 1/(Ω m) and condition (8) is satisfied with a considerable margin so that the angle ψ may be neglected as compared to π, and ρ is close to unity.

The reflected-to-incident wave power ratio (i.e., the reflection coefficient α_{ref}) is equal to the squared ρ: $\alpha_{ref} = \rho^2$. It follows from the power conservation law that, when condition (8) is satisfied, the absorption coefficient α_σ, defined as the ratio of the power absorbed in the mirror due to the skin effect to the incident power, is

$$\alpha_\sigma \equiv \gamma^2 = 1 - \rho^2 = 2\sqrt{2(\varepsilon_0\omega/\sigma)}. \quad (11)$$

Finally, for a mirror with a high conductivity, the following approximation is valid:

$$\rho = 1 - (1/2)\alpha_\sigma. \quad (12)$$

If the mirror is perforated with apertures, then a part of the incident electromagnetic energy will penetrate through them. Let the field be linearly polarized and the apertures be circular with radius $r_{con} \ll \lambda/(4\pi)$ and be punched at the nodes of a rectangular mesh with cell sizes of h and χ (both less than λ). One of the sides of the mesh is parallel to **E** and the other side is perpendicular to it. Let the mirror thickness be $\Delta < 2r_{con}$. In this case, the transmitted-to-incident wave power ratio (i.e., the coupling coefficient) is

$$\alpha_{con} \equiv \Theta^2 = [(16\pi r_{con}^3)/(3h\chi\lambda)]^2. \quad (13)$$

Further, we will consider the case $\alpha_{con} \ll 1$ and will be interested in the question whether the relationship

$$\rho = 1 - (1/2)\alpha_{con} - (1/2)\alpha_\sigma \quad (14)$$

is valid.

3. ENERGY CHARACTERISTICS OF A TWO-MIRROR RESONATOR

In view of the above considerations, we will present and discuss the expressions that relate the field amplitude E_0 at the resonator focus and the energy W_{ac} accumulated in the resonator to the power P_{osc} of the feeding microwave oscillator and the resonator characteristics. We first consider a simpler resonator composed of two infinite plane mirrors and assume that the distance $2L$ between the mirrors satisfies the resonance conditions. Figure 1 schematically illustrates the field structure in the resonator a time t after a primary unit-amplitude wave has impinged on semitransparent mirror *1* normally from the left. The letter C indicates the superposition of waves that form the reflected wave, and E_0 is the superposition of waves in the resonator (it is seen that the latter is composed of two waves $E_\leftarrow$ and $E_\rightarrow$ traveling in opposite directions). The individual waves

in the superpositions C and E_0 are marked with their relative amplitudes, whose signs allow for their relative phases and the indices at the coefficients ρ and γ are related to the first or second mirror.

Individual terms in these superpositions are the terms of geometric progressions. We can write

$$C_k = -\rho_1 + \frac{\Theta^2\rho_2[1-(\rho_1\rho_2)^k]}{1-\rho_1\rho_2}, \quad (15)$$

$$C = -\rho_1 + \frac{\Theta^2\rho_2}{1-\rho_1\rho_2}, \quad (16)$$

$$E_k = E_{k\rightarrow} + E_{k\leftarrow}$$
$$= \frac{\Theta[1-(\rho_1\rho_2)^k]}{1-\rho_1\rho_2} + \frac{\Theta\rho_2[1-(\rho_1\rho_2)^k]}{1-\rho_1\rho_2}, \quad (17)$$

$$E_0 = E_{\rightarrow} + E_{\leftarrow}$$
$$= \frac{\Theta}{1-\rho_1\rho_2} + \frac{\Theta\rho_2}{1-\rho_1\rho_2} = \frac{\Theta(1+\rho_2)}{1-\rho_1\rho_2}, \quad (18)$$

where the symbols C and E with indices k refer to the sums of k terms and those without indices refer to the sums of an infinite number of terms.

Figure 1 shows that, when passing over from the sums to the functions C_k and E_k smoothed in time t, one should take into account the relationship

$$k = t/(4L/c), \quad (19)$$

where c is the speed of light.

We introduce the time constant

$$\tau = (4L/c)[1/(\alpha_\sigma + \alpha_{con}/2)]. \quad (20)$$

Then, expressions (15) and (16) and the identity $(\rho_1\rho_2)^k \equiv \exp(k\ln(\rho_1\rho_2))$ yield the time dependence of the reflected wave:

$$C_k = (C_0 - C)e^{-(t/\tau)} + C, \quad (21)$$

where $C_0 = -\rho_1 \cong -1$. With allowance for expressions (12) and (14), we obtain at $\gamma_1 \cong \gamma_2 = \gamma$

$$C = -1 + 2\alpha_{con}/(2\alpha_\sigma + \alpha_{con}). \quad (22)$$

Formula (21) shows that, at $t = 0$, the wave incident on mirror *1* is almost completely reflected from it and, then, the amplitude of the reflected wave tends exponentially to the value C defined by formula (22). It follows from formula (22) that C tends to zero at

$$\alpha_{con} = 2\alpha_\sigma. \quad (23)$$

This is the familiar condition for the optimal coupling between the resonator and oscillator, which provides a zero reflected wave at $t \gg \tau$ in the feeder that guides microwave energy to the resonator. Similar

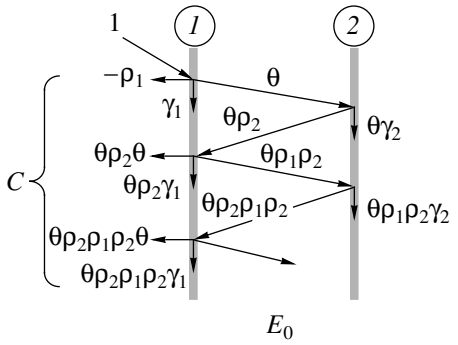

Fig. 1. Electromagnetic field structure in a resonator.

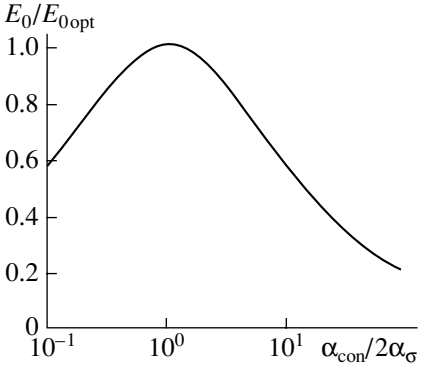

Fig. 2. Field amplitude in a resonator vs. coupling with the oscillator.

transformations applied to formulas (17) and (18) yield the expression for the field in the resonator:

$$E_k = E_0(1 - e^{-(t/\tau)}), \quad (24)$$

where

$$E_0 = (2/\sqrt{\alpha_\sigma})\sqrt{\alpha_{con}/\alpha_\sigma}/[1 + \alpha_{con}/(2\alpha_\sigma)]. \quad (25)$$

An analysis of formula (25) shows that condition (23) provides the maximum saturation field in the resonator:

$$E_{0opt} = \sqrt{2/\alpha_\sigma}. \quad (26)$$

Figure 2 plots E_0/E_{0opt} versus the ratio $\alpha_{con}/2\alpha_\sigma$.

The time constant τ defined by formula (20) allows us to write an expression for the Q factor of the resonator, which, according to one of its possible definitions, is the number of electromagnetic field oscillations during the time τ multiplied by π:

$$Q \equiv (\omega\tau)/2 = \pi[2L/(\lambda/2)][1/(\alpha_\sigma + \alpha_{con}/2)]. \quad (27)$$

This is the so-called loaded Q. The Q factor of an unloaded resonator is higher; it is given by formula (27) at $\alpha_{con} = 0$.

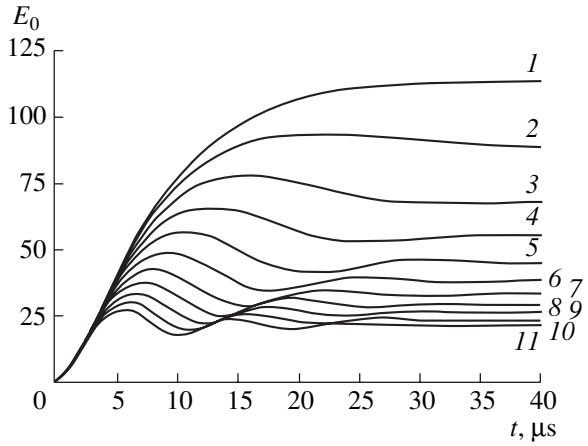

Fig. 3. Amplitude of the electric field in a resonator vs. time for different deviations of its length from the resonant value ΔL = (*1*) 0, (*2*) 1.5, (*3*) 3,(*4*) 4.5, (*5*) 6, (*6*) 7.5, (*7*) 9, (*8*) 10.5, (*9*) 12, (*10*) 13.5, and (*11*) 15×10^{-4} cm.

This wave summation procedure can be performed at an arbitrary $2L/\lambda$. This approach gives the following formula for the saturation field in the resonator:

$$E_0 = \frac{\Theta\sqrt{1 + 2\rho_2\cos[(4\pi/\lambda)2L] + \rho_2^2}}{\sqrt{1 - 2\rho_1\rho_2\cos[(4\pi/\lambda)2L] + (\rho_1\rho_2)^2}}. \quad (28)$$

Formula (28) describes resonance curves $E_0(\lambda)$ or $E_0(2L)$. Near the resonance values of λ or $2L$, it can be reduced to the known expressions

$$\frac{E_0(\lambda)}{E_0} = \frac{1}{\sqrt{1 + [Q(\Delta\lambda/\lambda)]^2}}$$

or

$$\frac{E_0(2L)}{E_0} = \frac{1}{\sqrt{1 + [Q(\Delta L/2L)]^2}}, \quad (29)$$

where E_0 and Q are given by formulas (18) and (27), respectively, and $\Delta\lambda$ and ΔL are the full widths of the resonance curves at a level of $1/\sqrt{2}$ of the resonant value E_0.

Expressions (29) are also used as a possible definition of the Q factor.

The shape of the incident wave front can differ from the step function. For example, it may be described as $1 - \exp(-t/\tau_{in})$. In this case, applying the above wave summation procedure, we obtain (for $\alpha_{con} = 2\alpha_\sigma$ as an example) that the field in the resonator grows as

$$E_k = E_0[1 - (\tau_{res}e^{-(t/\tau_{res})} - \tau_{in}e^{-(t/\tau_{in})})/(\tau_{res} - \tau_{in})], \quad (30)$$

where τ_{res} is the time constant, which is an intrinsic characteristic of the resonator and, according to formula (27), is determined by its quality factor.

Figure 3 plots the function $E_0(t)$ calculated from expressions (28) and (30) for different deviations of the resonator length from the resonant value at $\alpha_\sigma = 1.6 \times 10^{-4}$, $2L/(\lambda/2) = 11$, $\lambda = 8.9$ cm (see Section 4), $\alpha_{con} = 2\alpha_\sigma$, and $\tau_{in} = 1.5$ μs. The upper curve corresponds to $\Delta L = 0$; the higher ΔL, the lower the curve.

Let the incident field and the field in a resonator with plane mirrors be symmetric about the x axis and the amplitude have a Gaussian radial profile with the characteristic scale length a. Also, let the coupling between the resonator and source be optimal and $t \gg \tau$. At the input of this resonator, only the incident wave exists. It may be characterized by the Poynting vector. The integration of the magnitude of the Poynting vector over the surface perpendicular to the x axis gives the power of the wave traveling from the oscillator to resonator:

$$P_{osc} = [E_{in}^2/(2z_0)](\pi a^2/2), \quad (31)$$

where $z_0 = 120\pi\ \Omega$ and E_{in} is the amplitude of the incident wave.

We use expression (31) to find E_{in}; then, taking into account formula (26), which implies the incident wave amplitude is equal to unity, we obtain the relationship between the oscillator power and the saturation field in the resonator:

$$E_0 = (2/a)\sqrt{(2\eta P_{osc}z_0)/(\pi\alpha_\sigma)}, \quad (32)$$

where η is the oscillator power utilization factor, which is less than unity, e.g., due to the mismatch between wave fronts at the entrance mirror of the resonator.

Taking into account expressions (5) and (27), relationship (32) can be written as

$$E_0 = \frac{4}{\pi a}\sqrt{\frac{Q\eta P_{osc}z_0}{2L/(\lambda/2)}} = 2\sqrt{\frac{Q\eta P_{osc}z_0}{\pi L\sqrt{L(R_{mir} - L)}}}. \quad (33)$$

We note that formula (32) is convenient when designing the resonator, while formula (33) contains quantities that can be measured experimentally. Furthermore, formula (32) implies that diffraction losses, estimated by formula (7), are small as compared to thermal losses in the mirrors:

$$\alpha_{dif} \ll \alpha_\sigma. \quad (34)$$

In the resonance, the field distribution along the resonator has the form of a standing wave. Unlike the traveling wave, the **E** and **B** vectors in the standing wave are not only orthogonal, but are also shifted in phase by π. In this case, the notion of the Poynting vector becomes meaningless. At the same time, the standing wave is equivalent to the sum of two waves $E_\leftarrow$ and $E_\rightarrow$ traveling at equal velocities in opposite directions. These waves, whose amplitudes are twice as small as the standing wave amplitude, can be characterized by the Poynting vector and, similarly to expression (31), their power can be written as

$$P_\rightarrow = P_\leftarrow = (E_0/2)^2\pi a^2/4z_0. \quad (35)$$

With relationship (32), this formula yields $P_{\leftarrow}\alpha_{con} = P_{osc}$ and $(P_{\leftarrow}\alpha_{\sigma} + P_{\rightarrow}\alpha_{\sigma}) = P_{osc}$; i.e., as it should be for the optimal coupling in the saturation regime, the wave that exits from the resonator through the coupling apertures completely compensates for the reflected wave and the energy that enters the resonator is completely absorbed by the resonator mirrors.

It was found experimentally that gas breakdown in a resonator with a highly focused field occurs mostly in the focal region [4]. A significant absorption of electromagnetic energy was observed in the discharge channel only in the final (about 1-ns-long) stage of its evolution. This time is comparable to that needed for the accumulated energy to discharge from the resonator:

$$t_{min} = 2L/c. \quad (36)$$

We define the resonator power P_{res} as the total power of waves traveling in both directions through its central plane. Then, expressions (32) and (35) yield

$$P_{res} = P_{\leftarrow} + P_{\rightarrow} = \eta P_{osc}(1/\alpha_{\sigma}). \quad (37)$$

The value of P_{res} determines the maximum possible rate of supplying the microwave discharge with electromagnetic energy. It increases with P_{osc} and the conductivity of the mirror material. If an imaginary surface with a 100% absorption is instantly introduced into the resonator central plane, the product $P_{res}t_{min}$ will determine the energy accumulated in the resonator:

$$W_{ac} = \eta P_{osc}(2L/c)(1/\alpha_{\sigma}). \quad (38)$$

Using the above relationships, expression (38) can be reduced to

$$W_{ac} = \frac{\varepsilon_0 E_0^2}{2}\frac{\pi a^2}{2}\frac{2L}{2} = \frac{2Q\eta P_{osc}}{\omega} = \eta P_{osc}\tau. \quad (39)$$

4. EXPERIMENTAL SETUP

A layout of the experimental setup used to study the two-mirror open resonator is shown in Fig. 4. A distinctive feature of the setup is that it operates at the low-frequency range of the centimeter-wave band. The setup is built around pulsed magnetron *1*, which generates an electromagnetic wave at the circular frequency $\omega = 2.12 \times 10^{10}$ s^{-1}. It feeds a waveguide line, which contains circulator *2*, switch *3*, attenuator *4*, lens system *5*, and two-mirror resonator *6* with measurement circuit *7*.

Lens system *5* formed a linearly polarized TEM wave with a plane wave front over a circular aperture of diameter $2a_{osc} = 60$ cm. The normalized radial power distribution in the exit aperture is shown in Fig. 5. The maximum measured radiated power was $P_{osc} = 1$ MW. The aperture produced rectangular microwave pulses with duration $t_{pul} \cong 40$ μs and characteristic rise and fall times $\tau_{in} \cong 0.3$ μs and $\tau_{fall} \cong 0.8$ μs, respectively, at $\lambda = 8.9$ cm with the vector **E** perpendicular to the axis of the microwave beam. The time between individual pulses was no shorter than 10 s.

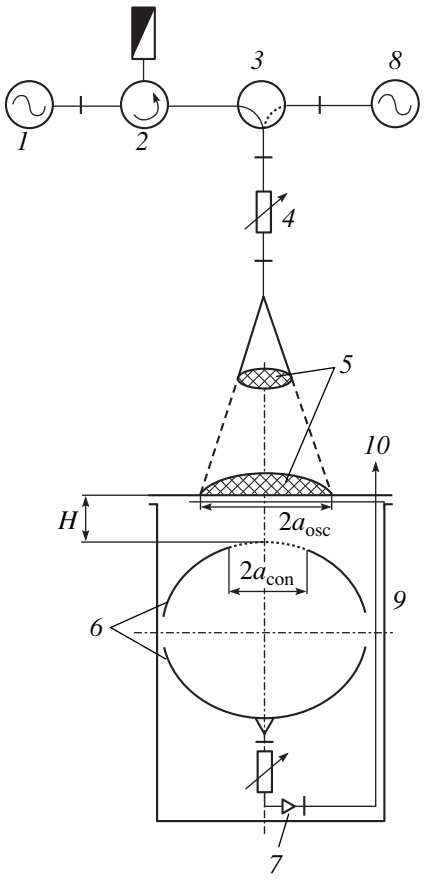

Fig. 4. Layout of the experimental setup.

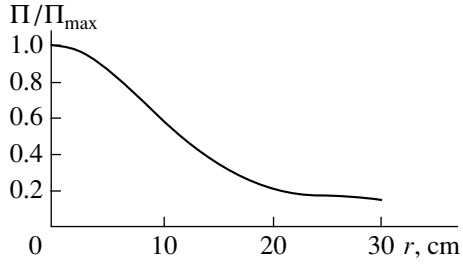

Fig. 5. Normalized microwave power distribution over the radiating aperture.

Resonator *6* was placed at a distance of $H = 7.8$ cm from the aperture. The mirrors were fabricated from 0.2-cm-thick sheet copper and had a diameter $2a_{mir} = 64$ cm and radius of curvature $R_{mir} = 35$ cm. The reference copper conductivity is $\sigma = 5.8 \times 10^7$ 1/(Ω m). Therefore, $\alpha_{\sigma} = 1.6 \times 10^{-4}$ at the operating frequency ω. The mirror that is the nearest to the aperture was fixed. Its central region of diameter $2a_{con} = 20$ cm was perforated with apertures of diameter $2r_{con} = 0.89$ cm over a rectangular grid with step sizes $h = \chi = 1.5$ cm and one

side parallel to **E**. The second mirror was movable such that the distance $2L$ between the mirrors could be varied in the range from 45 to 70 cm. This distance could be initially installed in steps with an accuracy of $\pm 5 \times 10^{-2}$ cm and, then, could be continuously varied within ± 1 cm about the chosen position with a 2.5×10^{-2}-cm-per revolution vernier whose rotation angle was measured to a $\pm 10°$ accuracy.

In the central part of the movable mirror, there were several openings through which a small control signal was supplied from the resonator to measurement circuit *7*, consisting of a waveguide-to-coaxial converter, attenuator, amplitude detector, amplifier, and storage oscilloscope. This circuit almost undistortedly displayed the top of a 40-μs-long test rectangular video pulse with characteristic rise and fall times of less than 0.1 μs. The time constants of the leading and trailing edges of the output pulse were 0.17 and 0.3 μs, respectively. In the experiments with microwave field, the attenuation in the measurement circuit was chosen such that it operated in an almost linear portion of the circuit characteristic and the interference signal observed on the screen of the oscilloscope was negligible.

The output signal of measurement circuit *7* was related to the absolute values of the field amplitude E_0 at the focus of the resonator through the known air breakdown field at atmospheric pressure, $E_{br} = 32$ kV/cm. The microwave pulse of the maximal power applied to the resonator tuned to the resonance mode with $m = 0$ and $n = 1$ could cause a breakdown in air at the focus. At the instant of breakdown, the signal on oscilloscope *10* dropped abruptly. The maximum amplitude of the signal before breakdown was associated with the field strength $E_0 = 32$ kV/cm.

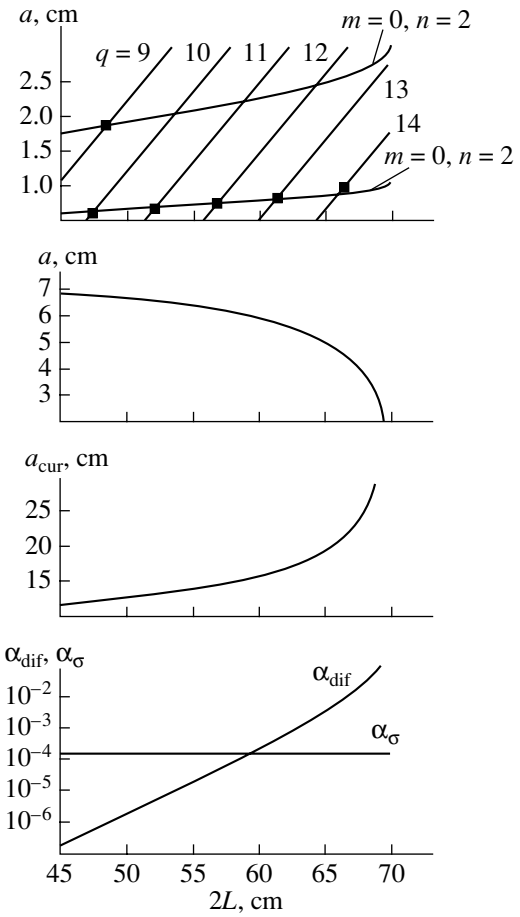

Fig. 6. Parameters of the resonator vs. its length.

Waveguide switch *3* allowed us to use any service oscillator *8* to measure the resonator parameters in the cold mode. The waveguide line (from the output of magnetron *1* through the smaller lens of lens system *5*) was sealed hermetically and filled with SF_6 gas to an excessive pressure of 1 atm. The resonator was placed into sealed chamber *9*, the air pressure p in which could be varied in the range from $p = 760$ to 3 torr. Photographs of the microwave discharge could be taken through a chamber window in the direction perpendicular to the $\mathbf{E}_0$ vector and the resonator axis.

5. EXPERIMENTAL RESULTS AND DISCUSSION

In the first experiment, the resonator was excited by the magnetron at the maximum power P_{osc} at $p = 760$ torr. The distance $2L$ was continuously varied over the entire range allowed by the setup design. The signal in the measurement circuit was almost always zero and abruptly increased only at certain values of $2L$, which we will further refer to as the resonance dimensions. This increase in the field intensity in the resonator could be accompanied by air breakdown in its central part. The range ΔL of the distances between the mirrors, at which the increase in the signal was recorded, was no larger than several hundredths of a millimeter. When the distance $2L$ approached the resonance value, characteristic beatings (Fig. 3) were observed on the top of the recorded signal, which facilitated tuning the setup to the resonance.

Results of this experiment are summarized in the two left columns of Table 1.The first column lists the resonance values of $2L$; the plus symbols in the second column indicate cases in which breakdown occurred. The table also gives the values of $2L$ calculated from Eq. (1) closest to the experimental ones along with the corresponding values of m, n, and q. The graphical solution of Eq. (1) at $m = 0$ and $n = 1$ and 2 is illustrated in the upper panel of Fig. 6, which plots the functions $F_1 = 2L/(\lambda/2) - q$ and $F_2 = (2/\pi)(m + 2n - 1)\arcsin\sqrt{2L/2R_{mir}}$ versus $2L$. The resonance values of $2L$ are given by their intersection points.

The square symbols in Fig. 6 show the measured values. It is seen that, for $n = 1$, the difference between the experimental and theoretical values becomes negligible only when foci of the mirrors come sufficiently close together. It is seen from Fig. 5 and Table 1 that the

feeding circuit also excites the axially symmetric resonator mode with $n = 2$. This could be expected. As is shown in Fig. 4, the mirror through which the resonator is coupled to the oscillator faces the incident plane wave with its convex side, which causes a significant phase difference between the center of the mirror and a point displaced by a_{con} in the radial direction. This circumstance creates conditions for the excitation of this mode. This oscillation mode was not observed at $q > 9$, which is presumably associated with a low value of the quality factor at these q. As follows from the theory, the current-carrying region on the mirror surface increases with n and, consequently, α_{dif} significantly increases, because the mirror diameter is fixed.

Figure 6 shows a, a_{cur}, and α_{dif} versus $2L$ for the 0, 1, q oscillation mode. As could be expected, the focusing of the field at the center of the resonator becomes stronger as $L \longrightarrow R_{mir}$. However, Table 1 shows that, at $q > 13$, the field intensity drops to such a level that breakdown in air becomes impossible. As follows from Fig. 6, this can be attributed to the increase in a_{cur} and α_{dif}. For example, for modes with $n = 1$, α_{dif} becomes even greater than α_σ when $2L > 60$ cm.

It follows from formula (3) that, for the same frequency ω, the wavelength λ_{res} in the resonator is greater than that in free space λ. In the next experiment, we verified this formula. For this purpose, a nylon filament 0.073 cm in diameter and marked every 1 cm was stretched along the resonator axis. The resonator was excited at $p = 760$ torr by the magnetron at the maximum power P_{osc}. The resonator was tuned to the resonance at $2L = 51.65$ cm, which corresponds to $\lambda_{res} = 9.4$ cm according to expression (3). Each microwave pulse caused breakdown with a discharge channel about 2.5 cm long and 7×10^{-2} cm in diameter extended along $\mathbf{E}_0$. Breakdowns occurred randomly at one of the antinodes of the standing wave. Discharges observed in a sequence of pulses visualize positions of the maxima. Figure 7 shows the images of 40 discharges and the marked filament. Vector $\mathbf{E}_0$ is perpendicular to the filament. The distance between the centers around which the discharge channels were localized was 4.7 cm, which corresponds to $\lambda_{res} = 9.4$ cm.

In the next experiment, the resonator with the same length, $2L = 51.65$ cm, was excited by a low-power microwave service oscillator. When the frequency was varied, the resonance spikes in the measured signal were also observed. The first and second columns in Table 2 list the resonance frequencies f taken from the oscillator scale and those calculated from formula (1), respectively, which are seen to be in good agreement with each other. As in the first experiment, the mode with $n = 2$ was also excited in the resonator. At the length $2L$ used in the experiment, Q factors of these modes were high enough to record them.

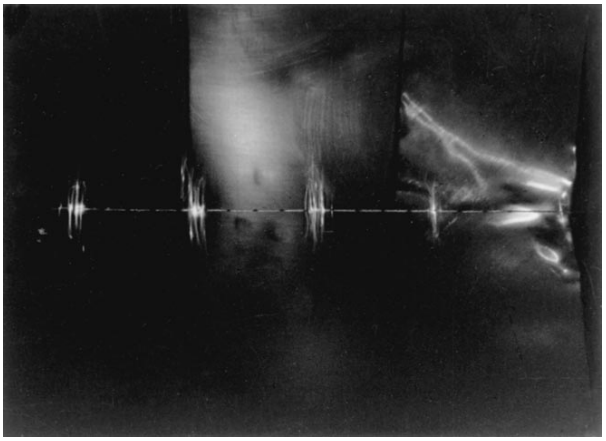

Fig. 7. Electrodeless microwave discharge in atmospheric air in an open resonator.

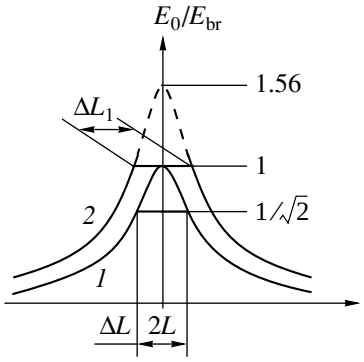

Fig. 8. Resonance curves.

Our service oscillator was capable of measuring the mode frequency within an accuracy of no higher than 100 kHz, while the frequency ranges in which the spikes of the measured signal were observed were also narrower than 100 kHz. Therefore, with this instrument, we could only roughly estimate the resonator Q factor. It was no less than several tens of thousands. Using a swept-frequency service oscillator capable of displaying the resonance curve confirmed this estimate, but more accurate measurements were also impossible

Table 1

Experiment, $2L$ [cm]	Breakdown	Theory, $2L$ [cm]	m, n, q
47	+	47	0, 1, 10
48.2		48.3	0, 2, 9
51.6	+	51.6	0, 1, 11
56.25	+	56.3	0, 1, 12
61.15		60.8	0, 1, 13
66.2		65.7	0, 1, 14

Table 2

f, GHz		*m*, *n*, *q*
experiment	theory	
3.48	3.47	0, 2, 10
3.38	3.38	0, 1, 11
3.18	3.18	0, 2, 9
3.09	3.09	0, 1, 10
2.9	2.9	0, 2, 8
2.8	2.8	0, 1, 9

because the Q factor of the studied resonator was beyond the instrument resolution.

In the next experiment, the Q factor of the resonator with a resonance length $2L = 51.65$ cm was estimated by mechanically detuning the resonator length. For this purpose, the resonator was fed by a magnetron whose signal was attenuated with an attenuator by a factor of 1.56 in amplitude. Experiments showed that, in this case, the level E_0 corresponded to the air breakdown field E_{br} at $p = 760$ torr (Fig. 8, curve *1*). Then, the chamber in which the resonator was placed was evacuated to $p = 760/\sqrt{2} = 540$ torr and the range ΔL was measured in which air breakdown occurred at this value of p. The measured value was $\Delta L = 3.1 \times 10^{-3}$ cm; i.e., $Q = 2L/\Delta L = 1.7 \times 10^4$ from expression (29).

In the test experiment, the same resonator was fed with full power and the range $(\Delta L)_1$ of the resonator lengths was measured in which breakdown in air occurred at $p = 760$ torr. Our measurements gave $(\Delta L)_1 = 8.7 \times 10^{-3}$ cm, which, with formula (29) and $Q = 1.7 \times 10^4$ measured above, predicts that the field E_0 for the exact tuning to the resonance is 1.53 times stronger than E_{br}. This result almost coincides with the attenuation introduced above. We note that the portion of curve *2* in Fig. 8 shown with the dashed line is not realized in the experiment because the field E_0 could not exceed E_{br} at $p = 760$ torr.

In the final experiment, the Q factor of the resonator with the same $2L$ was estimated from the measured time constant τ, which characterizes the leading edge. For this purpose, the resonator was fed by the magnetron, but attenuation was introduced so that breakdown in atmospheric air was not observed. The measured signal had a typical shape with an exponentially saturating leading edge, a flat top, and an exponentially dropping trailing edge. The measured rise time was $\tau = 2$ μs, which gives $Q \cong 2 \times 10^4$ from expression (27).

Let us use the formulas of Section 3 to calculate the maximum field strength E_0 at the focus of the resonator and compare it with the experimental value $E_0 = 1.56 \times 32$ kV/cm = 50 kV/cm. In our calculations, we take $P_{osc} = 1$ MW, $2L = 51.65$ cm, and $Q = 1.7 \times 10^4$.

Formula (27) allows us to compute the experimental value of α_{con}. It gives $\alpha_{con} = 3.9 \times 10^{-3}$. This coefficient can also be found from formula (13) taking into account that the perforated region of the mirror, through which the resonator is excited, accepts only 70% of the power of the wave incident on the mirror from the resonator side. At r_{con}, h, and χ used in the experiment, this formula gives $\alpha_{con} = 3.6 \times 10^{-3}$. It is easily seen that the two estimates are almost identical. Thus, in our experiment, the coupling between the oscillator and resonator was not optimal. We had $\alpha_{con}/(2\alpha_\sigma) \cong 12$ and the field E_0 could be no stronger than $0.6E_{0opt}$, as follows from Fig. 2.

To calculate E_0, we use the second relationship in formula (33). The coefficient η in this formula is determined by the distribution of the power P_{osc} over the radiating aperture (Fig. 4) and by the ratio of the area of this aperture (of diameter $2a_{osc}$) to the area of the perforated region of the resonator mirror (of diameter $2a_{con}$). This coefficient is equal to 0.3. Formula (33) with allowance for the ratio E_0/E_{0opt} gives $E_0 = 48$ kV/cm, which almost coincides with the experimental value.

CONCLUSION

We have shown that the present theory quite satisfactorily describes the properties of quasi-optical open resonators with spherical mirrors. This refers to their possible oscillation modes, resonance conditions, the coupling between the oscillator and resonator, etc. A certain discrepancy becomes noticeable only when the configuration becomes close to confocal. The study reported above allows us to design systems for the excitation of electrodeless microwave discharges in this type of resonators at ultrahigh gas pressures [11]. Such resonators can also serve as a fine tool for studying breakdown fields in various gases at high pressures, the rate and degree of electromagnetic energy dissipation in electrodeless discharges, etc.

REFERENCES

1. A. M. Prokhorov, Zh. Éksp. Teor. Fiz. **34**, 1658 (1958) [Sov. Phys. JETP **7**, 1140 (1958)].
2. F. S. Rusin and G. D. Bogomolov, Élektron. Bol'sh. Moshchn., No. 5, 45 (1968).
3. A. L. Vikharev, A. M. Gorbachev, O. A. Ivanov, *et al.*, Zh. Tekh. Fiz. **66** (7), 56 (1996) [Tech. Phys. **41**, 665 (1996)].
4. L. P. Grachev, I. I. Esakov, G. I. Mishin, *et al.*, Zh. Tekh. Fiz. **64** (2), 26 (1994) [Tech. Phys. **39**, 130 (1994)].
5. A. L. Vikharev and B. G. Eremin, Zh. Éksp. Teor. Fiz. **68**, 452 (1975) [Sov. Phys. JETP **41**, 219 (1975)].

6. A. S. Zarin, A. A. Kuzovnikov, and V. M. Shibkov, *Free Localizated Microwave Discharge in Air* (Neft' i Gaz, Moscow, 1996).
7. L. P. Grachev, I. I. Esakov, M. P. Knyazev, *et al.*, Zh. Tekh. Fiz. **54**, 1353 (1984) [Sov. Phys. Tech. Phys. **29**, 782 (1984)].
8. A. D. MacDonald, *Microwave Breakdown in Gases* (Wiley, New York, 1966; Mir, Moscow, 1969).
9. W. Kies, G. Decker, U. Berntien, *et al.*, Pis'ma Zh. Tekh. Fiz. **25** (20), 5 (1999) [Tech. Phys. Lett. **25**, 802 (1999)].
10. M. A. Gulin, A. N. Dolgov, O. V. Nikolaev, *et al.*, Fiz. Plazmy **16**, 1015 (1990) [Sov. J. Plasma Phys. **16**, 590 (1990)].
11. L. P. Grachev, I. I. Esakov, G. I. Mishin, *et al.*, Preprint No. 1577 (Ioffe Physicotechnical Institute, Russian Academy of Sciences, St. Petersburg, 1999).
12. L. A. Vaĭnshteĭn, *Open Cavities and Open Waveguides* (Sov. Radio, Moscow, 1966).
13. A. I. Barchukov and Yu. N. Petrov, Radiotekh. Élektron. (Moscow), No. 3, 414 (1962).
14. G. D. Bogomolov, Élektron. Bol'sh. Moshchn., No. 9, 154 (1963).

Translated by A. Khzmalyan

Technical Physics, Vol. 46, No. 6, 2001, pp. 718–722. Translated from Zhurnal Tekhnicheskoĭ Fiziki, Vol. 71, No. 6, 2001, pp. 75–79.

ELECTRON AND ION BEAMS, ACCELERATORS

Amplitude Characteristic of Cyclotron Resonance

V. N. Komarov

Saratov State University, Saratov, 410601 Russia

Received June 8, 2000; in final form, November 8, 2000

Abstract—The motion of a charged particle under the combined action of a magnetostatic field and a circularly polarized electromagnetic wave of phase velocity u higher than c, the wave being aligned with the field, is studied theoretically. A nonlinear resonance curve is found. Certain integrals of motion are derived. © *2001 MAIK "Nauka/Interperiodica".*

Let us consider the motion of a charged particle under the combined action of a magnetostatic field and a circularly polarized electromagnetic wave of phase velocity u, the wave being aligned with the field. For the case $u = c$, concomitant resonant phenomena were addressed in [1]. It was established that the cyclotron frequency relates to the integral of motion $\Psi_3 = \varepsilon - up_z$ and is time-independent. Here, ε is the total energy of the relativistic particle and p_z is the projection of the momentum onto the direction of the magnetostatic field. If $u \neq c$, the cyclotron frequency as a function of the momentum components is not an integral of motion and the resonance becomes nonlinear. Let us consider a number of specific cases.

(1) Let the magnetostatic field be aligned with the z axis, $\bar{\mathbf{H}} = (0, 0, H)$ and the electromagnetic wave be defined by the vector potential

$$\bar{\mathbf{A}}(\xi) = -\frac{cE}{w}(\mathbf{i}\sin\xi - g\mathbf{j}\cos\xi), \quad \xi = \omega t - kz, \quad (1)$$

where ω is the frequency of the wave, k is the wave number, and g is a polarization parameter. Then, the equations of motion have the form

$$\frac{dp_x}{dt} = eE\left(1 - \frac{v_z}{u}\right)\cos\xi + \frac{e}{c}v_y H,$$

$$\frac{dp_y}{dt} = eE\left(1 - \frac{v_z}{u}\right)g\sin\xi - \frac{e}{c}v_x H, \quad (2)$$

$$\frac{dp_z}{dt} = \frac{eE}{u}(v_x\cos\xi + v_y g\sin\xi).$$

Multiplying the first and second equations of system (2) by p_x and p_y, respectively, and taking the sum of the results yields

$$\frac{d}{dt}\frac{p_x^2 + p_y^2}{2} = \left(1 - \frac{v_z}{u}\right)eE(p_x\cos\xi + p_y g\sin\xi). \quad (3)$$

Then, we multiply the first and second equations of system (2) by p_y and p_x, respectively, and subtract the latter result from the former to obtain

$$p_y\frac{dp_x}{dt} - p_x\frac{dp_y}{dt} = \left(1 - \frac{v_z}{u}\right)eE(p_y\cos\xi - p_x g\sin\xi) + \frac{e}{c}H(v_y p_y + v_x p_x). \quad (4)$$

In the transverse (x, y) plane, we pass to polar coordinates, so that $p_x = p\cos\varphi$ and $p_y = p\sin\varphi$. After rearrangements, we arrive at

$$\frac{dp}{dt} = \left(1 - \frac{v_z}{u}\right)eE\cos\theta,$$

$$\frac{d\theta}{dt} = \left(g\omega - \frac{eE\sin\theta}{p}\right)\left(1 - \frac{v_z}{u}\right) + \frac{ecH}{\varepsilon}, \quad (5)$$

$$\theta = g\xi - \varphi, \quad \varepsilon = \sqrt{m^2c^4 + c^2p^2 + c^2p_z^2}.$$

System (5) enables us to determine the amplitude characteristic of steady-state oscillations in the transverse plane.

(2) We eliminate $\cos\theta$ and $\sin\theta$ from Eqs. (5). This yields

$$\left(1 - \frac{v_z}{u}\right)^2(eE)^2 = \left(\frac{dp}{dt}\right)^2 + \left[\frac{-d\theta}{dt} + g\omega\left(1 - \frac{v_z}{u}\right) + \frac{ecH}{\varepsilon}\right]^2 p^2. \quad (6)$$

Steady-state oscillations are characterized by the condition $dp/dt = 0$ and $d\theta/dt = 0$ [2]. Hence,

$$\left(\frac{eE}{\omega}\right)^2 = \left[g + \frac{ecH}{\omega(1 - v_z/u)\varepsilon}\right]^2 p^2. \quad (7)$$

Here, p is the amplitude of the steady-state oscillation.

Now, let us revert to Eqs. (2). We multiply the first and second equations by $v_x = p_x c^2/\varepsilon$ and v_y, respec-

tively, and take the sum of the results. Integration in view of the third equation gives the integral of motion

$$\Psi_3 = \varepsilon - up_z. \tag{8}$$

For the case $H = 0$, integral (8) is described in [3]. We thus obtain

$$p_z = \frac{-u\Psi_3 + \sqrt{c^2\Psi_3^2 + (u^2 - c^2)(m^2c^4 + c^2p^2)}\,\mathrm{sgn}(u - v_z)}{u^2 - c^2}; \tag{9}$$

hence,

$$\varepsilon(1 - v_z/u) = \frac{c}{u}\sqrt{\Psi_3^2 + (u^2 - c^2)(m^2c^2 + p^2)}\,\mathrm{sgn}(u - v_z).$$

Thus, we arrive at the resonance curve equation

$$A^2 = \left[g + \frac{eHu\,\mathrm{sgn}(u - v_z)}{\omega\sqrt{\Psi_3^2 + (u^2 - c^2)(m^2c^2 + p^2)}}\right]^2 p^2, \qquad A = \frac{eE}{\omega}. \tag{10}$$

If $p \ll mc$, we can expand Eq. (10) and obtain the equation of weakly nonlinear oscillations [2, 4]:

$$A^2 = \left\{g + \frac{ecH\,\mathrm{sgn}(u - v_z)}{\omega\sqrt{\Psi_3^2 + (u^2 - c^2)m^2c^2}} \times \left[1 - \frac{(u^2 - c^2)p^2}{2[\Psi_3^2(u^2 - c^2)m^2c^2]}\right]\right\}^2 p^2. \tag{11}$$

If $u = c$, the term with H in (10) equals $ecH/(\omega\Phi_3)$ and the resonant frequency is constant [5]. If $u < c$, formula (9) sets a limit on the growth of p. From here on, we assume that $u > c$ and $\mathrm{sgn}(u - v_z) = 1$. It follows from Eq. (10) that

$$\frac{dp^2}{d\omega} = \frac{2p^2euH}{\omega^2X}\left(g + \frac{euH}{\omega X} - \frac{euH(u^2 - c^2)p^2}{\omega X^3}\right)^{-1}, \qquad X = \sqrt{\Psi_3^2 + (u^2 - c^2)(m^2c^2 + p^2)}. \tag{12}$$

The derivative becomes infinite at two values of the frequency [see Fig. 1a]:

$$\omega_1 = 0, \quad \omega_2 = \frac{euH}{gX^3}(-\Psi_3^2 - (u^2 - c^2)m^2c^2). \tag{13}$$

The expression for ω_2 indicates that resonance is possible if $eH/g < 0$, as is the case with an electron ($e < 0$) and a clockwise polarized wave ($g = +1$) traveling along the magnetostatic field ($H > 0$). If ω is between ω_1 and ω_2, three values of the steady-state amplitude are possible. If $\omega > \omega_2$, the amplitude is determined uniquely.

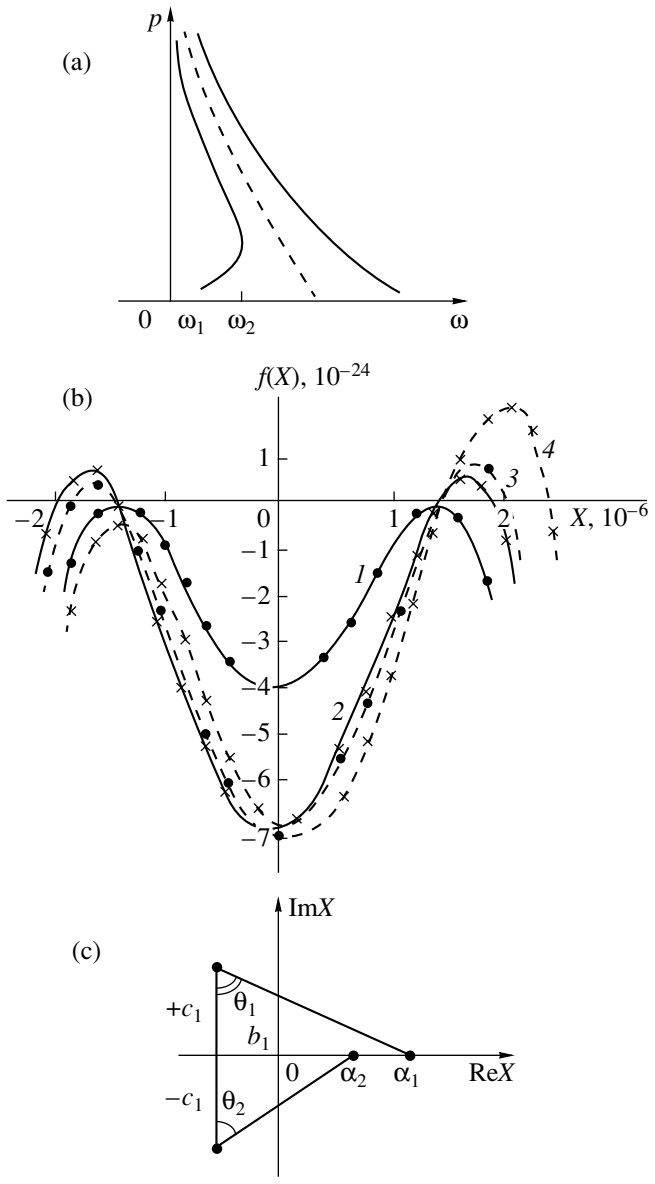

Fig. 1. (a) General form and the characteristic frequencies of the resonance curve; (b) graphs of $f(X)$ for (*1*) $A = 0$ and $H = 0$, (*2*) $A = 2 \times 10^{-17}$ and $H = 0$, (*3*) $A = 2 \times 10^{-17}$ and $2\frac{eH}{k} = -10^{-7}$, and (*4*) $A = 2 \times 10^{-17}$ and $2\frac{eH}{k} = -5 \times 10^{-7}$; and (c) the location of two real and two complex roots of $f(X)$ in the complex X plane.

(3) System (2) comprises delay differential equations, with the delay depending on time. Generally speaking, they can be solved by the method of steps for individual time intervals [6]. Some motion parameters can be found from the integrals of Eqs. (5). If we derive an expression for dt from the first equation in (5) and

substitute the result into the second equation, we will have after rearrangements:

$$\frac{d}{dp}A\sin\theta + \frac{A\sin\theta}{p} = g + \frac{eH}{k\sqrt{\Psi_3^2 + (u^2 - c^2)(m^2c^2 + p^2)}}; \quad (14)$$

hence,

$$2Ap\sin\theta = g(p^2 - p_0^2) + 2\frac{eH}{k(u^2 - c^2)} \times \left(\sqrt{\Psi_3^2 + (u^2 - c^2)(m^2c^2 + p^2)} - \sqrt{\Psi_3^2 + (u^2 - c^2)(m^2c^2 + p_0^2)}\right) + 2C.$$

Here, p_0 is the initial value of the momentum and $2C$ = const. If $u \longrightarrow c$, the term with H changes into $(p^2 - p_0^2)/(k\Psi_3)$. If $H = 0$ or $p \ll mc$, we obtain the well-known integral

$$(\bar{\mathbf{p}} + (e/c)\bar{\mathbf{A}}(\xi))^2 = \text{const}.$$

In what follows, $2C$ includes the terms with the lower limit p_0. Combining the integral $2C$ with the first equality of (5), we arrive at the constraint on p the magnitude of:

$$\left[\frac{2pdp/dt}{\omega(1 - v_z/u)}\right]^2 = 4p^2A^2 - \left[gp^2 + \frac{2eH}{k(u^2 - c^2)} \times \sqrt{\Psi_3^2 + (u^2 - c^2)(m^2c^2 + p^2)} + 2C\right]^2. \quad (15)$$

For the longitudinal direction, we have the integral

$$1 - \frac{v_z}{u} = (u^2 - c^2)X/(\Psi_3 cu + u^2X), \quad (16)$$

which allows us to derive

$$\left[2\frac{dX}{dt}\left(X - \Psi_2\frac{c}{u}\right)\right]^2 = \frac{\omega^2}{u^4}(u^2 - c^2)f(X), \quad (17)$$

where

$$f(X) = 4A^2(X^2 - a^2)(u^2 - c^2) - \left[2Cg(u^2 - c^2) + (X^2 - a^2) + 2g\frac{eH}{k}X\right]^2,$$

$$a = \sqrt{\Psi_3^2 + (u^2 - c^2)m^2c^2}.$$

If the wave is absent, relation (15) indicates that p is conserved in a magnetostatic field. Equations like (17) describe the time variation of the total energy [7]. They also apply to other particular cases of the motion of a relativistic charged particle in the field of a transverse wave [8]. Separating variables, we express the solution in terms of elliptic integrals:

$$t - t_0 = \frac{2u^2}{\omega(u^2 - c^2)}\left[\int_{X_0}^{X}\frac{XdX}{\sqrt{f(X)}} - \Psi_3\frac{c}{u}\int_{X_0}^{X}\frac{dX}{\sqrt{f(X)}}\right]. \quad (18)$$

The values of the integrals depend on the location of the roots of $f(X)$ in the complex plane.

(4) The expression for $f(X)$ is represented by a fourth-order algebraic curve that has two maxima and a single minimum. The curve may be situated variously with respect to the X axis. The four roots of $f(X)$ may be all real; furthermore, there may be two multiple roots among them. Otherwise, $f(X)$ has two real and two complex conjugate roots.

When the wave is turned on, $f(X)$ increases for $X < -a$ or $X > a$ and decreases for $-a < X < a$. When the magnetostatic field is turned on, $f(X)$ becomes asymmetric, since the coefficients of odd powers depend on H. In the case $g = +1$ and $e < 0$, the turn-on of the magnetostatic field reduces the left-hand peak. The wave field and the magnetostatic field have different effects on the left-hand peak if it is located at $X < a$. In a sufficiently strong magnetostatic field, this peak is at $X > -a$. Then, the wave field and the magnetostatic field reduce the left-hand peak; if we increase one of the two fields, complex roots may result.

Figure 1b shows $f(X)$ for $g = +1$, $H > 0$, $u = 1.5c$, $\omega = 6.28 \times 10^{10}$ rad/s, $k = 1.4$ rad/cm, $\Psi_3 \approx mc^2$, $p_0 = mc/10$, and $\theta_0 = 0$, where m and e are the mass and the charge of an electron, respectively. In the figure caption, the quantities come in Gaussian units.

Let the real roots satisfy the inequalities $\alpha_4 < \alpha_3 < \alpha_2 < \alpha_1$. Using [9], we calculate the integrals in (18) for $\alpha_2 < X < \alpha_1$ to obtain

$$t = \frac{u^2}{\omega(u^2 - c^2)}\frac{4}{\sqrt{\alpha_1 - \alpha_3(\alpha_2 - \alpha_4)}} \times \left[\alpha_3 F(\varphi, k) + (\alpha_2 - \alpha_3)\Pi\left(\varphi, \frac{\alpha_1 - \alpha_2}{\alpha_1 - \alpha_3}, k\right) - \Psi_3\frac{c}{u}F(\varphi, k)\right] + J_1, \quad (19)$$

where

$$k^2 = \frac{(\alpha_1 - \alpha_2)(\alpha_3 - \alpha_4)}{(\alpha_1 - \alpha_3)(\alpha_2 - \alpha_4)}, \quad \sin^2\varphi = \frac{(\alpha_1 - \alpha_3)(X - \alpha_2)}{(\alpha_1 - \alpha_2)(X - \alpha_3)}.$$

From here on, k is the modulus of a corresponding elliptic function. The constant J_1 depends on the lower limits of integration. If $\alpha_3 = \alpha_4$, we have

$$t = \frac{u^2}{\omega(u^2 - c^2)}$$

$$\times\left\{-2\arcsin\frac{\alpha_1+\alpha_2-2X}{\alpha_1-\alpha_2}+\frac{2(\alpha_3-\Psi_3 c/u)}{\sqrt{(\alpha_1-\alpha_3)(\alpha_2-\alpha_3)}}\right. \quad (20)$$

$$\left.\times\arcsin\frac{(\alpha_3-\alpha_2)(\alpha_1-X)+(\alpha_1-\alpha_3)(X-\alpha_2)}{(\alpha_1-\alpha_2)(X-\alpha_3)}\right\}+J_2.$$

With two complex and two real roots, well-known substitutions [10] provide

$$t=\frac{\mu u^2}{\omega(u^2-c^2)}\left\{\frac{\alpha_1+\alpha_2}{2}-\Psi_3\frac{c}{u}-\frac{\alpha_1-\alpha_2}{\nu}F(\varphi,k)\right.$$

$$+\frac{\alpha_1-\alpha_2}{2\nu}\Pi\left(\varphi,\frac{\nu^2}{\nu^2-1},k\right)+\frac{\sqrt{1-\nu^2}(\alpha_1-\alpha_2)}{4\sqrt{\nu^2+k^2-\nu^2k^2}} \quad (21)$$

$$\left.\times\arcsin\frac{(2k^2-2k^2\nu^2+\nu^2)\sin^2\varphi+\nu^2-1}{1-\nu^2\cos^2\varphi}\right\}+J_3.$$

Here,

$$\left(\tan\frac{\varphi}{2}\right)^2=\frac{\cos\theta_1}{\cos\theta_2}\frac{\alpha_1-X}{X-\alpha_2},\quad k^2=\sin^2\frac{\theta_1-\theta_2}{2},$$

$$\tan\theta_1=\frac{\alpha_1-b_1}{c_1},\quad \tan\theta_2=\frac{\alpha_2-b_1}{c_1},$$

$$\nu=\tan\frac{\theta_2-\theta_1}{2}\tan\frac{\theta_2+\theta_1}{2},\quad \alpha_3=b_1+ic_1,$$

$$\alpha_4=b_1-ic_1,$$

$$\mu=\sqrt{\cos\theta_1\cos\theta_2}/c_1.$$

(5) Let us investigate the function $X(t)$. This entails the inversion of the expressions obtained. If the wave is turned on, then α_1, α_2, α_3, and α_4 diverge. The difference $\alpha_1-\alpha_2$ relates to the change in p and evaluates the width of the right-hand peak. The difference $\alpha_1-\alpha_3$ evaluates the space between like sides of the peaks in $f(X)$, so that $(\alpha_1-\alpha_2)/(\alpha_1-\alpha_3)<1$. The weaker the wave, the stronger this inequality. Thus, the Π function in (19) is expressed as

$$\Pi(\varphi,n,k)=\int_0^\varphi\frac{d\varphi}{(1-n\sin^2\varphi)\sqrt{1-k^2\sin^2\varphi}}\approx F(\varphi,k), \quad (22)$$

so that

$$t\approx\frac{u^2}{\omega(u^2-c^2)}\frac{4}{\sqrt{(\alpha_1-\alpha_3)(\alpha_2-\alpha_4)}}\times\left(\alpha_2-\Psi_3\frac{c}{u}\right)F(\varphi,k)+J_1. \quad (23)$$

According to [11], the inversion of the elliptic integral of the first kind results in

$$X\approx\left[\alpha_2-\frac{\alpha_1-\alpha_2}{\alpha_1-\alpha_3}\alpha_3\mathrm{sn}^2(\gamma,k)\right]\Big/\left[1-\frac{\alpha_1-\alpha_2}{\alpha_1-\alpha_3}\mathrm{sn}^2(\gamma,k)\right], \quad (24)$$

where

$$\gamma=\frac{(t-J_1)\omega(u^2-c^2)}{4u^2(\alpha_2-\Psi_3 c/u)}\sqrt{(\alpha_1-\alpha_3)(\alpha_2-\alpha_4)},$$

$$\mathrm{sn}(\gamma,k)=\frac{1}{\sqrt{k}}\frac{t_1(\nu)}{t_4(\nu)},\quad \nu=\frac{\gamma}{2K},$$

$$K(k)=\frac{\pi}{2}\left[1+\left(\frac{1}{2}\right)^2k^2+\left(\frac{1\cdot3}{2\cdot4}\right)^2k^4+\ldots\right],$$

$$t_1(\nu)=2\left(h^{\frac{1}{4}}\sin\pi\nu-h^{\frac{9}{4}}\sin3\pi\nu+h^{\frac{25}{4}}\sin5\pi\nu\ldots\right),$$

$$h=\exp\left(-\pi\frac{K'(k)}{K(k)}\right),$$

$$t_2(\nu)=1-2h\cos2\pi\nu+2h^4\cos4\pi\nu-2h^9\cos6\pi\nu\ldots),$$

$$K'(k)=K(k'),\quad k'=\sqrt{1-k^2}.$$

As a crude approximation, we can write

$$X\approx\alpha_2+(\alpha_2-\alpha_3)\frac{\alpha_1-\alpha_2}{\alpha_1-\alpha_3}\mathrm{sn}^2(\gamma,k).$$

For a weak wave, we also have $\alpha_1-\alpha_3\approx\alpha_2-\alpha_3$; then,

$$X\approx\alpha_2+(\alpha_1-\alpha_2)\mathrm{sn}^2(\gamma,k). \quad (25)$$

Quantity k^2 is divisible by the width-to-spacing ratios of the peaks. If the wave is weak, then $k^2\longrightarrow0$ and $\mathrm{sn}\longrightarrow\sin$. In the general case, the oscillations are anharmonic. With a stronger wave and a larger α_1, the coefficient of the second term on the right-hand side of (20) may be small. Then, in the case of multiple roots, the inversion provides

$$X\approx\frac{\alpha_1+\alpha_2}{2}-\frac{\alpha_1-\alpha_2}{2}\sin\frac{(t-J_2)\omega(u^2-c^2)}{2u^2}. \quad (26)$$

With complex roots, (26) can be simplified if $\alpha_1+\alpha_2\gg\alpha_1-\alpha_2$. Then, (21) becomes

$$t\approx\frac{\mu u^2}{\omega(u^2-c^2)}\left(\frac{\alpha_1+\alpha_2}{2}-\Psi_3\frac{c}{u}\right)F(\varphi,k)+J_3,\quad \theta_1\approx\theta_2.$$

Hence,

$$\left(\tan\frac{\varphi}{2}\right)^2=\frac{1-\cos\varphi}{1+\cos\varphi}\approx\frac{\alpha_1-X}{X-\alpha_2}.$$

$$X \approx \frac{\alpha_1 + \alpha_2}{2} + \frac{\alpha_1 - \alpha_2}{2} \times \mathrm{cn}\frac{(t - J_3)\omega(u^2 - c^2)}{u^2\mu((\alpha_1 + \alpha_2)/2 - \Psi_3 c/u)}. \quad (27)$$

Here,

$$\mathrm{cn}(\varphi, k) = \sqrt{\frac{k'}{k}}\frac{t_2(v)}{t_4(v)}, \quad v = \frac{\varphi}{2K},$$

$$t_2(v) = 2\left(h^{\frac{1}{4}}\cos\pi v + h^{\frac{9}{4}}\cos 3\pi v + h^{\frac{25}{4}}\cos 5\pi v \ldots\right).$$

If $k \ll 1$, the oscillations are sinusoidal: cn $\longrightarrow$ cos. The integral $2C$ enables one to find the cyclotron $\varphi(t)$ provided that $z(t)$ is known. This function, in turn, can be determined from the condition $v_z = p_z c^2/\varepsilon$ with the help of the integral Ψ_3:

$$z(t) = z_0 + \int_{t_0}^{t} c\frac{-\Psi_3 u + cX(t)}{-\Psi_3 c + uX(t)}dt. \quad (28)$$

The function $z(t)$ can be expanded into a linear and an oscillating term, the latter depending on the roots of $f(X)$. In the case of four real roots, the linear term also includes the constant appearing in the expression for sn^2. This constant depends on the strength of wave field (25). In the other cases, there is no such contribution to the linear term. The function $\varphi(t)$ has similar properties. In accord with $X(t)$, there are three possible types of behavior for $\varphi(t)$. This agrees with the conclusions of [12].

(6) For any u higher than c, the dependence of the cyclotron frequency on the momentum components has the form $euH/\sqrt{\Psi_3^2 + (u^2 - c^2)(m^2c^2 + p^2)}$. The resonance curve gives a single value of the steady-state amplitude for $\omega > \omega_2$ and three such values for $0 < \omega < \omega_2$. The motion of the particle in the momentum space is described by the integrals $2C$, J_i, and Ψ_3 (the known one), as well as by the basic equations of motion. Integrals J_i are governed by the roots of $f(X)$. Roots α_1 and α_2 determine turning points in the momentum space. Root α_2 depends on the field strengths only slightly. The oscillation is always anharmonic. In the case of four real roots, the oscillation-period averages of $z(t)$ and $\varphi(t)$ still depend on the wave field strength. Fluctuations of the fields or the initial conditions obviate the need to consider the case of multiple roots.

REFERENCES

1. E. M. Boldyrev, Zh. Tekh. Fiz. **67** (2), 94 (1997) [Tech. Phys. **42**, 206 (1997)].
2. I. I. Ol'khovskiĭ, *Course of Theoretical Mechanics for Physicists* (Nauka, Moscow, 1970).
3. V. Ya. Davydovskiĭ, Fiz. Plazmy **5**, 446 (1979) [Sov. J. Plasma Phys. **5**, 254 (1979)].
4. L. D. Landau and E. M. Lifshitz, *Course of Theoretical Physics*, Vol. 1: *Mechanics* (Nauka, Moscow, 1973; Pergamon, New York, 1988).
5. V. P. Milant'ev, Usp. Fiz. Nauk **167** (1), 3 (1997) [Phys. Usp. **40**, 1 (1997)].
6. L. É. Él'sgol'ts and S. B. Norkin, *Introduction to the Theory of Delay Differential Equations* (Nauka, Moscow, 1971).
7. C. S. Roberts and S. J. Buchsbaum, Phys. Rev. **135**, A381 (1964).
8. V. V. Ternovskiĭ and A. M. Khapaev, Zh. Vychisl. Mat. Mat. Fiz. **36** (6), 114 (1996).
9. A. P. Prudnikov, Yu. A. Brychkov, and O. I. Marichev, *Integrals and Series* (Nauka, Moscow, 1981; Gordon and Breach, New York, 1986).
10. *Higher Transcendental Functions (Bateman Manuscript Project)*, Ed. by A. Erdelyi (McGraw-Hill, New York, 1955; Nauka, Moscow, 1967).
11. V. I. Smirnov, *Course of Higher Mathematics* (Nauka, Moscow, 1974), Vol. III, part 2.
12. B. A. Volodin and A. M. Khapaev, Zh. Vychisl. Mat. Mat. Fiz. **27** (2), 245 (1987).

Translated by A. Sharshakov

Technical Physics, Vol. 46, No. 6, 2001, pp. 723–728. Translated from Zhurnal Tekhnicheskoĭ Fiziki, Vol. 71, No. 6, 2001, pp. 80–86.

Dynamics of a Magnetized Relativistic Electron Beam in Composite Drift Tubes with Virtual Cathodes

A. E. Dubinov and I. A. Efimova

Sarov Physicotechnical Institute, Sarov, Nizhni Novgorod oblast, Russia

e-mail: dubinov@ntc.vniief.ru

Received July 3, 2000; in final form, December 13, 2000

Abstract—A computer simulation of the dynamics of a magnetized electron beam in composite drift tubes with multiple virtual cathodes is presented. For a single-cavity tube, the value of the limiting current is found to equal that given by an exact formula. For two- and three-cavity tubes, it is revealed that the values of the limiting currents are smaller than those reported previously and that the current diagram may have a different structure. These phenomena are attributed to Pierce instability. The efficiency of microwave generation as a function of injection current is examined. It is established that the efficiency is minimum if the current equals any of the limiting values refined. © *2001 MAIK "Nauka/Interperiodica".*

INTRODUCTION

Let us consider a high-current electron beam injected into a closed equipotential cavity. As is known, the cavity develops a potential barrier hindering the passage of the beam if the beam current exceeds a critical level, so that some of the electrons are reflected by the barrier toward the entrance. The region where the electrons injected are stopped and turn about is called the virtual cathode (VC), and the critical value of the beam current (at which the VC is formed) is called the vacuum beam limiting current (VBLC).

The VBLC has been evaluated for cylindrical drift tubes immersed in a strong axial magnetic field; for the early overview, see [1]. In general, the VBLC is expressed as

$$I_{\lim} = \frac{mc^3}{e} G(\gamma^{2/3} - 1)^{3/2} \approx 17 G(\gamma^{2/3} - 1)^{3/2} [\text{kA}], \quad (1)$$

where m and e are the mass and the charge of an electron, respectively; c is the velocity of light; γ is the Lorentz factor of the electrons in the injection plane; and G is a dimensionless geometric factor.

Electron beams with VCs find wide application in many areas of high-current electronics, such as the generation of high-power microwaves by VC oscillations [2–4]; the collective acceleration of positive ions [5, 6]; the generation of intense bursts of soft X-rays by forcing electrons to pass back and forth through a thin electron-to-bremsstrahlung converter [7, 8]; the measurement of the residual gas pressure in an ultrahigh vacuum [9]; etc. Nevertheless, some aspects of the beam dynamics have yet to be understood. Also note that the VBLC values were determined only for a few simple configurations of the drift tube and the beam.

This paper addresses the dynamics of a magnetized relativistic electron beam in composite drift tubes that are made up of coaxial closed cylindrical resonant cavities separated by electron-penetrable sheets of foil. Under certain conditions, such tubes have multiple VCs, whose number may reach $N = 2n - 1$, where n is the number of the cavities. Furthermore, a beam injected into a composite drift tube may pass to the so-called squeezed state [10–12]. The electron dynamics under the transition to this state has not been adequately investigated.

The dynamics is studied by computer simulation using the particle-in-cell (PIC) method. Specifically, we exploited the well-known PIC code KARAT (version 707) for self-consistent simulation in the relativistic case [13].

COMPARING EXACT AND SIMULATED VALUES OF THE LIMITING CURRENT

To check the accuracy of the simulation, we chose a single-cavity configuration with foil sheets at the ends (Fig. 1). It was assumed that the entire computational box is covered by an axial magnetic field. The magnetic

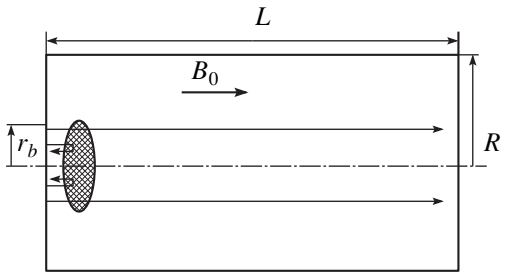

Fig. 1. Schematic diagram of a single-cavity drift tube.

1063-7842/01/4606-0723$21.00 © 2001 MAIK "Nauka/Interperiodica"

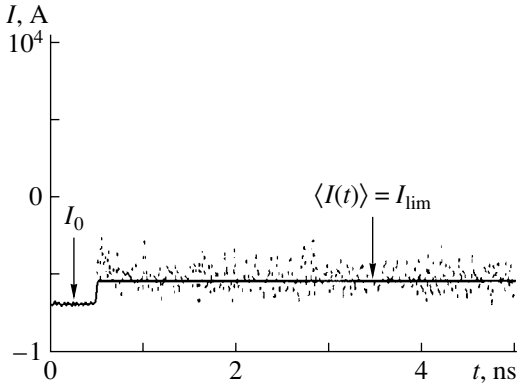

Fig. 2. Single-cavity drift tube with a VC: typical simulated dependence of beam current on time.

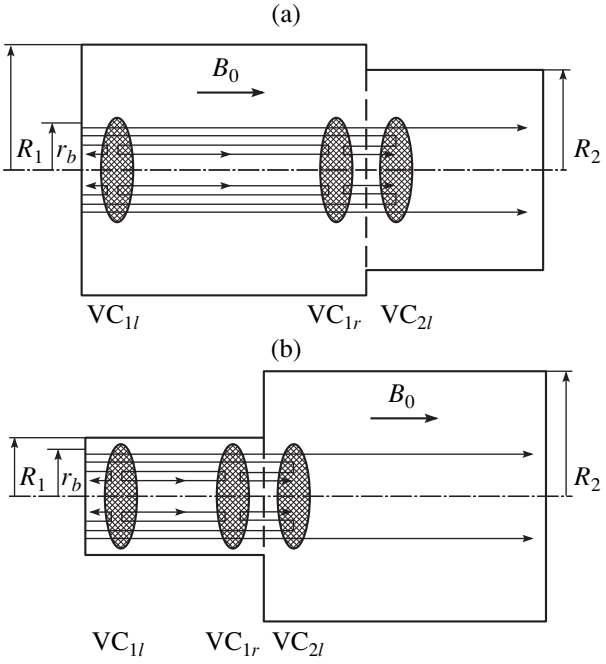

Fig. 3. Geometry of a two-cavity drift tube for (a) case I and (b) case II.

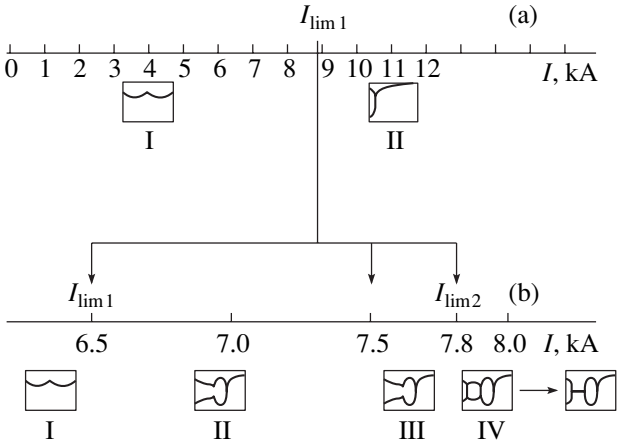

Fig. 4. Case I of the two-cavity configuration: the current diagrams provided by (a) theory and (b) simulation. The insets show sketched phase portraits of the beam.

induction was taken to be 5 T, and the energy of electrons injected was set equal to eU_0 = 511 keV (γ = 2). For a monoenergetic hollow beam, the VBLC is given by the exact formula [14]

$$I_{\lim}^{\text{exact}} = \frac{mc^3}{e}\frac{(\gamma^{2/3}-1)^{3/2}}{\left(\frac{\Delta r}{r_b}+2\ln\frac{R}{b}\right)\left(1-\operatorname{sech}\frac{\mu_1 L}{2R}\right)}, \qquad (2)$$

where μ_1 is the first zero of the Bessel function $J_0(\mu)$.

As already mentioned, the simulation employed the KARAT code [13, 14]. It is useful for solving a wide range of problems in electrodynamics. The code embodies the explicit leapfrog scheme with the conservation of energy, using shifted meshes. Self-consistent solutions of Maxwell equations are thus generated. They are second-order accurate with respect to the coordinates and time. The relativistic equations of particle motion are treated by the PIC method.

The simulation was carried out on a 65×210 mesh. The accuracy was monitored with reference to the energy balance (its maximum deviation was within 2%). It was assumed that the current I_0 injected at the left-hand end of the tube is a step function of time. Different levels of the beam current I_0 were taken. The minimum current at which a VC is formed, $I_{\lim}^{\text{calc}}$, was compared with $I_{\lim}^{\text{exact}}$ evaluated by (2). The results for three values of R are shown in the table (L = 20 cm, r_b = 1.01 cm, and Δr = 0.02 cm). Note that a similar procedure has been performed with the RUBIN code, an early version of KARAT [15].

Another test for accuracy was based on the conception that transit current oscillates about the VBLC in the presence of a VC [16]. We computed the beam currents $\langle I_{\text{up}}(t)\rangle$ and $\langle I_{\text{down}}(t)\rangle$ (see table) at certain cross sections upstream and downstream of the VC, respectively (Fig. 2); their average values are included in the table. The currents vary identically because the total beam current flows through a closed circuit. Initially, the beam current equals the injection current I_0, with the latter exceeding the VBLC in magnitude. Once the VC has formed, the beam current begins oscillating about the VBLC, with $\langle I(t)\rangle = I_{\lim}$, as anticipated. Thus, as follows from the table, the KARAT code can compute the VBLC with a good accuracy.

DYNAMICS OF VC FORMATION IN A TWO-CAVITY DRIFT TUBE

Now that we have checked the capability of KARAT to evaluate the VBLC, let us investigate the behavior of an electron beam in a two-cavity drift tube (Fig. 3). Let us recall that a configuration similar to Fig. 3b but with no foil sheets was considered in [10]. This section pursues the study [11].

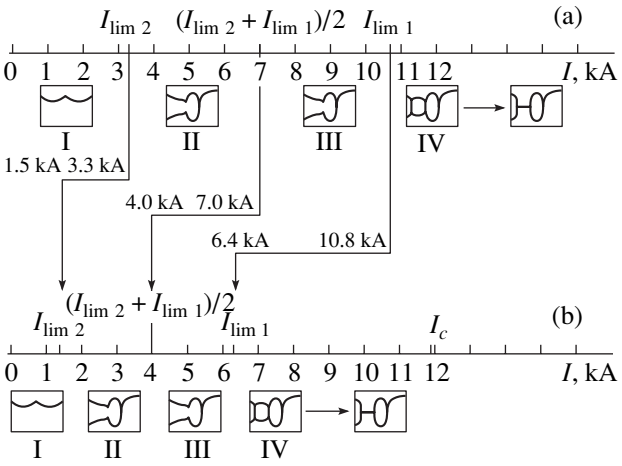

Fig. 5. The same as in Fig. 4 for case II.

Let the left- and the right-hand cavity be labeled 1 and 2, respectively, and let the beam enter the drift tube at its left-hand end. In what follows, the nonzero numerals in subscripts refer to the corresponding cavities.

Current diagrams obtained with the formalism of [10] showed the following.

Case I: $I_{lim\,1} < I_{lim\,2}$ (Fig. 3a). Two regimes of electron flow are possible. (1) If $I_0 < I_{lim\,1}$, the beam passes through the tube with no reflection. (2) If $I_0 > I_{lim\,1}$, then a VC_{1l} is formed near the left-hand end of cavity 1. (From here on, the subscript l or r indicates the cavity end near which the VC is situated.)

Case II: $I_{lim\,1} > I_{lim\,2}$ (Fig. 3b). Four regimes of electron flow are possible. (1) If $I_0 < I_{lim\,2}$, the beam passes through the tube with no reflection. (2) If $I_{lim\,2} < I_0 < 1/2(I_{lim\,1} + I_{lim\,2})$, then a VC_{2l} forms. (3) If $1/2(I_{lim\,1} + I_{lim\,2}) < I_0 < I_{lim\,1}$, then VC_{2l} and VC_{1r} form. (4) If $I_0 > I_{lim\,1}$, then VC_{2l}, VC_{1r}, and VC_{1l} forms and the beam portion between the VC_{1r} and VC_{1l} passes to the squeezed state. Under regime 4, the VC_{2l} arises earlier than the VC_{1l} if $I_0 - I_{lim\,1}$ is not too large; if the difference is high enough, the two VCs arise in reverse order. In what follows, I_c denotes the current at which the VC_{2l} and VC_{1l} form simultaneously.

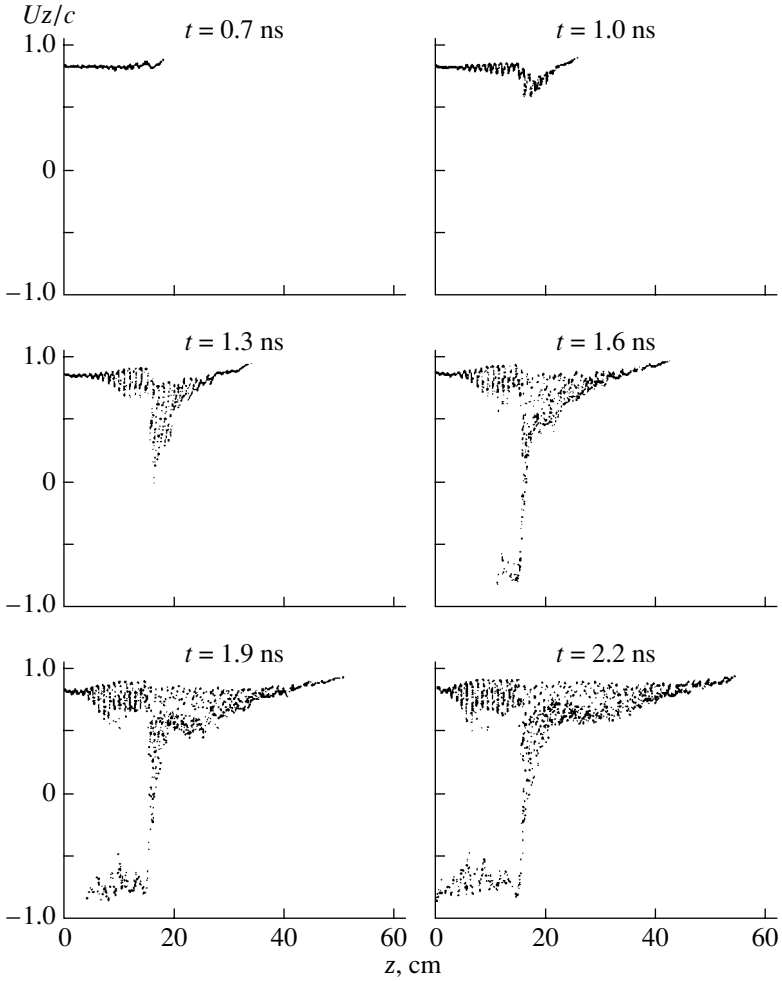

Fig. 6. Regime 2 for case II of the two-cavity configuration: beam evolution in the phase space.

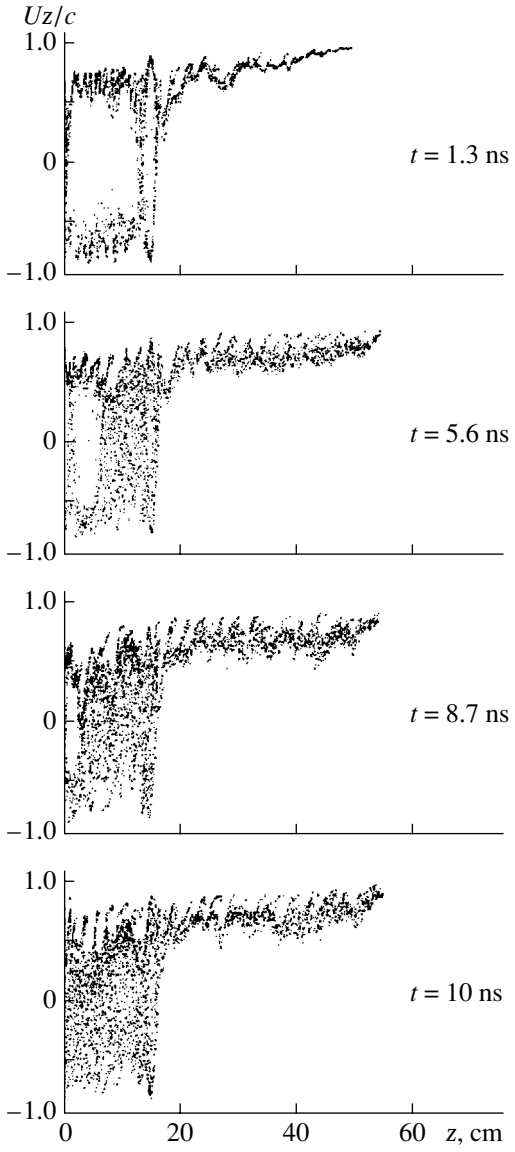

Fig. 7. Regime 4 for case II of the two-cavity configuration: beam evolution in the phase space.

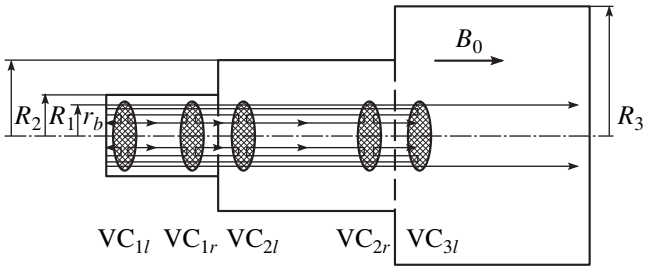

Fig. 8. Geometry of a three-cavity drift tube.

Our simulation yielded a different picture. In the current diagram for case I when $I_{\lim 2} - I_{\lim 1}$ is small, the borderland between the two regimes has a fine structure indicating that two or three VCs are possible (Fig. 4). Also, this interval is shifted toward lower currents. As regards case II, we observed only a marked decrease in $I_{\lim 1}$ and $I_{\lim 2}$: they are lower by a factor of about 2 (Fig. 5).

These findings were explained by analyzing the evolution of the phase portraits of the beam under different regimes. For example, consider regime 2 in case II. Figure 6 shows that the beam produces monotron Pierce instability [17], which arises against the background of the Bursian instability of VC formation and is related to shorter wavelengths. The Pierce instability causes a pronounced beam modulation in momentum. In this situation, at the separating sheet, the total number of electrons with energies lower than the injection energy is much larger than that of higher-energy electrons. Consequently, the electrons enter cavity 2 with lower energies [according to (1)], which results in a decreased $I_{\lim 2}$ and, hence, in restructuring the current diagrams.

Thus, we revealed that the Pierce instability is responsible for the shift and restructuring of the current diagrams for the two-cavity drift tube. Furthermore, we believe that forward- and backward-moving electrons (the two-stream state) cannot coexist in cavity 1 for long, since instabilities may arise in the beam, as suggested by the phase portraits with VC_{2l} (cavity 2). It was estimated that the length of cavity 1 and the strengths of the forward and backward currents may be sufficient to produce two-stream instability [18].

We conducted a special investigation into this matter. It was found that there occurs another type of instability under the conditions in hand, namely, the formation of the squeezed state in the beam. This type of instability develops at a higher rate than the two-stream instability. The evolution of the phase portrait in this case is depicted by Fig. 7. Notice that the switching from the two-stream to the squeezed state is a wave phenomenon, in accord with [10–12]. The switching wave travels in the direction opposite to the forward stream with a speed estimated at $\approx 3 \times 10^9$ cm/s. Again, the domains favorable for the squeezed state were found to be shifted to lower currents.

CURRENT DIAGRAMS OF A THREE-CAVITY DRIFT TUBE

For a three-cavity drift tube, we have to consider as many as six cases, some of them having up to ten regimes.

Here, we restrict ourselves to the case $I_{\lim 1} > I_{\lim 2} > I_{\lim 3}$ (Fig. 8). Figure 9 presents a current diagram obtained by the simulation. Some regimes exist over narrow or even overlapping intervals of the current, making analysis difficult; therefore, the diagram displays six main intervals only. Figure 9 also shows the order in which VCs form. Just as with the two-cavity configuration, the limiting currents were found to be somewhat lower. The other cases can be represented by

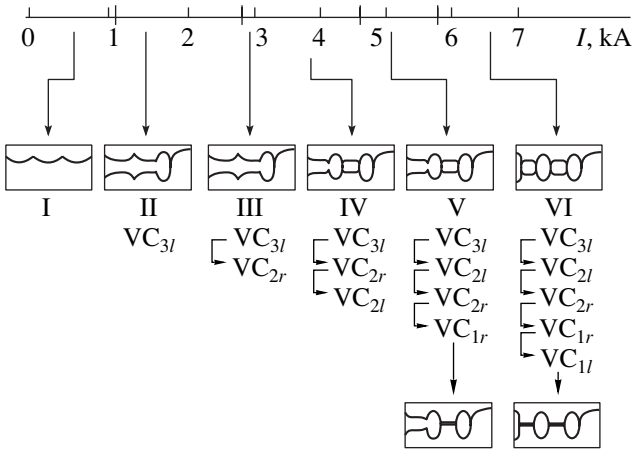

Fig. 9. Current diagram for the three-cavity configuration.

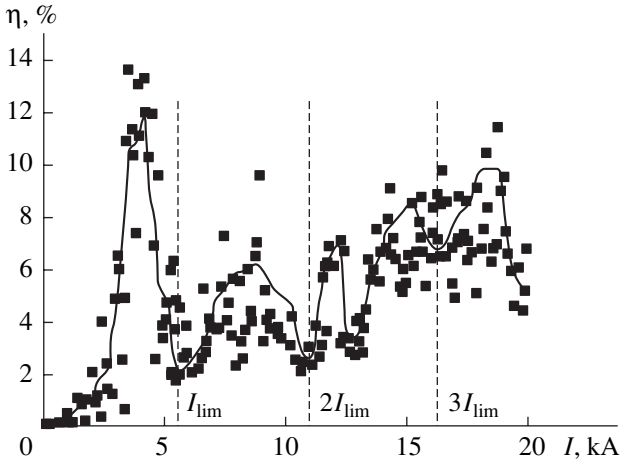

Fig. 10. Microwave generation efficiency vs. beam current for the single-cavity configuration.

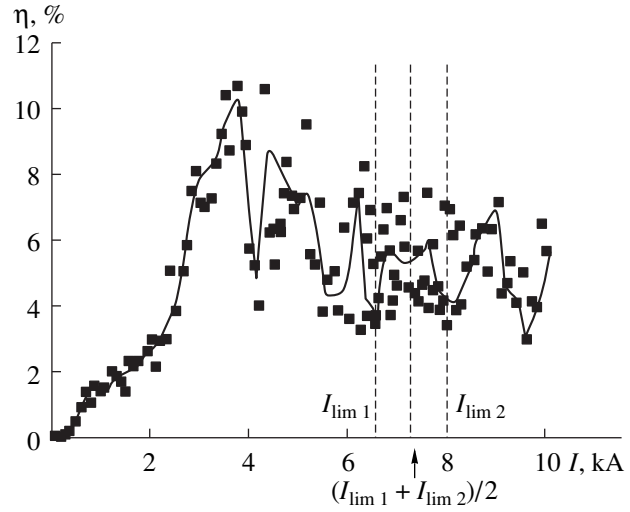

Fig. 11. Microwave generation efficiency vs. beam current for the two-cavity configuration in case I.

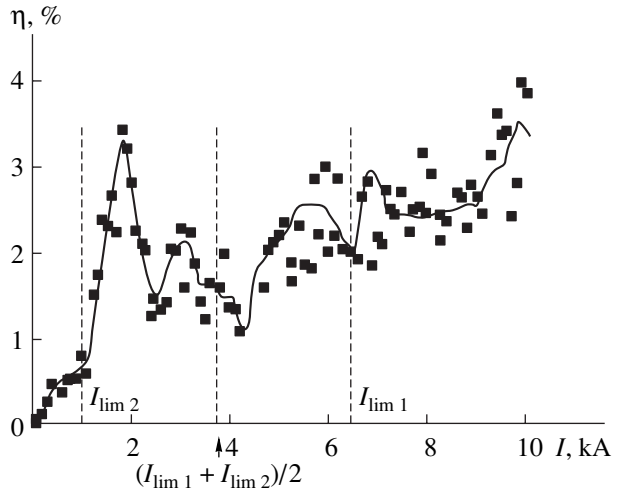

Fig. 12. Microwave generation efficiency vs. beam current for the two-cavity configuration in case II.

similar diagrams, but the order of VC formation may change.

EFFICIENCY OF MICROWAVE GENERATION IN SINGLE- AND TWO-CAVITY DRIFT TUBES

An important issue in microwave design is the efficiency with which electromagnetic radiation is generated. In the context of our study, this line of research should address two main problems: (1) What are the ways to make VCs emit in phase? (2) What are the ways to match the waves emitted with the oscillations resulting from the Pierce instability? Hopefully, there may be regimes under which the waves generated would amplify each other. The idea could be instrumental in creating more efficient vircators, which would use multiple VCs.

To answer the above questions, the following investigation was performed. We consider a two-cavity configuration with an open output end, at which radiation conditions are defined. The profile of the magnetic field was tailored so as to allow the transit electrons to reach the wall of cavity 2 downstream of the rightmost VC. The trick enabled us to create a closed circuit for the transit current and to compute the electromagnetic

Table

R, cm	$I_{\text{lim}}^{\text{exact}}$, kA	$I_{\text{lim}}^{\text{calc}}$, kA	$\langle I_{\text{up}}(t)\rangle$, kA	$\langle I_{\text{down}}(t)\rangle$, kA
2.0	5.55	5.6	5.59	5.63
2.5	4.12	4.1	4.14	4.12
3.0	3.51	3.4	3.50	3.51

wave emerging from the drift tube. In this way we evaluated (1) the flux P of the Poynting vector through the tube cross section near the output end and (2) the generation efficiency $\eta = 100\% P/I_0U_0$.

Earlier [19], the problem of maximizing the generation efficiency and power was solved analytically and numerically for a single-cavity configuration. The analytical treatment yielded that the generation efficiency is maximum at $I_0 = 2I_{\lim}$ and that the power is maximum at $I_0 = 3I_{\lim}$. These conclusions were supported by the numerical simulation [19]. However, the analysis neglected the Pierce instability and the simulation used a large step size for I_0.

Our investigation covers a single-cavity drift tube as well. We closely examined the dependence of η on the injection current I_0 for $R = 2$ cm (see the table). An example is given in Fig. 10. It shows that the maximum efficiency (14%) relates to the Pierce instability, when no VC forms, and that the local minima of $\eta(I_0)$ are at $I_0 = I_{\lim}$, $2I_{\lim}$, $3I_{\lim}$, and so on. Similar behavior was observed for the other values of R.

The two-cavity case (Fig. 3a) is illustrated by Figs. 11 and 12. Note that the currents that minimize η are the limiting currents refined (see the section on the dynamics of VC formation in a two-cavity drift tube). These results have yet to be understood. As a possible explanation, we conjecture that the increment δ of the Bursian instability is very small when the injection current is near limiting currents: $\lim_{(I_0 - I_{\lim}) \to 0} \delta = 0$ [3].

CONCLUSIONS

We have computed the limiting currents and simulated the dynamics of a magnetized electron beam in composite drift tubes with multiple VCs. The main findings are as follows.

For a single-cavity tube, the computed values of the limiting current are very close to those given by the exact formula.

For two- and three-cavity tubes, the values of the limiting currents are lower than those reported previously, which results in shifted or even restructured current diagrams. The values refined appear to reflect the build-up of Pierce instability.

The transition to the squeezed state is a wave phenomenon. The domains with the squeezed state are also found to be shifted toward lower currents.

The microwave generation efficiency as a function of injection current is minimum if the current equals a limiting value. This behavior may be due to a decrease in the corresponding increments of the Bursian instability.

ACKNOWLEDGMENTS

We are grateful to A.A. Rukhadze for helpful consultation. The assistance of V.P. Tarakanov is appreciated as well. The support received by one of the authors within the program “George Soros Associate Professors” is gratefully acknowledged.

REFERENCES

1. L. S. Bogdankevich and A. A. Rukhadze, Usp. Fiz. Nauk **103**, 609 (1971) [Sov. Phys. Usp. **14**, 163 (1971)].
2. A. A. Rukhadze, S. D. Stolbetsov, and V. P. Tarakanov, Radiotekh. Éektron. (Moscow) **37**, 385 (1992).
3. B. V. Alyokhin, A. E. Dubinov, V. D. Selemir, *et al.*, IEEE Trans. Plasma Sci. **22**, 945 (1994).
4. A. E. Dubinov and V. D. Selemir, Zarubezhn. Radioélektron., No. 4, 54 (1995).
5. Ya. B. Faĭnberg, in *Proceedings of the Conference on Nuclear Research Devoted to the 50th Anniversary of the First Fission Reaction in the USSR* (TsNII Atominform, Moscow, 1983), part 1, p. 222.
6. V. M. Bystritskiĭ and A. N. Didenko, *High-Power Ion Beams* (Énergoatomizdat, Moscow, 1984).
7. N. I. Zavada, I. A. Troshkin, K. F. Zelenskiĭ, *et al.*, Vopr. At. Nauki Tekh., Ser. Fiz. Radiats. Vozdeĭstv. Radiofiz. Apparat., Nos. 3–4, 23 (1994).
8. T. W. L. Sanford, J. A. Halbleib, G. Cooperstein, and B. V. Weber, IEEE Trans. Nucl. Sci. **42**, 1902 (1995).
9. O. Lloyd, Br. J. Appl. Phys. **17**, 357 (1996).
10. A. M. Ignatov and V. P. Tarakanov, Phys. Plasmas **1**, 741 (1994).
11. A. E. Dubinov, Pis’ma Zh. Tekh. Fiz. **23** (22), 29 (1997) [Tech. Phys. Lett. **23**, 870 (1997)].
12. A. E. Dubinov, Radiotekh. Élektron. (Moscow) **45**, 875 (2000).
13. V. P. Tarakanov, *User’s Manual for Code Karat* (Berkley Research Associate Inc., Springfield, 1992).
14. P. V. Koteteshvili, P. V. Rybak, and V. P. Tarakanov, Preprint No. 44, IOFAN (General Physics Institute, Academy of Sciences of USSR, Moscow, 1991).
15. B. A. Al’terkop, A. Yu. Sokulin, and V. P. Tarakanov, Fiz. Plazmy **15**, 974 (1989) [Sov. J. Plasma Phys. **15**, 564 (1989)].
16. A. E. Dubinov and V. D. Selemir, Pis’ma Zh. Tekh. Fiz. **24** (4), 41 (1998) [Tech. Phys. Lett. **24**, 142 (1998)].
17. D. N. Klochkov, M. Yu. Pekar, and A. A. Rukhadze, Zh. Éksp. Teor. Fiz. **115**, 2037 (1999) [JETP **88**, 1115 (1999)].
18. R. Briggs, in *Advances in Plasma Physics*, Ed. by A. Simon and W. B. Thompson (Wiley, New York, 1971; Mir, Moscow, 1974).
19. B. A. Al’terkop, A. A. Rukhadze, A. Yu. Sokulin, and V. P. Tarakanov, Zh. Tekh. Fiz. **61** (9), 115 (1991) [Sov. Phys. Tech. Phys. **36**, 1033 (1991)].

Translated by A. Sharshakov

Technical Physics, Vol. 46, No. 6, 2001, pp. 729–735. Translated from Zhurnal Tekhnicheskoĭ Fiziki, Vol. 71, No. 6, 2001, pp. 87–94.

Low-Temperature Oxidation of CoCu Films with Long-Term Irradiation by Oxygen Ion Beams

A. I. Stognij, S. V. Koryakin, and V. A. Virchenko

Institute of Solid-State and Semiconductor Physics, Belarussian Academy of Sciences, ul. Brovki 17, Minsk, 220072 Belarus

e-mail: stognij@ifttp.bas-net.by

Received July 17, 2000

Abstract—The surface and surface layers of Co_xCu_{100-x} inhomogeneous thin films irradiated by an oxygen ion beam for a long time (to 100 min) are studied. The films are obtained by electrolytic deposition. With X-ray photoelectron spectroscopy and conversion electron Mössbauer spectroscopy, it is shown that the irradiation leads to the formation of an oxidized surface layer. The continuity and thickness of the layer depend on the roughness of the initial film. For a cobalt content of $8 \le x \le 20$ at. %, the oxide layer is continuous and nonuniform in thickness, the mean thickness being estimated at several tens of nanometers. The interface between the layer and the underlying film is sharp. The films irradiated are smoother than the as-deposited ones. The formation of the oxide layer is treated in terms of a qualitative model. *© 2001 MAIK "Nauka/Interperiodica".*

INTRODUCTION

Low-temperature oxidation of metals and thin metal films has been the subject of much investigation over many years because of its fundamental and practical importance [1, 2]. The structure and properties of inhomogeneous CoCu films have been extensively studied over the past 20 years [3]. These films seem to be promising for the practical implementation of the giant magnetoresistance effect at room temperature. The stability of the films against environmental effects, corrosive gases, and irradiation by charged particles is less well understood. However, thin-film-based electronic devices frequently operate under severe environmental conditions. The effect of ion irradiation on the properties of electrodeposited inhomogeneous CoCu films was reported in [4, 5]. It was shown that long-term low-energy oxygen ion irradiation produces an oxidized layer on the film surface. This layer stabilizes the properties of the initial films and prevents their degradation during temperature cycling (from –50 to +150°C) in air. In this work, we explore the properties of the oxide layer further so as to establish possible formation mechanisms.

EXPERIMENT

Co_xCu_{100-x} (x = 5–20 at. %) inhomogeneous films used in this work were obtained with the technique developed in [3]. Substrates were pyroceramic plates covered by an amorphous nickel phosphide layer, as well as copper and aluminum foils. The thickness of the films was no more than 2.5 μm. Some of the films deposited on the aluminum foil were doped by ^{57}Fe isotopes during electrodeposition. The concentration of the isotopes was no more than 1 at. %. Tentative studies have shown that the undoped and iron-doped films have similar X-ray diffraction spectra and surface morphologies, as well as equal resistivities.

The films were irradiated in a vacuum setup with a residual pressure no higher than 1×10^{-3} Pa. The oxygen pressure did not exceed 8×10^{-3} Pa. Radiation from a wide-aperture ion source with a hollow cold cathode was employed [6]. The energy and current density of the oxygen ions were E = 650 eV and j = 0.25 mA/cm^2, respectively.

The films to be irradiated were mounted on a movable water-cooled support. The temperature was kept with an accuracy of 1°C by chromel–alumel thermocouples. During the irradiation, the film temperature was no more than 50°C. This was provided by using the continuous–periodic regime of irradiation. In a single vacuum cycle, the films were repeatedly irradiated for 5 min and then cooled for 6 min until a required irradiation time was achieved. The total irradiation time was taken as the irradiation duration.

During the irradiation, products of surface sputtering were deposited on single-crystal silicon wafers thinned down to 50 μm and then were examined by electron probe analysis and optical methods. Since the surface of the samples was very rough and irregular, the sputtering process was characterized by the intensity of sputtering rather than by its rate. The sputtering intensity was defined as the weight of the deposit that was sputtered in a unit time across a unit surface area onto the mirror surface of the single-crystal silicon wafers. To collect the necessary amount (weight) of the deposit, several films of the same composition and of

1063-7842/01/4606-0729$21.00 © 2001 MAIK "Nauka/Interperiodica"

the total surface area 40 cm^2 were sputtered simultaneously.

The composition of the surface layer and the nature of chemical bonds in it were examined with X-ray photoelectron spectroscopy (XPS). A magnesium anode (MgK_α radiation with a photon energy of 1253.6 eV) was used as an X-ray source. The resolution of the electrical analyzer was 0.5 eV, and the escape depth of photoelectrons was no more than 15 nm. The bond energy scale was calibrated against the Cu(K_{LMM}) line with an energy of 918.6 eV. The lines C(1*x*), O(1*s*), Co(2*p*), and Cu(2*p*) were recorded.

The surface morphology and the composition of the surface layer (to a thickness of 150 nm) were examined with an SEM equipped with an energy dispersion X-ray spectrometer.

The surface layer (to a depth of 150 nm) was also studied by conversion electron Mössbauer spectroscopy (CEMS). ^{57}Co isotopes embedded in the Rh matrix served as a gamma source. Isomeric chemical shifts were found with respect to α-Fe.

The resistivity of the films was measured with the standard four-point probe technique [7].

EXPERIMENTAL RESULTS

In appearance, the as-deposited films can be subdivided into two groups. Those from group 1 (Co < 8 at. %) have a rough and dull surface. The films from group 2 (Co > 8 at. %) have a mirror surface with metallic luster. A fragment of an as-deposited Co_6Cu_{94} film with the highly rough surface is shown in Fig. 1a (×1500 and ×10 000 magnifications). The smoother surface of an as-deposited $Co_{11}Cu_{89}$ film is shown in Fig. 1b (the same magnifications).

During the irradiation, the sheet resistivity of the films grows and the sputtering intensity drops. For the group-1 films, the sheet resistivity does not saturate,

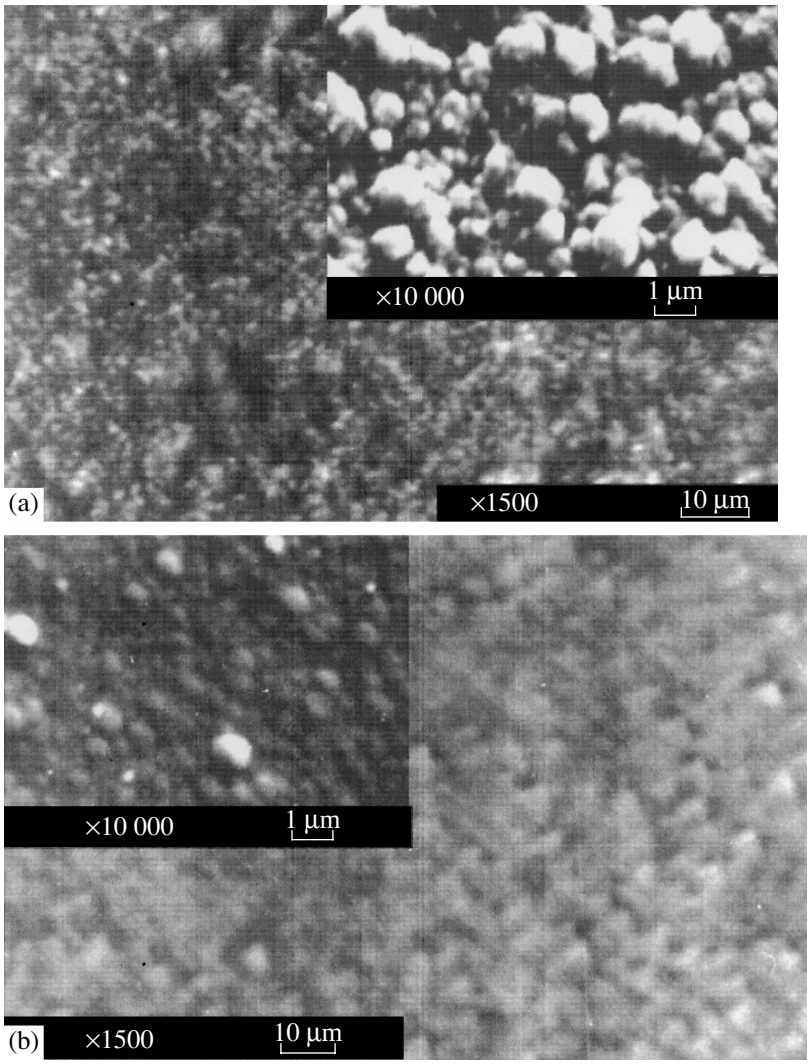

Fig. 1. Surface of the as-deposited CoCu films. The cobalt content is (a) 6 and (b) 11 at. %.

while the resistivity of the films from group 2 exhibits a plateau after 40-min irradiation. For both groups, the sputtering intensity sharply drops within the first 10–15 min and then varies insignificantly. Simultaneously, the films change color. The group-1 films turn dark. The group-2 films change initial metallic luster to blue color (within 40 min of irradiation), which is subsequently retained.

Long-term (for more than 40 min) irradiation noticeably changes the surface relief. Large irregularities on the surface of the Co_6Cu_{94} film irradiated (Fig. 2a) become smoother. The spread in their sizes and their mean size decrease compared with the as-deposited films (Fig. 1a). The relief is also smoothed out for the group-2 films: fine irregularities coalesce to form larger clusters and surface asperities flatten (Fig. 2a).

Electron probe microanalysis data show that the irradiation changes the composition of the surface layer (to a depth of 0.1 μm). It becomes enriched with copper (but by no more than 10% against the initial composition). However, the mean composition of the film before and after the irradiation remains the same.

Postirradiation XPS spectra for the group-1 and group-2 films differ. Figures 3 and 4 demonstrate the C(1*s*), O(1*s*), and Cu(2*p*) lines for the Co_6Cu_{94} and $Co_{11}Cu_{89}$ films before and after 50-min irradiation. For the as-deposited films from both groups, the photoelectron C(1*s*) and O(1*s*) lines are rather broad, which is usually associated with the fact that carbon and oxygen atoms form various chemical bonds on the surface and in the surface layer [8]. As follows from the changes in these lines, the carbon content on the surface increases for the group-1 films and decreases for the films of group 2. However, it is known [9] that irradiation by low-energy ions removes carbon from the surface and increases the oxygen content. This is observed for the group-2 films. The rise in the intensity of the C(1*s*) line

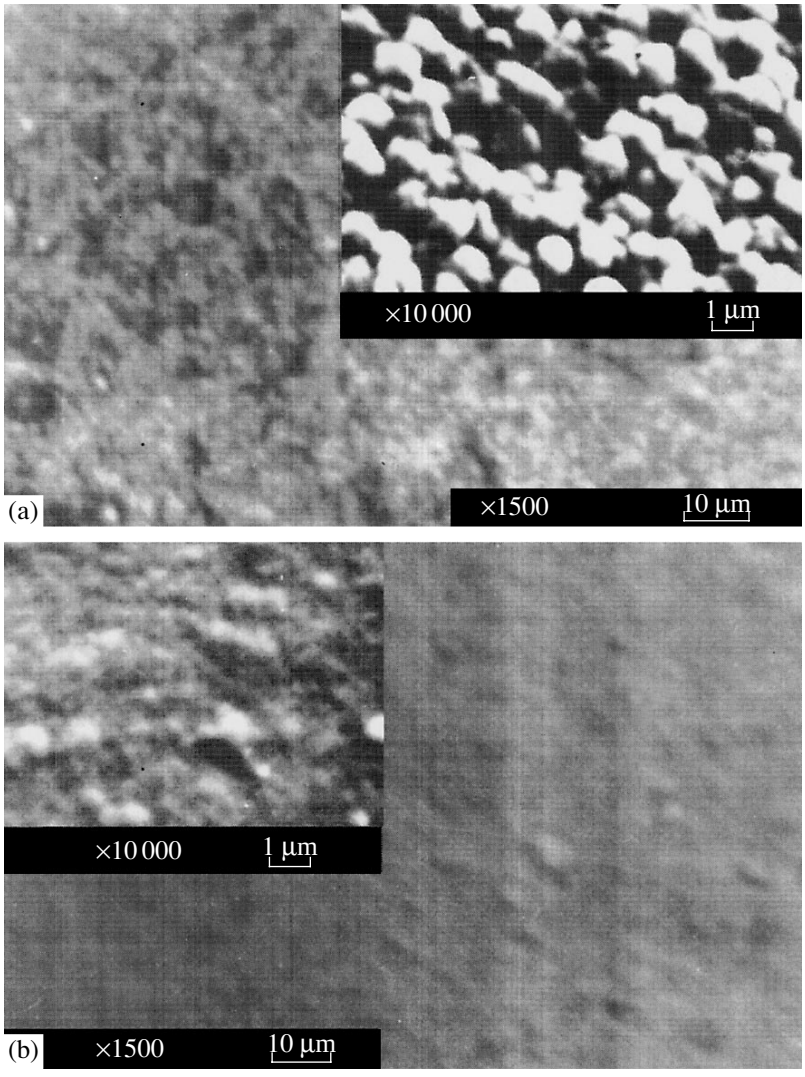

Fig. 2. Surface of the oxygen-irradiated CoCu films (irradiation time 50 min). The cobalt content is (a) 6 and (b) 11 at. %.

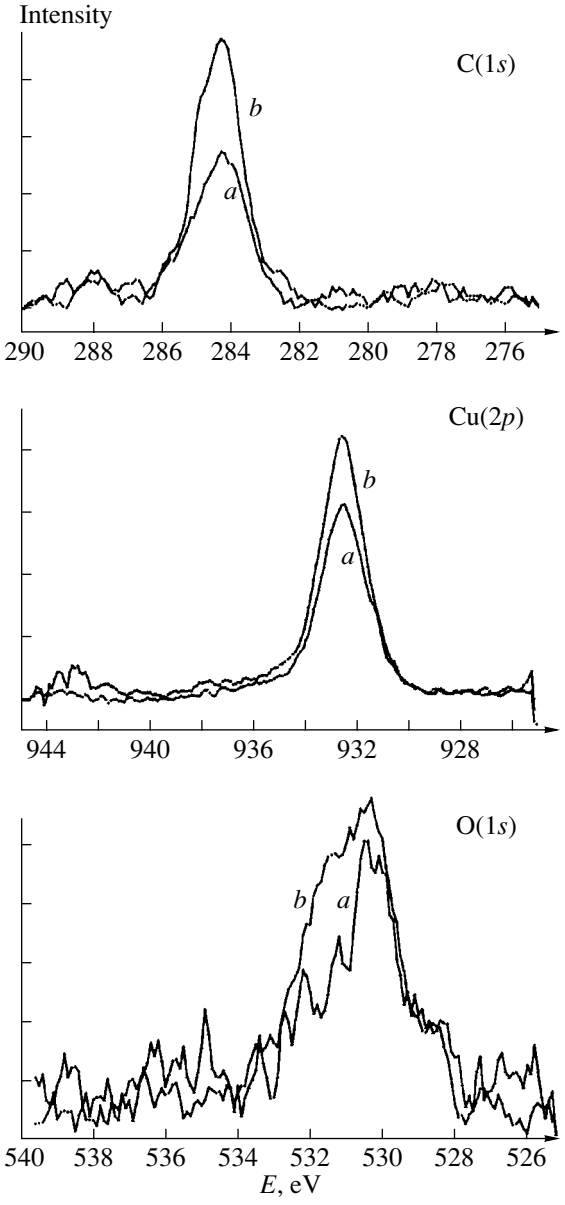

Fig. 3. XPS spectra for the (*a*) as-deposited and (*b*) irradiated (for 50 min) CoCu films with the Co content 6 at. %.

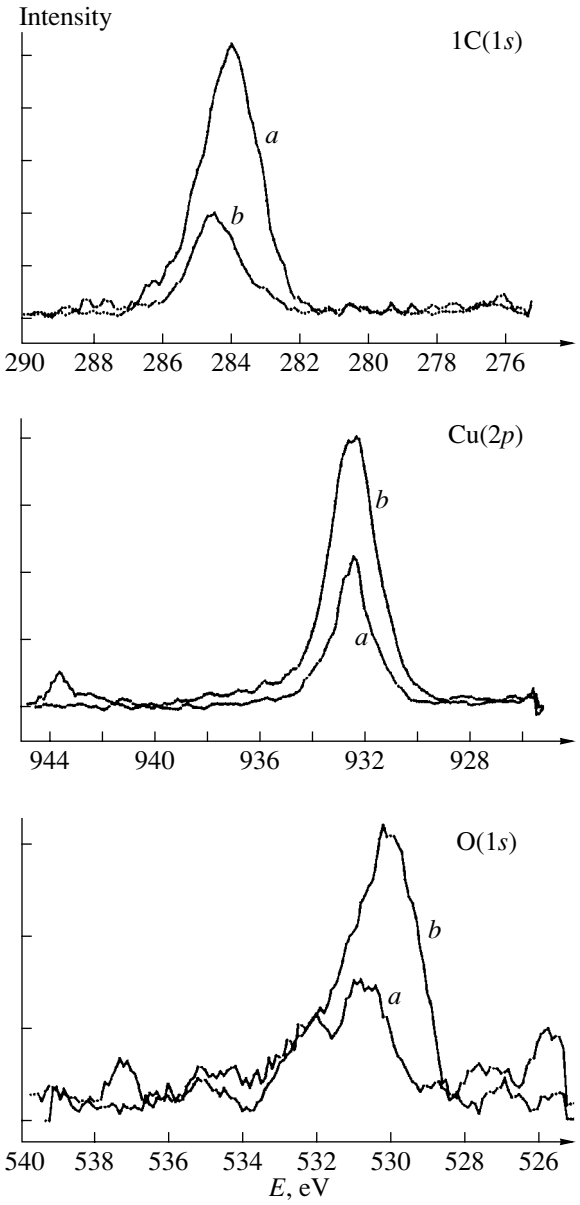

Fig. 4. The same as in Fig. 3 for the films with the Co content 11 at. %.

for the group-1 films may be related to specific features of sputtering of the very rough surface (Figs. 1a, 2a), where the sorptive capacity of "shaded" areas (beyond the reach for irradiation) increases because of the accumulation of products of resputtering there. The slight growth of the oxygen content is also observed for the first group.

After the irradiation, the XPS Cu(2*p*) line for group 1 slightly shifts toward higher bond energies and its intensity somewhat grows. For group 2, prior to the irradiation, this line has a small peak at energies slightly less than 932.5 eV and a higher and sharper peak at greater energies. After the irradiation, the line becomes stronger and has two peaks with nearly the same heights at energies slightly less and slightly more than 932.5 eV. The peaks are 1 eV apart. Such postirradiation modifications of the Cu(2*p*) line may be interpreted as the formation of CuO oxide on the surface [10]. The rise in the intensity of the Cu(2*p*) line for the films of both groups can be explained by smoothening the surface relief. In this case, the relative surface area that is parallel to the film plane (normal to the direction of ion incidence) increases and, hence, the probability of photoelectron escape from the surface grows. According to Figs. 1a and 2a, for group 1, large irregularities flatten for the most part and smoothing is less pronounced than for the films of group 2 (Figs. 1b, 2b).

In the latter case, smoothing is more distinct and takes place over the entire surface.

Both before and after the irradiation, the XPS Co(2*p*) lines are broken and faint even for the films with a Co content as high as 20 at.%. Therefore, we failed to treat changes in the cobalt state on the surface. Note, however, that the magnetic and crystallographic properties of inhomogeneous CoCu films in general and those obtained by electrodeposition in particular [11] depend on the uniformity of the cobalt distribution over the copper matrix and on the state in which cobalt particles are present. The Co(2*p*) lines obtained indicate at least that the cobalt clusters are absent on the surface on the copper matrix. This is indirect evidence that the cobalt distribution in electrodeposited CoCu films is highly uniform, which agrees with earlier results [3, 11].

Electron probe analysis data for the material deposited on the silicon wafers show that the cobalt content in the deposit differs from the mean content of cobalt in the films subjected to irradiation by no more than 10% and does not depend on the irradiation time. Therefore, the low intensity of the cobalt lines even if its amount in the films is high may be an indication of its specific state in the surface layer of the films.

CEMS spectra for Co_6Cu_{94}, $Co_{11}Cu_{89}$, and $Co_{20}Cu_{80}$ films that were recorded before irradiation and after 50-min irradiation are shown in Fig. 5.

For the as-deposited Co_6Cu_{94} film (Fig. 5a), the spectrum consists of two lines of roughly equal intensities. The spectrum was analyzed within the model of two singlets as applied to the iron ion positions. The lines are characterized by the isomeric shift δ_1 = 0.24 mm/s (on the right) and δ_2 = –0.09 mm/s (on the left). The value of δ_1 corresponds to the solid solution of iron in copper [12]. The second component, δ_2, is related to iron atoms with CoCu around. The introduction of Co atoms causes a decrease in the concentration of *d* electrons around the iron atoms and, hence, an increase in that of *s* electrons. The latter effect leads to a decrease in the isomeric shift, which is observed experimentally. The insignificant broadening of the singlets (Γ = 0.35–0.40 mm/s) is due to local inhomogeneities in the surroundings of the resonant atom. The irradiation of the Co_6Cu_{94} film by oxygen ions causes no appreciable changes in the initial spectrum (Fig. 5b). This means that the local state of the iron atoms remains the same and that the effect of the irradiation on the composition of the surface layer about 150 nm thick is negligible.

The spectrum of the initial $Co_{11}Cu_{89}$ alloy (Fig. 5c) is in many ways similar to that of Co_6Cu_{94}. The only difference is the change in the ratio of the intensities of the partial lines in the spectrum. The ratio of the integral intensities of the right- and left-hand components is about 85% in this case. This means that iron is incorporated into the combined CoCu environment more readily than into the purely copper one. This statement is corroborated by the higher concentration of cobalt in the initial composition of the film. One more feature is worth noting. The difference in the positions of the peaks on the velocity axis for the as-deposited Co_6Cu_{94} and $Co_{11}Cu_{89}$ films is the same. In the case of a doublet, this difference depends on the amount of quadrupole splitting. A change in the Co/Cu ratio in the system would alter the electric field gradient across the iron nucleus and, hence, the amount of quadrupole splitting, which is not the case. Thus, our model for spectrum analysis, which deals with two singlets instead of one doublet, seems to be valid.

The spectra for inhomogeneous oxygen-irradiated and as-deposited $Co_{11}Cu_{89}$ films (Figs. 5b, 5d, respectively) considerably differ. After the irradiation, the spectrum broadens and its centroid shifts toward positive velocities. In Fig. 5d, the hyperfine lines are poorly resolved in the spectrum, presumably because of the redistribution of their intensities. Simultaneously, the intensity at the center of the spectrum grows and a new component appears in the positive range of velocities. Therefore, this experimental spectrum can be considered as consisting of two singlets and one doublet. For the singlets, the isomeric shifts do not change after the irradiation. It can therefore be argued that the Fe–Cu and Fe–(CoCu) environments around the resonant atom are retained and a new component with a quadrupole doublet appears. The isomeric shift and the amount of quadrupole splitting for the doublet are found to be δ = 0.46 mm/s and ΔE = 0.80 mm/s. Such values are typical of the ^{57}Fe Mössbauer spectrum taken from CuO oxide [12, 13]. Along with the copper oxide, cobalt oxides may form. CEMS studies of CoO using impurity iron atoms were reported in [14]. At 298 K, the spectrum had two isolated lines with the isomeric shifts δ_1 = 0.22 mm/s and δ_2 = 0.87 mm/s. The former corresponded to the Fe^{3+} oxidation state in the cobalt oxide, and the latter was assigned to the Fe^{2+} state. The ^{57}Fe Mössbauer spectral lines in the copper and cobalt oxides partially overlapped. The doublet in the $Co_{11}Cu_{89}$ film irradiated is also broadened; therefore, the possibility of cobalt oxide formation in the 150-nm-thick surface layer must not be ruled out. This is also supported by the fact that the intensity of the Fe–Cu and Fe–(CoCu) singlets decreases after the irradiation, indicating that some copper and cobalt atoms produce associated oxides.

The spectrum of the as-deposited $Co_{20}Cu_{80}$ film (Fig. 5e) has two lines with the isomeric shifts δ_2 = –0.14 mm/s and δ_1 = 0.30 mm/s. They refer to iron atoms in the Fe–(CoCu) and Fe–Cu environments. The minor decrease in the isomeric shift for the first line is due to a larger number of cobalt atoms around iron because of the larger cobalt content in the alloy. The irradiation causes changes (Fig. 5f) similar to those for

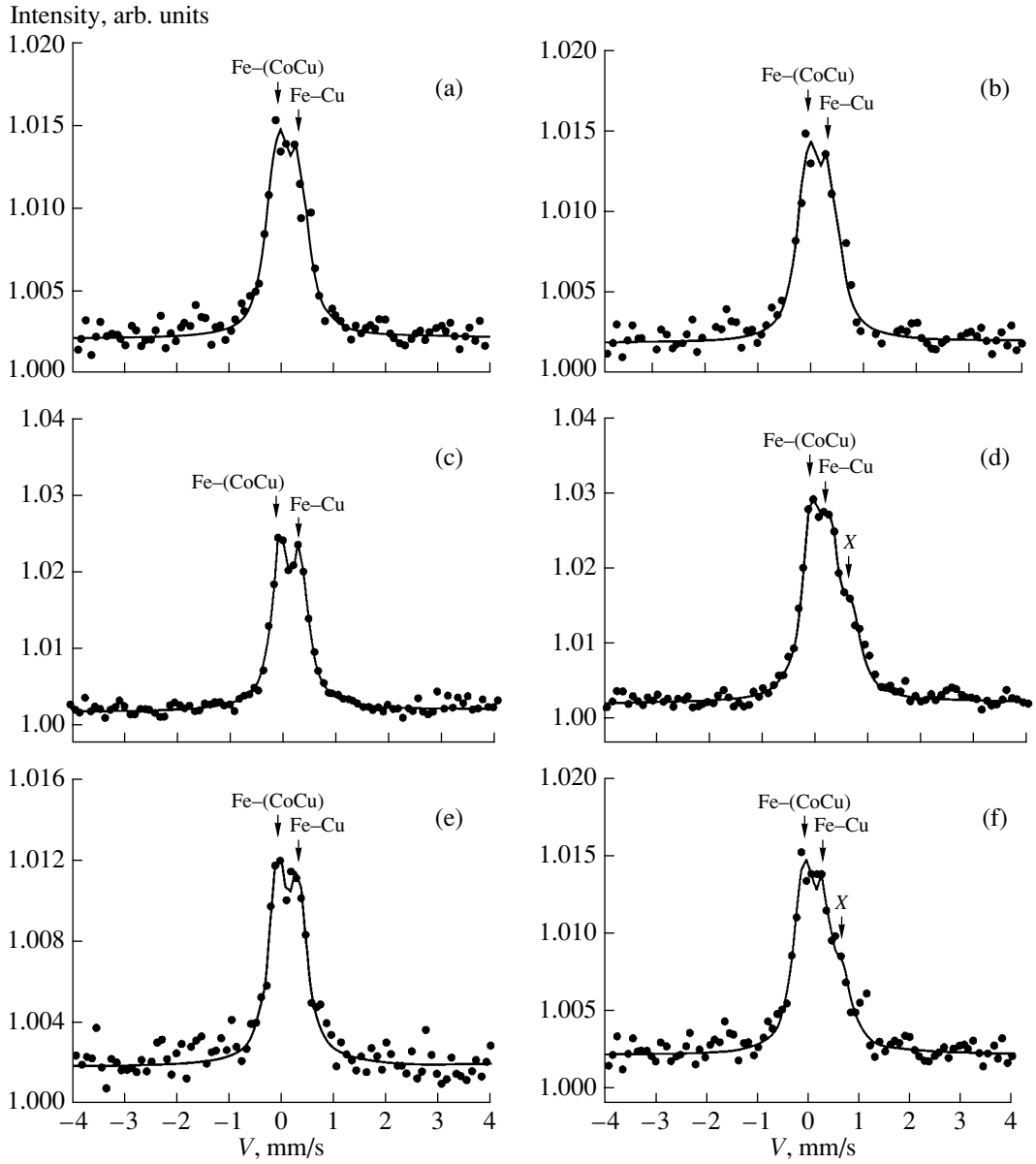

Fig. 5. CEMS spectra for the (a, c, e) as-deposited and (b, d, f) oxygen-irradiated CoCu films. The Co content is (a, b) 6, (c, d) 11, and (e, f) 20 at. %.

the $Co_{11}Cu_{89}$ film (Fig. 5d). The partial components of both spectra also behave in a like manner.

On the whole, the CEMS spectra of the oxygen-irradiated films with the cobalt content $x \geq 8$ at. % testify that the oxide layer does form on the surface, its average thickness being several tens of nanometers.

To directly measure the thickness of this oxide, the films with $x \geq 8$ at. % were exposed to 0.5-keV argon ions with a beam current density of 0.3 mA/cm^2. The oxide was removed for 3–5 min, as indicated by metallic luster recovered and the resistivity value close to that for the nonirradiated films.

DISCUSSION

Thus, we studied long-term low-temperature (50°C) irradiation of electrodeposited inhomogeneous CoCu films (with the cobalt content x = 6–20 at. %) by low-energy (E = 650 eV, j = 0.25 mA/cm^2) oxygen ions. The basic results are as follows.

(i) A continuous layer nonuniform in thickness and consisting of cobalt and copper oxides forms on the surface of the films where the Co content varied from 8 to 20 at. %. It is several tens of nanometers thick and favors surface planarization.

(ii) After the irradiation, the surface of these films becomes free of organic impurities.

(iii) The structure of the layer is essentially dependent on the surface roughness of the as-deposited films.

Based on the aforesaid, we have developed a qualitative nonthermal model of an oxide layer growing on the oxygen-irradiated surface to a thickness of several tens of nanometers. The overall process is subdivided into three stages. At the first stage, lasting 10 min, oxide islands about 1 nm thick form directly by the action of reactive oxygen ions on those areas oriented normally to the direction of ion incidence. On these oxidized areas, the rate of sputtering slows down in comparison with the bare surface because of the difference in the partial sputtering yields for the metals and their oxides [15, 16]. Subsequently, the relative surface area normal to the direction of ion incidence slowly increases, because unoxidized microasperities are sputtered out and oxidized products of sputtering are removed (resputtered) from areas accessible to the ion beam to those beyond its reach (shaded). Eventually, the microasperities on the as-deposited films flatten and the mean thickness of the oxide layer increases. At the third stage (the irradiation time is more than 40 min), the processes of sputtering and oxide formation equilibrate. At this stage, the oxide is present on the surface and the film condition remains almost unchanged for as long as the mass sputtered is much less than the mass of the initial film.

It should be noted that this mechanism also applies to CoCu films where the Co content is less than 8 at. %. In this case, however, the very rough initial surface precludes the formation of a continuous oxide layer because of the impossibility to fill large surface irregularities by products of resputtering.

That a continuous oxide layer can be grown on the surface of electrodeposited CoCu films directly by the action of oxygen ions at 50°C may be of practical significance in our opinion. This layer can prevent the degradation of the films under severe environmental conditions [1]; hence, the magnetic properties of the as-deposited and long-stored films will be nearly the same. In addition, the oxide layer can serve as a transition or an insulating layer in fabricating multilayer microelectronic devices based on these films.

REFERENCES

1. *Oxydation des métaux*, Vol. 1: *Processus fondamentaux*, Ed. by J. Bénard (Gauthier-Villars, Paris, 1962; Metallurgiya, Moscow, 1968).
2. P. V. Thomas, V. K. Vaidyan, and A. T. Johny, Vacuum **47** (1), 83 (1996).
3. V. M. Fedosyuk, O. I. Kasyutich, and H. I. Blythe, Poverkhnost, No. 3, 62 (2000).
4. A. I. Stognij, S. V. Koryakin, and Yu. V. Sukhodolov, in *Proceedings of the International Conference "Plasma Physics and Plasma Technology-2"* (Nats. Akad. Nauk Belorussii, Minsk, 1977), Vol. 3, p. 574.
5. A. I. Stognij and S. V. Koryakin, in *Proceedings of the XVII International School-Workshop "Novel Magnetic Materials of Microelectronics"* (URSS, Moscow, 2000), pp. 124–125.
6. A. I. Stognij and V. V. Tokarev, Prib. Tekh. Éksp., No. 3, 142 (1990).
7. V. M. Koleshko, P. P. Goĭdenko, and L. D. Buĭko, *Control in Technology of Microelectronics* (Nauka i Tekhnika, Minsk, 1979).
8. *Practical Surface Analysis by Auger and X-ray Photoelectron Spectroscopy*, Ed. by D. Briggs and M. P. Seach (Wiley, New York, 1983; Mir, Moscow, 1987).
9. S. Tada, Y. Sakamoto, T. Suzuki, *et al.*, Vacuum **53**, 321 (1999).
10. É. M. Sher, V. M. Mikushkin, S. E. Sysoev, *et al.*, Zh. Tekh. Fiz. **70** (3), 78 (2000) [Tech. Phys. **45**, 365 (2000)].
11. V. M. Fedosyuk, in *Proceedings of the NATO Advanced Research Workshop (ARW) on Nanostructured Films and Coatings, Santorini, 1999*, p. 22.
12. G. K. Wertheim, *Mössbauer Effect: Principles and Applications* (Academic, New York, 1964; Mir, Moscow, 1966).
13. V. F. Nesterov, F. S. Nasredinov, and G. T. Daribaeva, Fiz. Tverd. Tela (Leningrad) **33**, 2699 (1991) [Sov. Phys. Solid State **33**, 1525 (1991)].
14. Prasanna and Ajay Gupta, Phys. Rev. B **45**, 483 (1992).
15. G. K. Wertheim, Phys. Rev. **124**, 764 (1961).
16. V. S. Smentkowski, Prog. Surf. Sci. **64** (5), 1 (2000).

Translated by V. Isaakyan

Technical Physics, Vol. 46, No. 6, 2001, pp. 736–742. Translated from Zhurnal Tekhnicheskoĭ Fiziki, Vol. 71, No. 6, 2001, pp. 95–103.

The Use of Carbonaceous Materials as Field-Emission Cathodes

A. F. Bobkov, E. V. Davydov, S. V. Zaĭtsev, A. V. Karpov, M. A. Kozodaev, I. N. Nikolaeva, M. O. Popov, E. N. Skorokhodov, A. L. Suvorov, and Yu. N. Cheblukov

Institute of Theoretical and Experimental Physics, Bol'shaya Cheremushkinskaya ul. 25, Moscow, 117259 Russia

Received July 23, 2000

Abstract—The advantages and disadvantages of carbon fibers and graphite plates with a developed surface as field-emission cathode materials are discussed. Experimental data for the chemical composition of the materials and the effect of thermal annealing on their structure and emission properties are presented. A correlation between the work function and the amount of cesium implant is studied. The feasibility of preparing planar cold cathodes with a developed surface by means of radiation technologies is considered, and the evolution of the emitting surface during bombardment by low-energy residual gas ions is traced. Cold cathode designs for various applications are recommended. © *2001 MAIK "Nauka/Interperiodica"*.

INTRODUCTION

The idea of using carbonaceous materials as field-emission (FE) cathodes was first realized in 1972 [1]. In pioneering works [2, 3], experiments were performed with carbon fibers [4]. Earlier, beginning in 1957, carbides of refractory metals as FE cathodes have been applied [5]. Later, a variety of reports dealing with FE cathodes made of various bulk carbonaceous materials with a developed surface appeared (see, e.g., [6, 7]). Interest in using carbonaceous materials in emission electronics has been aroused primarily because they are compatible with industrial vacuum conditions. The basic arguments in favor of carbon fibers as FE cathodes are as follows. (1) They do not require special sharpening (the surface of fracture of the fiber contains emitting centers) and are stable against bombardment by residual gas ions, which takes place in high-voltage devices and in those operating in an industrial vacuum; (2) during sputtering, their surface structure remains dynamically stable and retains a sufficient number of emitting centers (it has been established that, as one centers disappear, other arise under such conditions); and (3) the fibers do not deteriorate vacuum conditions and are produced by many manufacturers; hence, they are relatively cheap. Of importance also is that they are produced in the form of bundles containing several hundred or thousands of individual fibers.

To date, many patents concerning the designs of fiber-based FE cathodes have been published (see [8] and references therein). An example is an FE cathode incorporated into an emitting device with memory functions (US Patent no. 4728851). It consists of a single fiber of diameter 2.0 μm corona-tapered to form an apex of diameter 0.2 μm. An FE cathode for a pulsed source of electrons is described in US Patent no. 4 272 699. This cathode consists of a bundle of carbon fibers from 2.0 to 10.0 μm in diameter, each having the emitting surface obtained by simply cutting the fibers without using special procedures. US Patent no. 5 588 893 [9], which is the latest and perhaps the most informative in this field, describes the design of the cathode and method of fabrication. Up to now, encouraging results of using radiation technologies in creating or processing FE cathodes made of bulk carbon plates or plates of highly oriented pyrolytic graphite (HOPG) have been obtained [1].

Today, however, nanometer carbon clusters, in particular, nanotubes—extended structures largely consisting of hexatomic rings [11, 12]—seem to be the most promising carbon material for FE cathodes. Their emission properties were qualitatively considered in [13], and in [14], the work function in the nanotubes was estimated at about 1 eV. If this unique value is confirmed, FE cathodes made from carbon nanoclusters will have no equals in the majority of cases.

In this work, we discuss the advantages and disadvantages of cold cathodes made from carbon fibers and carbon plates with a developed surface and report recent experimental results concerning these cathodes. Conceptually, many of the results will be considered in subsequent papers. This article to some extent summarizes our original works.

EXPERIMENT

The geometry of the FE cathodes was examined with conventional scanning electron microscopy (the operating surface of the fibers) and scanning tunnel microscopy (the surface of the bulk cathodes with a developed surface). The elemental composition of the cathode material was studied with magnetic-scan mass spectrometers and solid-state laser ion sources. The internal structure of the fibers was investigated by the X-ray diffraction method. The emission properties of

1063-7842/01/4606-0736$21.00

the cathodes were studied in a specially designed computerized setup [15]. Its vacuum chamber is made of stainless steel and has high-voltage bushings and a watch window. The original part of the chamber is a positioner that can control the spatial arrangement of the components of the measuring system (cathode, modulator, and anode) with a high accuracy. The anode diameter varies between 10 and 40 mm according to the cathode type and design (individual carbon fibers, bundle of fibers, nanotubes, silicon or tungsten tips, or planar carbon or graphite plates with a developed surface), anode–cathode distance, and aim of experiments. The temperatures of the anode and modulator are measured with temperature sensors. The uniformity of the emission current is estimated using all-metal and sectional (up to four sections in the form of a circular arc) anodes. As modulators, grids of various transparencies, perforated plates, wires, etc. are used. The electronic unit of the setup, the core of the data acquisition and processing system, includes programmable power supplies, a divider, an amplifier, and an L-264 card connected to a computer. The system is adjusted and controlled by a DMM-VC-506 multimeter (Conrad Electronic GmbH, Germany). It passes digital data for the emission currents and the temperatures of the setup elements to the computer, where the information is processed and then used to construct *I–V* characteristics (including in the Fowler–Nordheim coordinates), dependences of the temperatures on the emission currents, etc.

In experiments where the emission properties of the materials and the efficiency of the cathodes and entire modules were studied, the necessary potential difference was provided by HCN 35-6500 and HCN 35-12 500 power supplies (both from F.u.G. Electronic GmbH, Germany), which can also operate in the current source mode. This mode was used when we investigated the stability of the cold cathodes against long-term bombardment by residual gas ions. The voltage applied to the anode and to the modulator was positive, since the material of the chamber markedly affects the electric field distribution in the interelectrode gap. Both power supplies are equipped with analog-to-digital converters (ADCs) and are connected to the computer, which specifies time parameters and a voltage-varying program. The voltage values, as well the currents and temperatures, are filed in the digital form using the L-264 ADC card embedded in the computer. The card serves as a device for data input, output, and processing (in both the analog and digital forms). The card also has an ADSP-2105 off-line signal processor, which provides analog data input and analysis and generates a report on measurement results. During the adjustment and calibration of the entire data acquisition and processing system, graphic and numeric data obtained with the computer are compared with processed experimental data obtained with the DMM-VC-506 digital multimeter. In both cases, instantaneous values of the parameters measured are displayed in real time.

COMPOSITION OF THE CARBONACEOUS MATERIALS

The elemental identification of the materials was performed with the MI-1201 mass spectrometer and ÉMAL-2 mass spectrograph (both from AO Selmi, Sumy, Ukraine). We studied UKN-P, UKN-400, UKN-5000, VMN-RK, VMN-4, VÉN-280, and Kulon-P poly(acrylonitrile) fibers (all from the All-Russia Research Institute of Polymer Fibers, RIPF [16]); T-50 and T-300 poly(acrylonitrile) fibers from Thornel (USA); carbon fibers made from R-25 and R-75 isotropic petroleum pitch from Thornel (USA) [17]; and pilot samples of cellulose hydrate–based fibers from the RIPF. Also, we analyzed MPG-6, MPG-8, KPG, GMP-1011, GR-1, GR-280, and VPG domestic nuclear graphites and domestic HOPG. It was found that all the materials have a considerable amount of impurities (up to 3%). These are nitrogen (2 to 2.3%) and F, Na, Mg, Al, Si, S, Cl, Ca, K, Ti, Fe, Cr, Ni, Co, Cu, Zn, and Sr (several hundredths of a percent each). The amount of the impurities markedly depends on the type of the material. One can suggest that this is the basic reason for the difference in the mechanical and emission properties of the carbonaceous materials, as well as in their stability against bombardment by low-energy ions in the FE current generation mode under conditions of an industrial vacuum. Some results on the elemental composition of the materials are available from the appendices to the quarterly reports on project no. 467-97, which is supported by the International Research Center. Altogether, the results will be published in the preprint of the Institute of Theoretical and Experimental Physics (currently in press).

ANNEALING OF CARBON FIBERS

It was reported [18, 19] that thermal treatment of carbon fibers improves their field emission capacity. For the majority of the fibers, heat treatment at 500°C for 10 min seems to be optimal. It is believed that heating "improves" the internal structure of the fibers, making it optimal for the formation of a developed working surface that is dynamically stable against ion bombardment.

To gain a better understanding of this phenomenon, we investigated the evolution of the phase state of several types of the fibers during annealing with an HZG-4A X-ray diffractometer (Carl Zeiss GmbH, Germany). In X-ray experiments, the fibers in the cell were packed parallel to each other, perpendicularly to each other, or in a random way. The X-ray tube has a copper target ($\lambda = 0.154$ nm) and a nickel filter. Fibers annealed in air in an LM 111.10 furnace (Linn Elektro Therm GmbH, Germany) at 100, 300, 500, and 600°C for 10 min were examined. Typical results for UKN-400 poly(acrylonitrile) fibers are shown in Fig. 1. The fibers are highly amorphous. The spectrum has a single peak, which corresponds to the interplanar spacing $d = 0.36$ nm. The

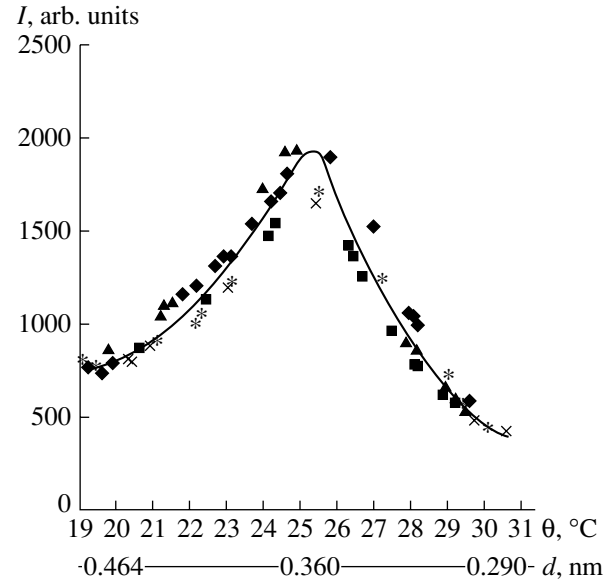

Fig. 1. Diffraction patterns from the (◆) unannealed reference sample and from UKN-400 poly(acrylonitrile) fibers annealed at (■) 100, (▲) 300, (×) 500, and (∗) 600°C for 10 min.

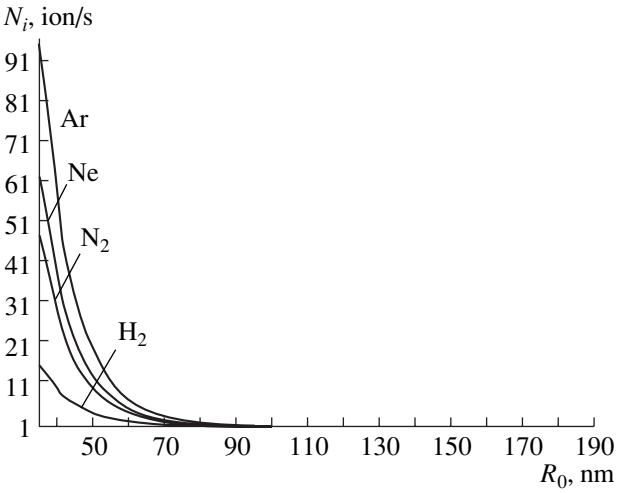

Fig. 2. Calculated number of ions striking the surface of the carbon tip in a second for the gas pressure $P_0 = 10^{-4}$ Pa and the voltage $V_0 = 5.0$ kV.

half-width of the peak is about 0.15 nm, indicating a low degree of ordering. This diffraction pattern gives no chance to judge the degree of texturing of the fibers and the effect of annealing (in the range 100–600°C) on the structure and phase state of the fibers.

The SEM examination (XL 30 TMP scanning electron microscope from the Philips Electron Optics, Netherlands) of the working surfaces of individual fibers after they had been trained for about 1 h at a voltage of ≥5 kV and a residual pressure on the order of 1×10^{-4} Pa showed that the most developed surface is observed for the fibers annealed at $T \le 400$°C or not heat-treated at all. Hence, we can conclude that heat treatment at the above temperatures merely removes (completely or partially) the organic binder from the bundles. The binder benefits the formation of the developed fiber surface during ion bombardment in the FE current generation mode. On the other hand, its presence (even in minor amounts) plagues the use of the bundles as FE cathodes and makes it difficult to maintain necessary vacuum conditions in sealed-off glass tubes.

ION BOMBARDMENT OF THE SURFACE: COMPUTER SIMULATION AND EXPERIMENTAL DATA

It is known that the continuous bombardment of the cathode surface by residual gas ions is one of the most important effects that accompanies field emission and strongly affects its parameters. The ions are generated in the interelectrode space by the electron impact mechanism. This effect becomes of special importance when the cathode operates at a pressure of about 10^{-4} Pa and the voltage across the diode gap is several kilovolts [20].

To estimate the effect, we elaborated a procedure to compute and predict the variation of the cathode surface during long-term operation. The essence of our approach is the rigorous quantitative estimation of radiation load on FE cathodes. When analyzing the formation and evolution of the surface relief of the cathodes, we take into account the following factors: (1) the initial geometry of the surface; (2) the structure and chemical composition of the cathode material, including the composition of the surface layer; (3) the composition and pressure of the gas in the operating space; (4) the energy distribution of the ions; and (5) the parameters of ion sputtering of the surface (sputtering yield and possibility of resputtering) and type of sputtering (chemical, physical, atomwise, or cluster) [21–23]. The radiation load was estimated by the formulas derived in [24] and modified for the multi-tip surface with overlapping electron flows. The load was estimated with a specially developed computational program for pure compact carbon, porous carbon, tungsten, tungsten carbide, and tungsten oxide that are irradiated by ions of pure H_2, D_2, He, and Ar. By way of example, Fig. 2 plots the calculated number of ions striking the surface of the carbon tip per unit time, N_i, and Fig. 3 shows the time variation of the volume of the carbon and tungsten FE cathodes that is sputtered by He ions. It follows from the calculations that the carbonaceous materials do not have any advantages over the other materials in terms of radiation hardness and material loss (here we do not consider carbon nanoclusters [12], which call for special theoretical and experimental investigation).

Using the original experimental technique (it was described in part in [25, 26]), we measured the sputter-

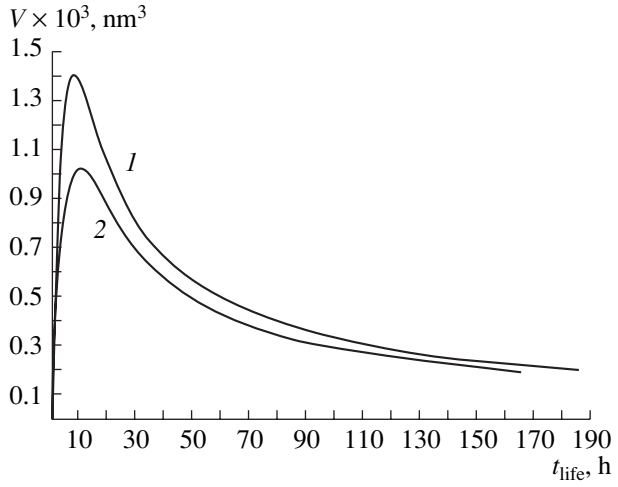

Fig. 3. Calculated time variation of the volume of the (*1*) tungsten and (*2*) carbon FE cathodes that is sputtered by He ions (ideal tips). The gas pressure P_0 is 10^{-4} Pa, and the voltage V_0 is 5.0 kV.

ing yields Y_s for the carbonaceous materials considered in a wide range of energies. It was shown that, for the graphites, $Y_s \le 0.5$ atom/ion when the maximum energy of residual ions is $V \approx 8$ keV. For the carbon fibers, Y_s is more than one order of magnitude higher even if the "resputtering" of carbon atoms onto working surface asperities is taken into consideration. Thus, for the bulk graphite cathodes with a developed surface, the sputtering (removal) of surface atoms may substantially change the surface relief and, thereby, the emission parameters after long-term operation. In the case of the fibers, the sputtering process (including cluster sputtering) will cause extensive mass transfer from the cathode to the anode (or to the modulator).

RADIATION TECHNOLOGIES FOR FIELD-EMISSION CATHODE FABRICATION

It has been shown recently [7, 10] that the irradiation of bulk carbonaceous materials by various particles may successfully be used for fabricating flat FE cathodes with a developed surface. The surface irradiated may be irregular (see, e.g., Fig. 4) or have a periodic relief (Fig. 5). The surfaces of HOPG and MPG-6 high-strength nuclear graphite (both irradiated by protons, a laser-induced plasma, cesium ions, and fission fragments) were thoroughly examined by STM [27], which is known to quantitatively characterize the degree of surface development in terms of fractal dimensions [28, 29]. The experiments were performed with an SMM-2000T scanning multimicroscope operating in air (KPD Company Ltd., Russia). The HOPG surface irradiated by Xe^+ ions is shown in Fig. 6. Concurrently, *I–V* characteristics were taken from each of the samples. For a developed surfaces, they qualitatively agreed (typical *I–V* curves are presented in [7]). The emissive power (current per unit emitting surface area) increased with the fractal dimension. This dependence was not linear but tended to saturation.

REDUCTION OF THE WORK FUNCTION

As is known, carbonaceous materials rank below many others in emission properties and primarily in work function ($\varphi \approx 4.7$ eV) [30]. However, they are promising FE cathode materials in a number of specific applications, because their developed surface remains dynamically stable and retains a sufficient number of emission centers during sputtering due to low-energy ion bombardment. In addition, carbon is a suitable material for industrial vacuum conditions. Therefore, it would be logical to reduce the work function of carbonaceous materials, e.g., by implanting a material with a

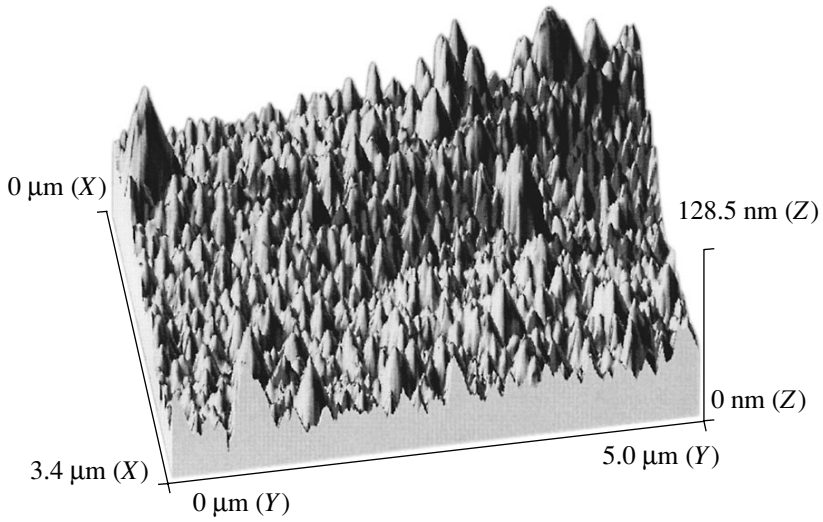

Fig. 4. STM image of the HOPG surface irradiated by the high-intensity laser-induced SiO_2 plasma.

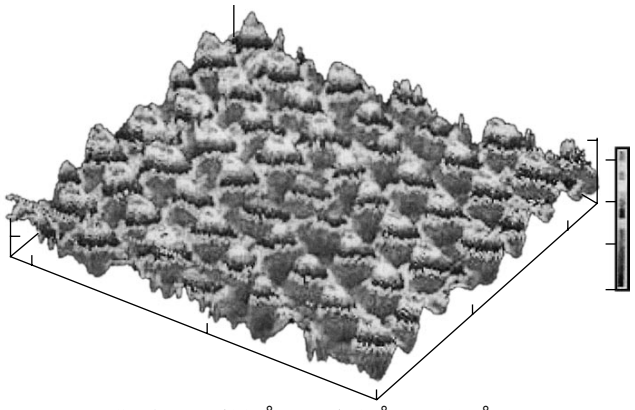

Fig. 5. STM image of the HOPG surface irradiated by 210-MeV Xe^+ ions. The relief depicted forms only on separated sites of the surface.

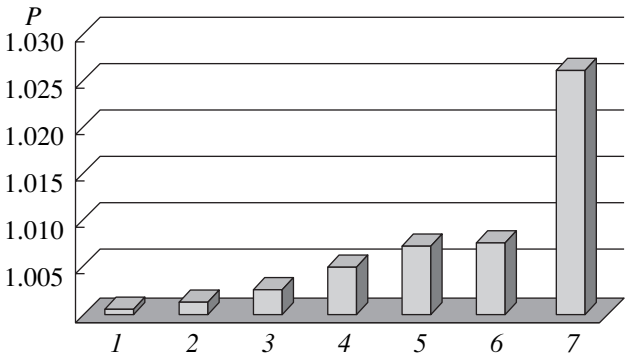

Fig. 6. Graphic representation of the degree of surface development (profile fractal dimension *P*) for HOPG samples subjected to various irradiations: (*1*) reference; (*2*) p^+, 3 MeV, angle of incidence on the surface 90°; (*3*) p^+, 90 keV, 45°; (*4*) fission fragments; (*5*) cesium ions, 25 keV; (*6*) laser-induced SiO_2 plasma; and (*7*) p^+, 90 keV, 90°.

much lower work function φ. We tried to decrease the value of φ for the HOPG and carbon fibers by implanting cesium ions (φ ≈ 1.80 eV). Note, however, that for graphite, cesium ion bombardment can also be used for developing the surface (the STM image in Fig. 7). The HOPG and fibers were irradiated by 25-eV Cs ions. In the former case, the ion beams struck the surface at right angles, while in the latter, the beams were perpendicular or parallel to the fiber axis. The value of φ was measured with the original technique. It involves statistical analysis of many *I–V* characteristics obtained from the same sample and plotted in the Fowler–Nordheim coordinates and comparison with similar data for nonirradiated cathodes. Actually, the relative value of φ (or, what is the same, a decrease in φ relative to its initial value φ_0 for nonirradiated carbon) was measured. Cesium implantation was found to decrease φ by a factor of 1.5 for the fibers and twofold for the as-obtained HOPG surface. However, during the generation of FE current, both factors (1.5 and 2) decreased (φ grew) and became unstable. The reasons may be the insufficient Cs ion energy, specific range distribution of cesium ions in carbon, and sputtering of carbon during emission. We suppose that the best practical results will be obtained if cesium ions implanted into the carbon fibers have an energy corresponding to the mean projective range $\bar{R} \approx d/2$, where *d* is the fiber diameter. In principle, multistage implantation processes that ensure the adequate uniformity of the Cs distribution over the material can be applied to both "bulk" graphite plates and carbon fibers.

DESIGN AND PROPERTIES OF FIELD-EMISSION CATHODES

If FE cathodes include modulators as the basic components, a cathode–modulator unit as a whole should be considered. The role of the modulators and the possible designs of the units are discussed elsewhere [8]. In

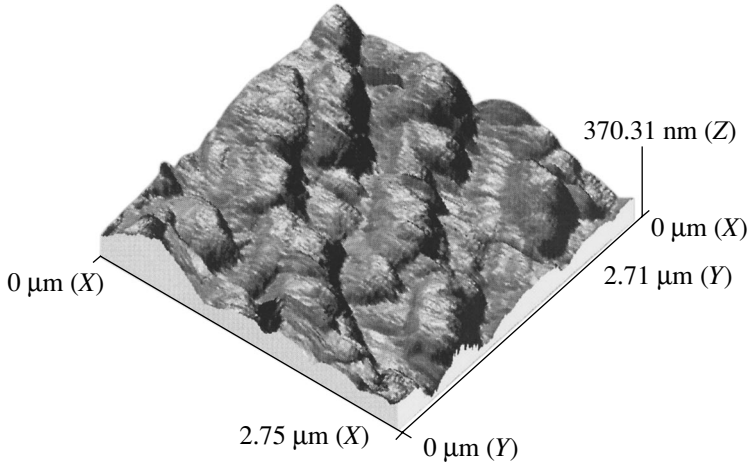

Fig. 7. STM image of the HOPG surface irradiated by 25-keV Cs^+ ions.

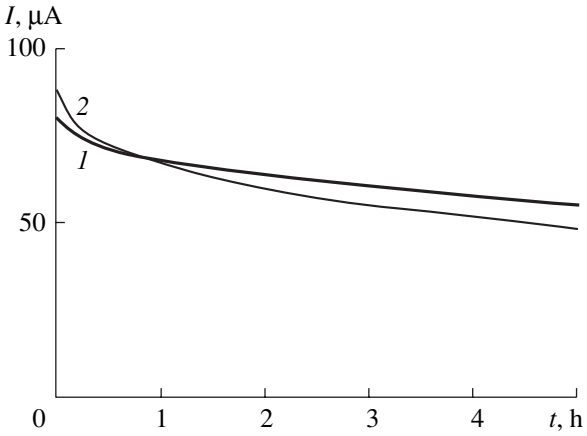

Fig. 8. Time variations of the cold current emitted by the (*1*) single carbon fiber and (*2*) single tungsten wire. Modulators are metallic plates with holes coaxial with the fiber and wire. No special sharpening of the cathodes was made in both cases. The cathodes were trained prior to the measurements. The pressure in the vacuum chamber is $P_0 = 10^{-4}$ Pa, and the voltage between the electrodes is 6.0 kV.

that work, detailed comparative analysis of the cathode–modulator units was given for the following systems:

(1) A bundle of carbon fibers (cathode) and grid (modulator);

(2) A single carbon fiber and grid;

(3) A single carbon fiber and metallic plate with a hole coaxial with the fiber;

(4) Regularly arranged individual carbon fibers and grid;

(5) Regularly arranged individual carbon fibers and metal plate with holes opposite to each of the fibers;

(6) A single tungsten wire and grid;

(7) A single tungsten wire and metallic plate with a hole coaxial with the wire;

(8) Regularly arranged individual tungsten wires and grid;

(9) Regularly arranged individual tungsten wires and metal plate with holes opposite to each of the wires;

(10) HOPG with a developed surface and grid.

In all cases, the carbon fibers and tungsten wires were cut normally to the axis and were not specially sharpened.

The measurements were performed under the same conditions. That is, in all the cases, the cathode, modulator, and anode potentials were the same, the potential difference between the cathode and the anode was 6 kV, the cathodes were trained in a similar way, and the residual gas pressure was 10^{-4} Pa. Quantitative results of this study will be published later; here, we report only qualitative data.

First, it was established that the use of the bundles is inappropriate, since the fibers differ widely in length. Moreover, the FE current is generated only in several fibers, while they number in the tens or even hundreds in the bundles. The best results were obtained for cathode–modulator system 5. The systems having similar designs but dissimilar cathode materials (such as 2 and 6, 3 and 7, 4 and 8, and 5 and 10) have close characteristics (at least over a time interval of 5 h), which appears to be rather unexpected and surprising. Figure 8 depicts the time dependence of the FE current for systems 2 and 5.

CONCLUSIONS

(1) The thermal treatment of carbon fibers at 500–600°C in air for $t \geq 10$ min removes the organic binder from the bundles without affecting the surface structure and the phase state of the fibers. The presence of the binder on the fiber surface adds to its development during ion bombardment but greatly deteriorates vacuum conditions in sealed-off glass tubes.

(2) Computer analysis of the formation and evolution of the surface relief must take into consideration the initial surface geometry; structure and chemical composition of the cathodes, including the composition of the surface layer; composition of the gas in the operating space; energy distribution of bombarding ions; parameters of ion sputtering of the surface material [sputtering yield, possibility of resputtering, and sputtering mechanism (physical, chemical, atomwise, or cluster)].

(3) As follows from the computer simulation, the carbonaceous materials have no advantages over the others in terms of stability against low-energy ion bombardment and cathode material loss due to sputtering. The experimentally found fact that the sputtering yield for the fibers far exceeds that for the graphite plates indicates extensive mass transfer to the anode and to the modulator. Hence, the lifetime of the carbon-fiber cathodes generally ranks below that of the cathodes made of the graphite plates. On the other hand, the lifetime of the latter is limited by the possible change in the surface relief and the gradual elimination (sputtering-out) of the emitting centers. With cluster sputtering of graphite, the sputtering yield will inevitably increase.

(4) Flat FE cathodes may successfully be produced by radiation technologies. For HOPG plates, both randomly and regularly oriented developed surfaces may be obtained with these technologies. Their efficiency can be characterized with STM by measuring the fractal dimensions of the surfaces formed. These dimensions were found to be proportional to the specific FE current.

(5) The work function of the carbonaceous cathodes can considerably be decreased by implantation of Cs (or any other material with the work function much lesser than that of carbon). The energy and fluence of the ions must provide the implant uniformity over the cathode. In practice, implantation may decrease the

work function of the carbonaceous materials down to 2.5–3.0 eV.

(6) The use of the bundles appears to be inappropriate, since the fibers differ widely in length. Moreover, the FE current is only generated by a few fibers, while they number in the tens or even hundreds in the bundles. The best results are observed when the regularly arranged fibers are used as a cathode and a metal plate with holes coaxial with the fibers, as a modulator.

(7) Based on information currently available, we can conclude that carbon nanoclusters seem to be the most promising material for high-efficiency FE cathodes.

ACKNOWLEDGMENTS

This work was partially supported by the International Research Center (project no. 467-97).

REFERENCES

1. F. S. Baker, A. R. Osborn, and J. Williams, Nature **239**, 96 (1972).
2. C. Lea, J. Phys. D **6**, 1105 (1973).
3. F. S. Baker, A. R. Osborn, and J. Williams, J. Phys. D **7**, 2105 (1974).
4. *Carbon Fibers*, Ed. by S. Simamura (Omsya, Tokio, 1984; Mir, Moscow, 1987), translated from Japanese.
5. M. I. Elinson and G. F. Vasil'ev, Radiotekh. Élektron. **2** (3), 126 (1957).
6. B. V. Bondarenko, V. I. Makukha, and E. P. Sheshin, Élektron. Tekh., Ser. 1: Élektron. SVCh, No. 10, 44 (1984).
7. A. L. Suvorov, E. P. Sheshin, V. V. Protasenko, *et al.*, Zh. Tekh. Fiz. **66** (7), 156 (1996) [Tech. Phys. **41**, 719 (1996)].
8. A. L. Suvorov, A. F. Bobkov, S. V. Zaĭtsev, *et al.*, Preprint No. 25-98 (Institute of Theoretical and Experimental Physics), Moscow, 1998.
9. V. S. Kaftanov, A. L. Suvorov, and E. P. Sheshin, US Patent No. 5588893 (December 31, 1996).
10. D. V. Kulikov, A. L. Suvorov, R. A. Suris, *et al.*, Pis'ma Zh. Tekh. Fiz. **23** (14), 89 (1997) [Tech. Phys. Lett. **23**, 573 (1997)].
11. T. W. Ebbesen and P. M. Ajayan, Nature **358**, 220 (1992).
12. A. V. Eletskiĭ and B. M. Smirnov, Usp. Fiz. Nauk **165**, 977 (1995) [Phys. Usp. **38**, 935 (1995)].
13. Yu. V. Gulyaev, L. A. Chermozatonskii, Z. Ya. Kosakovskaya, *et al.*, in *Proceedings of the 7th International Vacuum Microelectronics Conference, IVMC'94, Grenoble, 1994*, Revue "Le Vide, les Couches Minces," Supplement au No. 271, Mars-Avril, 1994, p. 322.
14. L. A. Chernozatonskii, Z. Ya. Kosakovskaya, Yu. V. Gulaev, *et al.*, J. Vac. Sci. Technol. B **14**, 2080 (1996).
15. M. O. Popov, A. F. Bobkov, S. V. Zaĭev, *et al.*, Prib. Tekh. Éksp. (1999).
16. M. T. Azarova, Khim. Volokna, No. 3, 5 (1991).
17. H. O. Pierson, *Handbook of Carbon, Graphite, Diamond and Fullerenes: Properties, Processing, and Applications* (Noyes Publ., Park Ridge, 1992).
18. B. V. Bondarenko, V. A. Seliverstov, and E. P. Sheshin, Radiotekh. Élektron. (Moscow) **30**, 1601 (1985).
19. E. P. Sheshin, Doctoral Dissertation (Moscow, 1996).
20. A. L. Suvorov, *Field-ion Microscopy of Radiation-induced Defects in Metals* (Énergoizdat, Moscow, 1982).
21. A. L. Suvorov, *Structure and Properties of Surface Atomic Layers of Metals* (Énergoatomizdat, Moscow, 1990).
22. *Sputtering by Particle Bombardment*, Ed. by R. Behrisch (Springer-Verlag, New York, 1981, 1983; Mir, Moscow, 1984, 1986), Vols. I and II.
23. A. D. Bekkerman, N. Kh. Dzhemilev, and V. M. Rotshteĭn, Pis'ma Zh. Tekh. Fiz. **19** (6), 52 (1993) [Tech. Phys. Lett. **19**, 177 (1993)].
24. P. A. Bereznyak and V. V. Slezov, Radiotekh. Élektron. (Moscow) **17**, 354 (1972).
25. D. E. Dolin, A. A. Sosunov, A. L. Suvorov, and E. P. Sheshin, Zh. Tekh. Fiz. **60** (12), 115 (1990) [Sov. Phys. Tech. Phys. **35**, 1430 (1990)].
26. M. I. Guseva, A. L. Suvorov, S. N. Korshunov, and N. E. Lazarev, J. Nucl. Mater. **266–269**, 222 (1999).
27. S. S. Magonov and M.-H. Whangbo, *Surface Analysis with STM and AFM: Experimental and Theoretical Aspects of Image Analysis* (Willey–VCH, West Sussex, 1995).
28. S. Talibuddin and J. P. Runt, J. Appl. Phys. **76**, 5070 (1994).
29. Yu. N. Cheblukov, A. S. Fedotov, M. A. Kozodaev, *et al.*, Mater. Sci. Eng. A **270**, 102 (1999).
30. V. S. Fomenko, *Emission Properties of Materials: Handbook* (Naukova Dumka, Kiev, 1981).

Translated by V. Isaakyan

Technical Physics, Vol. 46, No. 6, 2001, pp. 743–748. Translated from Zhurnal Tekhnicheskoĭ Fiziki, Vol. 71, No. 6, 2001, pp. 104–109.

Solid-Phase Reactions and the Order–Disorder Phase Transition in Thin Films

V. G. Myagkov, L. E. Bykova, G. N. Bondarenko, G. V. Bondarenko, and F. V. Myagkov

Kirenskiĭ Institute of Physics, Russian Academy of Sciences, Siberian Branch, Krasnoyarsk, 660036 Russia

e-mail: kim@ksc.krasn.ru

Received August 29, 2000

Abstract—A comparative analysis was carried out of the initiation temperatures of solid-phase reactions in bilayer solid films and the Kurnakov temperatures of the phases forming in the reaction products. It has been shown that in superstructures where ordering is usually observed, the Kurnakov temperature coincides with the initiation temperature of the solid-phase reactions if no other solid-phase structural transformation precedes the order–disorder phase transition in the state diagram. A rule was proposed by which pairs of films capable of entering into solid-phase reactions and their initiation temperatures can be determined. © *2001 MAIK "Nauka/Interperiodica".*

INTRODUCTION

Solid-phase reactions in thin films, the backbone of modern microelectronics technology, have been intensively studied for the past three decades [1–8]. The majority of the solid-phase reactions in thin metal films occur in the temperature range 400–800 K and fall into two classes. The first class are reactions in which new phases are formed. The second class are reactions whose products contain no new phases while the layers intermix at temperatures below the eutectic temperature [1]. It is believed that the basic mechanism of the low-temperature solid-phase reactions in thin films is the diffusion along grain boundaries, which is several orders of magnitude faster than diffusion in bulk samples [1]. The grain boundary diffusion and high imperfection of the films are the main factors in the formation of compounds at the interfaces of film condensates. As in bulk samples, the formation of new phases in films occurs by nucleation and growth obeying the kinetic Kolmogorov–Avrami–Johnson–Mehl law. Such an analysis supposes that, by virtue of the Arrhenius dependence of diffusion on temperature, the formation of new phases at the interface occurs at any temperature and the thickness of the layer of reaction products depends only on temperature and the annealing time. However, calorimetric data and Rutherford backscattering investigations of many solid-phase reactions in thin films show that the phase formation begins at a certain temperature and proceeds at a fast rate in a narrow temperature interval [2, 3]. Generally, as the temperature is increased, a so-called first phase forms at the interface. Further increase of the temperature can result in the emergence of new phases and the formation of a phase sequence [2–8]. Different rules have been proposed to predict the first phase and the phase sequence [6–8]; however, not one of them can embrace the diversity of experimental data. Nevertheless, prediction of the pairs between which the solid-phase reactions are possible, of the initiation temperature values, of the first phases, and of the phase sequences is extremely important for technical applications.

One of the thermal treatment methods causing solid-phase reactions in thin films to yield compounds is rapid thermal annealing [9]. Rapid thermal annealing includes rapid heating of the sample to a certain temperature, exposure for 1–100 s, and subsequent rapid cooling. It has been shown [10, 11] that solid-phase reactions in metallic thin films can proceed as a self-propagating high-temperature synthesis (SHS). Unlike SHS in powders [10,11], SHS in thin films can occur spontaneously only when the sample temperature T_s exceeds the initiation temperature T_0 ($T_s > T_0$) and represents a surface combustion wave. The SHS front velocity increases exponentially with the sample temperature T_s, and at a sample temperature close to the initiation temperature it is equal to $\sim 2–10 \times 10^{-2}$ m/s. So, the time of travel of the SHS wave over the sample surface in the experiments is equal to ~5–15 s. This suggests that many of the solid-phase reactions taking place in the course of the rapid temperature annealing are SHS reactions. SHS in thin films, the same as the solid-phase reactions, can be of two types. The reaction products formed in the wake of an SHS wave of type I contain compounds. SHS of type II comprises a combustion wave and a phase immiscibility wave, which arises when the sample temperature T_s drops below the initiation temperature T_0. Reaction products of type II SHS in bilayer film systems described by a simple eutectic state diagram contain initial components. Therefore, in such samples, the reaction produces the effect of intermixing of the layers. SHS of type II, called multiple SHS [12, 13], corresponds to the transi-

1063-7842/01/4606-0743$21.00 © 2001 MAIK "Nauka/Interperiodica"

tion through the eutectic temperature in bulk samples. Unlike the eutectic crystallization of the bulk samples, the multiple SHS in thin films is a reversible solid-state structural phase transition. This result is absolutely unexpected since the phase immiscibility observed during eutectic crystallization is currently believed to be the result of the transition of the liquid eutectic into a solid one. Therefore, the multiple SHS should be considered as a "solid-phase melting" of eutectic systems.

The SHS initiation temperatures in many of the bilayer film samples are found in the temperature range 400–800 K, characteristic for solid-state reactions. Comparison with the binary phase equilibrium diagrams of the bulk samples shows that in the temperature range 400–800 K, many structural solid-phase transformations take place. This is an indication that the temperatures of the solid-phase reactions (including SHS) coincide with the phase transformation temperatures. However, it is considered that all these transformations depend on diffusion (excluding the martensite transitions), which is slow in this temperature range and cannot create the considerable mass transfer across the interface between the layers characteristic for SHS and solid-state reactions. Nevertheless, the supposition that the SHS initiation temperatures in thin films are the same as the temperatures of other solid-phase transformations was verified for bilayer systems S/Fe and Cu/Au. In [14], the SHS initiation temperature in S/Fe thin films has been shown to be in agreement with the temperature of the metal-dielectric phase transition in ferric monosulfide FeS. It was shown in [15] that the Kurnakov temperature of the order–disorder phase transition in the classic Cu–Au system determines the initiation temperature of SHS in the Cu/Au bilayer film system.

The present study aims to provide an experimental proof that, in other bilayer film systems as well, the initiation temperature of the solid-phase reactions is determined by the Kurnakov temperature of the ordering phases forming in the reaction products.

SAMPLES AND EXPERIMENTAL TECHNIQUE

The objects studied were bilayer film samples, which could contain ordered phases in the reaction products after passage of an SHS wave or a solid-phase reaction. The systems chosen for comparing Kurnakov temperatures and the initiation temperatures of solid-phase reactions were those in which the ordering phenomenon typically occurs, namely, Cu–Zn, Ni–Zn, Mn–Ni, Co–Al, Fe–Al, Ni–Al, Cu–Al, Ti–Al, Co–Pt, Au–Cu [16–18]. Bilayer film samples were prepared by consecutive vacuum deposition of the above metals onto glass and mica substrates as well as onto freshly cleaved MgO(001) surfaces. The thickness of the layers was chosen such that the composition of the samples after the reactions have been completed was in the region of homogeneity of the ordering alloys studied. The total thickness of the film sample did not exceed 250 nm. In order to improve adhesion and obtain monocrystalline layers on the MgO(001) surface, on all substrates the first layers were deposited with the substrate temperature kept at 500–520 K. To prevent the reaction from occurring during deposition, the second layer was deposited at room temperature. The samples obtained were placed on a tungsten heater in vacuum and heated to the SHS initiation temperature at a rate of no less than 20 K/s. After passage of the SHS front, which was monitored visually, the samples were cooled down at ~10 K/s. In the cases where passage of the SHS front was discernible poorly or not at all, the samples were subjected to rapid thermal annealing. The rapid thermal annealing (RTA) included heating of the bilayer samples at a rate of no less than 20 K/s to a temperature 20–40 K above T_0 and exposition at that temperature for 15 s (the time necessary for passage of the SHS front) with subsequent cooling at a rate of ~10 K/s. Sample preparation and thermal annealing were carried out in a vacuum of $\sim 1 \times 10^{-5}$ torr. The initiation temperature depended strongly not only on the heating rate but also on the thickness of the substrate. Therefore, in the experiments, the substrate thickness was kept at a minimum. For the glass and mica substrates, it was 0.10–0.18 mm; for the MgO substrates, 0.35–0.40 mm. The phase composition was determined using a DRON-4-07 (LOMO) instrument and K_α radiation. The X-ray spectral fluorescence method was used for determining the chemical composition and thickness of the layers. Measurements of the magnetic crystallographic anisotropy were carried out by the method of rotation moments. The degree of transformation η was determined from variation of the magnetic moment of the ferromagnetic sample layer before and after the reaction following the method described in [10, 11].

EXPERIMENTAL RESULTS AND DISCUSSION

Cu–Zn system. In the Cu–Zn system, a β'-CuZn phase of type B2 ordering exists. The Kurnakov temperature of the bulk β'-CuZn phase is in the range T_k = 741–727 K [16]. It was found that, indeed, in the Zn/Cu film samples deposited onto mica and glass substrates, the SHS reaction between copper and zinc films took place as the temperature T_s was increased to T_0 ($T_s = T_0$). The initiation temperature was in the range 550–600 K, and the SHS front propagation could easily be observed visually (Fig. 1). The initiation temperature T_0 in Zn/Cu/MgO(001) samples was higher by 50–100 K than in the samples deposited on glass substrates, and the SHS front propagation was not distinctly noticeable. The diffraction patterns of the Zn/Cu/MgO(001) samples taken prior to initiation showed that the copper layer grew on the MgO(001) surface epitaxially with the (001) orientation. The absence of reflections from the zinc film deposited on

top of the copper film suggests that it was either finely dispersed or amorphous. As a result of SHS, the copper layer reacted completely since its reflections disappeared. The analysis of diffraction patterns showed that the ordered β' phase and the high-temperature β_2 phase formed in the reaction products (Fig. 2). The ordered β'-CuZn phase is a typical example of the *B*2 phase ordering. The high-temperature β_2 phase probably owes its stability to the higher cooling rate occurring behind the SHS front.

Ni–Zn system. The Ni–Zn system includes only one type *B*2 ordered phase, namely, NiZn. An ordered β_1-NiZn phase of the Cu–Au type is formed as a result of the eutectic-like decomposition at a temperature of T_k = 888 K [16]. The β_1-NiZn phase is stable at room temperature. The Zn/Ni film samples deposited onto the glass substrates, just like the Zn/Cu films (Fig. 1), exhibit a well-defined front when SHS is initiated. The SHS initiation temperature was in the range T_0 = 430–480 K. In Fig. 3, the dependence of the degree of transformation η on the substrate temperature T_s typical of SHS reactions in thin films is shown [10, 11]. The same samples on the MgO(001) substrate had T_0 = 600–650 K. X-ray diffraction by the initial Zn/Ni/MgO(001) samples showed that the nickel film grown on MgO(001) was monocrystalline and contained no zinc reflections (Fig. 4a). The reason for the absence of these reflections is the same as for the Zn/Cu/MnO(001) samples. The measured values of the magnetic crystallographic anisotropy constant of the initial Zn/Ni/MgO(001) samples are close to the value for bulk nickel and confirm that the Ni film grew on MgO(001) epitaxially in the (100) plane. Magnetic and X-ray diffraction measurements showed that SHS in Zn/Ni/MgO(001) samples can penetrate the film thickness only partially. This is possibly caused by intensive heat removal to the substrate and is also observed in Al/Ni/MgO(001) samples [17]. Figures 4b and 4c show diffraction patterns corresponding to the transformation degrees of η = 0.5 and 1, respectively. The new phase must grow epitaxially on the Ni(100) surface since only the strong reflection at d = 0.178 nm is present. However, this reflection does not belong to the ordered β_1-NiZn phase. It has been shown previously [10, 11, 18] that the formation of phases at high SHS front velocities occurs in non-steady-state conditions and the formation of metastable phases and quasi-crystals is possible in the reaction products. Probably, the reflection at d = 0.178 nm belongs either to an unknown metastable phase, a δ-phase, or a $ZnNi_3$ phase with a lattice similar to γ-brass [19]. The large discrepancy between the temperatures T_k = 888 K and T_0 = 430–480 K suggests that the initiation temperature of the first phase in the Zn/Ni film is determined not by the Kurnakov temperature of the β_1-NiZn phase but by an unknown low-temperature structural transformation in the Ni–Zn system.

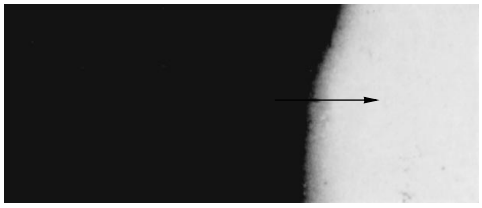

Fig. 1. SHS front in a (150 nm)Zn/(50 nm)Cu film grown on glass substrate. The arrow indicates the front propagation direction.

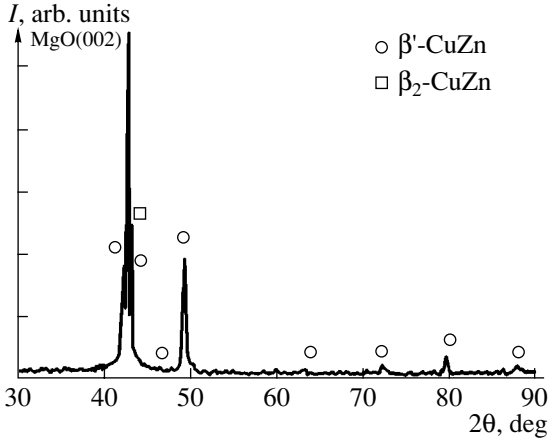

Fig. 2. X-ray diffraction patterns of a (150 nm)Zn/(50 nm)Cu/MgO(001) film sample after passage of the SHS wave.

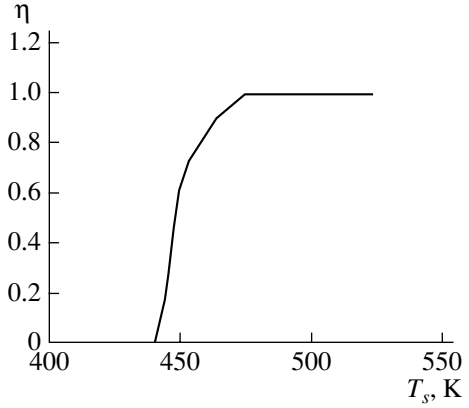

Fig. 3. Degree of transformation η as a function of the substrate temperature T_s in a (150 nm)Zn/(50 nm)Ni bilayer film system.

Ni–Mn system. In the Ni–Mn system, a NiMn phase having $L1_0$ ordering and a Ni_3Mn phase with the $L1_2$ structure are known. The NiMn phase is formed as a low-temperature modification; the Kurnakov temperatures of these phases are T_k(NiMn) = 753 K and $T_k(Ni_3Mn)$ = 778 K, respectively [16]. In the Mn/Ni bilayer samples, propagation of the SHS front could not be seen; therefore, these samples were subjected to RTA. Between the nickel and manganese layers, a

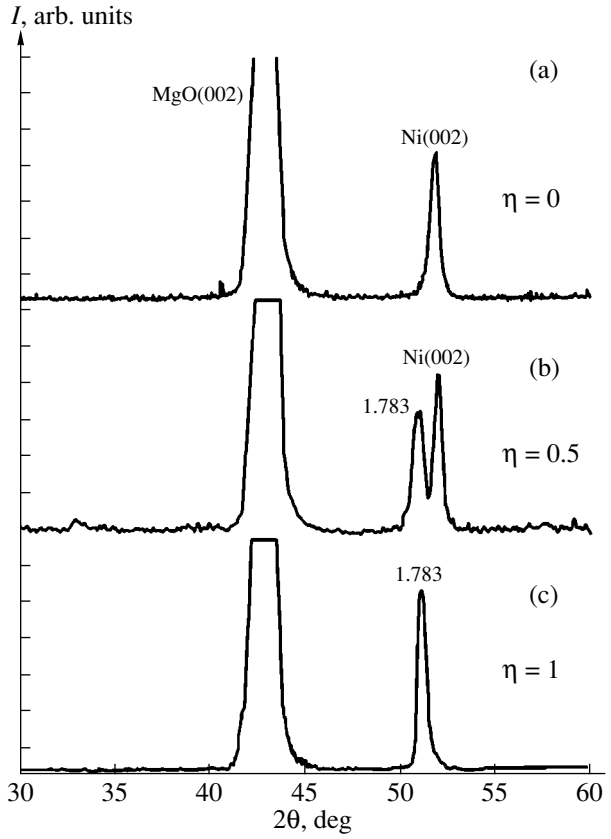

Fig. 4. X-ray diffraction patterns of a (150 nm)Zn/(50 nm)Ni/MgO(001) film sample: (a) initial sample; (b, c) after passage of the SHS front at η = 0.5 and 1, respectively.

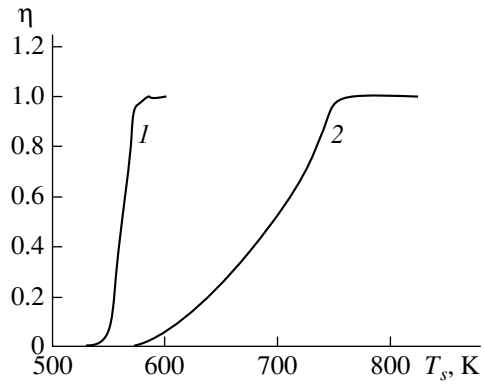

Fig. 5. Degree of transformation η as a function of the substrate temperature T_s in a (100 nm)Mn/(100 nm)Ni bilayer film sample: (*1*) in the course of deposition of the manganese layer onto the nickel layer; (*2*) after rapid thermal annealing.

solid-state reaction took place; in Fig. 5 (curve *1*), the dependence of the degree of transformation η on the substrate temperature is presented for Mn/Ni bilayer samples deposited onto mica substrates. However, it was not expected that $\eta(T_s)$ would depend on the substrate temperature for the Mn layer deposited onto a Ni film (Fig. 5, curve *2*), its initiation temperature (T_0^1 = 570 K) being lower than in the bilayer samples (T_0^2 = 850 K). It has been shown in [10, 11] that during both heating of bilayer samples and consecutive layer deposition from the substrate temperature, the SHS initiation temperature T_0 will be the same. The significant difference between T_0^1 and T_0^2 values suggests different phase formation processes for these two cases of initiation. The Ni–Mn system has been intensively studied mostly on account of the superstructure in Ni_3Mn, which is ferromagnetic in the ordered state. However, no compounds of this system are listed in the JCPDS catalogue. This complicates interpretation of the diffraction patterns of Ni and Mn films successively deposited onto the MgO(100) surface and samples subjected to RTA, which are presented in Figs. 6a and 6b, respectively. The samples containing a reflection for d = 0.178 nm in their diffraction patterns were always ferromagnetic. Therefore, this reflection should correspond to the (002)$MnNi_3$ phase with a lattice constant of a = 0.357 nm [20]. The ordered MnNi phase has a lattice similar to that of CuAu, with a = 0.3714 nm and c = 0.3524 nm [20]. Thus, the reflections for d = 0.221 and 0.185 nm were tentatively assigned to MnNi(111) and MnNi(200) phases. With increase of the RTA temperature, the diffraction patterns change considerably owing to the great diversity of the phase transformations in the Mn–Ni system.

Al–Co system. In the Al–Co system an AlCo alloy with *B*2 ordering is of interest. SHS in thin Al/Co films on glass substrates is initiated at temperatures of 650–680 K. The plots of the degree of transformation as a function of the substrate temperature $\eta(T_s)$ for SHS initiated during deposition and during heating of the Al/Co film samples are identical [10, 11]. The SHS initiation temperature in Al/Co/MgO(001) films is in the range 750–780 K. In Fig. 7, diffraction patterns are presented of the initial Al/Co/MgO(001) samples (Fig. 7a) and after the reaction has taken place (Fig. 7b). The initial samples produced only reflections of the (001)β-Co phase and had no reflection from the aluminum layer deposited on top. As in the film systems discussed above, the top layer was either amorphous or disperse. Analysis of the diffraction patterns and the data on magnetocrystallographic anisotropy of the initial samples showed that the relative orientations of the monocrystalline β-Co film and the substrate were as (001)[100]β-Co ‖ (001)[100]MgO. After passage of the SHS front, which was observed visually, only the AlCo phase was found in the reaction products (Fig. 6b). The presence of the (100) superstructure reflection indicates that the AlCo phase is ordered. Formation of the superstructure in the reaction products suggests that the temperature of the order–disorder transition in the AlCo phase coincides with the SHS initiation temperature in Al/Co bilayer film samples.

Besides the systems considered above, SHS is initiated in bilayer thin samples of Al/Cu (T_0 = 350–400 K), Al/Ti (T_0 = 450–500 K). In respective Al–Cu and Al–Ti systems, CuAl, TiAl, and Ti_3Al superstructures occur [16, 21, 22]. Earlier, it was found [17] that in Al/Fe/MgO(001) films, SHS produces a FeAl superstructure (T_0 = 610–630 K), which, as a film, has an ordering temperature of T_k < 680 K [23]. The closeness of the experimental values of the SHS initiation temperature T_0 in Al/Fe samples and the Kurnakov temperature of the FeAl superstructure suggests that their exact values should coincide. In the Al/Ni/MgO(001) film system, in SHS products, a compound is formed that has been identified as an Al_3Ni_2 phase [17]. This phase is also found after SHS on glass substrates occurring at the initiation temperature (T_0 = 500 K) [10, 11]. Solid-phase reactions in Al/Ni thin films that occur at a temperature T_r ~ 500 K are fairly well studied, with Al_3Ni_2, Al_3Ni, and AlNi phases observed in the reaction products [1, 20, 24, 25]. Equality of the temperatures $T_0 = T_r$ = 500 K testifies that the solid-phase reactions observed in [1, 23–25] proceed in the SHS mode. In the equilibrium state diagram of the Al–Ni system, there is no singularity at a temperature of 500 K. From the foregoing it can be concluded that this temperature might coincide with the ordering temperatures of the phases formed in the reaction products after SHS involving nickel and aluminum layers. It has been shown in [26] that the SHS initiation temperature in Co/Pt, both in bilayers and multilayer films, is close to the Kurnakov temperature of the CoPt bulk alloy [27, 28], which also indicates that these temperatures should be equal in the film state.

Solid-phase reactions were initiated in all thin-film pairs if ordered phases were able to form in the reaction products. However, the initiation temperature of the solid-phase reactions was always lower than the Kurnakov temperature of the alloys formed in the course of the reaction ($T_0 < T_k$). In thin films, the equality $T_0 = T_k$ turns into the inequality $T_0 < T_k$ due to a number of factors: (i) considerable heat removal to the substrate reducing the Kurnakov temperature of thin films in comparison with similar bulk samples; (ii) a high concentration of defects in film condensates; and (iii) the effect on the temperature T_0 of other structural transformations preceding the order–disorder transition and originating in the reaction products.

The foregoing suggests that a one-to-one relation exists between the order in which, with increase of the annealing temperature, the phases form in the bilayer thin films, and the structural transformations in the corresponding binary systems. It appears that the first phase forming at the interface between the films is that which comes first in the phase equilibrium diagram and has the lowest structural phase transitions temperature This rule was first proposed in [26]. Formation of further phases with increase of the annealing temperature

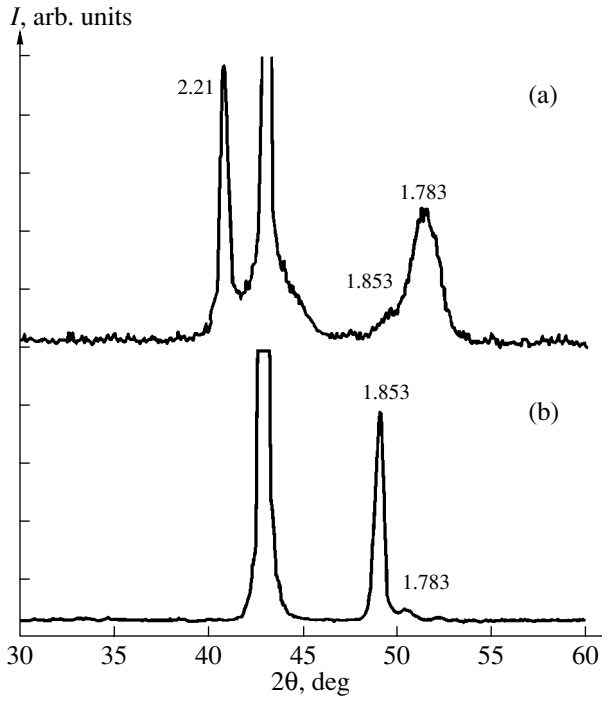

Fig. 6. X-ray diffraction patterns of a (100 nm)Mn/(100 nm)Ni/MgO(001) film sample: (a) after the solid-state reaction during deposition of the manganese layer onto the nickel layer; (b) after rapid thermal annealing cycle.

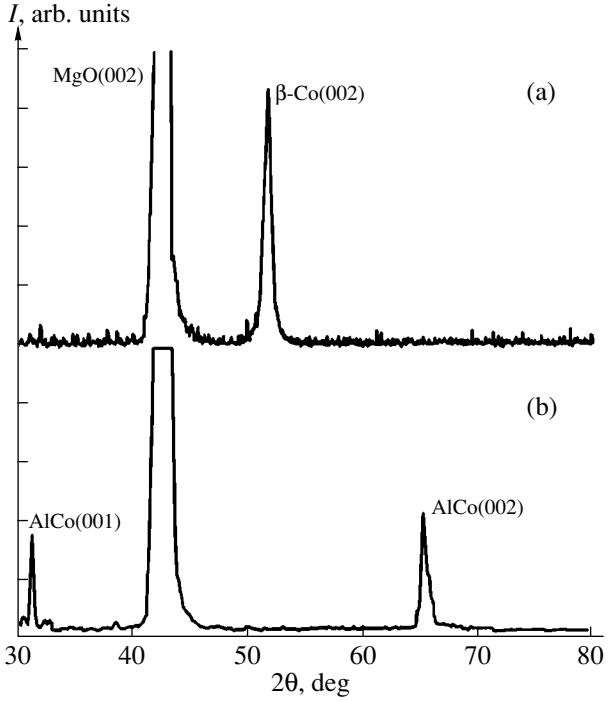

Fig. 7. X-ray diffraction patterns of a (100 nm)Al/(100 nm)Co/MgO(001) film sample: (a) initial sample; (b) after passage of SHS front.

during solid-phase reactions in thin films is governed by structural transitions in a given binary system. The maximum annealing temperature at which the solid-phase reactions occur should coincide with the temperature of the multiple SHS. Therefore, the solid-phase reactions occur in the temperature range found in the phase equilibrium diagram between the eutectic temperature and the minimum temperature of structural phase transformations in a given system. Hence, using the known binary state diagram, the pairs of the component and the initiation temperatures of the solid-phase reactions in the bilayer thin films can be determined. The opposite is possible as well, namely, phase sequences during solid-phase reactions in bilayer thin films can be studied in order to refine the corresponding state diagrams.

It is now widely believed that ordering of atoms into a superstructure occurs via the atoms of the lattice interchanging places. The results of the present work demonstrate that a considerable mass transfer (up to ~200 nm) takes place at the Kurnakov temperature in the film condensates with the formation of alloys. The ordering at $T = T_k$ is only a secondary process. It follows that the long-range mechanism of synthesis determines the ordering processes. The long-range forces can determine the stability of the formed phases and, together with the elastic forces, influence the character of antiphase boundaries in the long-period superstructures, as well as participate in the formation of modulated phases at spinodal and eutectic-like decompositions and in polytype structures.

ACKNOWLEDGMENTS

The work was support in part by the Russian Foundation for Basic Research (project no. 99-03-32184) and the Krasnoyarsk Regional Science Foundation (grant no. 9F12).

REFERENCES

1. *Thin Films: Interdiffusion and Reactions*, Ed. by J. M. Poate, K. Tu, and J. Meier (Wiley, New York, 1978; Mir, Moscow, 1982).
2. E. G. Colgan, C. Cabral, Jr., and D. E. Kotecki, J. Appl. Phys. **77**, 614 (1995).
3. U. A. Clevenger, B. Arcort, W. Ziegler, *et al.*, J. Appl. Phys. **83**, 90 (1998).
4. D. B. Bergstrom, I. Petrov, L. H. Allen, *et al.*, J. Appl. Phys. **78**, 194 (1995).
5. M. Wittmer, P. Oelhafer, and K. N. Tu, Phys. Rev. B **35**, 9073 (1987).
6. W. H. Wang and W. K. Wang, J. Appl. Phys. **76**, 1578 (1994).
7. M. Zhang, W. Yu, W. H. Wang, *et al.*, J. Appl. Phys. **80**, 1422 (1996).
8. T. Nakanishi, M. Takeyama, A. Noya, *et al.*, J. Appl. Phys. **77**, 948 (1995).
9. R. Singh, J. Appl. Phys. **63**, R59 (1988).
10. V. G. Myagkov and L. E. Bykova, Dokl. Akad. Nauk **354**, 777 (1997).
11. V. G. Myagkov, V. S. Zhigalov, L. E. Bykova, *et al.*, Zh. Tekh. Fiz. **68** (10), 58 (1998) [Tech. Phys. **43**, 1189 (1998)].
12. V. G. Myagkov, Dokl. Akad. Nauk **364**, 330 (1999).
13. V. G. Myagkov, L. E. Bykova, and G. N. Bondarenko, Zh. Éksp. Teor. Fiz. **115**, 1756 (1999) [JETP **88**, 963 (1999)].
14. V. G. Myagkov, L. E. Bykova, V. S. Zhigalov, *et al.*, Dokl. Akad. Nauk **371**, 763 (2000) [Dokl. Phys. **45**, 157 (2000)].
15. V. G. Myagkov, L. E. Bykova, G. N. Bondarenko, *et al.*, Pis'ma Zh. Éksp. Teor. Fiz. **71**, 268 (2000) [JETP Lett. **71**, 183 (2000)].
16. N. M. Matveeva and É. V. Kozlov, *Ordered Phase in Metallic Systems* (Nauka, Moscow, 1989).
17. V. G. Myagkov, L. E. Bykova, and G. N. Bondarenko, Dokl. Akad. Nauk **368**, 615 (1999) [Dokl. Phys. **44**, 667 (1999)].
18. V. G. Myagkov, L. E. Bykova, and G. N. Bondarenko, Pis'ma Zh. Éksp. Teor. Fiz. **68**, 121 (1998) [JETP Lett. **68**, 131 (1998)].
19. N. I. Ganina, A. M. Zakharova, V. G. Oleĭnicheva, *et al.*, in *Constitution Diagrams of Metallic Systems* (VINITI, Moscow, 1988), Vol. XXXII.
20. M. Hansen and K. Anderko, *Constitution of Binary Alloys* (McGraw-Hill, New York, 1958; Metallurgizdat, Moscow, 1962), Vol. 2.
21. T. Muto and J. Tacagi, *The Theory of Order-Disorder Transitions in Alloys*, in *Solid State Physics: Advances in Research and Applications*, Ed. by F. Seitz and C. D. Turnbull (Academic, New York, 1955; Inostrannaya Literatura, Moscow, 1959).
22. C. S. Barrett and T. B. Massalski, *Structure of Metals: Crystallographic Methods, Principles and Data* (Pergamon, Oxford, 1980; Metallurgiya, Moscow, 1984), Part 1.
23. V. Y. Kudryavtsev, V. V. Nemoshkalenko, Y. P. Lee, *et al.*, J. Appl. Phys. **82**, 5043 (1997).
24. E. Ma, C. V. Thompson, L. A. Clevenger, *et al.*, Appl. Phys. Lett. **57**, 1262 (1990).
25. J. C. Liu, J. W. Mayer, and J. C. Barbour, J. Appl. Phys. **64**, 656 (1988).
26. C. Michaelsen, G. Lucadamo, and K. Barmak, J. Appl. Phys. **80**, 6689 (1996).
27. V. G. Myagkov, L. A. Li, L. E. Bykova, *et al.*, Fiz. Tverd. Tela (St. Petersburg) **42**, 937 (2000) [Phys. Solid State **42**, 968 (2000)].
28. K. Barmak, R. A. Ristau, K. R. Coffey, *et al.*, J. Appl. Phys. **79**, 5330 (1996).

Translated by M. Lebedev

Technical Physics, Vol. 46, No. 6, 2001, pp. 749–754. Translated from Zhurnal Tekhnicheskoĭ Fiziki, Vol. 71, No. 6, 2001, pp. 110–115.

EXPERIMENTAL INSTRUMENTS AND TECHNIQUES

Determination of the Thermal Physical Properties of Ceramics and Parameters of Cracks by a Laser Optical-Beam Deflection Method

K. L. Muratikov and A. L. Glazov

Ioffe Physicotechnical Institute, Russian Academy of Sciences, Politekhnicheskaya ul. 26, St. Petersburg, 194021 Russia

Received May 16, 2000

Abstract—A formation model for optical-beam deflection signals in ceramics is constructed. The generation of temperature waves by laser radiation in ceramics with regard for the anisotropy of their thermal physical properties is considered. The thermal physical parameters of silicon nitride ceramic are measured with a laser optical-beam deflection method. The method is shown to be useful for detecting and characterizing subsurface cracks in ceramics. *© 2001 MAIK "Nauka/Interperiodica".*

The thermal physical properties of today's ceramics are the object of much investigation [1, 2]. They offer high hardness, are wear- and corrosion-resistant, and have low density. In addition, the ceramics can be used at high temperatures. Of interest are the properties of homogeneous ceramics, as well as the formation and detection of defects in the material. Subsurface cracks are defects that are the most important and, at the same time, the most difficult to detect [3–6]. In this work, we try to tackle the problem with the laser optical-beam deflection (OBD) method [7, 8]. In [9], a modified OBD method was suggested. It is based on the concepts of wave optics and allows thermal physical measurements to be made for a variety of temperature waves.

The formation of an OBD signal in terms of wave optics was considered in [10–12]. In those works, diffraction effects due to probing laser radiation were described at length for a nonstationary thermal lens that is produced near an object to be studied by pumping radiation. It was shown that these effects must be taken into consideration in finding the OBD signal. Therefore, the detailed calculation of the signal will be omitted.

For the typical arrangement of laser beams and an object in OBD experiments (Fig. 1), the expressions for the normal and tangential components of the signal are as follows [10–12]:

$$S_n = \frac{KI_0}{\lambda r\sqrt{\pi}}\frac{\partial n}{\partial T}\int_0 dz\int dk_y \exp\left[ik_y y_0 - \gamma_g z - \frac{k_y^2 r^2}{4} - \frac{(z-z_0)^2}{r^2}\right]\operatorname{erfi}\left(\frac{z-z_0}{r\sqrt{2}}\right)\hat{T}_s(0, k_y, \omega), \quad (1)$$

$$S_t = \frac{KI_0}{2\lambda r\sqrt{\pi}}\frac{\partial n}{\partial T}\int dy\int dk_y \exp\left[ik_y y - \gamma_g z_0 + \frac{\gamma_g^2 r^2}{4} - \frac{(y-y_0)^2}{r^2}\right]\operatorname{erfi}\left(\frac{y-y_0}{r\sqrt{2}}\right) \times\left[1 + \operatorname{erf}\left(\frac{z_0}{r} - \frac{\gamma_g r}{2}\right)\right]\hat{T}_s(0, k_y, \omega), \quad (2)$$

where K is a proportionality factor that relates the light intensity at the photodetector to the electrical signal; I_0, the intensity of the probing laser radiation; $\partial n/\partial T$, the partial derivative (rate of change) of the refractive index of the medium near the object with respect to temperature; λ, laser radiation wavelength; $\hat{T}_s(k_x, k_y, \omega)$, the

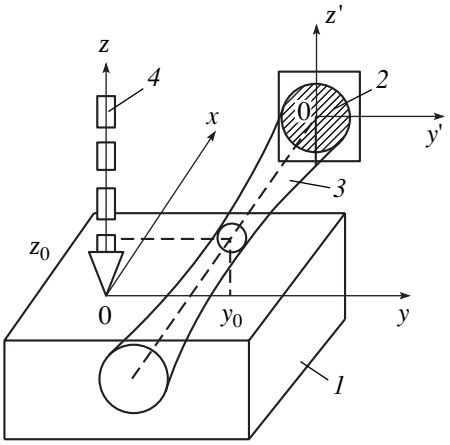

Fig. 1. Thermal OBD experiment: (*1*) object; (*2*) photodetector; (*3*) reading laser beam; and (*4*) warming radiation.

1063-7842/01/4606-0749$21.00

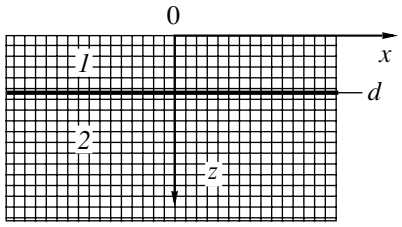

Fig. 2. Object with a horizontal crack (at a depth d) separating layers *1* and *2*.

Fourier transform for the nonstationary component $T_s(x, y, 0, \omega)$ of the temperature on the object surface in the coordinates x and y; $\omega = 2\pi f$; f, the modulation frequency of the exciting radiation; r, radius of the exciting beam in its focal plane; $\gamma_g = \sqrt{k_y^2 + (i\omega/\kappa_g)}$, the thermal diffusivity of the medium near the object; y_0, the transverse displacement of the probing laser beam from the center of the thermal lens; z_0, the height of the beam over the object surface; and

$$\mathrm{erfi}(x) = \frac{2}{\sqrt{\pi}}\int_0^x \exp(x^2)dx, \quad \mathrm{erf}(x) = \frac{2}{\sqrt{\pi}}\int_0^x \exp(-x^2)dx.$$

According to expressions (1) and (2), the OBD signals can be determined if the nonstationary component of the surface temperature is known. To find the latter, it is necessary to study the generation of temperature waves and their propagation in the object and in the environment. To do this, we use a two-layer model (Fig. 2). Here, it is assumed that a crack is at the depth $z = d$ and its width is much less than the length of the temperature wave. Then, the crack can be simulated by some thermal resistance at the depth $z = d$. Next, we assume for generality that layers *1* and *2* have different thermal physical properties.

Most ceramics are anisotropic by the physical properties. They are usually classed as orthotropic materials, for which two principal values of the thermal conductivity tensor coincide in one plane and the third principal value lies in the direction normal to this plane. In practice, the orientation of these planes depends on the hot pressing direction during fabrication. Let planes where two principal values of the tensor coincide be parallel to the plane $z = 0$.

For the problem stated, the thermal conduction equations for the gaseous medium around the sample, as well as for its first and second layers, can be written as

$$\rho_g C_g \frac{\partial T_g}{\partial t} = K_g\left(\frac{\partial^2}{\partial x^2} + \frac{\partial^2}{\partial y^2} + \frac{\partial^2}{\partial z^2}\right)T_g, \qquad (3)$$

$$\rho_1 C_1 \frac{\partial T_1}{\partial t} = K_1^{(\parallel)}\frac{\partial^2 T_1}{\partial z^2} + K_1^{(\perp)}\left(\frac{\partial^2 T_1}{\partial x^2} + \frac{\partial^2 T_1}{\partial y^2}\right) + \alpha I_p(x, y, t)e^{-\alpha z}, \qquad (4)$$

$$\rho_2 C_2 \frac{\partial T_2}{\partial t} = K_2^{(\parallel)}\frac{\partial^2 T_2}{\partial z^2} + K_2^{(\perp)}\left(\frac{\partial^2 T_2}{\partial x^2} + \frac{\partial^2 T_2}{\partial y^2}\right). \qquad (5)$$

Here, ρ_g, ρ_1, and ρ_2 are the densities of the surrounding gas (air), first layer, and second layer, respectively; C_g, C_1, and C_2 are the specific heats of the three media; K_g is the thermal conductivity of air; $K_1^{(\perp)}$, $K_2^{(\perp)}$ and $K_1^{(\parallel)}$, $K_2^{(\parallel)}$ are the components of the thermal conductivity tensor in the (x, y) plane and along the z axis for the first and second layers, respectively; α is the laser radiation absorption coefficient of the sample; and $I_p(x, y, t)$ is the distribution of the radiation intensity over the surface of the sample.

In OBD experiments, temperature waves are usually excited by a radiation that is readily absorbed by the sample. Therefore, Eqs. (4) and (5) assume that the exciting radiation is totally absorbed in the first layer of the object.

To solve the problem, the thermal conduction equations must be supplemented by boundary conditions. For our model, the conditions at the boundaries $z = 0$ and $z = d$ can be written as

$$T_1 = T_g\big|_{z=0}, \quad K_1^{(\parallel)}\frac{\partial T_1}{\partial z} = K_g\frac{\partial T_g}{\partial z}\bigg|_{z=0},$$
$$K_1^{(\parallel)}\frac{\partial T_1}{\partial z} = K_2^{(\parallel)}\frac{\partial T_2}{\partial z}\bigg|_{z=d}, \quad T_1 - T_2 = -R_t K_1^{(\parallel)}\frac{\partial T_1}{\partial z}\bigg|_{z=d}, \qquad (6)$$

where R_t is the thermal resistance between layers *1* and *2*.

Equations (3)–(5) are easily solved by using Fourier transformation in coordinates lying in the surface plane of the object:

$$T(x, y, z, t) = \int dk_x \int dk_y e^{ik_x x + ik_y y}\hat{T}(k_x, k_y, z, t), \qquad (7)$$

where $\hat{T}(k_x, k_y, z, t)$ is the Fourier transform of the nonstationary temperature component in the x and y coordinates.

We assume that the temperature waves are excited by a periodic heat source and, hence, the temperature is varied according to the harmonic law $e^{i\omega t}$. In this case, the equation for the Fourier transform of the tempera-

ture, for example, in the first layer takes the form

$$\frac{i\omega}{\kappa_1^{(\parallel)}}\hat{T}_1(k_x, k_y, z, \omega) = \left[-\frac{K_1^{(\perp)}}{K_1^{(\parallel)}}(k_x^2 + k_y^2) + \frac{\partial^2}{\partial z^2}\right] \times \hat{T}_1(k_x, k_y, z, \omega) + \frac{\alpha\hat{I}_p(k_x, k_y)e^{-\alpha z}}{K_1^{(\parallel)}}, \quad (8)$$

where $\hat{I}_p(k_x, k_y)$ is the Fourier transform for the distribution of the exciting radiation intensity on the surface of the object.

Equations for the Fourier transforms $\hat{T}_g$ and $\hat{T}_2$ of the temperatures T_g and T_2 are obtained in a similar way. We assume that the laser radiation intensity on the object surface obeys the Gaussian distribution; that is,

$$I_p(x, y) = \frac{W_0}{\pi a^2}e^{-\frac{x^2+y^2}{a^2}}, \quad (9)$$

where W_0 is the power of the laser beam and a is its radius in the focal plane.

Then, the Fourier transform for the radiation intensity is given by

$$\hat{I}_p(k_x, k_y) = \frac{W_0}{(2\pi)^2}e^{-\frac{a^2(k_x^2+k_y^2)}{4}}. \quad (10)$$

To find the nonstationary component of the surface temperature and then the normal and tangential components of the OBD signal [expressions (1) and (2)], it is necessary to solve thermal conduction equations (3)–(5) with boundary conditions (6). In the explicit form, the solution of the problem has the form

$$\hat{T}_g(k_x, k_y, z, \omega) = Ge^{q_g z}, \quad (11)$$

$$\hat{T}_1(k_x, k_y, z, \omega) = F_1e^{q_1 z} + F_2e^{-q_1 z} + Ae^{-\alpha z}, \quad (12)$$

$$\hat{T}_2(k_x, k_y, z, \omega) = Se^{-q_2 z}, \quad (13)$$

where

$$q_g = \sqrt{\frac{i\omega}{\kappa_g} + k_x^2 + k_y^2}, \quad q_{1,2} = \sqrt{\frac{i\omega}{\kappa_{1,2}^{(\parallel)}} + \frac{K_{1,2}^{(\perp)}}{K_{1,2}^{(\parallel)}}(k_x^2 + k_y^2)},$$

$$G = A\left(\cosh q_1 d\frac{q_1K_1^{(\parallel)}Pe^{-\alpha d} - N(\alpha K_1^{(\parallel)} + q_gK_g)}{NM + q_1K_1^{(\parallel)}} + 1\right),$$

$$A = \frac{\alpha\hat{I}_p}{K_1^{(\parallel)}}\frac{1}{\frac{i\omega}{\kappa_1^{(\parallel)}} + \frac{K_1^{(\perp)}}{K_1^{(\parallel)}}(k_x^2 - k_y^2) - \alpha^2},$$

$$F_1 = \frac{1}{2}\frac{A}{NM + q_1K_1^{(\parallel)}}[(\alpha K_1^{(\parallel)} + q_gK_g)(1 - Ne^{-q_1 d}) + Pe^{-\alpha d}(M + q_1K_1^{(\parallel)}e^{-q_1 d})],$$

$$F_2 = \frac{1}{2}\frac{A}{NM + q_1K_1^{(\parallel)}}[-(\alpha K_1^{(\parallel)} + q_gK_g)(1 + Ne^{q_1 d}) + Pe^{-\alpha d}(q_1K_1^{(\parallel)}e^{q_1 d} - M)],$$

$$S = -\frac{q_1K_1^{(\parallel)}}{q_2K_2^{(\parallel)}}\frac{MA}{NM + q_1K_1^{(\parallel)}}e^{q_2 d}\cosh q_1 d\left(\frac{\alpha K_1^{(\parallel)} + q_gK_g}{M} + Pe^{-\alpha d}\right) + \frac{\alpha AK_1^{(\parallel)}}{q_2K_2^{(\parallel)}}e^{-(\alpha + q_2)d},$$

$$M = q_gK_g\cosh q_1 d + q_1K_1^{(\parallel)}\sinh q_1 d,$$

$$N = \sinh q_1 d + (1 + R_t q_2 K_2^{(\parallel)})\frac{q_1K_1^{(\parallel)}}{q_2K_2^{(\parallel)}}\cosh q_1 d,$$

$$P = \frac{\alpha K_1^{(\parallel)}}{q_2K_2^{(\parallel)}}(1 + R_t q_2 K_2^{(\parallel)}) - 1.$$

The nonstationary component of the surface temperature can be derived from Eqs. (11) and (12) if $z = 0$. Unfortunately, the resulting expressions for the OBD signal are very complicated and cannot be represented in the analytical form. In view of this circumstance, we developed a computer program to determine the normal and tangential components of the signal.

The problem stated can also be solved in terms of the theory of temperature wave scattering. In this case, it is necessary to consider incident, transmitted, and reflected waves, as well as the coefficients of reflection and transmission of temperature waves at the interfaces [15]. We will extend the results of [13] to the case where the laser radiation penetrates into the object and the thermal resistance exists at the boundary between the layers.

The incident wave, the wave reflected from the boundary $z = d$ along the z axis, and the wave transmitted into layer *2* are expressed as

$$\hat{I}_1(k_x, k_y, z) = C_Ie^{q_1 z} \quad \text{for} \quad 0 \le z \le d, \quad (14)$$

$$\hat{R}_1(k_x, k_y, z) = C_Re^{-q_1 z} \quad \text{for} \quad 0 \le z \le d, \quad (15)$$

$$\hat{T}_2(k_x, k_y, z) = C_Te^{q_2 z} \quad \text{for} \quad d \le z \le \infty, \quad (16)$$

where C_I, C_R, and C_T are coefficients depending on the components k_x and k_y of the wavevector.

Thus, the incident, reflected, and transmitted waves are given by expressions (14), (15), and (16), respectively. The resulting temperature wave in layer *1* is described by the expression

$$\hat{T}_1(k_x, k_y, z) = C_Ie^{q_1 z} + C_Re^{-q_1 z}. \quad (17)$$

By definition, the coefficients of reflection and

transmission of temperature waves [13] are specified as

$$\hat{R}_{12}(k_x, k_y) = \frac{\hat{R}_1(k_x, k_y, d)}{\hat{I}_1(k_x, k_y, d)} = \frac{C_R}{C_I}, \quad (18)$$

$$\hat{T}_{12}(k_x, k_y) = \frac{\hat{T}_2(k_x, k_y, d)}{\hat{I}_1(k_x, k_y, d)} = \frac{C_T}{C_I}. \quad (19)$$

In view of boundary conditions (6) and Eqs. (16) and (17), expressions (18) and (19) can be represented in the explicit form:

$$\hat{R}_{12} = \frac{1 - \xi_{12}(1 - R_t q_1 K_1^{(\parallel)})}{1 + \xi_{12}(1 + R_t q_1 K_1^{(\parallel)})},$$
$$\hat{T}_{12} = \frac{2}{1 + \xi_{12} + R_t q_2 K_2^{(\parallel)}}, \quad (20)$$

where

$$\xi_{12} = \frac{q_2 K_2^{(\parallel)}}{q_1 K_1^{(\parallel)}}.$$

For $R_t = 0$, these expressions coincide with those obtained in [15], where the associated coefficients were found for a planar interface in the absence of the thermal resistance.

The temperature of the object surface can be found with regard for multiple reflections of the waves from the boundaries $z = 0$ and $z = d$, as well as for their interference at the boundary $z = 0$ [13]. Eventually, the surface temperature is given by

$$\hat{T}_1(k_x, k_y, 0, \omega) = \frac{\alpha \hat{I}_p \hat{T}_{1g}}{2 q_1 K_1^{(\parallel)} (1 - \hat{R}_{1g} \hat{R}_{12} e^{-2 q_1 d})} \times \int_0^d dz [e^{-q_1 z} + \hat{R}_{12} e^{-q_1 (2d - z)}], \quad (21)$$

where

$$\hat{T}_{1g} = \frac{2}{1 + \xi_{1g}}, \quad \xi_{1g} = \frac{q_g K_g}{q_1 K_1^{(\parallel)}}, \quad \hat{R}_{1g} = \frac{1 - \xi_{1g}}{1 + \xi_{1g}}.$$

Substituting coefficients (20) into (21) yields the surface temperature in the form

$$\hat{T}_1(k_x, k_y, 0, \omega) = \frac{\alpha \hat{I}_p}{(\alpha^2 - q_1^2) K_1^{(\parallel)}} \times \frac{(r-1)[1 + \xi_{12}(1 + R_t)][1 - e^{-(\alpha + q_1)d}] + (r+1)[1 + \xi_{12}(R_t - 1)][e^{-2 q_1 d} - e^{-(\alpha + q_1)d}]}{(1 + \xi_{1g})[1 + \xi_{12}(1 + R_t)] + (1 - \xi_{1g})[1 + \xi_{12}(R_t - 1)] e^{-2 q_1 d}}, \quad (22)$$

where $r = \alpha / q_1$.

Note that expression (22) for the surface temperature coincides with the expression obtained by directly solving thermal conduction equations (3)–(5) [expressions (11) or (12)]. For $R_t = 0$, expression (22) coincides with the earlier result [13]. Also, along with the surface temperature, such an approach allows the determination of the reflection and transmission coefficients at interfaces having the thermal resistance.

With the Fourier transform of the surface temperature known [expression (12) or (22)], the normal and tangential components of the signal are found from (1) and (2). The possibility of finding the OBD signal can be used in several applications.

First, our results may help to determine the thermal diffusivity of objects by the OBD method. In this work, the thermal physical properties of silicon nitride ceramic were found. To do this, we took dependences of the normal and tangential components of the signal on the exciting radiation frequency and on the distance between the beams of the exciting and reading lasers. Then, with expressions (1) and (2), we computed the signals and, varying the thermal diffusivities $\kappa^{(\perp)}$ and $\kappa^{(\parallel)}$, found the least standard deviation between the analytical and measured data. Previously, such a procedure was applied to various bulk materials and thin films [14, 15].

In the experiments, temperature waves in the ceramic were excited by argon laser radiation ($\lambda = 0.512$ μm) focused into a spot of a radius about 2 μm on the sample surface. The He–Ne laser ($\lambda = 0.6328$ μm) was used as a reading laser. The radius of the reading beam near its waist was 42 μm, and the distance between this beam and the surface was approximately 160 μm. Figure 3 shows the experimental and analytical dependences of the normal and tangential components of the signal on the modulation frequency of the exciting radiation. In Figs. 4 and 5, the components are plotted against the distance between the exciting and reading laser beams for the fixed modulation frequency. The standard deviation between the experimental and analytical data is minimized at $\kappa^{(\perp)} = 0.18$ cm^2/s and $\kappa^{(\parallel)} = 0.13$ cm^2/s for both components. The results obtained are in good quantitative agreement with the literature data for this ceramic: $\kappa^{(\perp)} = 0.169$ cm^2/s and $\kappa^{(\parallel)} = 0.1237$ cm^2/s [2].

Second, OBD data can be employed for determining the parameters of subsurface cracks in ceramics. To demonstrate this possibility, we performed OBD experiments with the Vickers-pyramid-indented material.

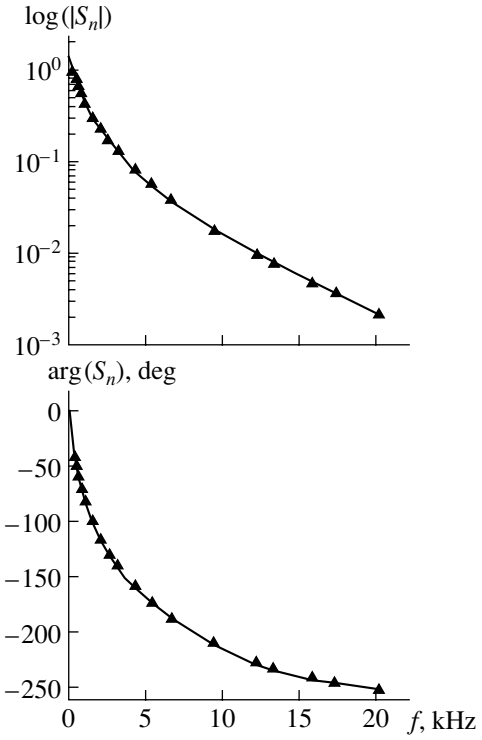

Fig. 3. Amplitude and phase of the normal component of the signal vs. modulation frequency of warming radiation. (▲) Data points; solid line depicts the theoretical curve after the model parameters for the homogeneous material have been adjusted.

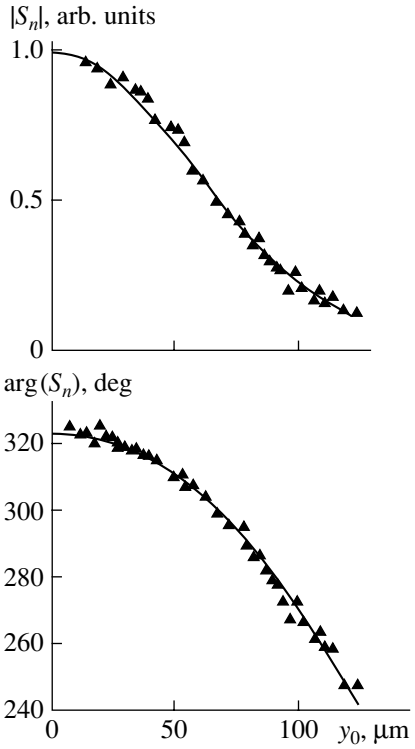

Fig. 4. Amplitude and phase of the normal component of the signal vs. distance between the exciting and reading beams. The modulation frequency of warming radiation is 9825 Hz.

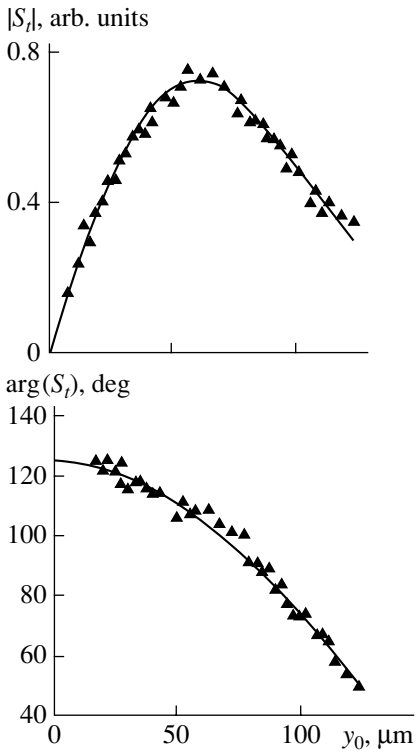

Fig. 5. The same as in Fig. 4 for the tangential component of the signal. The modulation frequency of warming radiation is 9825 Hz.

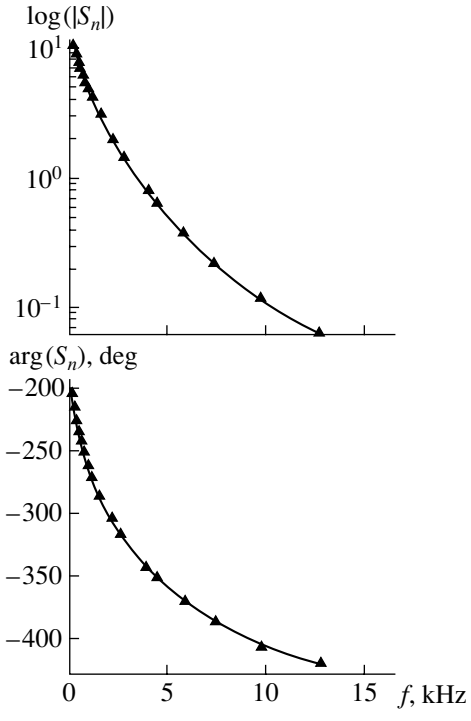

Fig. 6. Amplitude and phase of the normal component of the signal vs. modulation frequency for the Vickers-pyramid-indented ceramic. (▲) Data points; solid line depicts the theoretical curve after the model parameters for the material with the lateral crack have been adjusted.

Indentation causes the growth of lateral subsurface cracks in the ceramic [5]. To estimate their effect on the OBD signal, the ceramic was indented by a load of 98 N. The side of the indent was 72 μm long. The OBD signal was measured at a point 60 μm away from the center of the indent. This distance was measured along the median between radial cracks. At the point of measurement, the normal component of the signal as a function of the modulation frequency of the exciting radiation was determined. The associated experimental and theoretical results are depicted in Fig. 6. The least standard deviation was attained at $R_t \cong 0.27$ (cm^2 K)/W and $d = 22$ μm. If R_t is defined as the ratio d/K_g, which is valid when the length of temperature waves far exceeds the crack width, the latter is estimated at 0.6 μm. This value is consistent with typical values that characterize crack opening in ceramics [16].

In the above analysis of the formation of the OBD signal, the two problems were solved under the simplifying assumption that the laser radiation is completely absorbed at the surface. However, since we are not familiar with the literature data for the coefficient of absorption of argon laser radiation, this parameter was estimated for $\lambda = 0.512$ μm.

The normal and tangential components of the OBD signal in the silicon nitride ceramic were measured in the modulation frequency range 1–20 kHz. Then, the standard deviation between the experimental and theoretical results was minimized by varying the absorption coefficient in expressions (1) and (2). Eventually, the coefficient of absorption of argon laser radiation in the nitride ceramic was found to be $\alpha > 3 \times 10^3$ cm^{-1}. At such a value of α, light penetration into the material was shown to have a negligible effect on the OBD measurements and, hence, on the thermal properties of the material and the parameters of the lateral subsurface cracks. This means that the generation of temperature waves by 0.512-μm radiation in silicon nitride ceramic can be considered as a purely surface process.

Thus, our theoretical and experimental results indicate that OBD measurements can help to determine the thermal physical parameters of today's ceramics and estimate the parameters of subsurface cracks.

REFERENCES

1. D. P. H. Hasselman, L. F. Johnson, L. D. Bentsen, *et al.*, Am. Ceram. Soc. Bull. **66**, 799 (1987).
2. J. F. Chudecki, Bull. Am. Ceram. Soc. **69**, 1113 (1990).
3. K. R. Grice, L. J. Inglehart, L. D. Favro, *et al.*, J. Appl. Phys. **54**, 6245 (1983).
4. J. Rantala, J. Hartikainen, and J. Jaarinen, Appl. Phys. A **A50**, 465 (1990).
5. R. F. Cook and G. M. Pharr, J. Am. Ceram. Soc. **73**, 787 (1990).
6. M. Bashkansky, M. D. Duncan, M. Kahn, *et al.*, Opt. Lett. **22** (1), 61 (1997).
7. W. B. Jackson, N. M. Amer, A. C. Boccara, and D. Fournier, Appl. Opt. **90**, 1333 (1981).
8. L. C. Aamodt and J. C. Murphy, J. Appl. Phys. **52**, 4903 (1981).
9. A. L. Glazov and K. L. Muratikov, Opt. Commun. **84**, 283 (1991).
10. A. L. Glazov and K. L. Muratikov, Zh. Tekh. Fiz. **63** (4), 160 (1993) [Tech. Phys. **38**, 344 (1993)].
11. A. L. Glazov and K. L. Muratikov, Zh. Tekh. Fiz. **64** (1), 118 (1994) [Tech. Phys. **39**, 66 (1994)].
12. A. L. Glazov and K. L. Muratikov, J. Appl. Phys. **76**, 3279 (1994).
13. C. A. Bennet and R. R. Patty, Appl. Opt. **21**, 49 (1982).
14. A. L. Glazov, K. L. Muratikov, and H. G. Walther, High Temp.-High Press. **31**, 69 (1999).
15. A. L. Glazov and K. L. Muratikov, Opt. Eng. **36**, 358 (1997).
16. G. Pezzotti, N. Muraki, B. Maeda, *et al.*, J. Am. Ceram. Soc. **82**, 1249 (1999).

Translated by V. Isaakyan

Technical Physics, Vol. 46, No. 6, 2001, pp. 755–760. Translated from Zhurnal Tekhnicheskoĭ Fiziki, Vol. 71, No. 6, 2001, pp. 116–121.

EXPERIMENTAL INSTRUMENTS AND TECHNIQUES

Condensation of Monosilane–Argon and Monosilane–Helium Mixtures in Free Jets

S. Ya. Khmel, S. Yu. Fedorov, and R. G. Sharafutdinov

Kutateladze Institute of Thermophysics Research, Siberian Division, Russian Academy of Sciences, pr. Akademika Lavrent'eva 1, Novosibirsk, 630090 Russia

e-mail: khmel@itp.nsc.ru

Received August 2, 2000

Abstract—Condensation of gaseous monosilane–argon and monosilane–helium mixtures was investigated in free jets by a Rayleigh scattering laser diagnostic technique. The condensation of a SiH_4–Ar mixture begins to develop at a lower stagnation pressure and at a shorter distance from the nozzle, and proceeds at a higher rate, as compared to condensation in monosilane–helium and pure argon jets. The results of Rayleigh scattering measurements in condensing monosilane–argon jets scale with the parameter $P_0 d^{0.8}$. An analysis of the results obtained in this study and found in literature suggests that simultaneous monosilane–argon condensation leading to the formation of mixed clusters takes place in the monosilane–argon mixture. © *2001 MAIK "Nauka/Interperiodica".*

INTRODUCTION

Current advancements in electronics include fast progress in the development of semiconductor structures grown on large-area substrates (solar cells, thin-film transistors for use in LCDs, etc.). This field is referred to as large-area electronics [1]. Conventional thin-film deposition techniques, which are based on the use of electric discharges of various types, impede the development of large-area electronics. For this reason, thin films of various compositions are increasingly produced by means of gas jet techniques, which use various methods for activating the gaseous reactants [2–8]. These methods make it possible to attain high local deposition rates [4, 8] and thus solve the problem of layer growth on large area substrates.

In the jets of gaseous reactants used in thin-film deposition, the gas cooling due to adiabatic expansion may result in condensation [9, 10]. The influence of this process on the film deposition rate and the quality of synthesized films is poorly understood to this day [11]. In [4], amorphous hydrogenated silicon film was produced by using a monosilane–argon free jet activated by an electron beam. As the gas jet pressure was increased, a number of phenomena were observed, such as a constant limit approached by the deposition rate and anomalous light emission by argon atoms and monosilane molecules [11–13]. The authors attributed these phenomena to jet condensation.

It was mentioned in [14] that condensation, i.e., the formation and subsequent growth of monosilane clusters, was observed in a monosilane–argon jet, but no data were presented. In [15], clustering was observed by means of molecular beam mass spectrometry in a pulsed monosilane–argon jet flowing out of a nozzle 1 mm in diameter.

In this paper, we present the results of a systematic study of condensation in free jets of gaseous monosilane–argon and monosilane–helium mixtures by means of laser Rayleigh scattering diagnostics. The diagnostic technique was used to measure the particles of condensate directly in the gas stream.

EXPERIMENTAL

The experiments were conducted in the VS-4 low-density gas flow facility of the Institute of Thermophysics Research (Siberian Division of the Russian Academy of Sciences). The setup is schematized in Fig. 1. As a gas source (*1*), we used axisymmetric sonic nozzles made from tapered-end quartz tubing with an inner diameter of 20–21 mm and with a round opening of diameter d = 0.54, 1.07, 1.98, 3.6, or 4.8 mm. Diaphragm gauges were used to measure the stagnation pressure (in the nozzle prechamber). The prechamber was equipped with an ohmic heater used to vary the stagnation temperature from room temperature to 300°C. The gas temperature in the prechamber was monitored by a thermocouple and was equal to room temperature in most experiments. The gas source was mounted on a 3D traversing mechanism, which was used to adjust the nozzle position and the distance between the nozzle and laser beam within 0.1 mm. The gas expanded from the nozzle into a vacuum chamber evacuated by means of booster pumps at a total pumping rate of 35 000 l/s. During experiments, the vacuum-chamber pressure was maintained at 10^{-3}–10^{-2} torr. The gaseous mixtures used in most experiments consisted of argon with a 5% monosilane content. In some exper-

1063-7842/01/4606-0755$21.00 © 2001 MAIK "Nauka/Interperiodica"

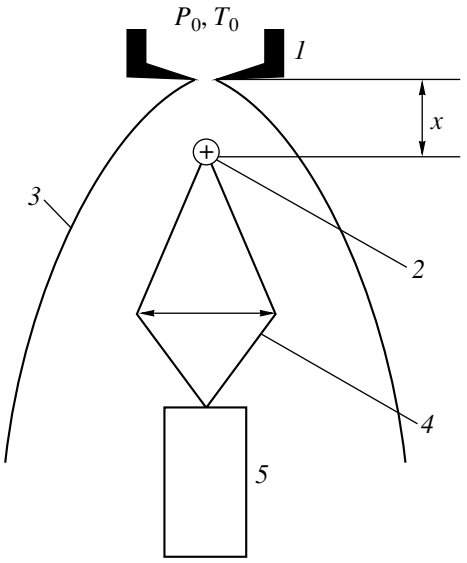

Fig. 1. Schematic of the experimental setup.

iments, we also used helium with a 10% monosilane content.

A Q-switched Nd : YAG laser was used in the experiments, with conversion to second harmonic generation (532 nm, 10 mJ/pulse, 20 ns, 10 Hz). The laser beam was directed into the chamber through a polarizing rotator and an inlet window. A dual-lens system with $F = 300$ mm focused the beam (*2*) within a measurement region in the jet (*3*, see Fig. 1), creating a measurement volume of diameter 0.1 mm. The scattered light was collected by a lens with $F = 100$ mm (*4*) and focused through an outlet window onto an aperture restricting the measurement volume length to 0.2 mm. The axes of the focusing and light-collection systems were mutually perpendicular, the light-collection axis being aligned with the nozzle axis. This arrangement of optical elements facilitated their adjustment and focusing, whereas the jet was not disturbed since the nozzle and collecting lens were well separated. The signal generated by an FEU-97 photomultiplier (*5*) passed through a delay line and was fed into input channel *1* of a ZTsP-4 charge-to-digital converter installed in a CAMAC crate. The data acquisition system was synchronized by a signal from an avalanche photodiode. The signal timing within a 200-ns integration window was monitored on an S1-75 oscilloscope. The laser pulse energy was monitored by tapping laser radiation to a photodiode whose output was fed into input channel *2* of the ZTsP-4 converter. The ZTsP-4 converter was controlled by a PC through the CAMAC crate controller to facilitate data acquisition and subsequent processing. The results of single-pulse measurements were used to calculate "instantaneous" densities, which were then averaged over an ensemble of 100 samples.

Prior to experiments, we measured background noise (in vacuum) and calibration signal (in air at a pressure of 20–40 torr). After that, the scattered signal in the jet was measured as depending on spatial location and prechamber pressure and temperature. The calibration-signal samples that substantially exceeded the average level were attributed to scattering by dust particles and discarded as outliers. No dust was detected in jet measurements.

The intensity of Rayleigh scattering by a gas is expressed as follows [16]:

$$I = A(n-1)^2 WN, \tag{1}$$

where N is the number density of gas particles, W is the laser radiation intensity, and n is the refractive index of the gas under standard conditions.

The constant A was determined by calibration at a known air density. The refractive indices of air (1.000292), argon (1.000284), and helium (1.000035) were taken from [17]; the refractive index of monosilane (1.000833), from [18]. The refractive index n_{mix} of a gaseous mixture was calculated as follows [16]:

$$(n_{\text{mix}}-1)^2 = \alpha(n_1-1)^2 + (1-\alpha)(n_2-1)^2, \tag{2}$$

where n_1 and n_2 are the refractive indices of binary-mixture components and α is the concentration of mixture component 1.

These formulas were used to measure the absolute density in free argon, argon–monosilane, and helium–monosilane jets in the absence of condensation.

For a gas–condensate mixture, the scattered light intensity I is proportional to

$$I = A(n-1)^2 W \sum_{g=1}^{\infty} N_g g^2, \tag{3}$$

where N_g is the concentration of clusters of size g (i.e., clusters consisting of g monomers) [19].

In the absence of clustering, Eq. (3) reduces to Eq. (1). Formula (3) can be rewritten as follows [20]:

$$I = A(n-1)^2 WN[(1-q) + q\langle g\rangle], \tag{4}$$

where $N = \sum_{g=1}^{\infty} N_g g$ is the total number density of a gas–condensate mixture, $q = \sum_{g=2}^{\infty} N_g g/N$ is the fraction of condensate, and $\langle g\rangle = \sum_{g=2}^{\infty} N_g g^2 / \sum_{g=2}^{\infty} N_g g$ is the mean cluster size.

The condensate content is a relatively conservative quantity. Normally, it does not exceed 30%, while clusters may consist of tens or hundreds of monomers. Thus, the relative contribution of the cluster phase to the scattered light intensity rapidly increases with the cluster size. This makes it possible to detect even a low concentration of large clusters in a gas. When the fraction of condensate is known, Eq. (4) can be used to calculate the average cluster size in a gas–condensate mixture.

RESULTS

First, we studied condensation in a pure argon jet both to verify our diagnostic method and to obtain reference data for a comparative analysis of condensation in a monosilane–argon mixture. Figure 2 shows the normalized Rayleigh scattering intensity I/I_0 on the centerline of an argon jet flowing out of a nozzle with exit diameter 1.98 mm versus the relative distance downstream of the nozzle, measured at a stagnation pressure of 562 torr and room temperature in the gas source. Here, I_0 is equal to the value of I corresponding to the gas number density N_0 in the prechamber at the stagnation pressure and temperature indicated above. The figure also shows experimental and numerical results borrowed from [20, 21] and the normalized density N/N_0 predicted by isentropic calculations for a monatomic gas. In the absence of condensation, Eq. (1) yields $I/I_0 = N/N_0$. The densities measured at relative distances less than 3.5 was found to be lower than the corresponding calculated densities by approximately 30%. However, both measured and calculated results have similar slopes. The discrepancy between the experimental and predicted results may be explained by a deviation from the perfect nozzle geometry. The measured quantities tend to increase with the distance and deviate from the calculated isentropic curve at larger distances from the nozzle. This trend is due to the onset of clustering in the flow. The corresponding results are proportional to $Nq\langle g\rangle$, as predicted by Eq. (4), and reflect the cluster concentration and size rather than the gas density. Because of the very high rate of condensation in the flow, a condensation front develops. For this portion of the curve, the increase in scattering intensity due to the growth of cluster size and concentration exceeds its decrease with decreasing density. As the flow expands further, condensation is "frozen" because of a lack of collisions, and both measured and calculated quantities decrease similarly again. The figure also shows the distribution of normalized intensity along the centerline of a free argon jet obtained by measuring the Rayleigh scattering intensity in [20]. The present results are consistent with those measured in [20] under similar flow conditions for a nozzle of diameter 1.93 mm. The experimental results presented in [20] are in much better agreement with isentropic predictions, as compared to the present measurements. This is explained by the fact that nozzles of higher quality, made of steel and having carefully designed subsonic sections, were used in that study. Figure 2 also shows the results calculated for condensation in a gas flow flowing out of a sonic nozzle of diameter 1.93 mm under similar conditions [21]. The satisfactory agreement between calculations and experiment corroborates the results obtained in the present study.

Figure 3 shows the distributions of normalized scattering intensity I/I_0 along the centerline of a jet flowing out of a sonic nozzle of diameter 1.98 mm, measured for pure argon and a monosilane–argon mixture at constant stagnation pressures with an error not greater than 5%. The figure also shows the curve of N/N_0 predicted by isentropic calculations for the mixture. Since the curve calculated for the mixture is close to the isentropic prediction for the pure gas (being lower by 3–5%), the latter is not shown here. Accordingly, the density distributions in both pure argon and mixture jets were similar upstream of the condensation front. The mixture started to condense at a shorter distance from the nozzle, and the condensation rate was much higher in the mixture as compared to the pure gas. The mixture and pure argon condensation fronts were located at relative distances of 2 and 3.5, respectively. The Rayleigh scattering intensity measured downstream of the con-

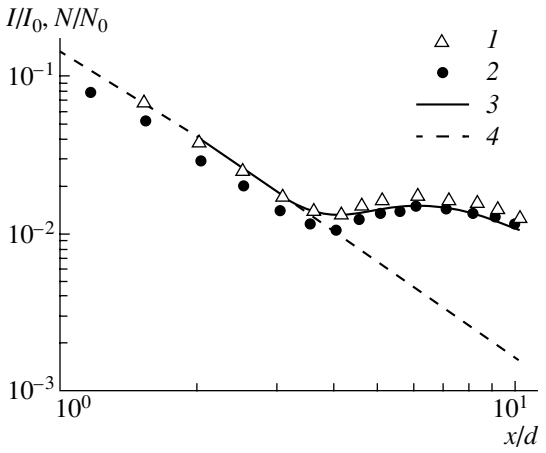

Fig. 2. Normalized Rayleigh scattering intensity I/I_0 and gas density N/N_0 versus relative distance x/d on the centerline of a free argon jet: (*1*) experiment, $d = 1.93$ mm [20]; (*2*) experiment, $d = 1.98$ mm (present study); (*3*) calculations [21]; (*4*) isentropic curve.

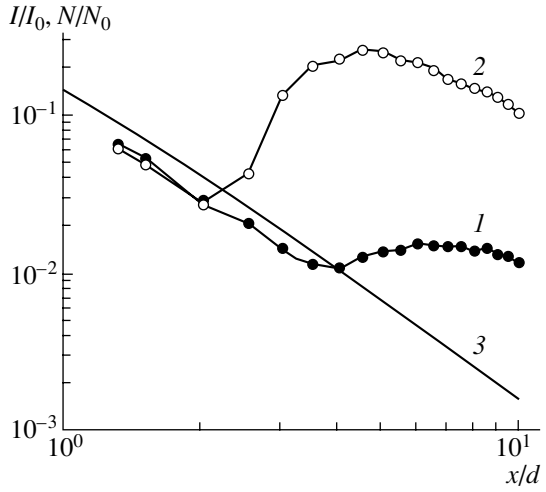

Fig. 3. Normalized Rayleigh scattering intensity I/I_0 and gas density N/N_0 versus relative distance x/d on the centerline of free argon and monosilane–argon jets: (*1*) Ar, $P_0 = 537$ torr; (*2*) Ar + 5% SiH_4, $P_0 = 554$ torr; (*3*) isentropic curve.

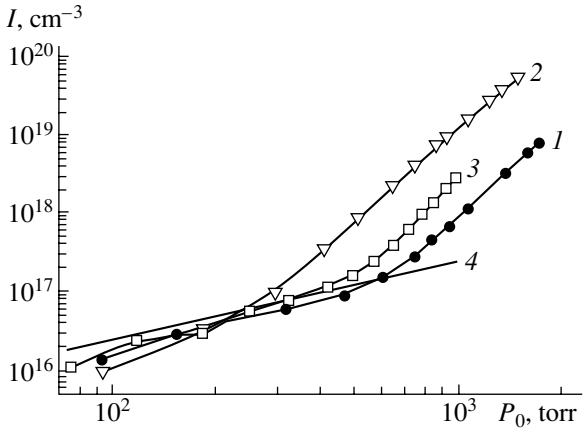

Fig. 4. Rayleigh scattering intensity I versus stagnation pressure P_0 in free argon, monosilane–argon, and monosilane–helium jets: (*1*) Ar, (*2*) Ar + 5% SiH_4, (*3*) He + 10% SiH_4, (*4*) isentropic curve.

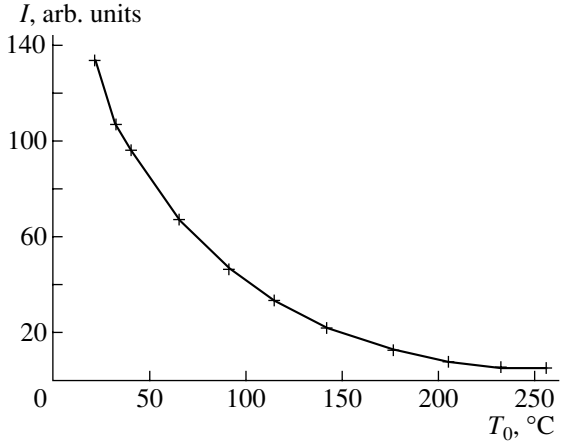

Fig. 5. Rayleigh scattering intensity I versus stagnation temperature T_0 on the centerline of the free 5% monosilane–argon jet. Initial pressure: P_0 = 1740 torr.

densation front in the mixture jet is higher than in the case of the pure gas jet by an order of magnitude.

Figure 4 shows the scattering intensity I as a function of stagnation pressure measured, with an error not greater than 10%, at the distance x = 5 mm from the nozzle for pure argon, monosilane–argon, and monosilane–helium jets flowing out of a nozzle of diameter 1.07 mm. Here, the intensity is measured in the units of equivalent gas number density. In the absence of condensation (at low P_0), the intensity and gas density are equal. The graph implies that condensation develops at $P_0 \sim 600$ torr in the argon jet and at $P_0 \sim 250$ torr in the mixture jet. At lower pressures, the measured densities are mutually consistent and agree with the isentropic predictions obtained for the mixture jet. As in the measurements described above, condensation proceeds at a higher rate in the mixed jet as compared to the argon jet. The condensation observed in the 10% monosilane–helium jet starts at a noticeably higher pressure (~450 torr), as compared to condensation in the monosilane–argon jet (~250 torr), and proceeds at a substantially lower rate.

Figure 5 shows the scattering intensity measured for a free monosilane–argon jet flowing out of a nozzle of diameter 0.54 mm at a distance of 5 mm as a function of stagnation temperature. As the gas-source temperature was increased to 250°C, the scattering intensity decreased by a factor of about 30. This is an expected result since the rate of condensation strongly depends on the gas stagnation temperature [9, 10].

Figure 6 shows the distributions of normalized Rayleigh scattering intensity along the centerlines of free monosilane–argon jets issuing from nozzles with diameters of 1.07, 1.98, 3.6, and 4.8 mm measured at constant stagnation pressures with an error not greater than 10%. The figure demonstrates that condensation takes place in the jet flowing out of each of these nozzles. However, the condensation rate is higher for nozzles of smaller diameters. The condensation front is located at a relative distance of 2–3.5, and the distance decreases with nozzle diameter. When the nozzle diameter was 1.07 mm, measurements were difficult to perform in the jet region upstream of the condensation front because of interference with the light scattered by the nozzle. Note that the condensation front developing in the monosilane–helium jet was located at a slightly greater relative distance from the nozzle (~2.5).

DISCUSSION

The Rayleigh scattering measurements showed that condensation takes place in free jets of 5% monosilane–argon mixture issuing from each of the nozzles tested in this study if the value of P_0d^2 is at least ~2500 torr mm^2 (see Fig. 6). The rate of condensation increases with decreasing nozzle diameter, and the distance between the condensation front and the nozzle exit decreases from $x/d \approx 3.5$ to $x/d \approx 1$–2 as the nozzle diameter is varied from the largest to the smallest. Condensation is suppressed by heating the gas (see Fig. 5). The results presented here are in satisfactory agreement with those obtained in mass-spectrometric measurements conducted in a pulsed jet flowing out of a nozzle of diameter 1 mm [15]. In particular, well-developed condensation was observed at pressures above $P_0 \sim$ 250 torr in this study and above $P_0 \sim 160$ torr in [15]. When comparing these results, one should bear in mind that the Rayleigh diagnostic technique is more sensitive to large clusters and, therefore, begins to detect condensation at a higher pressure.

The experimental results presented here imply that condensation starts at lower pressures and smaller distances from the nozzle exit, and is characterized by substantially higher rates, in monosilane–argon jets as compared to pure argon or monosilane–helium jets. One plausible explanation of these results is that simul-

taneous condensation of both monosilane and argon was actually detected.

Formula (4) can be used to estimate the average cluster size for a given scattering intensity. However, the fraction of condensate must be known in this expression. For a pure argon jet, the condensate content can be reliably determined by calculation [21]. The average argon cluster size is 300 at the highest pressure under the conditions represented in Fig. 4 and 110 at the largest distance under the conditions represented in Figs. 2 and 3. Note that the corresponding condensate contents were 8.1 and 8.3%, respectively. For mixture jets, no data on the condensate content are available. However, it is well known that the component characterized by the lowest saturation vapor pressure condenses first in a premixed flow at a constant temperature. In our study, monosilane was such a component. In a flow with well-developed condensation, a highly volatile component can condense almost completely when its initial concentration is below 5–10% [9]. It can be presumed that the flow regimes in 5% monosilane–argon and 10% monosilane–helium jets under the conditions represented in Fig. 4 are characterized by well-developed condensation, and monosilane has condensed completely. Accordingly, the respective estimated condensate contents are 5 and 10%. Since the results concerning the latter mixture were obtained only for pressures below 1000 torr, extrapolation should be used. Then, the estimated average monosilane cluster sizes are ≈800 and ≈70 for the monosilane–argon and monosilane–helium mixtures, respectively. These estimates may seem to suggest that the rate of monosilane condensation in an argon jet was much higher than in a helium jet. However, this is unlikely to be the case (for explanation, see [9]), and simultaneous condensation of both monosilane and argon resulting in the formation of mixed clusters is a more plausible scenario. Accordingly, a different value of the fraction of condensate should be used in estimating the cluster size. This scenario is practically impossible in the case of a helium-containing mixture, because helium is characterized by low rates of condensation in jet flows and is unlikely to contribute to any clustering (including formation of mixed clusters).

In view of these estimates, it is of interest to determine which scaling parameter should be used to unify the Rayleigh scattering data on condensation in monosilane–argon jets: $P_0d^{0.8}$ (as in the case of condensation in a pure argon jet [10]) or P_0d (as in the case of condensation in a mixture jet [9]). Figure 7 shows the curves of $I/I_{is} = f(P_0d^{0.8})$ corresponding to two nozzles of different diameters and single experimental data points obtained for each of two additional nozzles. Here, I_{is} is the Rayleigh scattering intensity corresponding to the isentropic density distribution. The results scale with P_0d near the condensation threshold (for $P_0d^{0.8} \sim$ 100–200 torr mm$^{0.8}$) and with $P_0d^{0.8}$ at higher values of the parameter. This observation suggests that monosilane and argon condense simultaneously at high stagnation pressures, and mixed clusters are formed. The formation of mixed argon–monosilane clusters was also observed in other studies [15, 22]. In [22], monosilane–argon dimerization was detected in a 1% mixture jet. In [15], Ar_nSiH_x cluster ions (with n = 1–4 and x = 2–4) were detected in a mass spectrometric study of a 5% monosilane–argon mixture jet, which also points to the formation of mixed clusters.

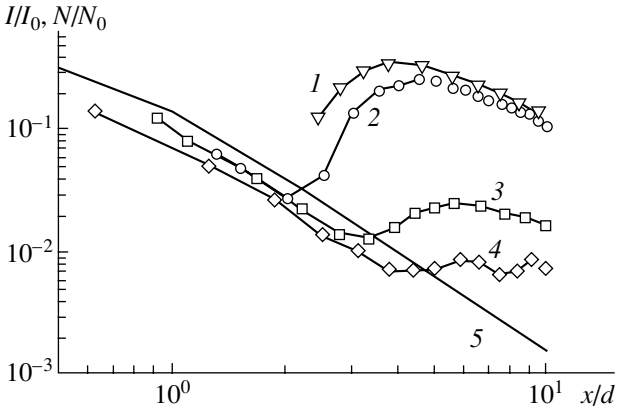

Fig. 6. Normalized Rayleigh scattering intensity I/I_0 and gas density N/N_0 versus relative distance x/d on the centerline of free 5% monosilane–argon jets issuing from various nozzles: (*1*) d = 1.07 mm, P_0 = 937 torr; (*2*) d = 1.98 mm, P_0 = 554 torr; (*3*) d = 3.6 mm, P_0 = 182 torr; (*4*) d = 4.8 mm, P_0 = 111 torr; (*5*) isentropic curve.

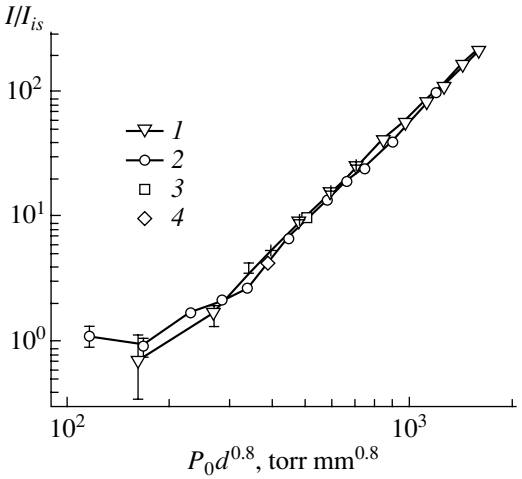

Fig. 7. Normalized Rayleigh scattering intensity I/I_{is} versus scaling parameter $P_0d^{0.8}$ for free 5% monosilane–argon jets at x/d = 9.24 with d = (*1*) 1.07, (*2*) 1.98, (*3*) 3.6, and (*4*) 4.8 mm.

These observations suggest that condensation in a monosilane–argon jet develops as follows: monosilane condenses first, and the resulting clusters play the role of nuclei for argon condensation. As a consequence, argon condensation starts at a lower pressure and a shorter distance from the nozzle exit. This leads to a

higher rate of condensation and a larger cluster size in a monosilane–argon jet as compared to a pure argon jet. In a monosilane–helium jet, the rate of condensation is substantially lower because the formation of mixed monosilane–helium clusters is unlikely to occur.

The phenomena mentioned in the Introduction and observed in a monosilane–argon jet activated by an electron beam [11–13] definitely correlate with the development of jet condensation and may be explained by interaction between electrons and newly formed monosilane and monosilane–argon clusters. Therefore, condensation should be taken into account in studies and applications of film deposition from free jets.

CONCLUSIONS

A Rayleigh scattering diagnostic technique was used to study condensation in free gaseous 5% monosilane–argon jets for nozzles with diameters varying from 0.5 to 4.8 mm and 10% monosilane–helium jets for a nozzle of diameter 1.07 mm. It was found that condensation takes place in the SiH_4–Ar jet flowing out of each nozzle used in the study when the value of P_0d^2 is at least ~2500 torr mm^2. It was shown that the Rayleigh scattering intensities corresponding to condensation in the monosilane–argon jets scale with $P_0d^{0.8}$. The SiH_4–Ar mixture is characterized by a substantially higher condensation rate, as compared to the monosilane–helium mixture and pure argon. The last two observations, combined with an analysis of available literature, suggest that these results should be explained by simultaneous condensation of monosilane and argon and formation of mixed clusters.

ACKNOWLEDGMENTS

We thank P.A. Skovorodko for calculations of condensing argon jets under the present experimental conditions.

This work was supported by the Russian Foundation for Basic Research, project no. 96-03-33924.

REFERENCES

1. R. A. Street, Phys. Status Solidi A **166**, 695 (1998).
2. A. E. Belikov, S. A. Biryukov, G. I. Sukhinin, *et al.*, in *Proceedings of the 17th International Symposium on Rarefied Gas Dynamics, Aachen, 1990*, Ed. by A. Beylich (VCH, Weinheim, 1991), p. 1568.
3. B. L. Halpern, J. J. Schmitt, J. W. Golz, *et al.*, Appl. Surf. Sci. **48/49**, 19 (1991).
4. R. G. Sharafutdinov, A. V. Skrinnikov, A. V. Parakhnevich, *et al.*, J. Appl. Phys. **79**, 7274 (1996).
5. C. B. Mullins, K. A. Pacheco, and S. Banerjee, J. Appl. Phys. **82**, 6281 (1997).
6. T. Motooka, H. Abe, and P. Fons, Appl. Phys. Lett. **63**, 3473 (1993).
7. Y. Ikoma, T. Endo, F. Watanabe, *et al.*, Jpn. J. Appl. Phys., Part 2 **38**, L301 (1999).
8. A. De Graaf, G. Dinescu, J. L. Longueville, *et al.*, Thin Solid Films **333**, 29 (1998).
9. O. F. Hagena, Surf. Sci. **106**, 101 (1981).
10. O. F. Hagena and W. Obert, J. Chem. Phys. **56**, 1793 (1972).
11. R. G. Sharafutdinov, S. Yu. Fedorov, S. Ya. Khmel, *et al.*, in *Proceedings of 14th International Symposium on Plasma Chemistry, Prague, 1999*, Vol. 3, p. 1297.
12. S. Ya. Khmel, R. G. Sharafutdinov, and A. V. Skrinnikov, *Europhys. Conf. Abstracts*, Vol. 20E (13th ESCAMPIC, Poprad, Slovakia, 1996), Part B, p. 425.
13. S. Ya. Khmel, S. Yu. Fedorov, and R. G. Sharafutdinov, in *Proceedings of XXIV International Conference on Phenomena in Ionized Gases, Warsaw, 1999*, Vol. 4, p. 105.
14. A. Ding, R. A. Cassidy, L. S. Cordis, *et al.*, J. Chem. Phys. **83**, 3426 (1985).
15. R. G. Sharafutdinov, A. E. Zarvin, N. G. Korobeĭshchikov, *et al.*, Pis'ma Zh. Tekh. Fiz. **25** (21), 47 (1999) [Tech. Phys. Lett. **25**, 865 (1999)].
16. A. C. Eckbreth, *Laser Diagnostics for Combustion Temperature and Species*, 2nd ed. (Gordon and Breach, Amsterdam, 1996).
17. *Tables of Physical Data: Reference Book* [in Russian], Ed. by I. K. Kikoin (Atomizdat, Moscow, 1976).
18. H. E. Watson and K. L. Ramaswamy, Proc. R. Soc. London, Ser. A **156**, 144 (1936).
19. J. W. L. Lewis and W. D. Williams, Phys. Fluids **19**, 951 (1976).
20. E. M. Abornev, O. A. Nerushev, S. A. Novopashin, *et al.*, Pis'ma Zh. Tekh. Fiz. **22** (21), 84 (1996) [Tech. Phys. Lett. **22**, 900 (1996)].
21. S. V. Nedosekova and P. A. Skovorodko, in *Proceedings of the X All-Union Conference on Dynamics of Rarefied Gases, Moscow, 1989*, Vol. 3, p. 116.
22. R. W. Randall and B. J. Howard, J. Chem. Phys. **100**, 7051 (1994).

Translated by A. Betev

Technical Physics, Vol. 46, No. 6, 2001, pp. 761–766. Translated from Zhurnal Tekhnicheskoĭ Fiziki, Vol. 71, No. 6, 2001, pp. 122–126.

On the Transformation of Carbon Vapor in the Gas-Plasma Jet of an Arc Discharge

N. I. Alekseev*, F. Chibante, and G. A. Dyuzhev***

** Ioffe Physicotechnical Institute, Russian Academy of Sciences, St. Petersburg, 194021 Russia*

*** BuckyUSA, Houston, TX, USA*

e-mail: dgan@hm.csa.ru

Received August 28, 2000

Abstract—Experimental data on measuring the amounts of fullerene-containing soot deposited in different areas of a fullerene arc are obtained. It is shown that, relying on a fairly general model of the spectra of clusters, a simple gas-dynamic model, and existing knowledge of the transformation stages of carbon clusters, the area of the arc where fullerenes are produced can be determined. *© 2001 MAIK "Nauka/Interperiodica".*

In experimental work [1], flows of carbon onto cylindrical probes introduced into the gas-plasma jet of an arc discharge, where fullerene-containing soot is produced, were measured, and the results obtained were found to give a qualitative picture of the carbon vapor transformations in the jet. In this study, quantitative calculations and estimates are made and compared with the experiment.

CALCULATION OF THE CAPTURE PARAMETER AND COMPARISON WITH EXPERIMENT

From experiments with drift tubes [2], it is known that the topology of carbon clusters depends on the number of atoms N approximately as follows. Chains are formed by $N \le 10$ atoms; the number of atoms in rings is $10 \le N \le 30$–40, and $N \ge 30$–40 atoms form into multiring clusters whose topology is not unique. In fullerenes and nearly closed fullerene-like clusters, the basis of soot associates, the number of atoms is $N > 36$ [3]. Kinetic characteristics of the rings and chains are very close [4], and the quantity of fullerenes with $N \le 60$ in negligible. Therefore, in calculations of integrated characteristics such as the current per probe, it is sufficient to describe clusters having a distribution function over the number of atoms in the cluster $n(N)$ using a natural normalization

$$\int Nn(N)dN = n_\Sigma,$$

where n_Σ is the total concentration of the carbon impurity in the carrier gas, helium.

Then the mass of carbon deposited from the gas flow onto a single cylindrical probe oriented at a normal to the flow direction in a radial-slit source is defined by an integral [5]

$$M = 2am_C VL_{\text{eff}} \int Nn(N)\varepsilon(N)dN. \quad (1)$$

Here, a is the probe radius; m_C is the mass of the carbon atom; V is the radial gas velocity; L_{eff} is the effective rod length; $\varepsilon(N) = J/(2anV)$ is the capture parameter for a cluster of given N; and J is the carbon flux per probe unit length. For determining the variables relating to the flow, we use standard formulas of the theory of a free turbulent jet in the form given by Prandtl [5]. In this case; (i) $L_{\text{eff}} = 2xr_0\tan(\zeta)$ is the thickness of the jet displacement layer, where r_0 is the electrode radius; $x = r/r_0$ is the dimensionless distance from the discharge axis; and ζ is the jet angle; (ii) the gas velocity, $V = V_0\Theta_V/x$, and temperature, $T = T_0\Theta_T/x$, and the impurity concentration, $n_\Sigma = n_0\Theta_n/x$, where V_0, T_0, and n_0 are the values of these parameters in the source section and Θ_V, Θ_T, and Θ_n are the parameters of the theory. In our case $\Theta_V \approx \Theta_T \approx \Theta_n = \Theta \approx 3.5$.

It is evident that the formulas for V, T, and n_Σ are true for $x > \Theta$. In the region of potential jet nucleus, $x < \Theta$, the variation of the parameters is insignificant.

The expression for the capture parameter ε in the case of slow aerosol-like impurity particles has been obtained in [6] by solving the problem of steady-state diffusion, which is expressed by the equation

$$\text{div}(nV_S) = D\Delta n. \quad (2)$$

Here, V_S is the directional velocity of the carrier gas and D is the diffusion coefficient. Equation (2) was solved with boundary conditions

$$n|_{r=a} = 0, \quad n|_{r=\infty} = n_\infty, \quad n|_{\varphi=0} = n_\infty, \quad (3)\text{–}(5)$$

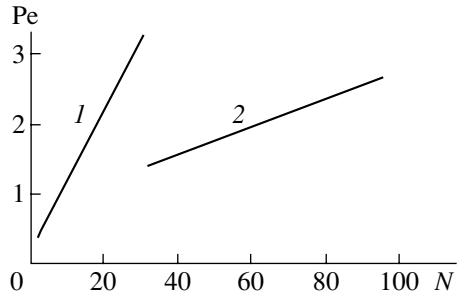

Fig. 1. Dependence of the Peclet number of the number of carbon atoms in a cluster: (*1*) chains and rings; (*2*) fullerenes; $T = 0.3$ eV.

where the angle φ is that made with the direction opposite to the flow.

Condition (5) is required for the existence of a line of maximum onflow; it is asymptotic in character and holds only for Peclet diffusion numbers $\mathrm{Pe} = aV/D \longrightarrow \infty$ [7].

In [6] the following dependence of the capture parameter on Peclet number has been obtained:

$$\varepsilon = 2.32 \times \mathrm{Pe}^{-2/3}\omega, \tag{6}$$

where $\omega = 1/\{2[2 - \ln(\mathrm{Re})]\}^{1/3}$ and $\mathrm{Re} = 2aV/\nu$ is the Reynolds number.

Figure 1 gives Peclet numbers of the carbon clusters forming chains (or rings, whose characteristics are very similar, see curve *1*) and fullerenes (curve *2*) for a typical helium concentration of 3×10^{17} cm^{-3}. Data for collision cross sections determining the diffusion coefficient $D \approx 0.33V_{T(\mathrm{He})}/\sigma N_{\mathrm{He}}$, where $V_{T(\mathrm{He})}$ is the thermal velocity and N_{He} is the helium concentration, have been borrowed from [8]. It is seen that, for most clusters, $\mathrm{Pe} \geq 1$ and formula (6) is applicable. An exception is presented by small chains with $N \leq 10$, for which Pe can be significantly less than unity. In this case there is no maximum onflow line and the current is defined by corrections to the known formula for a diffusion probe in the absence of directional gas flow [9]:

$$\frac{J}{2\pi} = \frac{Dn_\infty}{\ln(R/a)},$$

where $R \sim V_T\tau$ is the cut-off length determined by the lifetime of a given cluster and its thermal velocity V_T; the corrections should have the form of an expansion over a small parameter, the Peclet number.

Let us expand n in Eq. (2) over Legendre polynomials

$$n = n_0 + n_1\cos\varphi + \ldots \tag{7}$$

and equate the coefficients of the same order in the right- and left-hand sides. Taking into account only the first two terms we get

$$\begin{aligned} d^2n_0/dr^2 + (1/r)dn_0/dr \\ = (-\mathrm{Pe}/3)(Udn_1/dr + 2\Phi n_1/r), \end{aligned} \tag{8}$$

$$d^2n_1/dr^2 + (1/r)dn_1/dr - n_1/r^2 = -\mathrm{Pe}Udn_0/dr, \tag{9}$$

where $U(r)$ and $\Phi(r)$ are absolute dimensionless variables of radial and angular velocities of the carrier gas divided by cosφ and sinφ, respectively, and differentiating is done over a dimensionless coordinate r/a denoted with the same symbol r.

Equation (8) was solved as a boundary problem with boundary conditions (3), (4), and Eq. (9) as an ordinary differential equation with conditions

$$\left.\frac{dn}{dr}\right|_{r = R/a} = n|_{r = R/a} = 0. \tag{10}$$

In a zero approximation,

$$n_0^0 = n_\infty\frac{\ln(r)}{\ln(R/a)}, \quad n_1^0 = \frac{C}{r}. \tag{11), (12}$$

Though n_1^0 does not satisfy condition (10), we will use it for defining the right-hand side of Eq. (8). The constant C is determined from condition (9):

$$C = \mathrm{Pe}n_\infty. \tag{13}$$

Substituting Eq. (13) into Eq. (8) we get in the next (first) approximation

$$d^2n_0/dr^2 + (1/r)dn_0/dr = (-\mathrm{Pe}^2n_\infty/3r^2)(U - 2\Phi). \tag{14}$$

In the case of viscous circumfluence, functions U and Φ are calculated only over distances $r - 1 \leq 1/\mathrm{Re}$ from the probe using the known formula for the Lamb potential and have the form

$$U = U_L = [1/r^2 - 1 + 2\ln r]\omega, \tag{15}$$

$$\Phi = \Phi_L = [-1/r^2 + 1 + 2\ln r]\omega. \tag{16}$$

At $r - 1 > 1/\mathrm{Re}$, the form of these functions is unknown, but it is easy to find that the result of integration in Eq. (14)

$$n_0 = \left.\frac{dn_0}{dr}\right|_{r = 1}\ln r + \frac{\mathrm{Pe}^2n_\infty}{3}\int_1^r\frac{dr'}{r'}\int_1^{r'}\frac{1}{r''}(U - 2\Phi)dr''$$

under obvious constraints for U and Φ

$$(U - 2\Phi)|_{r = R/a} = -1,$$

$$\frac{d}{dr}(U - 2\Phi)|_{r = 1} = \frac{d}{dr}(U_L - 2\Phi_L)|_{r = 1} = 8\omega$$

depends but weakly on the particular form of the function. Having thus determined $dn_0/dr|_{r = 1}$, we find that

the current per unit length of probe is

$$\frac{J}{2\pi} = \frac{Dn_\infty}{\ln(R/a)}\left(1 - \frac{\mathrm{Pe}^2}{3}\int_1^{R/a}\frac{dr'}{r'}\int_1^{r'}\frac{1}{r''}(U-\Phi)dr''\right). \quad (17)$$

Dependence of the capture parameter given by Eq. (17) on the Peclet number Pe is shown in Fig. 2 (curve *2*). It is seen that at low Pe, curve *2* can differ from curve *1* by a factor of 2 and this difference should be taken into account in the following consideration. It is interesting to note that at Pe = 1, in which case both Eqs. (6) and (17) introduce very large errors but of different sign, the curves differ by no more than 20%.

Comparing Fig. 2 of this study and Fig. 2 of [1], it is seen that calculated and experimental values of the capture parameter are roughly the same. Indeed, in the region $r < 1$ cm, where the jet contains carbon atoms and small clusters, the Pecklet number is much less than unity and, correspondingly, the capture parameter can be far in excess of unity. At larger r, where the cluster size is larger and Pe approaches 1, the capture parameter also becomes about unity. For large particles, $\mathrm{Pe} \gg 1$ and $\varepsilon < 1$.

However, it should be noted that neither Eq. (6) nor Eq. (17) can ensure greater accuracy. Already at Re ~ 0.1, which is much less than our experimental values, the boundary layer breaks away and a turbulent flow emerges beyond the probe. Therefore, it would appear that the real value of ε should be lower than that given by both formulas.

On the other hand, the probe is completely immersed in the turbulent mixing layer. If the turbulent flow is presented as a sequence of large-scale vortices extending over most of the mixing layer [5], then inside a vortex the movement of particles towards the probe will have a tangential component. This should, on the contrary, increase the capture parameter because the probe cross section for a current tube inside the vortex is considerably larger than for normal incidence. In addition, the particles in the vortex swirl past the probe quite a number of times.

If over the time of passage of the vortex the flux of particles rises by a factor of M and the relative time of staying in a given vortex point (intermittence factor) is Γ, then the relative increase of the flux per probe is $M\Gamma + (1 - \Gamma)$. This factor can hardly exceed 2.

It is possible that the rise of the capture parameter due to "external" turbulence and the decrease because of "intrinsic" turbulence compensate one another and formulas (6) and (17) (each in its own region) give correct results. In this study we will process experimental data using formula (6).

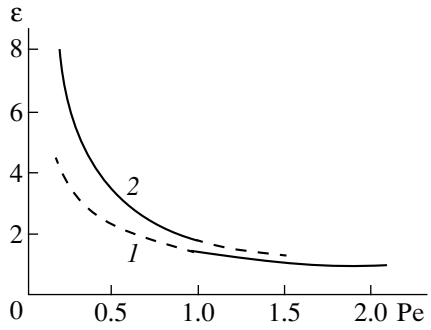

Fig. 2. Dependence of the capture parameter ε on Peclet number: (*1*) calculation by formula (6); (*2*) calculation by Eq. (17): Re = 1, $R/a = 6$.

CALCULATION OF THE MASS FLUX PER PROBE FOR DIFFERENT CLUSTER SIZE DISTRIBUTION FUNCTIONS

Analysis of the experimental data was done for three alternative assumptions regarding the carbon carrier.

(1) All carbon atoms are contained in chains or rings whose distribution varies as

$$\frac{n(N)}{n_0} = \alpha_\mathrm{C}\left[1 - \left(\frac{N}{N_1}\right)^q\right] \quad (18)$$

at $N < N_1(r)$. The function $N_1(x)$ gives the maximum number of carbon atoms in a given cluster type. The collision cross section of the cluster with helium determining their diffusion was taken equal to $\sigma \approx 0.5N\sigma_0$, where $\sigma_0 = 7.54 \times 10^{-16}$ cm^2 [8]. The adopted approximation is indirectly supported by calculation results in [8], where at $N \sim 35$–45 the number of chains and rings was found to fall drastically because of the peculiar growth of the cluster coagulation cross section with increasing N.

Besides the power-law approximation, an exponential approximation of the function $n(N)$ was used:

$$\frac{n(N)}{n_0} = \alpha_\mathrm{C}\exp\left(-\gamma\frac{N}{N_1}\right), \quad (19)$$

where parameter γ represents simulation of a decrease of $n(N)/n_0$ over the scale of N_1, say, by a factor of 10^3; the result of such an approximation and conclusions nearly coincide with approximation (18) for $q \sim 1/2$–$1/5$. Substituting Eq. (19) into Eq. (1) we get

$$\mu = \frac{M}{M_0} = B\alpha_\mathrm{C}\left(\frac{4}{x}\right)^{1/3}N_1^{4/3}\frac{9q}{4(3q+4)}, \quad (20)$$

where $M_0 = 2\pi r_0 n_0 V_0 2dm_\mathrm{C}$ is the total mass flux from

the arc, $2d$ being the separation between the electrodes,

$$B = a\Theta^{4/3}\frac{\tan\zeta}{\pi d}2.32\omega\left(0.33\frac{V_{T0}/V_0}{\sigma_0 N_{\mathrm{He}0}a}\right)^{2/3}, \qquad (21)$$

where V_{T0} and $N_{\mathrm{He}0}$ are the thermal velocity and concentration of helium atoms in the jet source.

The normalization condition has the form

$$\frac{\Theta}{x} = \alpha_{\mathrm{C}}N_1^2\frac{q}{2(q+2)}. \qquad (22)$$

(2) All carbon atoms are contained simultaneously in chains whose distribution is described by formula (19) with a fixed boundary $N_1 = N_{10} = 38$ and fullerenes with the number of atoms $N_F = 60$. The normalization coefficients of the chains α_{C} and fullerenes α_F are assumed to be unknown:

$$\frac{n(N)}{n_0} = \alpha_{\mathrm{C}}\left[1-\left(\frac{N}{N_{10}}\right)^q\right] + \alpha_F\delta_{60,N}. \qquad (23)$$

Similar to section 1 we find

$$\mu = \frac{M}{M_0} = \frac{B}{x^{1/3}} \times\left[2^{2/3}\alpha_{\mathrm{C}}N_{10}^{4/3}\frac{9q}{4(3q+4)} + \frac{\alpha_F N_F}{3.71+0.1N_F}\right]. \qquad (24)$$

Here, $\delta_{60,N}$ is the fullerene distribution function represented by a discrete Chronicler symbol and the collision cross section of fullerenes with helium atoms expressed as $\sigma_F = (3.71 + 0.1N_F)\sigma_0$ [18]. The normalization condition has the form

$$x\left[\alpha_{\mathrm{C}}N_{10}^2\frac{q}{2(q+2)} + \alpha_F N_F\right] = \Theta. \qquad (25)$$

Thus, determination of the functions α_C and α_F is reduced to solving two equations with two unknown quantities.

(3) All carbon clusters depositing on the probe are associates of fullerenes and fullerene-like particles [3]. In describing them it is assumed that the number of "elementary particles" in an associate $s = \Omega\sigma$, where σ is the average area of the associate projection approximately equal to the cross section of its collision with a helium atom; $\Omega = \omega/4\pi R_0^2$, R_0 being the radius of the "elementary particle" and ω a geometric constant, assuming that the associate is a random packing of hard spheres, $\omega = 0.637$.

Suppose for simplicity that R_0 is equal to the fullerene radius, that the number of particles in all associates is the same and equal to $S_a(x)$, and that their concentration is $n = n_0\alpha_a(x)$. Then the relative mass of associates deposited on a probe is

$$\mu = 60\frac{B}{x^{1/3}}\left(\frac{\sigma\omega}{\pi R_0^2}\right)S_a^{1/3}\alpha_a \qquad (26)$$

provided that the normalization condition is met:

$$\frac{\Theta}{x} = 60S_a\alpha_a. \qquad (27)$$

Now the number of elementary particles in an associate can be easily determined:

$$S_a = \frac{\sigma\omega}{\pi R_0^2}\frac{1}{\sqrt{x}}\left(\frac{\Theta B}{\mu x}\right)^{3/2}. \qquad (28)$$

(4) Comparison with the experiment consisted in trying to find out whether, with the cluster distribution function proposed above, the distances from the discharge axis can be determined at which transitions from one cluster type to another take place. The following parameters were used in the calculation: the temperature $T_0 = 0.3$ eV, helium pressure 80 torr, and mass flow rate 2.5 mg/s. At a velocity of $V_0 = 4.6\times10^3$ cm/s, this flow rate produces a concentration of carbon atoms in the gap section equal to $n_0 = 2.4\times10^{16}$ cm^{-3}.

Figure 3 shows the values of $\alpha_{\mathrm{C}} = \alpha_{\mathrm{C}}^{(1)}$ derived by solving the system of equations (19)–(22) for chains

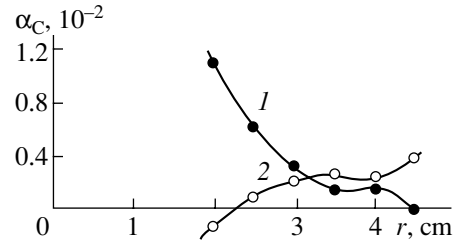

Fig. 3. Radial variation of the normalization factor $\alpha_{\mathrm{C}}(x)$ for chains and rings $\alpha_{\mathrm{C}}^{(1)}$ and the chain-ring-fullerene mixture $\alpha_{\mathrm{C}}^{(2)}$. $V_0 = 4.6\times10^3$ cm/s.

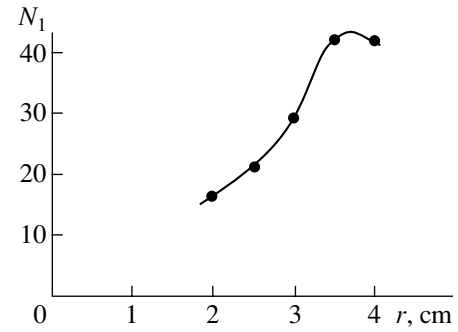

Fig. 4. Radial variation of the spectral boundary between chains and rings. $V_0 = 4.6\times10^3$ cm/s.

(curve *1*) and of $\alpha_C = \alpha_C^{(2)}$ derived from Eqs. (23)–(25) for a mixture of chains and fullerenes (curve *2*). The dependence $\mu(r)$ was determined from the experimental data. The fact that the curves intersect indicates that there is an area where fullerenes appear in the spectrum alongside chains and rings. The criterion of coherency of the calculation is $N_1 = N_{10}$ in this area, to be ensured by the proper choice of one of the unknown parameters of the problem. The dependence of N_1 on r for the same starting calculation data as in Fig. 3 is plotted in Fig. 4. It is evident that the behavior of $N_1(x)$ depends on V_0, T_0, and turbulent parameters Θ, ζ, which are not quite reliably known. Because the temperature T_0 is not expected to vary widely, the optimum variant will be the velocity V_0. Calculation has shown that at $V_0 < 2.5 \times 10^3$ cm/s, curves $\alpha_C^{(1)}$ and $\alpha_C^{(2)}$ do not intersect. In the velocity range $V_0 = 4–5 \times 10^3$ cm/s, the curves intersect and the value of N_1 at the intersection point approaches N_{10} (Fig. 5). The smallest difference between N_1 and N_{10} is achieved at $V_0 = 4.6 \times 10^3$ cm/s, corresponding to the distance $r_1 = 3.2$ cm from the discharge axis. Note that this initial velocity of the turbulent jet corresponds to a theoretical estimate [9, 10].

The position of the point where fullerenes emerge corresponds to the experimental data of [11]. Calculation shows that for this point, $\alpha_F \approx 3.5 \times 10^{-2}$ and the total absolute concentration of fullerenes and fullerene-like clusters is $n_F = \alpha_F n_0 \approx 8 \times 10^{14}$ cm^{-3}.

Consider now the transition from fullerenes to associates. Figure 6 shows the dependence on r of the number of particles in an associate S_a calculated by Eqs. (28). It is seen that associates begin to form at $r_2 \approx 4$ cm. Thus, the extent of the "life zone" for fullerenes until they merge into associates is $r_2 - r_1 \approx 0.5–1.0$ cm.

Let us make some estimates. The distance at which clusters coagulate is, by an order of magnitude,

$$L_F = V\tau_F \sim \frac{V}{V_T^F}\frac{1}{\sigma_{FF} n_F \lambda \exp(-\Delta E/T)},$$

where τ_F is the cluster free path time; $V_T^F \approx 2 \times 10^4$ cm/s is the cluster thermal velocity at $T = 0.2$ eV; $\sigma_{FF} \approx 4\sigma_F$ is the geometrical section for collisions between clusters; and ΔE is the energy barrier for the reaction.

According to the consideration in [12], most of the fullerene-like clusters contain small remains of the ring fragments and the possibility of "discarding" extra atoms in such clusters is very small. This is especially true of clusters with $N \le 60$. Such clusters should coagulate more readily if it is the ring fragments that are foremost in the approaching clusters. The barrier ΔE for such a reaction is close to that for approaching rings, $\Delta E \sim 0.5$ eV [13]. The preexponential geometrical factor $\lambda \sim 0.2–0.3$ determines the fraction of collisions in which clusters collide just in this manner, with their ring fragments at the fore. An estimate of the quantity L_F gives $L_F \sim r_2 - r_1$, which makes the adopted assumptions appear internally consistent.

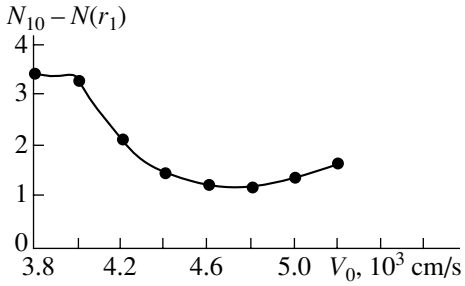

Fig. 5. Dependence of the difference between upper spectral boundary $N_0 = 38$ used in calculation by (23) and the upper boundary of the spectrum by (18) at the intersection point of curves $\alpha_C^{(1)}$ and $\alpha_C^{(2)}$ on the flow velocity V_0 at the source section.

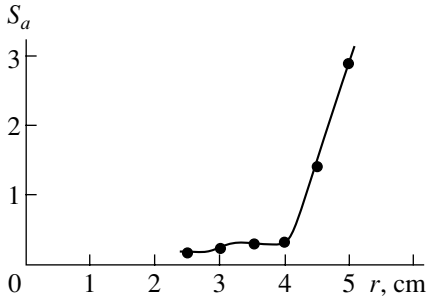

Fig. 6. Radial variation of the number S_a of "elementary particles" in an associate.

As already mentioned above while discussing the flux of particles onto the probe, we used expressions for a laminar flow in the conditions where these expressions are certainly not applicable. Therefore, it is important to find out to what extent the qualitative result obtained can be affected by hydrodynamic factors depending on the flow type.

Calculations have shown that the position of point r_1 practically does not change if the factor in expression (6) for the capture parameter is changed severalfold. Only the jet initial velocity changes. On the other hand, the position of point r_2 does not depend at all on the choice of velocity.

Thus, both the qualitative characteristics of the spectrum transformation depend on specific flow characteristics only weakly unless the nature of the flow changes qualitatively over a given spatial interval.

ACKNOWLEDGMENTS

This study was carried out in the framework of the Russian program "Fullerenes and Atomic Clusters" and

supported in part by the Russian Foundation for Basic Research (project no. 00-02-16928).

REFERENCES

1. D. V. Afanas'ev, G. A. Dyuzhev, and A. A. Kruglikov, Zh. Tekh. Fiz. **71** (5), 134 (2001) [Tech. Phys. **46**, 638 (2001)].
2. J. M. Hunter, J. L. Fye, and M. F. Jarrold, J. Chem. Phys. **99**, 1785 (1993); J. M. Hunter, J. L. Fye, E. J. Roskamp, and M. F. Jarrold, J. Phys. Chem. **98**, 1810 (1994).
3. O. P. Gorelik, G. A. Dyuzhev, D. V. Novikov, *et al.*, Zh. Tekh. Fiz. **70** (11), 118 (2000) [Tech. Phys. **45**, 1489 (2000)].
4. A. J. Alexandrov and V. A. Schweigert, Chem. Phys. Lett. **263**, 551 (1996).
5. G. N. Abramovich, *Theory of Turbulent Jets* (Nauka, Moscow, 1984).
6. G. L. Natanson, Dokl. Akad. Nauk SSSR **112**, 100 (1957).
7. A. D. Polyanin and Yu. N. Syskov, Izv. Akad. Nauk SSSR, Mekh. Zhidk. Gaza, No. 5, 162 (1976).
8. G. I. Sukhinin and O. A. Nerushev, Prikl. Mekh. Tekh. Fiz. **38** (4), 140 (1997).
9. F. G. Baksht, G. A. Dyuzhev, A. M. Martsinovskiĭ, *et al.*, in *Thermionic Converters and Low-Temperature Plasma*, Ed. by B. Ya. Moĭzhes and G. E. Pikus (Technical Information Center, Oak Ridge, 1973).
10. S. Ramakrishnan, A. D. Stokes, and J. J. Lowke, J. Phys. D **11**, 2267 (1978).
11. G. A. Dyuzhev and V. I. Karataev, Fiz. Tverd. Tela (St. Petersburg) **36**, 2795 (1994) [Phys. Solid State **36**, 1528 (1994)].
12. N. I. Alekseev and G. A. Dyuzhev, Zh. Tekh. Fiz. **71** (5), 67 (2001) [Tech. Phys. **46**, 573 (2001)].
13. A. L. Aleksandrov, V. M. Bedanov, Yu. N. Morokov, and V. A. Shveĭgert, Zh. Strukt. Khim. **36**, 991 (1995).

Translated by B. Kalinin

Technical Physics, Vol. 46, No. 6, 2001, pp. 767–769. Translated from Zhurnal Tekhnicheskoĭ Fiziki, Vol. 71, No. 6, 2001, pp. 127–129.

BRIEF COMMUNICATIONS

Anomalous Resistoacoustic Effect in a Piezoelectric–Conducting Liquid Structure

B. D. Zaĭtsev*, I. E. Kuznetsova*, and S. G. Joshi**

** Institute of Radio Engineering and Electronics, Russian Academy of Sciences, Saratov Branch, Saratov, 410019 Russia*

*** Marquette University, Milwaukee, WI 53201-1881, USA*

e-mail: zaitsev@ire.san.ru

Received July 3, 2000

Abstract—The presence of the anomalous resistoacoustic effect in the case of the propagation of a Bleustein–Gulyaev wave in a piezoelectric–conducting liquid structure is theoretically predicted. As the conductivity of the liquid increases, the wave velocity increases, reaches its maximum, and then decreases. The value of the positive variation of the wave velocity increases with decreasing dielectric constant of the liquid ε^{lq} and can reach 6% for potassium niobate at $\varepsilon^{lq} = 2.5$. It is shown that there exists a critical value of the wave localization depth above which the anomalous resistoacoustic effect in such a structure is absent. © *2001 MAIK "Nauka/Interperiodica".*

The normal resistoacoustic effect manifests itself as follows [1]: as the conductivity of a thin layer deposited on the surface of a piezoelectric substrate increases, the velocity of surface acoustic waves propagating in this system monotonically decreases, the value of the maximal velocity variation ($\Delta V/V$) being uniquely related to the electromechanical coupling coefficient of the wave. At the same time, the insertion loss as a function of conductivity exhibits a characteristic maximum and becomes zero when the layer is close to an ideal dielectric or an ideal conductor. Such dependences were observed in a structure consisting of a piezoelectric and a conducting liquid [2]. However, according to the recent theoretical prediction [3], in the case of weakly inhomogeneous acoustic waves such as the Bleustein–Gulyaev and Love waves, there exists an interval of the layer conductivity values within which the velocity of these waves first increases, reaches its maximum, and then decreases. This effect is called the anomalous resistoacoustic effect, and it can occur in any piezoelectric, the value of the maximal positive variation of the wave velocity increasing with the increase in the electromechanical coupling coefficient of the material. It was found that the anomalous resistoacoustic effect occurs when the localization depth of the surface wave exceeds some critical value [3]. Therefore, this effect is not observed for a strongly localized Rayleigh wave [1, 3]. The behavior of the insertion loss in the case of the anomalous effect is the same as in the case of the normal resistoacoustic effect. The interval of the conductivity values that correspond to considerable positive variations of the wave velocity proved to be quite narrow, so that we did not notice it in our previous study [4] of the effect of thin conducting layers on the characteristics of acoustic waves in potassium niobate.

Presumably, the anomalous effect can also occur in other situations with conducting layers, which affect the localization depth of weakly inhomogeneous waves propagating in piezoelectrics. From this point of view, surface acoustic waves propagating along the boundary between a piezoelectric and a conducting liquid are of particular interest. The theoretical study of such waves is the subject of this paper.

Let us analyze the propagation of an acoustic wave in a piezoelectric–conducting liquid structure. We assume that the x_3 axis is directed into the depth of a piezoelectric crystal occupying the half-space $x_3 > 0$, and the conducting liquid occupies the half-space $x_3 < 0$. The equations of motion for the piezoelectric medium and the liquid have the form:

$$\rho^{p}\frac{\partial^2 u_i^p}{\partial t^2} = \frac{\partial T_{ij}^p}{\partial x_j}, \quad \rho^{lq}\frac{\partial^2 u_i^{lq}}{\partial t^2} = \frac{\partial T_{ij}^{lq}}{\partial x_j}, \qquad (1), (2)$$

where u_i^p and u_i^{lq} are the particle displacements; x_j are the spatial coordinates; t is time; T_{ij}^p and T_{ij}^{lq} are the mechanical stresses; ρ^p and ρ^{lq} are the densities; and the superscripts p and lq refer to the piezoelectric and liquid media, respectively.

We write the Laplace equation for the piezoelectric medium and the Poisson equation and the charge conservation equation for the conducting liquid:

$$\mathrm{div}\mathbf{D}^p = 0, \quad \mathrm{div}\mathbf{D}^{lq} = \delta^{lq}, \quad \frac{\partial J_i^{lq}}{\partial x_i} + \frac{\partial \delta^{lq}}{\partial t} = 0. \qquad (3)–(5)$$

Here, $\mathbf{D}^p$ and $\mathbf{D}^{lq}$ are the electric inductions, δ^{lq} is the space charge density, and J_i^{lq} is the ith component of

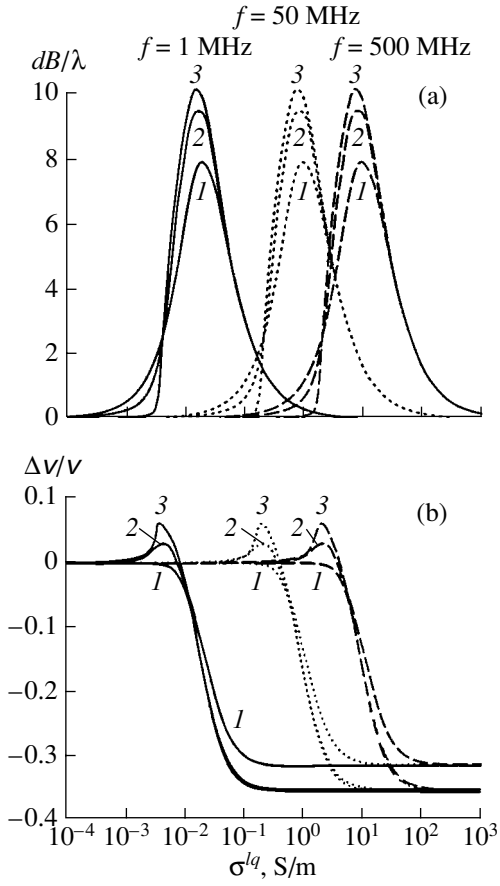

Fig. 1. Dependences of (a) the attenuation of a Bleustein–Gulyaev wave and (b) its relative velocity variation on the conductivity of the liquid for ε^{lq} = (*1*) 80, (*2*) 20, and (*3*) 2.5 and for the frequencies 1, 50, and 500 MHz (the solid, dotted, and dashed curves, respectively).

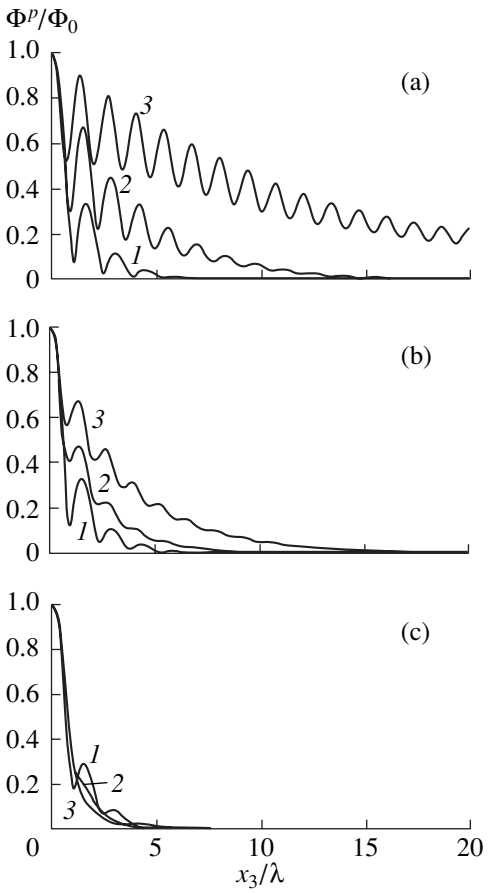

Fig. 2. Dependences of the normalized amplitude of the electric potential of a Bleustein–Gulyaev wave propagating in potassium niobate on the x_3 coordinate normalized to the wavelength for ε^{lq} = (*1*) 80, (*2*) 20, and (*3*) 2.5 and for σ^{lq} = (a) σ_1, (b) $\sigma^{lq}_{\max}$, and (c) σ_2.

the current density. Finally, we write the constitutive equations for an anisotropic piezoelectric medium

$$T^p_{ij} = C^p_{ijkl}\frac{\partial u^p_l}{\partial x_k} + e^p_{kij}\frac{\partial \Phi^p}{\partial x_k}, \tag{6}$$

$$D^p_j = -\varepsilon^p_{jk}\frac{\partial \Phi^p}{\partial x_k} + e^p_{jik}\frac{\partial u^p_l}{\partial x_k} \tag{7}$$

and for an isotropic liquid

$$T^{lp}_{ij} = C^{lq}_{ijkl}\frac{\partial u^{lq}_l}{\partial x_k}, \tag{8}$$

$$D^{lq}_j = -\varepsilon^{lq}\frac{\partial \Phi^{lq}}{\partial x_j}, \tag{9}$$

$$J^{lq}_i = -\sigma^{lq}\frac{\partial \Phi^{lq}}{\partial x_i} + d^{lq}\frac{\partial \delta^{lq}}{\partial x_i}. \tag{10}$$

Here, Φ^p and Φ^{lq} are the electric potentials, C^p_{ijkl} and C^{lq}_{ijkl} are the elastic constants, e^p_{kij} are the piezoelectric constants, ε^p_{jk} and ε^{lq} are the dielectric constants, σ^{lq} is the bulk conductivity, and d^{lq} is the diffusion coefficient.

To set the mechanical boundary conditions at the solid–liquid interface, we take into account the continuity of only the normal components of the displacements and mechanical stresses:

$$u^p_3 = u^{lq}_3, \quad T^p_{13} = T^p_{23} = 0, \quad T^p_{33} = T^{lq}_{33}. \tag{11}$$

The corresponding electric boundary conditions are based on the assumption that the surface charge and the normal component of the current are zero at the boundary:

$$\Phi^p = \Phi^{lq} = \Phi_0, \quad D^p_3 = D^{lq}_3, \quad J^{lq}_3 = 0, \tag{12}$$

where Φ_0 is the electric potential in the plane $x_3 = 0$.

To solve the above equations with the boundary conditions, we used the approach described in our previous publication [5]. The piezoelectric was assumed to be potassium niobate, which exhibits a strong piezoelectric effect [6]. The material constants used in the calculations were taken from the literature [7]. The analysis showed that, when the elastic and electric properties of the liquid vary over wide limits, we always obtain the normal resistoacoustic effect for a Rayleigh wave. The anomalous resistoacoustic effect occurs in the case of a Bleustein–Gulyaev wave propagating in the *Y*-cut, *X*-propagation potassium niobate [8]. In this case, the elastic properties of the liquid do not affect the characteristics of the wave. Therefore, we studied the effect of the dielectric constant and the conductivity of the liquid on the velocity and attenuation of a Bleustein–Gulyaev wave.

Figure 1 shows the dependences of (Fig. 1a) the attenuation and (Fig. 1b) the relative variation of the velocity of a Bleustein–Gulyaev wave on the conductivity of the liquid for different values of its dielectric constant ε^{lq} and different frequencies of the acoustic wave. From Fig. 1a, one can see that the attenuation exhibits the usual behavior and increases with decreasing dielectric constant of the liquid. This result can be explained by the increase in the effective electromechanical coupling coefficient with decreasing dielectric constant [9]. The velocity of the acoustic wave (Fig. 1b) increases with increasing conductivity, reaches its maximal value, and then drops; i.e., a pronounced anomalous resistoacoustic effect is observed. One can see that, as the dielectric constant decreases, the maximal value of the positive velocity variation $(\Delta v/v)^{+}_{\max}$ increases and can reach 6% at $\varepsilon^{lq} = 2.5$. It should also be noted that, as the frequency of the acoustic wave increases, the interval of the conductivity values σ^{lq} for which the anomalous resistoacoustic effect is observed moves toward higher conductivities of the liquid.

Figure 2 presents the dependences of the normalized amplitude of the electric potential in potassium niobate on the x_3 coordinate normalized to the wavelength for different values of the dielectric constant and conductivity of the liquid at a frequency of 1 MHz. The depth dependence of the potential was calculated for the values of the liquid conductivity (Fig. 2a) σ_1, (Fig. 2b) $\sigma_{\max}$, and (Fig. 1c) σ_2, which correspond to the relative velocity variations $(\Delta v/v)^{+}_{\max}/2$, $(\Delta v/v)^{+}_{\max}$, and $-(\Delta v/v)^{+}_{\max}$, respectively. For σ_2, we obtain the normal resistoacoustic effect. Thus, Fig. 2 shows that, as in the case of the structure with a thin conducting layer [3], there exists some critical value of the wave localization depth above which the anomalous resistoacoustic effect is absent. The wave penetration depth decreases with increasing dielectric constant of the liquid. It should be noted that the dependence of the amplitude of the potential on the x_3 coordinate exhibits an oscillatory behavior, which agrees well with the literature data [8]. As the conductivity of the liquid increases, the amplitude of these oscillations decreases.

Thus, this paper shows that, in the case of the propagation of weakly inhomogeneous waves in a piezoelectric crystal that is in contact with a conducting liquid, the anomalous resistoacoustic effect is possible. This effect is a fundamental property of weakly inhomogeneous surface acoustic waves and can serve as a criterion that allows one to discern the waves of the aforementioned type in practice.

ACKNOWLEDGMENTS

This work was supported by the Russian Foundation for Basic Research (project no. 01-02-16266) and the National Science Foundation (USA).

REFERENCES

1. A. Wixforth, J. Scriba, M. Wassermeier, *et al.*, Phys. Rev. B **40**, 7874 (1989).
2. S. Furukawa, M. Obaba, and T. Nomura, Proc.-IEEE Ultrason. Symp., 599 (1996).
3. B. D. Zaitsev, I. E. Kuznetsova, and S. G. Joshi, J. Appl. Phys. **86**, 6868 (1999).
4. Yu. V. Gulyaev, I. E. Kuznetsova, B. D. Zaĭtsev, *et al.*, Pis'ma Zh. Tekh. Fiz. **25** (8), 21 (1999) [Tech. Phys. Lett. **25**, 302 (1999)].
5. B. D. Zaĭtsev, I. E. Kuznetsova, and I. S. Nefedov, Pis'ma Zh. Tekh. Fiz. **20** (4), 60 (1994) [Tech. Phys. Lett. **20**, 159 (1994)].
6. K. Yamanouchi, H. Odagawa, T. Kojimi, *et al.*, Electron. Lett. **33** (3), 193 (1997).
7. M. Zgonik, R. Schlesser, I. Biaggio, *et al.*, J. Appl. Phys. **74**, 1287 (1993).
8. K. Nakamura and M. Oshiki, Appl. Phys. Lett. **71**, 3203 (1997).
9. E. Dieulesaint and D. Royer, *Elastic Waves in Solids* (Wiley, New York, 1981; Nauka, Moscow, 1982).

Translated by E. Golyamina

Technical Physics, Vol. 46, No. 6, 2001, pp. 770–772. Translated from Zhurnal Tekhnicheskoĭ Fiziki, Vol. 71, No. 6, 2001, pp. 130–132.

BRIEF COMMUNICATIONS

Effect of Preliminary Deformation on the Fine Structure of a TiNi-Based Alloy in the Premartensitic Region

A. A. Klopotov, T. L. Chekalkin, and V. É. Gyunter

Research Institute of Medical Materials and Implants with Shape-Memory Effect at the Siberian Physicotechnical Institute and Tomsk State University, Tomsk, 634034 Russia

Received July 11, 2000; in final form, November 20, 2000

Abstract—Results are given of an *in situ* X-ray diffraction study of the crystal-lattice state of a TiNi-based alloy during deformation under the effect of an external stress in the pretransition region preceding the *B*2–*R*–*B*19' martensitic transformations. The pretransition state preceding martensitic transformations in the alloy under study was found to manifest itself in a specific behavior of the lattice parameter and thermal expansion coefficient in the *B*2 phase. The magnitude of the thermal expansion coefficient in the *B*2 phase nonmonotonically depends on the amount of deformation and the applied stress. © *2001 MAIK "Nauka/Interperiodica".*

INTRODUCTION

The problem of pretransition phenomena preceding martensitic transformations in titanium nickelide–based alloys has been the focus of research for many years. This is due to the great scientific and practical interest in this material, which possesses unique properties, such as shape-memory effect, superelasticity, etc. [1].

In this paper, we present the results of an *in situ* X-ray diffraction research of the state of the crystal lattice of a TiNi-based alloy that was deformed or is under the effect of an external stress in the pretransition region preceding the *B*2–*R*–*B*19' martensitic transformation.

The study of the thermal expansion of metals and alloys yields information on the nature of interatomic interactions. Thermal expansion is due to the manifestation of anharmonic effects in the interatomic interactions [2]. In order to answer the question of how this interatomic interaction changes in the TN-10 alloy (a TiNi-based alloy [1]) in the pretransition region preceding the *B*2–*R*–*B*19' martensitic transformation and how this transformation responses to plastic deformation in a constrained sample, we studied the temperature dependences of the lattice parameter in the *B*2 phase (Fig. 1).

EXPERIMENTAL

The *in situ* X-ray diffraction investigations were performed using a DRON-2 diffractometer equipped with a special attachment [3] that made it possible to study the alloy in a required temperature range under a permanently applied load and fixed deformation. The measurements were conducted in a filtered CuK_α radiation. The method of preparation of a TN-10 alloy with a composition close to equiatomic was described in [1]. The samples for X-ray diffraction studies were annealed at 800°C for 1 h before the investigation.

RESULTS AND DISCUSSION

Figure 1 shows the temperature dependences of the lattice parameter of the *B*2 phase, $a_{B2}(T)$ in a temperature range preceding the martensitic transformation. In the $a_{B2}(T)$ dependences of the undeformed alloy, it is seen that the deviation from the linear behavior begins far before the onset of the martensitic transformation (Fig. 1a). Such a behavior of the lattice parameter in the region preceding the transformation indicates the development of a pretransition state [4]. The study of the $a_{B2}(T)$ dependence in a weakly deformed alloy in a constrained state revealed a feature near 100°C (Fig. 1b). This feature consists in the existence of an inflection point (the temperature T^*) in the $a_{B2}(T)$ curve. An increase in the degree of deformation led to a shift of the inflection point in the $a_{B2}(T)$ curve toward lower temperatures (Fig. 1c). In samples deformed to 10%, the pretransition region in the $a_{B2}(T)$ curve is markedly narrower than in the undeformed sample and has a more pronounced character (Fig. 1d).

Usually, upon an analysis of thermal expansion of solids, temperature dependences of the thermal expansion coefficient are used. We obtained the values of the thermal expansion coefficients from the experimental $a_{B2}(T)$ curves (Fig. 2). It is seen that in the undeformed state with approaching the temperature of the onset of the $B2 \longrightarrow R \longrightarrow B19'$ phase transition the thermal expansion coefficient in the *B*2 phase increases. This indicates a decrease in the interatomic interaction and, as a consequence, a decrease in the stability of the crystal lattice of the *B*2 phase (Fig. 2a). An insignificant

1063-7842/01/4606-0770$21.00 © 2001 MAIK "Nauka/Interperiodica"

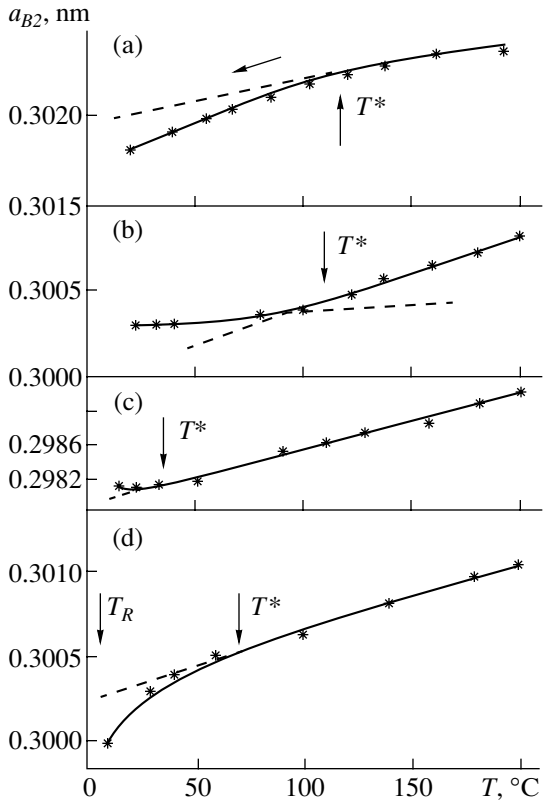

Fig. 1. Temperature dependences of the lattice parameter of the *B*2 phase: (a) in the undeformed state; (b)–(d) in a deformed state under constrained conditions; (b) ε = 2.5, (c) 3.7, and (d) 10%.

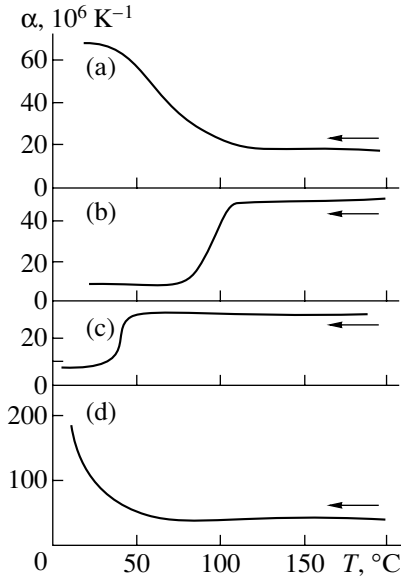

Fig. 2. Temperature dependences of the thermal expansion coefficient of the TN-10 alloy after deformation in a constrained state: (a) ε = 0, (b) 2.5, (c) 3.7, and (d) 10%.

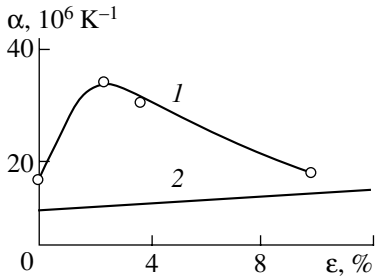

Fig. 3. Thermal expansion coefficient as a function of the degree of deformation for (*1*) the TN-10 alloy and (*2*) pure nickel. Calculated by the formula $\alpha = \alpha_0(1 + A\varepsilon)$.

deformation leads to a marked increase in the thermal expansion coefficient in the *B*2 phase far from the phase transition (not shown in the figure). At deformations of 2.5–4%, the thermal expansion coefficient in the *B*2 phase decreases in the temperature region preceding the phase transition (Figs. 2b, 2c). Greater deformations also lead to an increase in the thermal expansion coefficient in the *B*2 phase far from the phase transition, and in the temperature region preceding the phase transition leads to a noticeable growth of the thermal expansion coefficient in the *B*2 phase (Fig. 2d).

The changes in the thermal expansion coefficient depending on the degree of deformation are small. It was established in [2] that in the presence of deformation the thermal expansion coefficients obey the dependence $\alpha = \alpha_0(1 + A\varepsilon)$, where ε is the deformation caused by the external actions; α_0 is the thermal expansion coefficient at ε = 0; $A \approx \chi_T E\gamma/3$ is a coefficient that is determined by the elastic properties of the substance; and *E* is the elasticity modulus. We calculated the thermal expansion coefficient depending on the degree of plastic deformation for nickel with the coefficient *A* = 2.1 [2] (Fig. 3). This dependence is nonmonotonic for titanium nickelide, in which phase transitions occur. In metals, which suffer no phase transitions, the dependence of the thermal expansion coefficient from deformation is linear.

It is known that the thermal expansion coefficient of metals α is one of anharmonic characteristics of crystals [4]. The coefficient α depends on the binding energy |*U*|. For pure metals, the thermal expansion coefficient at $T > \Theta$ can be calculated by the formula [5] $\alpha = 3CR/2|U|$, where *C* is a coefficient that can take on values 3, 5, …, 10. This formula qualitatively reflects a realistic situation: the greater the binding energy and the deeper the potential well, the smaller the thermal expansion coefficient. An increase in the value of the thermal expansion coefficient α indicates a decrease in the binding energy, i.e., reflects the decrease in the stability of a given crystal modification. In our case, a discontinuous (jumpwise) increase in coefficient α shows that the crystal lattice of the phase with the *B*2-type structure passed into a new, less stable state with respect to the low-temperature state. This indicates the

preparation of the crystal lattice to the martensitic transition. By the magnitude of the jump $\Delta\alpha$, we can judge the magnitude of the binding energy change ΔU. The alloys that were subjected to small deformations in the immediate proximity to the temperature of the *B*2–*R* martensitic transformation ($T_R < T < T^*$), coefficient α decreases markedly. This indicates that the deformation converts the crystal lattice of the *B*2 phase into a more stable state. These data correlate with the revealed nonmonotonic dependence of the T_R and M_s curves on the degree of deformation with a minimum at deformations of 3–5% for the TN-10 alloy [6].

CONCLUSIONS

Thus, X-ray diffraction studies show that the pretransition state that precedes the martensitic transformation in the titanium nickelide-based alloy manifests itself in the behavior of the lattice parameter and thermal expansion coefficient in the *B*2 phase. The magnitude of the thermal expansion coefficient in the *B*2 phase depends nonmonotonically on the deformation and on the applied external stress.

REFERENCES

1. V. É. Gyunter, G. N. Dambaev, P. G. Sysolyatin, *et al.*, *Medical Materials and Implants with Shape Memory Effect* (Tomskiĭ Gos. Univ., Tomsk, 1998).
2. S. I. Novikova, *Thermal Expansion of Solids* (Nauka, Moscow, 1974).
3. L. A. Monasevich and Yu. I. Paskal', Zavod. Lab., No. 7, 32 (1983).
4. L. R. Testardi, Phys. Acoust. **10**, 193 (1973); M. Veger and I. Goldberg, Solid State Phys. **28**, 2 (1973).
5. A. G. Konyaeva, Zh. Fiz. Khim. **58**, 1243 (1984).
6. V. É. Gyunter, T. Yu. Maletkina, and A. A. Klopotov, Prikl. Mekh. Tekh. Fiz. **39** (2), 173 (1998).

Translated by S. Gorin

Technical Physics, Vol. 46, No. 6, 2001, pp. 773–777. Translated from Zhurnal Tekhnicheskoĭ Fiziki, Vol. 71, No. 6, 2001, pp. 133–138.

BRIEF COMMUNICATIONS

The Surface Morphology of Pyrolytic Graphite Irradiated by Hydrogen Atoms

Z. Vakar*, E. A. Denisov, T. N. Kompaniets**, I. V. Makarenko*, V. A. Marushchak*, and A. N. Titkov***

** Ioffe Physicotechnical Institute, Russian Academy of Sciences, Politekhnicheskaya ul. 26, St. Petersburg, 194021 Russia*

*** St. Petersburg State University (Petrodvorets Branch), Universitetskiĭ pr. 2, Petrodvorets, 198904 Russia*

e-mail: kompan@paloma.spbu.ru

Received August 16, 2000

Abstract—Interaction between atomic hydrogen and pyrolytic graphite is investigated by thermal desorption spectroscopy, atomic force microscopy, and scanning tunneling microscopy. After exposure in an atomic hydrogen flow, the initially smooth graphite surface becomes rough, with a height difference of several nanometers. When heated, the samples release hydrogen and their surface is smoothed out, showing monolayer-deep etch pits. After multiple sorption–desorption cycles, both the linear sizes and the depth of the pits increase. © *2001 MAIK "Nauka/Interperiodica".*

INTRODUCTION

The unique combination of the physical parameters of graphite, such as its small atomic number, as well as high thermal conductivity, heat capacity, and temperature of sublimation, makes it promising for protective coatings of both the first wall and the divertor in tokamak reactors. During the operation of the reactor, the graphite surfaces are subjected to intense flows of hydrogen atoms, ions, and molecules, which cause protective graphite tiles to degrade.

Hydrogen–graphite interaction depends on the state of hydrogen (ionic, atomic, or molecular) striking the graphite surface. For instance, molecular hydrogen interacts with the graphite surface only at high temperatures and in the presence of a catalyst [1–3]. The irradiation of graphite by hydrogen atoms produces hydrocarbons and causes the hydrogen to accumulate both on the surface and in the bulk of the sample [2, 4, 5]. H^+ ion bombardment gives rise to the formation of the near-surface layer, which is saturated by hydrogen to a concentration of roughly 0.4 atoms per C atom. Interaction between graphite and neutral hydrogen atoms is as yet little understood. A part (usually small) of the hydrogen is responsible for the formation of volatile hydrocarbon compounds and the rest of the hydrogen is sorbed either on or under the surface. On heating, the hydrogen sorbed leaves the sample mainly in the form of H_2 molecules [2]. A number of authors assume, without citing convincing evidence, that this hydrogen is adsorbed on the surface [2], whereas others believe that it is released from the bulk [6, 7]. The kinetics of hydrogen release from commercial and pyrolytic graphites irradiated by H^0 atoms was investigated in [8]. Results obtained in that work suggest that hydrogen is most likely to localize in the near-surface layer of graphite.

In this study, we pursue our investigation of atomic hydrogen sorption and its subsequent release on heating. Apparently, the sorption of hydrogen and the formation of hydrocarbons must change the morphology of the graphite surface. It can be expected that the methods of atomic-force and scanning-tunneling microscopies (AFM and STM, respectively), together with the method of thermal desorption spectroscopy (TDS), will provide valuable information on both hydrogen localization and the morphology of the graphite surfaces.

PREPARATION OF SAMPLES AND EXPERIMENTAL METHODS

The object under study is quasi-single-crystal pyrolytic graphite, since its surface has extensive planar regions needed for the reliable observation of morphological changes with the AFM and STM methods. A strip of pyrolytic graphite measuring $1 \times 40 \times 0.15$ mm was cut from a bulk sample (its upper damaged layers were removed with an adhesive tape) and placed into a high-vacuum chamber. The sample surface was parallel to the basal graphite plane. Prior to experiments (for details, see [8]), the samples were outgassed by high-vacuum heating for a long time. The AFM and STM images taken of various surface regions both before and after the treatment indicate that the high-temperature vacuum heating does not change the surface morphology of the samples.

The chamber can be connected to a mass-spectrometer and to a purified hydrogen delivery system. After outgassing, the sample was cooled to room temperature and the chamber was filled by molecular hydrogen up to a pressure of about 10^{-2} torr. Hydrogen molecules

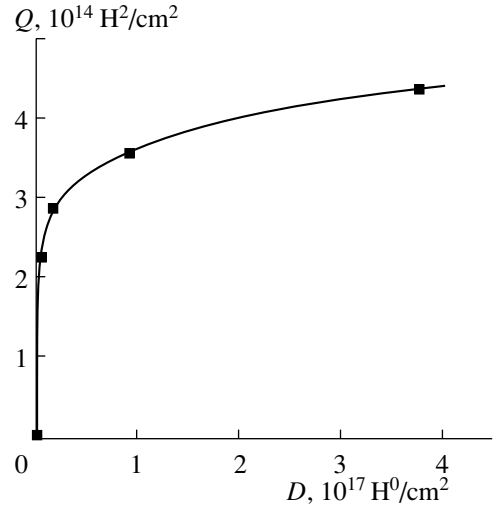

Fig. 1. Number of H^0 atoms desorbing from 1 cm^2 of the pyrolytic graphite surface vs. irradiation dose.

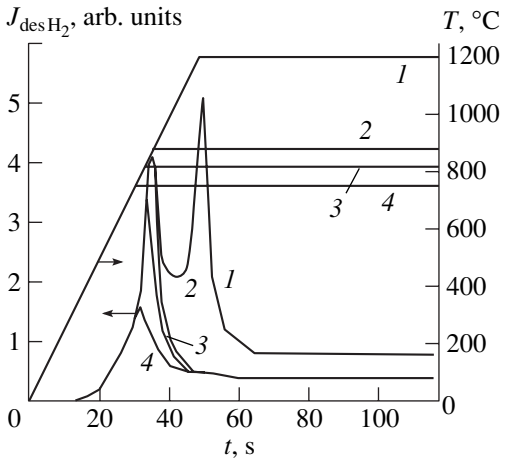

Fig. 2. Kinetic curves for hydrogen thermal desorption from graphite that were obtained after the sorption of H^0 atoms. Heating is stopped at the temperatures (*1*) 1200, (*2*) 880, (*3*) 820, and (*4*) 750°C. The heating rate is 25°C/s.

dissociated into neutral atoms on an atomizer—a fine tungsten wire heated to 2500°C. The atomizer was located parallel to the sample surface at a distance of 5–8 mm. In our experiments, the flux of incident hydrogen atoms was equal to $\sim 5 \times 10^{13}$ $H^0/(cm^2\ s)$ [8].

To determine the amount of hydrogen absorbed and to investigate the kinetics of absorption–desorption processes, we applied the TDS method. Today, different modifications of this method are well known and widely used in investigating the kinetics of gas–solid interactions [9]. If the temperature of the sample exposed to the flow of hydrogen atoms is increased, the gas sorbed (or its portion) leaves the sample. As a result, the pressure in the vacuum system grows, which is detected by a sector magnetic mass spectrometer. By measuring the change in the partial pressure during the heating of the sample, it is easy to find the amount of hydrogen desorbed provided that the pump capacity is known [10]. For a number of the samples, the kinetics of hydrogen release was also investigated in order to make sure that the process is similar to that described in [8]. In our experiments, the sample was heated by the linear law from some initial temperature T_0: $T = T_0 + \alpha t$, where α is the rate of heating and t is time. By varying the rate of heating, one can easily evaluate the energy of activation of desorption (see, for example, [11]).

The surface morphology was examined with a P4-SPM-MDT atomic force microscope operating in the contact mode and with a scanning tunneling microscope of the original design that provides an atomic resolution in studying the surface of graphite layers [12]. STM tunnel tips were prepared by etching tungsten wires in a 2 M NaOH solution with subsequently cleaning them in a vacuum by electron bombardment. The tunnel current upon scanning was maintained in the interval 0.1–5 nA to minimize noise. Samples for surface morphology examination were prepared in the same way as for the investigation of the hydrogen release kinetics. Then, they were taken out of the vacuum chamber and studied under environmental conditions.

EXPERIMENTAL RESULTS

The initial surface of the samples has extended regions of atomically smooth planes. At large scan fields, one can see clear-cut atomic steps (AFM image) and the distinct atomic structure (STM image). Long-term exposure of the samples to molecular hydrogen in the chamber (cold atomizer) does not lead to hydrogen absorption by graphite [3, 8]. Correspondingly, no changes in the surface morphology of graphite are observed.

Unlike molecular hydrogen, atomic hydrogen is vigorously sorbed by pyrolytic graphite [3, 8]. The rise in the temperature of the samples, after they have been irradiated by hydrogen atoms, causes a large amount of H_2 and a minor (less than 1%) amount of light hydrocarbon molecules to release. Figure 1 shows the amount of the hydrogen desorbed (per 1 cm^2 of the surface area) as a function of the H^0 irradiation dose. Hereafter, by the irradiation dose, we mean the product of the atomic flux (per 1 cm^2 of the surface) and the exposure time of the sample. It is worth noting that the efficiency of hydrogen atom capture by the graphite surface (the ratio of the number of atoms striking the surface to the number of those remaining in the sample) does not exceed 3–4% even at the initial stage of the sorption process. As the irradiation dose increases, the capture efficiency drops and the amount of hydrogen sorbed tends to saturation at doses on the order of $(2–4) \times 10^{17}$ H^0/cm^2.

A detailed analysis of the kinetic curves of thermal desorption was performed in [8]. Below, we only

briefly outline the basic results. The time dependence of the rate of H_2 desorption from the atomic-hydrogen-irradiated sample heated at a constant rate of 25°C/s has two sharp maxima at temperatures about 850 and 1250°C [8]. The temperatures corresponding to the maximal desorption rates (at a constant heating rate) were independent of the amount of hydrogen sorbed, which is characteristic of first-order desorption kinetics. The first order of desorption kinetics means that the formation of H_2 molecules from the atoms is not the limiting stage of hydrogen release. A characteristic feature of hydrogen release from the graphite is the rapid (for 20–30 s) decrease in the desorption rate almost to zero when heating is stopped (Fig. 2). Note that hydrogen release from the sample ceases although a significant amount of the gas still remains in the sample. However, with the further rise in the temperature, hydrogen evolves from the sample again (Fig. 3). The analysis performed in [8] demonstrates that the kinetics of adsorption–desorption processes in an atomic hydrogen–graphite system can adequately be described if it is assumed that the graphite has two types of traps the capture by which is accompanied by diffusion. However, only from kinetic measurements, it is virtually impossible to draw any conclusions concerning the physical nature of trapping centers, as well as the localization of hydrogen captured. Nevertheless, certain suggestions can be made. One is that during sorption, hydrogen atoms penetrate into the sample and become trapped between graphite layers; i.e., we are dealing with the process of intercalation.

The surface morphology was examined on samples exposed to hydrogen atoms for 2.5, 30, 60, and 125 min at temperatures of 50–70°C (with or without subsequent thermal desorption), as well as on those underwent several exposure–desorption cycles. The irradiation dose was varied between 7.5×10^{15} (2.5 min) and 3.75×10^{17} H^0/cm^2 (125 min). According to Fig. 1, these values correspond to the hydrogen concentrations in the samples from 2.2×10^{14} to 4.3×10^{14} H/cm^2. After the exposure to atomic hydrogen (before thermal desorption), the initially smooth surfaces facing the atomizer become rough, with the asperity height being equal to several nanometers (Figs. 4, 5). The hydrogen-exposed surfaces feature increased scan noise as compared to the initial surfaces. The figures presented allow us to conclude that, as the exposure time increases, the mean lateral sizes of the asperities diminish but their density grows. At the same time, the back sides of the samples (not exposed to the atoms) remain unchanged.

After hydrogen thermal desorption, the scan noise markedly decreases, the surface is smoothed out, and the fine, down to the atomic scale, relief can be resolved. The probe techniques detect many pits about 3 Å in depth on the surface (Fig. 6) (the spacing between graphite layers is approximately 3.35 Å). The distribution of the pits over the surface is nonuniform: from several tens per 1 μm^2 to zero. In addition, their

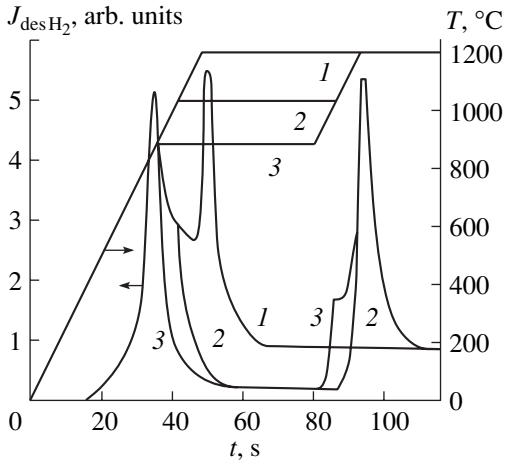

Fig. 3. Hydrogen desorption kinetics. Linear heating was stopped at the temperatures (*3*) 880 and (*2*) 1030°C and then was continued to (*1*) 1200°C. The heating rate 25°C/s.

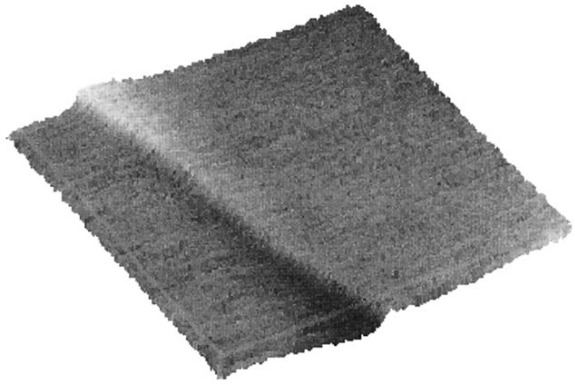

Fig. 4. AFM image of the graphite surface (1 × 1 μm) after outgassing but before interaction with atomic hydrogen. The asperity height is 0.8 nm.

density randomly changes when the probe moves along the length and width of the sample. When the time of exposure to hydrogen atoms increases or sorption–thermal desorption cycling takes place, the lateral sizes of the pits grow and they partially coalesce. Simultaneously, new pits also of a monoatomic depth start to grow at the bottom of the large pits (Fig. 7). On the back side of the samples, the pits are absent even if sorption–desorption cycles are repeated many times.

It is interesting to note that the long-term storage (for several weeks) of the samples exposed leads to a decrease in the scan noise and to smoothing the surface relief, as is the case with thermal desorption.

DISCUSSION

The surface morphology examination shows that the irradiation of the graphite by hydrogen makes its surface rough (the asperities disappear in the course of

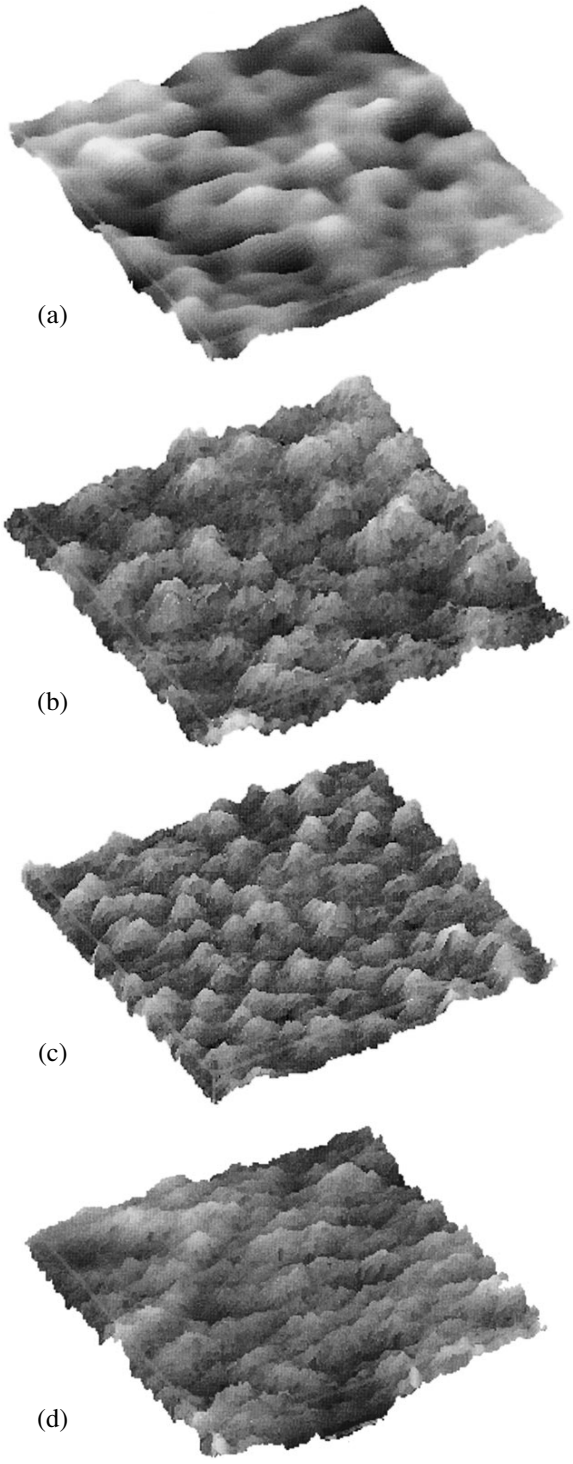

Fig. 5. AFM image of the graphite surface (1×1 μm) after the sorption of atomic hydrogen. Irradiation dose (asperity height) is (a) 7.5×10^{15} (2.76), (b) 8.9×10^{16} (4.1), (c) 1.78×10^{17} (3.4), and (d) 3.75×10^{17} H^0/cm^2 (5.5 nm).

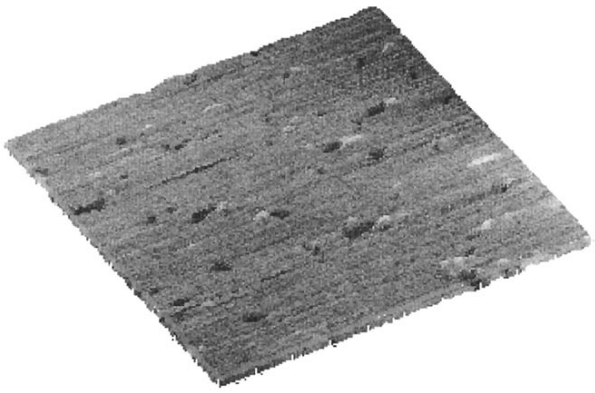

Fig. 6. AFM image of the graphite surface (1×1 μm) after 30-min exposure to hydrogen atoms and subsequent thermal desorption. The asperity height is 0.5 nm.

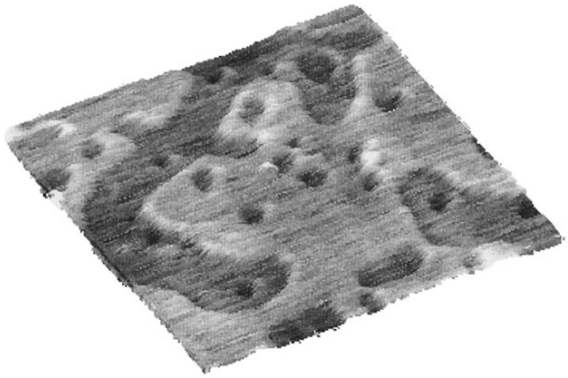

Fig. 7. AFM image of the graphite surface (0.33×0.33 μm) after six 30-min exposure to atomic hydrogen–thermal desorption cycles. The asperity height is 1.6 nm.

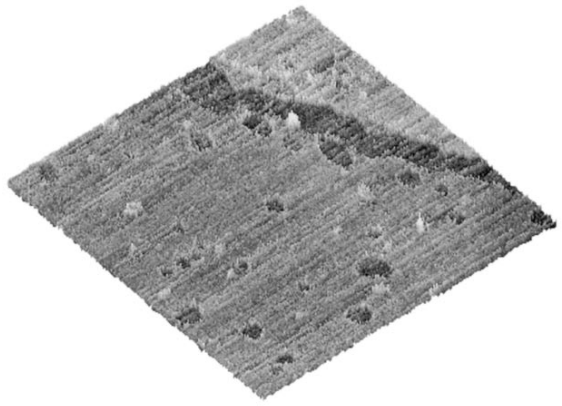

Fig. 8. STM image of the graphite surface (1×1 μm) after six 30-min exposure to atomic hydrogen–thermal desorption cycles. The asperity height 2.2 nm.

thermal desorption) and initiates a set of pits on the surface. The lateral size of the pits increases with exposure time. The weak dependence of the asperity height on the exposure time demonstrates that the near-surface region saturates very rapidly (Fig. 1): the amount of hydrogen being released at thermal desorption after a 125-min exposure is only twice as large as that after the exposure for 2.5 min. The appearance of asperities on

the surface confirms, in our opinion, the above assumption that atomic hydrogen penetrates into the near-surface graphite layers rather than is sorbed on its surface. In the latter case, a relief such as in Fig. 5 would hardly be probable to occur. Another point in favor of hydrogen accumulation in the near-surface layers is the increase in the scan noise, which is associated with a change in the mechanical properties of the surfaces exposed.

The appearance of the pits on the surfaces is the result of the erosion of the graphite surface during interaction with atomic hydrogen. The growth of the pits is irreversible. It seems likely that they begin to appear as soon as the hydrogen atoms strike the surface. However, the monolayer-deep pits are difficult to detect on the rough "noisy" surface. After the hydrogen is thermally desorbed, they are distinctly detected by the probe techniques. The increase in the exposure time results in the growth of the lateral pit sizes. The pits coalesce, and, thus, graphite planes are removed layer by layer (Fig. 7). The pit density strongly vary even between regions 100–200 μm distant from each other. One can therefore assume that the pits originate primarily at initially defect sites of the graphite surface. The essential role of defects during the erosion of the graphite surface was observed in [13, 14]. In the former article, the effect of high temperatures on the graphite surface under environmental conditions was studied; in the latter, oxygen–graphite interaction under UV irradiation was investigated at room temperature. In [14], it is assumed that only atomic oxygen or ozone can cause erosion, which develops where surface defects exist. Such surface defects may be, for example, atomic vacancies or steps. Where there are one or more dangling carbon bonds, hydrogen more readily reacts to produce volatile hydrocarbon compounds. The carbon atoms are removed, and pits form. It is not surprising that the distribution of defects over the surface is nonuniform. As is known, the density of defects (after removing the upper graphite layers with the help of an adhesive tape) varies from site to site by several orders of magnitude [13]. That the origination and evolution of erosion are defect-related is indirectly confirmed, in our case, by the sharp increase in the concentration of the pits at the steps (Fig. 8). In addition, the spontaneous formation of defects on the surface immediately during the irradiation must not be ruled out. The equal depths of the pits can be explained by the fact that the layers of pyrolytic graphite adhere to each other only via Van der Waals bonds. Therefore, if a defect is in an upper atomic layer, an undamaged underlying layer is not subjected to erosion. Hence, the pits grow only in the lateral direction, with the depth remaining equal to one monolayer.

Of interest is also the fact of surface smoothing after the samples have been stored under environmental conditions for a long time. We did not perform detailed investigations into this phenomenon, and its mechanism is still unclear. Hypothetically, there are unknown catalytic mechanisms of absorbed hydrogen release that are not so energy-consuming as hydrogen thermal desorption under a high vacuum.

CONCLUSION

Thus, the AFM and STM investigations of the interaction between atomic hydrogen and the graphite surface discovered the significant changes in the morphology of the surface. Being initially atomically smooth, it becomes rough when exposed to atomic hydrogen. This is related to the penetration of the hydrogen into the near-surface graphite layers during sorption. Under the graphite surface, hydrogen atoms recombine to form molecules, which exert an excess pressure. This pressure results in surface bulging, which is reversible and disappears after removing the hydrogen from the graphite. Simultaneously, the surface is covered by etch pits. This is associated with the partial desorption of the hydrogen in hydrocarbon compounds. The growth of the pits over the surface and the origination of new ones, as the exposure time increases or sorption–desorption cycles are repeated, indicates the effective mechanism of graphite erosion in atomic hydrogen.

REFERENCES

1. X. Chu, L. D. Schmidt, S. G. Chen, *et al.*, J. Catal. **140**, 543 (1993).
2. V. Phillips, E. Vietzke, M. Erdweg, *et al.*, J. Nucl. Mater. **145–147**, 292 (1987).
3. E. Denisov, T. Kompaniets, A. Kurdyumov, *et al.*, J. Nucl. Mater. **233–237**, 1218 (1996).
4. A. A. Haasz, J. V. Davis, O. Auciello, *et al.*, J. Nucl. Mater. **145–147**, 412 (1987).
5. R. A. Causey, J. Nucl. Mater. **162–164**, 151 (1989).
6. T. Tanabe and Y. Watanabe, J. Nucl. Mater. **179–181**, 231 (1991).
7. M. Balooch and D. R. Olander, J. Chem. Phys. **63**, 4772 (1975).
8. E. A. Denisov and T. N. Kompaniets, Zh. Tekh. Fiz. **71** (2), 111 (2001) [Tech. Phys. **46**, 240 (2001)].
9. R. G. Greenler, in *Surface Science: Recent Progress and Perspectives*, Ed. by T. S. Jayadevaiah and R. Vanselow (CRO Press, Cleveland, 1974; Mir, Moscow, 1977), Vol. 2.
10. Yu. I. Belyakov and T. N. Kompaniets, Zh. Tekh. Fiz. **42**, 855 (1972) [Sov. Phys. Tech. Phys. **17**, 674 (1972)].
11. D. Woodruff and T. Delchar, *Modern Techniques of Surface Science* (Cambridge Univ. Press, Cambridge, 1986; Mir, Moscow, 1989).
12. L. N. Bolotov, Z. Vakar, N. R. Gall', *et al.*, Fiz. Tverd. Tela (St. Petersburg) **40**, 1570 (1998) [Phys. Solid State **40**, 1423 (1998)].
13. H. Chang and A. J. Bard, J. Am. Chem. Soc. **113**, 5588 (1991).
14. S. Ozeki, T. Ito, K. Uozumi, *et al.*, Jpn. J. Appl. Phys. **35**, 3772 (1996).

Translated by Yu. Vishnyakov

Technical Physics, Vol. 46, No. 6, 2001, pp. 778–781. Translated from Zhurnal Tekhnicheskoĭ Fiziki, Vol. 71, No. 6, 2001, pp. 139–142.

BRIEF COMMUNICATIONS

Magnetooptical Faraday Effect in $La_{0.7}Sr_{0.3}MnO_{3-\delta}$ Films

Yu. P. Sukhorukov, A. M. Moskvin, N. N. Loshkareva, I. B. Smolyak, V. E. Arkhipov, Ya. M. Mukovskiĭ, and A. V. Shmatok

Institute of Metal Physics, Ural Division, Russian Academy of Sciences, Yekaterinburg, 620219 Russia

e-mail: suhorukov@imp.uran.ru

Received September 25, 2000

Abstract—The Faraday effect spectra were measured in $La_{0.7}Sr_{0.3}MnO_{3-\delta}$ films. A band attributed to *d–d* transitions $^4A_{2g} - {}^4T_{2g}$ in Mn^{4+} ions or octahedral complexes $(MnO_6)^{8-}$ was observed in the spectral region of ~2.7 eV. The position and value of the maximum of the Faraday rotation band and the figure of merit were found to depend on the degree of charge and magnetic uniformity of the films. The films can be used to develop magnetooptical modulators. © *2001 MAIK "Nauka/Interperiodica".*

The metal-to-insulator transition in lanthanum manganites with colossal magnetoresistance is accompanied by sharp changes in resistivity and light absorption. Lanthanum manganites with such properties can be used in various optoelectronic devices [1]. To determine possible applications of lanthanum manganites in engineering, it is necessary to study their magnetooptical properties. In addition, the study of magnetooptical effects provides information about electron transitions and the electron and spin structure of lanthanum manganites. The goal of this work was to study the Faraday effect in $La_{0.7}Sr_{0.3}MnO_{3-\delta}$ (LSMO) films.

Single-crystal LSMO films (thickness, 900 Å) were grown on $SrTiO_3$(100) (STO) substrates using the technique of ion-plasma evaporation in an $Ar : O_2$ (4 : 1) atmosphere at a pressure of 1–8 torr. The substrate temperature during evaporation was 600°C (film *1*) or 480°C (film *2*). The *c* axis of the film was perpendicular to the substrate surface. The chemical composition of the films, as well as the temperature dependence of their electric resistance, was described in the preceding work [2]. The maximum resistivity near the metal-to-insulator transition was attained at a temperature T_ρ of 227 K (film *1*) and 165 K (film *2*). The behavior of the resistivity of the films within the temperature range from T_ρ to 300 K was semiconductor-like; below T_ρ, the resistivity behavior was metal-like. The maximum resistivity of film *2* was almost two times higher than that of film *1*.

A double-beam optical setup based on the MDR-12 spectrometer was used to detect the Faraday effect. Upon passing through a polarizer and the sample, a monochromatic beam was split by a Wollaston prism into two beams. The prism was used as an analyzer for the two beams. The angle between the polarization planes of the polarizer and the Wollaston prism was 45°. Therefore, the intensities of the two beams were equal. The Faraday effect changed the beam intensities. The difference in the intensities of the beams was detected using an electronic system (*Y*). The magnetic field was directed in parallel to the film surface. The angle of incidence of light on the film surface was 68°. The value of specific Faraday rotation was determined from the equation $F = Q_F/(d\sin(\varphi))$, where *d* is the optical path in the film; φ is the angle between the direction of light propagation in the film and the normal to the film surface. The value of Q_F was calculated from the formula $Q_F = (\Delta Y K_1)/(8 Y_0 K_2)$, where ΔY is the difference in signals for two directions of the magnetic field; Y_0 is the signal generated by one of the beams in the absence of the plane-of-polarization rotation; and K_1 and K_2 are the coefficients of amplification of ΔY and Y_0, respectively. The spectra of Faraday rotation in the films were measured within a range of 2 to 3 eV in magnetic fields up to 1 kOe. The temperature range was 90–300 K. The spectra of light absorption in the films were measured within a range of 0.1 to 2.5 eV.

A typical absorption spectrum for $La_{0.7}Sr_{0.3}MnO_{3-\delta}$ films, in which the Faraday effect was observed, is shown in Fig. 1. A band is observed in the spectrum at 1.5 eV. The band maximum shifts toward a lower energy on cooling within the ferromagnetic range. An increase in the absorption is observed at energies higher than 2 eV. The temperature dependence of the intensity of light passed through the film in the region of light interaction with free charge carriers at an energy of 0.18 eV ($\lambda = 7$ μm) shows a bend at $T = 227$ K (see inset in Fig. 1). This temperature is equal to the temperature T_ρ, at which the resistivity maximum was observed. Such a change in the light intensity in the region of light interaction with charge carriers is typical of lanthanum manganites [1, 3].

1063-7842/01/4606-0778$21.00

Low-energy (2.4 eV) and high-energy (5.2 eV) bands are revealed in the spectra of optical conductivity of manganites $LaMnO_3$ [4]. These bands can be attributed to the *d–d* transition ${}^5E_g$–${}^5T_{2g}$ in Mn^{3+} ions and the lowest energy charge-transfer transition O2*p*–Mn3*d* in octahedral complexes $(MnO_6)^{9-}$, respectively [5]. Introduction of Ca^{2+} and Sr^{2+} ions (hole doping) causes a significant change in the optical properties of manganites within a wide spectral range. The low-energy (2.4 eV) band intensity decreases sharply, whereas the high-energy band shifts toward a lower energy. The spectral weight in general is shifted to the IR region. A sharp peak is observed at 1.5 eV [4]. The nature of this peak has been discussed at length in the literature. According to [4], the peak is caused by the charge-transfer transition O2*p*–Mn3*d*. Other researchers attributed this peak to various one-centered or two-centered *d–d* transitions. For example, according to [6], this absorption band can be caused by indirect transitions between occupied $e_{g\uparrow}^{(1)}$ and vacant $e_{g\uparrow}^{(2)}$ states. These $e_g^{(1)}$ and $e_g^{(2)}$ states belong to the e_g zone of Mn^{3+} ions. The e_g zone is split by the Jahn–Teller interaction. Such an electric-dipole *d–d* transition becomes possible because of hybridization of the e_g states of manganese with the 2*p* states of oxygen. The band shift and the increase in the IR absorption coefficient in the ferromagnetic region are caused by the contribution of the free charge carriers and redistribution of the spectral weight toward a lower energy [3]. In our opinion, such a transition can be also caused by the *d–d* transition ${}^5E_g$–${}^5T_{2g}$ in Mn^{3+} ions screened from the crystal field by the hole density located partially in nearby oxygen ions.

The largest part of the optical data on manganites was obtained by processing reflection spectra. This method did not allow many important effects to be observed and studied. These effects are caused by relatively weak *d–d* transitions and forbidden charge-transfer transitions. Though weak, these transitions are of high information value, in particular, such transitions as those in Mn^{4+} ions or octahedral complexes $(MnO_6)^{8-}$. The occurrence of these complexes in $La_{1-x}Sr_xMnO_3$ systems is due to hole doping. Magnetooptical studies of such transitions in pyrochlorine compounds of $A_2Mn_2O_7$ with the octahedral complexes $(Mn^{4+}O_6)^{8-}$ were performed within a spectral range of 1.5 to 4.5 eV using the Kerr effect [7]. Spectral bands at 2.6 and 3.1 eV were attributed to *d–d* transitions ${}^4A_{2g}$–${}^4T_{2g}$ and ${}^4A_{2g}$–${}^4T_{1g}$ in Mn^{4+} ions or the octahedral complexes $(MnO_6)^{8-}$, respectively. A band at 3.8 eV and a high-intensity band with a maximum at $E \geq 4.3$ eV can be attributed to forbidden and allowed charge-transfer transitions, respectively. This suggestion is sufficiently consistent with the data given in [8]. These data are based on measurements of the luminescence spectra of manganites. Thus, a study of the magnetooptical spectra of doped manganites could provide valuable information on Mn^{4+} ions, to which the unique properties of these oxides are attributed.

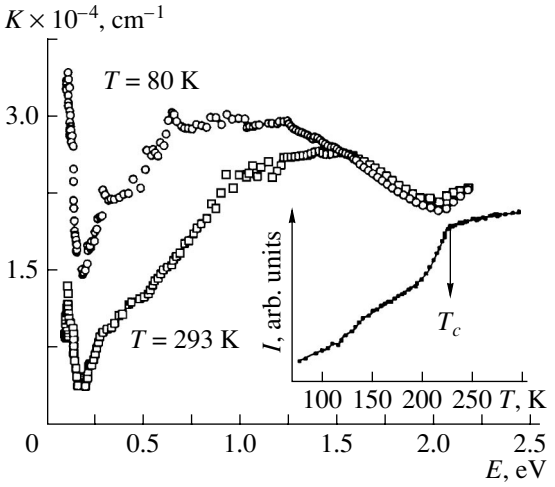

Fig. 1. Absorption spectrum of a $La_{0.7}Sr_{0.3}MnO_3$ film on a $SrTiO_3$ substrate at two temperatures. Inset: the temperature dependence of the intensity of light passed through the film at 0.18 eV (λ = 7 μm).

The Faraday effect in $La_{1-x}Ca_xMnO_3$ manganites within a range of 1.5 to 3.0 eV was studied only in [9]. Significant Faraday rotation with maximums located presumably at 1.2 and 3.1 eV was observed. However, work [9] does not contain any comprehensive analysis of the spectral and temperature dependences. The magnetooptical Kerr effect in $La_{1-x}Sr_xMnO_3$ within a range of 0.9 to 5.3 eV was studied in [10]. Spectral dependences of the complex polar Kerr effect or, more precisely, the off-diagonal components of the permittivity tensor calculated from these dependences were processed using a simple two-oscillator model. This model provides an adequate description of the low-frequency band with a maximum at 1.2 eV. However, the deviation of the calculated contribution of a single oscillator with an energy of 3.1 eV from the spectral behavior observed within a range of 2 to 5 eV goes far beyond the limits of error. The magnetooptical activity within the range under consideration was attributed in [10] to the charge-transfer transitions O2*p*–Mn3*d*. The Kerr effect in epitaxial films $(La_{0.35}Pr_{0.35})Ca_{0.3}MnO_3$ was measured within a spectral range of 1.5 to 3.8 eV [11]. A high-intensity magnetooptical transition centered at 2.7–3.0 eV was observed. Generally speaking, in the LSMO films under consideration, Mn^{4+} ions are expected to exhibit a high magnetooptical activity between 2 and 3 eV.

A band at $\hbar\omega$ = 2.69 eV was observed in the specific Faraday rotation spectrum of the film *1* at 90 K (Fig. 2). The Faraday effect value at the maximum was ~25 000 deg/cm. The Faraday rotation band in the spectrum of film *2* was shifted toward a higher energy. The Faraday effect value at the maximum (2.72 eV) was

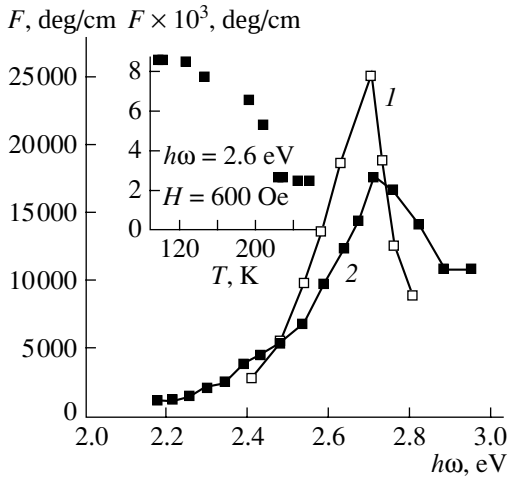

Fig. 2. Spectra of the specific Faraday rotation in $La_{0.7}Sr_{0.3}MnO_3$ films at T = 90 K and H = 0.06 T: (*1*) film with T_c = 228 K and (*2*) film with T_c = 165 K. Inset: the temperature dependence of the Faraday rotation at 2.6 eV in the film *1*.

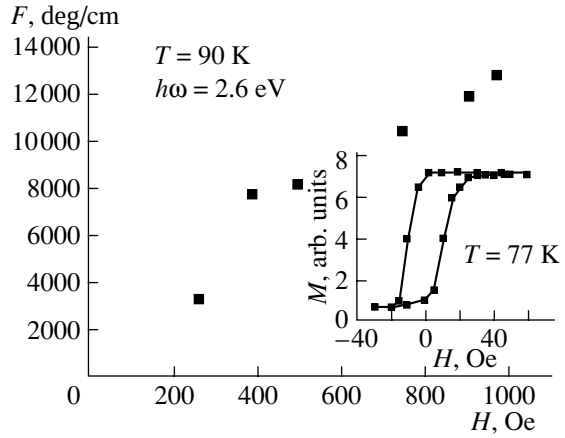

Fig. 3. Magnetic field dependence of the specific Faraday rotation in the $La_{0.7}Sr_{0.3}MnO_3$ film (film *1*) at 90 K and 2.6 eV. Inset: the magnetization hysteresis loop at 77 K (film *1*).

~18000 deg/cm. As reported in [9], a shoulder of ~25000 deg/cm was observed in the Faraday rotation spectrum of a $La_{0.7}Ca_{0.3}MnO_3$ film at 2.7 eV and a temperature of 100 K.

Comparison of the data obtained in this work with the results of the spectroscopic study of octahedral ions Mn^{4+} presented in [7, 8] allows the band at 2.7 eV to be attributed to the *d–d* transitions $^4A_{2g}$–$^4T_{2g}$ in Mn^{4+} ions. The magnetooptical activity of these transitions is caused by the exchange interaction and the spin–orbit interaction in $^4T_{2g}$ states with an effective orbital moment of L = 1. The volume of the magnetooptically active ferromagnetic phase in a film is determined by the presence of Mn^{4+} ions. Films of the same chemical composition may differ from each other in the number of ions. Presumably, the variations in the number of ions are caused by the nonstoichiometric oxygen composition of films. Donors (oxygen vacancies) compensate acceptors (Mn^{4+} ions) produced by Sr doping. The value of the Faraday rotation in film *2* is lower than in film *1*, presumably because the ferromagnetic phase volume in film *2* is smaller than in film *1*. The asymmetric shape of the bands is most probably caused by inhomogeneous broadening, as well as the proximity of the $^4A_{2g}$–$^4T_{1g}$ transition in Mn^{4+} ions, with a maximum at 3.1 eV [7, 8].

The temperature dependence of the specific Faraday rotation $F(T)$ in film *1* was measured at 2.6 eV in a magnetic field H of 600 Oe (see inset in Fig. 2). Curve $F(T)$ provides information about the temperature dependence of magnetization. The tail of the curve is extended. It can be assumed on the basis of curve $F(T)$ that the film contains several ferromagnetic regions with different T_c. Regions with an effective Curie temperature of $T_c \approx 228$ K make the largest contribution to the value of Faraday rotation (at $T \approx 228$ K, the first derivative of $F(T)$ is maximum). The temperature dependence of the intensity of light passed through the film shows a bend almost at the same temperature ($T \approx$ 227 K; see inset in Fig. 1). Using the same method, the Curie temperature T_c of film *2* was found to be approximately 165 K. The Curie temperatures of the films under study are considerably lower than T_c of single crystals and polycrystals of the same composition. Probably, this is also caused by the nonstoichiometric oxygen composition of films. Extended tails of the temperature dependences of the Faraday effect show that the films are magnetically nonuniform. Stresses caused by a 0.57% mismatch of the lattices of the STO substrate and $La_{0.7}Sr_{0.3}MnO_{3-\delta}$ film also induce various nonuniformities in the films.

The saturation magnetization H_s of the films was measured in the magnetic field parallel to the film surface at a temperature of 77 K using a vibrating-coil magnetometer. A saturation magnetization of H_s ~ 10 Oe was attained in fields of very low intensity. This indicates that the LSMO films have easy-plane anisotropy. The hysteresis loop is rectangular (see inset in Fig. 3). Similar results were obtained in [12] (measurements of magnetization of an LSMO film on the STO substrate using a vibrating-coil magnetometer; T_c = 350 K) and [13] (measurements of the Kerr effect). In these works, the saturation magnetization was attained in a magnetic field of ~5 Oe at a temperature of ~300 K.

The magnetic field dependence of the specific value of the Faraday effect in film *1* was measured in fields far exceeding H_s. As seen from Fig. 3, the Faraday effect saturation was not attained in magnetic fields of up to 1000 Oe at a temperature of 90 K and a photon energy of 2.6 eV. The magnetic field was parallel to the film surface during measurements of the Faraday effect, as well as during measurements of the saturation

magnetization. Therefore, a significant slope of the curve $F(H)$ in magnetic fields exceeding H_s is indicative of a considerable paraprocess in the film within a field range of up to 1000 Oe. This fact also substantiates the conclusion that the films under study are magnetically nonuniform. Thus, an increase in the nonuniformity of films causes an increase in the electrical resistance and a decrease in the value of the magnetooptical Faraday effect.

The figure of merit of LSMO films was evaluated from the measurement data of the absorption coefficient K for film *1* (Fig. 1) and a specific Faraday effect (Fig. 2): $D = 2F/K = 0.2$ at 2.69 eV and 90 K. Presumably, the figure of merit of the LSMO films can be increased by increasing the magnetic uniformity of these films. Films with increased figures of merit can be used in modulators based on the Faraday effect for light modulation at room temperature.

Thus, a high-intensity magnetooptical band centered at ~2.7 eV was observed in $La_{0.7}Sr_{0.3}MnO_{3-\delta}$ films. This band was attributed to the ${}^4A_{2g}$–${}^4T_{2g}$ transition in Mn^{4+} ions. The spectral, temperature, and magnetic field dependences of the Faraday effect show that the electronic and spin structures of the films under study are nonuniform. Developing methods for controlling of these nonuniformities would increase the practical value of the films under study.

ACKNOWLEDGMENTS

This work was supported by INTAS (project no. 97-30253) and the Russian Foundation for Basic Research (project no. 99-02-16280).

REFERENCES

1. Yu. P. Sukhorukov, N. N. Loshkareva, E. A. Gan'shina, *et al.*, Pis'ma Zh. Tekh. Fiz. **25** (14), 6 (1999) [Tech. Phys. Lett. **25**, 551 (1999)].
2. Ya. M. Mukovskii and A. V. Shmatok, J. Magn. Magn. Mater. **196–197**, 136 (1999).
3. N. N. Loshkareva, Yu. P. Sukhorukov, V. E. Arkhipov, *et al.*, Fiz. Tverd. Tela (St. Petersburg) **41**, 475 (1999) [Phys. Solid State **41**, 426 (1999)].
4. K. Takenaka, K. Iida, Y. Sawaki, *et al.*, J. Phys. Soc. Jpn. **68**, 1828 (1999).
5. J. M. Coey, M. Viket, and S. von Molnar, Adv. Phys. **48**, 167 (1999).
6. J. H. Jung, K. H. Kim, and Y. W. Noh, Phys. Rev. B **57**, R11043 (1998).
7. E. A. Balykina, E. A. Ganshina, G. S. Krinchik, *et al.*, J. Magn. Magn. Mater. **117**, 259 (1992).
8. A. G. Paulusz and H. I. Burrus, Chem. Phys. Lett. **17**, 527 (1972).
9. J. F. Lawler, J. G. Lunney, and J. M. D. Coey, Appl. Phys. Lett. **65**, 3017 (1994).
10. S. Yamaguchi, Y. Okimoto, K. Ishibashi, *et al.*, Phys. Rev. B **58**, 6862 (1998).
11. E. A. Ganshina, O. Yu. Gorbenko, *et al.*, J. Phys.: Condens. Matter **12**, 2857 (2000).
12. C. Kwon, M. C. Robson, K. C. Kim, *et al.*, J. Magn. Magn. Mater. **172**, 229 (1997).
13. J. F. Bodo, D. Magnoux, R. Porres, *et al.*, J. Appl. Phys. **87**, 6773 (2000).

Translated by K. Chamorovskiĭ